R-09-25

Groundwater flow modelling of periods with periglacial and glacial climate conditions – Laxemar

Patrik Vidstrand, TerraSolve AB

Ingvar Rhén, SWECO Environment AB

Nada Zugec, Bergab

December 2010

Svensk Kärnbränslehantering AB
Swedish Nuclear Fuel
and Waste Management Co

Box 250, SE-101 24 Stockholm
Phone +46 8 459 84 00

ISSN 1402-3091
SKB R-09-25

Groundwater flow modelling of periods with periglacial and glacial climate conditions – Laxemar

Patrik Vidstrand, TerraSolve AB

Ingvar Rhén, SWECO Environment AB

Nada Zugec, Bergab

December 2010

Keywords: SKBdoc 1261677, Hydrogeology, Groundwater, Modelling, Permafrost, Ice sheet, Periglacial, Glacial, Laxemar

Abstract

As a part of the license application for a final repository for spent nuclear fuel at Forsmark, the Swedish Nuclear Fuel and Waste Management Company (SKB) has undertaken a series of groundwater flow modelling studies. These represent time periods with different hydraulic conditions and the simulations carried out contribute to the overall evaluation of the repository design and long-term radiological safety. This report is concerned with the modelling of a repository at the Laxemar-Simpevarp site during periglacial and glacial climate conditions as a comparison to corresponding modelling carried out for Forsmark /Vidstrand et al. 2010/.

The groundwater flow modelling study reported here comprises a coupled thermal-hydraulic-chemical (T-H-C) analysis of periods with periglacial and glacial climate conditions. The objective of the report is to provide bounding hydrogeological estimates at different stages during glaciation and deglaciation of a glacial cycle at Laxemar. Three cases with different climate conditions are analysed here: (i) Temperate case, (ii) Glacial case without permafrost, and (iii) Glacial case with permafrost. The glacial periods are transient and encompass approximately 13,000 years. The simulation results comprise pressures, Darcy fluxes, and water salinities, as well as advective transport performance measures obtained by particle tracking such as flow path lengths, travel times and flow-related transport resistances. The modelling is accompanied by a sensitivity study that addresses the impact of the following matters: the direction of the ice sheet advance and the bedrock hydraulic and transport properties**.**

Sammanfattning

I Svensk Kärnbränslehanterings (SKB) ansökan om ett slutförvar för använt kärnbränsle i Forsmark ingår olika grundvattenmodelleringsstudier. Studierna hanterar perioder med olika hydrauliska förhållanden och beräkningsresultaten från simuleringarna bidrar till bedömningsunderlaget inom design och långsiktig säkerhet. Denna rapport presenterar modelleringsresultat för Laxemar-Simpevarp under periglaciala och glacial klimatförhållande i jämförande syfte med likvärdiga resultat för Forsmark /Vidstrand et al. 2010/.

Resultaten som redovisas i denna rapport kommer från en kopplad termisk-hydraulisk-kemisk (T-H-C) modell som simulerar grundvattenströmning under perioder med permafrost och inlandsis. Arbetet har som mål att via flödessimuleringar gränssätta diverse hydrogeologiska parametrar under olika skeden av nedisning och avsmältning i Laxemar. Simuleringarna omfattar tre fall med olika klimat: (i) tempererade förhållanden, (ii) glaciala förhållanden utan permafrost, och (iii) glaciala förhållanden med permafrost. De glaciala fallen är transienta och täcker en period av ca 13 000 år. Beräkningsresultaten omfattar tryck, darcyfluxer, grundvattnets salinitet, flödesvägar, advektiva transporttider och flödesrelaterat transportmotstånd. I arbetet ingår även en känslighetsstudie, som bland annat undersöker hur beräkningsresultaten påverkas av isen rörelsesriktning och bergets hydrauliska egenskaper.

Contents

1 Introduction

1.1 Background

The Swedish Nuclear Fuel and Waste Management Company (SKB) has conducted site investigations at two different locations, the Forsmark site and the Laxemar-Simpevarp site (Figure 1-1), with the objective of siting a final repository for spent nuclear fuel according to the KBS-3 concept. As a part of the application for a final repository for spent nuclear fuel at Forsmark[1], information from a series of groundwater flow modelling studies is evaluated to serve as a basis for an assessment of the repository design and long-term radiological safety premises. The present report is one of a series of three groundwater flow modelling studies that together handle different periods of the entire lifetime of a final repository at Laxemar-Simpevarp to provide a comparison to corresponding studies for Forsmark. The three reports are:

- Groundwater flow modelling of the excavation and operational phases – Laxemar /Svensson and Rhén 2010/.
- Groundwater flow modelling of periods with temperate climate conditions – Laxemar /Joyce et al. 2010/.
- Groundwater flow modelling of periods with periglacial and glacial climate conditions – Laxemar (this report).

1.2 Scope and objectives

The main objective of the work reported here is to provide quantifications of, and uncertainty indicators for, the effects on the performance measures studied by SKB (see section 1.3.4) as a function of the hydrogeological conditions associated with future periods with periglacial and glacial climate conditions at Laxemar-Simpevarp. Furthermore, the study is undertaken to strengthen the link between climate modelling and safety assessment, which was considered necessary by the authorities in their review of the SR-Can project /SKB 2006a/, see /Dverstorp and Strömberg 2008/[2].

To a large extent, the conclusions reached in this study are the results obtained, e.g. Darcy fluxes and fracture water salinities at repository level. Thus, the report presents and summarises the simulation results, but refrains from commenting on their safety implications. This is appropriate because such safety implications can only be evaluated when the results have been propagated through the safety assessment process.

1.3 Conceptual model

The literature review presented in /Vidstrand et al. 2010/ was undertaken with the objective of justifying hydraulic properties and boundary conditions of a groundwater flow model intended for a quantification of *bounding* hydraulic and chemical estimates during periglacial (permafrost) and glacial (ice sheet) conditions. This means that the objective of this report is different in several ways from the objectives of most periglacial and glacial studies reported in the literature, which generally are of a phenomenological character. The conceptual model behind the hydraulic properties and hydraulic top boundary condition applied here may be summarised as follows.

[1] The decision to go forward with developing the safety case for the Forsmark site was presented to the public in June 2009.

[2] In July 1 2008, the Swedish Radiation Safety Authority (SSM) replaced the former Swedish authorities, SKI and SSI, that reviewed the SR-Can project.

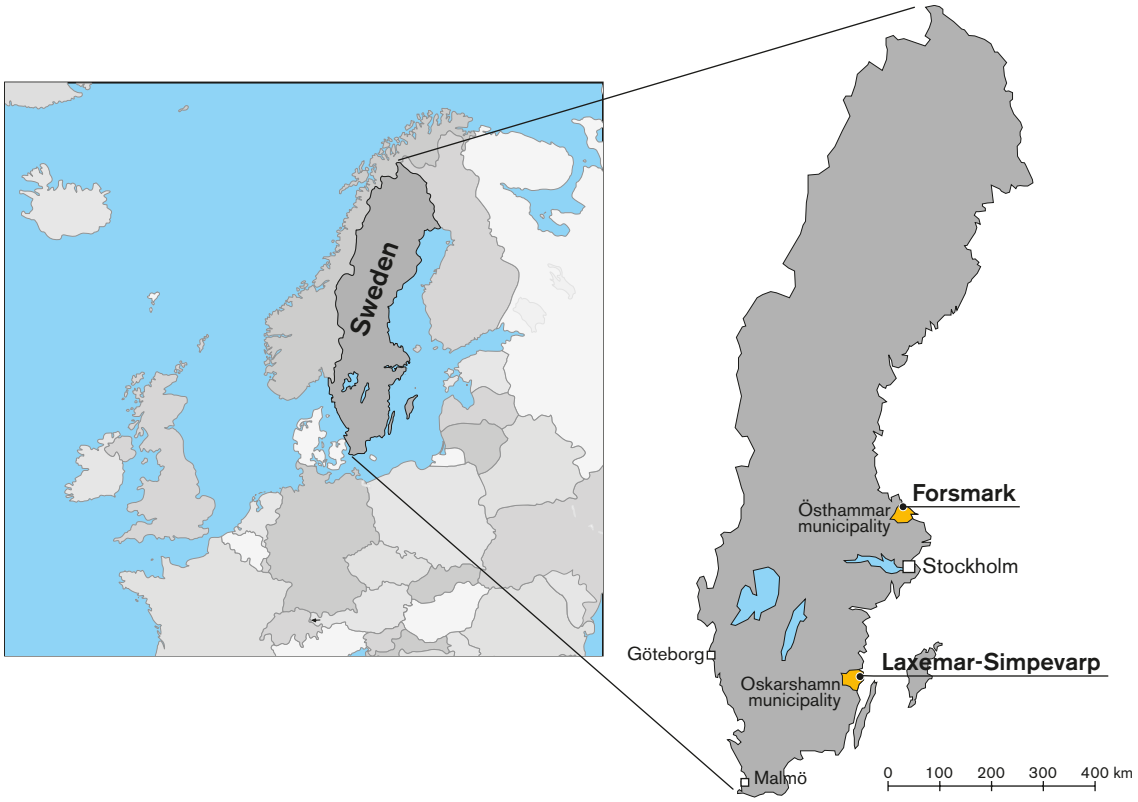

Figure 1-1. *Map of Sweden showing the location of the Forsmark and Laxemar-Simpevarp sites, located in the municipalities of Östhammar and Oskarshamn, respectively. (Source: Figure 1-1 in /SKB 2008/.)*

In front of an advancing ice sheet margin, the surface freezes because of low air temperatures. In the simulations that consider glacial conditions with permafrost, the freezing propagates into the subsurface and alters the flow and transport properties[3]. The freezing algorithm presented in /Vidstrand et al. 2010, Appendix A/ is used to modify the initial permeability values for water flow (hydraulic conductivity). The hydraulic properties derived during the site investigations at Laxemar-Simpevarp are in this regard considered as representative of initial, temperate, conditions, see Chapter 3 for an overview.

An infinite source of meltwater with a hydraulic head at the base of the ice sheet equal to 92% of the ice sheet thickness is assumed at all times in all simulations. The notion of a tongue of permafrost beneath the ice sheet margin can be simulated by assigning a lower hydraulic head beneath the ice sheet close to its margin. The imposed boundary condition implies that subglacial meltwater infiltrates the subsurface and flows from areas with high hydraulic heads to areas with lower hydraulic heads, where it discharges. The simulated discharge locations vary in space depending on the setup of the particular simulation considered. Likely locations of so-called taliks[4] are estimated from the forecast ongoing shoreline displacement /SKB 2006a/.

Finally, in accordance with the climate modelling in /SKB 2010/, subglacial runoff through structures embedded in the ice sheet or occurring at the ice/bedrock interface, e.g. sub-glacial meltwater tunnels, are not considered here. Further no mechanical coupling[5] is included, meaning that the classic hydraulic mass balance equation for transient groundwater flow is applied.

[3] For fractured crystalline rock below a thin layer of glacial till, which is the dominating stratigraphy in the Fennoscandian Shield, the scarceness of field information in the literature is evident compared with the database reported for other geological conditions.

[4] Taliks are unfrozen “holes” in the permafrost layer that can connect the flow system at depth with that close to surface.

[5] A simplified model of hydro-mechanical coupling is reviewed in /Vidstrand et al. 2010/.

1.3.1 Studied cases

The reference evolution in /SKB 2006a, 2010/ considers permafrost conditions in front of an advancing ice sheet margin. However, results for this case cannot be exported to the repository-scale and site-scale models of /Joyce et al. 2010/ as the hydraulic properties of the geosphere change continuously due to the presence of permafrost. Therefore, a Glacial case without permafrost in front of an advancing ice sheet margin constitutes a base case for all models (variant cases) treated in the work reported here including a Glacial case with permafrost in front of an advancing ice sheet margin, cf. cases (a) and (d) in Table 1-1. Another reason for the Glacial case without permafrost as a base case is that this case produces the largest hydraulic gradients at the ice sheet margin, hence the greatest effects on the studied performance measures with regard to Darcy flux and fracture (advective) flow salinity at repository depth.

The groundwater flow modelling of the base case is divided into three stages, pre-LGM[6], LGM and post-LGM, see Figure 1-2. During the pre-LGM stage, both unfrozen and frozen (permafrost) conditions are considered. During the LGM stage (not shown in Figure 1-2), the model domain is completely covered by a thick ice sheet for thousands of years. During the post-LGM stage, submerged conditions are considered in the area in front of the retreating ice sheet margin.

The glacial cycle simulated for Laxemar compromises approximately 13,000 years between the first ice front passage until the site once again becomes ice free, however sub-merged beneath a fresh water lake. The following flow simulations are carried out:

- **Pre-LGM stage.** Two different azimuth directions of ice sheet movement: 1. Advance from north-west, and 2. Advance from north; Two types of periglacial conditions: 1. No permafrost and 2. Permafrost in front of the ice sheet margin as well as 2 km beneath the tip of the ice sheet (permafrost tongue); Three types of permeability conditions: 1. Undistorted conditions, i.e. present-day conditions, 2. Elaborated permeability conditions based on an Elaborated Hydro DFN /Joyce et al. 2010, Appendix E/, i.e. variant of present-day conditions, and 3. Distorted conditions due to freezing and thawing.
- **LGM stage.** The period of complete ice coverage lasts approximately 11,000 years. During this time period groundwater flow is driven partly by buoyancy forces associated with the distorted salt water interface caused by the advancing ice sheet margin during the pre-LGM stage but mainly the small regional gradient caused by the slope of the ice sheet surface (2.1 m/km).
- **Post-LGM stage.** One azimuth direction of ice sheet movement (retreat from south-east); Submerged ground conditions in front of the ice sheet margin; Undistorted permeability conditions.

The different flow simulations are listed in Table 1-1. Figure 1-3 illustrates the differences between the main scenarios, without and with permafrost.

[6] LGM is a standard acronym used to denote the glacial maximum of the last glaciation (Weichsel), cf. /SKB 2010/.

1. Laxemar model domain (blue) vs SDM-Site model domain (red)

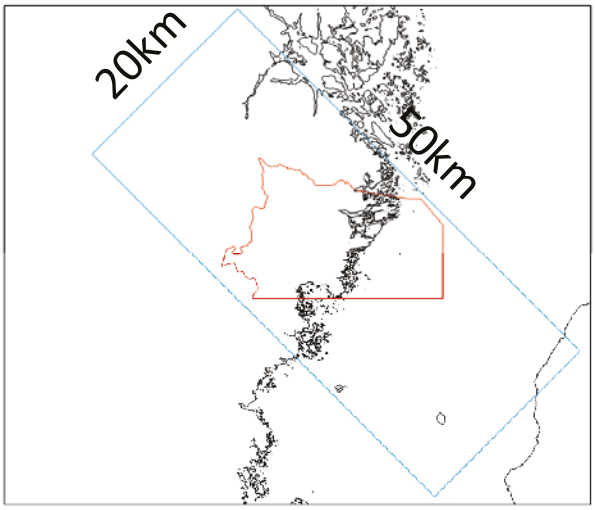

2. Hydraulic conditions for an advancing ice-sheet margin (pre-LGM)

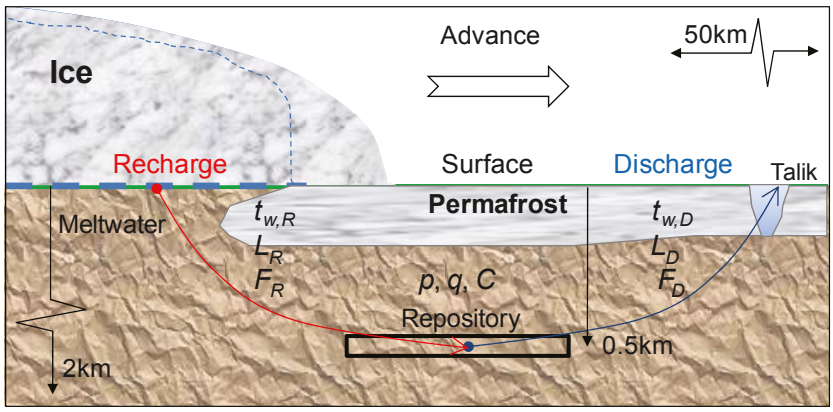

3. Hydraulic conditions for a retreating ice-sheet margin (post-LGM)

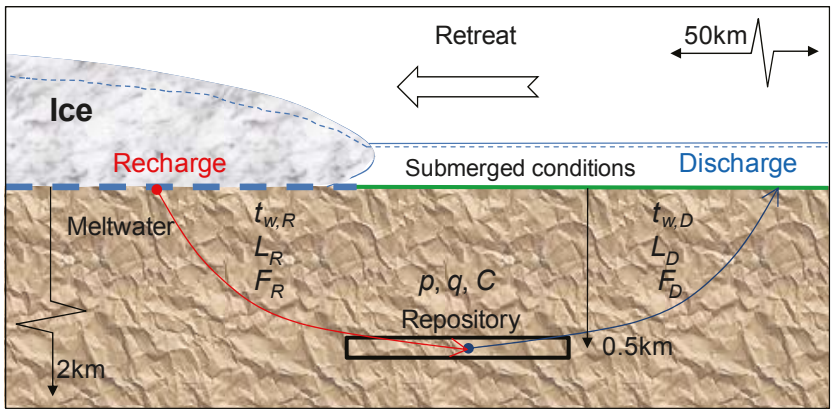

Figure 1-2. *Top: Map illustrating the size and location of the Laxemar model domain with regard to the model domain used in site-descriptive modelling (SDM-Site). Middle: Cartoon illustrating a repository beneath an advancing ice sheet margin with permafrost and taliks in the periglacial area in front of the margin. Bottom: Cartoon illustrating a repository beneath a retreating ice sheet margin with submerged ground conditions in front of the margin. The symbols shown denote the studied performance measures, see section 1.3.4. LGM = the glacial maximum of the last glaciation.*

Table 1-1. Overview of flow simulations. The main scenarios, A and B, are divided into four cases (a)–(d). The bullets indicate the particular conditions modelled with each case considered. Case (a) constitutes the base case in the work reported here.

A. Glacial climate conditions without permafrost		
(a)	**Pre-LGM stage** Ice sheet movement from north-west. No permafrost in front of the ice sheet margin. Undistorted permeability conditions.	**LGM stage** Entire model domain is covered by an ice sheet Undistorted permeability conditions. **Post-LGM stages** Submerged conditions in the ice free area. Undistorted permeability conditions.
	Variants	
	Pre-LGM stage	**LGM and Post-LGM stages**
(b)	As in (a), but ice sheet movement from north.	Not simulated
(c)	As in (a), but changed permeability conditions. Based on an elaborated Hydro-DFN.	
B. Glacial climate conditions with permafrost		
(d)	**Pre-LGM stage** Ice sheet movement from north-west. Permafrost in front of the ice sheet margin as well as to 2 km within the tip (tongue) of the ice sheet margin. Temperature-dependent permeability conditions.	**LGM and Post-LGM stages** Not simulated

1.3.2 Computational code

The groundwater flow modelling used version 3.2[7] of the DarcyTools computational code (see Chapter 4). This version of DarcyTools contains an algorithm that is used to simulate changes in the permeability due to freezing and thawing, see /Vidstrand et al. 2010, Appendix A/. Changes of the groundwater salinity due to freezing and thawing are not considered. The heat flux from the repository to the surface is also omitted.

The flow model domain is approximately 50 km by 20 km by 2.5 km (depth), see Figure 1-2. The top boundary conditions are reported in overview in Chapter 2. The parameter values used for the groundwater flow modelling with DarcyTools are presented in Appendix A. The values used are based on available hydraulic data from the site, see Chapter 3. In total, the model domain consists of 7.4 million cells.

1.3.3 Measurement localities (ML) and ice front locations (IFL)

The repository considered for hydrogeological modelling in Laxemar contains 8,031 deposition hole positions, see Figure 1-4. The thin lines in Figure 1-4 represent the deterministically modelled deformation zones. These are presented in greater detail in Chapter 3 (section 3.3.2). In Figure 1-4, the 8,031 deposition hole positions are coloured red or green depending on if the particular deposition hole had a position within a computational grid cell in DarcyTools that also contained one or several intercepts with the deterministically modelled deformation zones (red dot) or not (green dot) (cf. section 5.6).

The labeled dots in Figure 1-4 represent five “measurement localities”. These are denoted by ML 1-5 and are used to monitor changes in the hydrogeological quantities and performance measures specified in section 1.3.4. The coordinates of ML 1-5 and their associated hydraulic properties in the model at repository depth are presented in sections 5.3 and 5.7, respectively. The simulated hydrogeological quantities and performance measures are reported for four different ice-front locations, denoted by IFL I-IV, see Figure 1-5.

[7] It is noted that the current documentation of DarcyTools relates to version 3.4 /Svensson et al. 2010/, but that the differences are insignificant for the applications reported here.

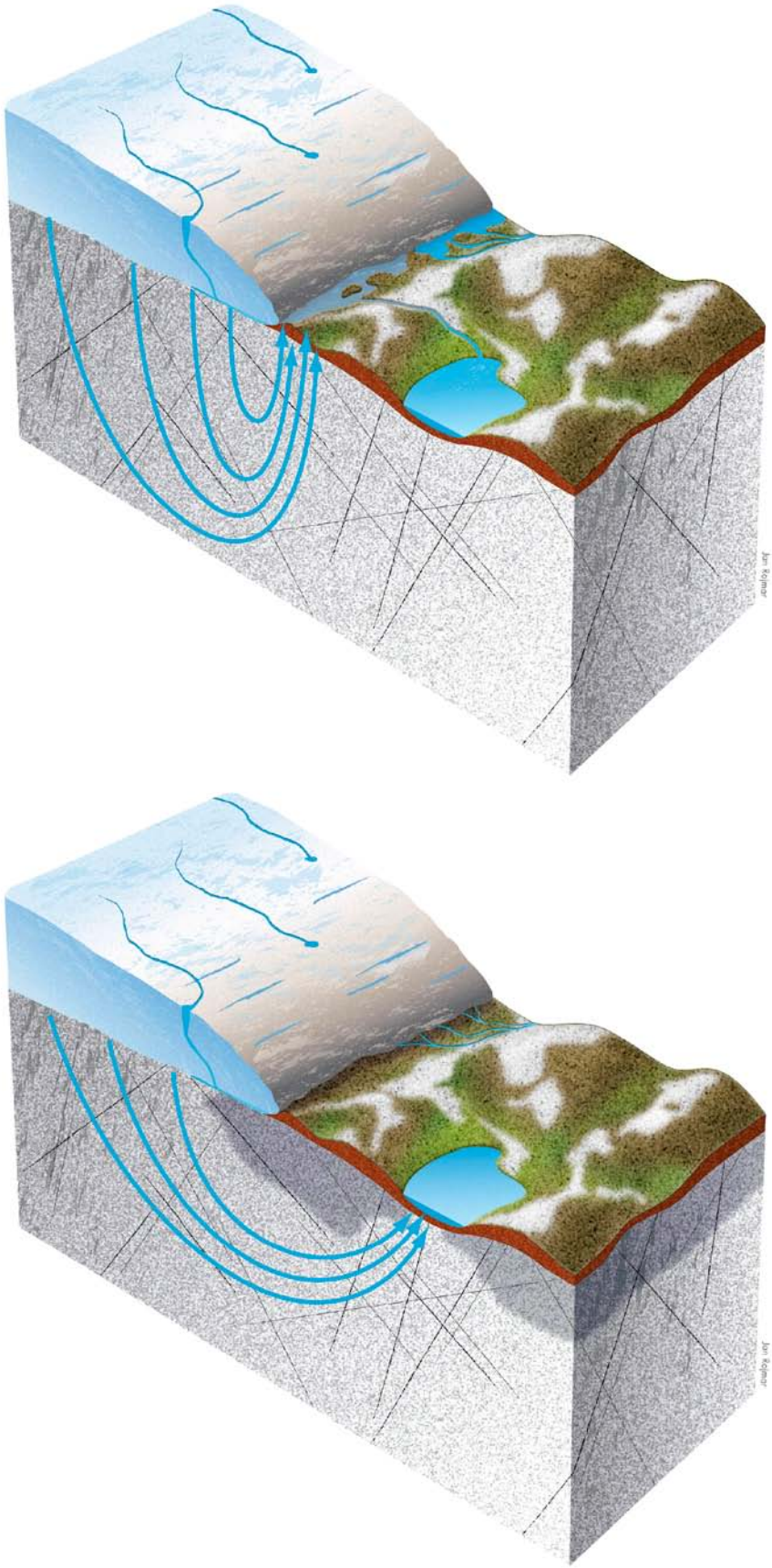

Figure 1-3. *Groundwater discharge for an advancing ice sheet margin occurs predominantly close to margin if there is no permafrost in the periglacial area (top) and in taliks if there is permafrost in the periglacial area (bottom).*

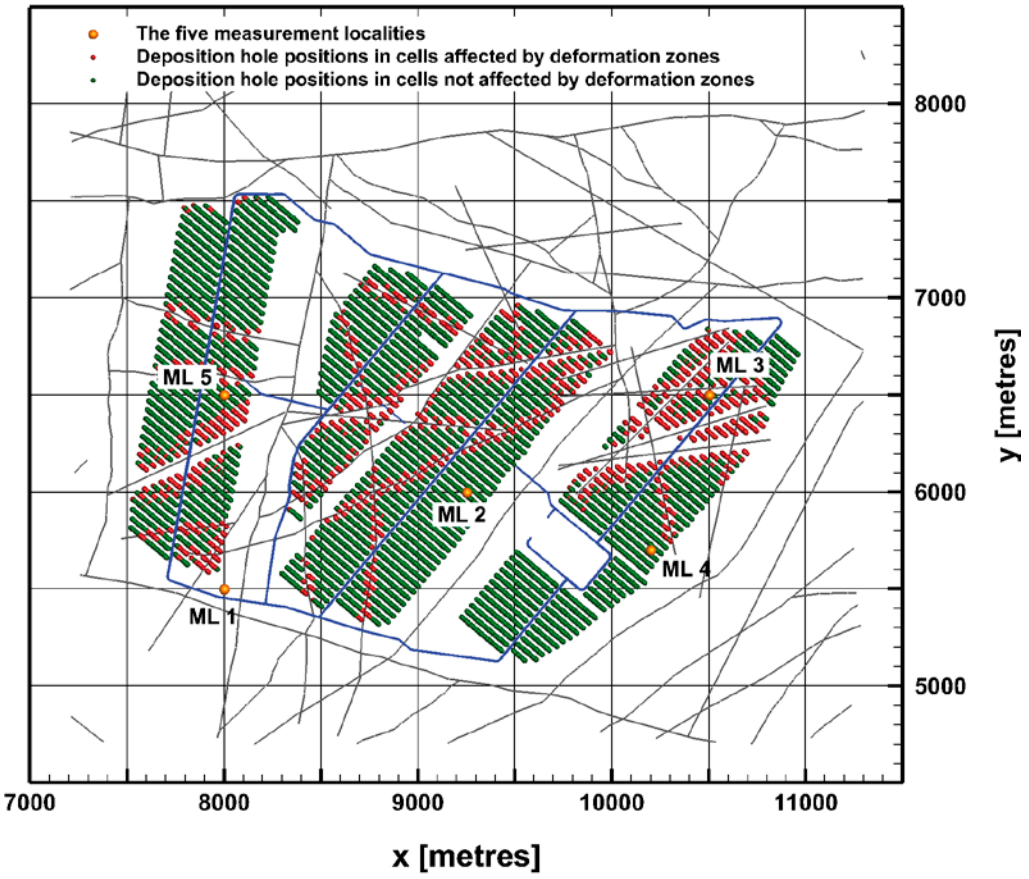

Figure 1-4. *Plane view of the studied repository layout at –500 m elevation. The thin lines represents deformation zones. It is noted that tunnels and deposition holes are not included in the model, but shown in the figure for context. The five dots labelled ML 1-5 represent five measurement localities. The hydraulic properties in the model at these localities are presented in section 5.7. The y-axis points towards north.*

Besides the four ice-front locations shown in Figure 1-5, two additional ice-front locations are discussed in the work reported here. These are denoted IFL 0 and IFL V and are located outside the model domain shown in Figure 1-5. IFL 0 is simply the start off position of the advancing ice sheet margin and IFL V is the start off position of the retreating ice sheet margin. In summary, the advancing ice sheet margin starts off at IFL 0 and passes IFL I-IV on its way to IFL V. At IFL V it stops and returns back to IFL 0. Conceptually, IFL 0 represents the temperate (initial) conditions at some time in the future (hence not 2,000 AD), whereas IFL V coincides with the situation at the LGM.

It is emphasised that no repository is implemented in the work reported here. However, one particle is released at the coordinates of each deposition hole position and all particles are tracked backwards and forwards as a means to identify their recharge and discharge locations and performance measures specified in section 1.3.4. It is noted that the Darcy fluxes are fixed in space and time during the particle tracking, which is a simplification since the boundary conditions at ground surface change with the speed of the advancing/retreating ice sheet margin.

The speed of the ice sheet margin varies a lot during a glacial cycle, although the general understanding is that the speed of the ice sheet margin during the pre-LGM stage is slower than the speed during the post-LGM stage, see /SKB 2010/. In the work reported here, a speed of 50 m/y is used during the pre-LGM stage, whereas a speed of 100 m/y is used during the post-LGM stage. (It is noted that the reference climate evolution in /SKB 2010/ considers an average retreat speed of 300 m/y. The general implications of using an average retreat speed of 100 m/y instead of 300 m/y are commented in /Vidstrand et al. 2010, Appendix D/.) Each time step in the flow model represents a time period of six years, which means that the ice sheet margin advances and retreats with a spatial increment of 300 m and 600 m, respectively. The period of complete ice coverage lasts approximately 11,000 years. In total, the simulation between IFL 0 to IFL V and back to IFL 0 represents a period of approximately 13,000 years.

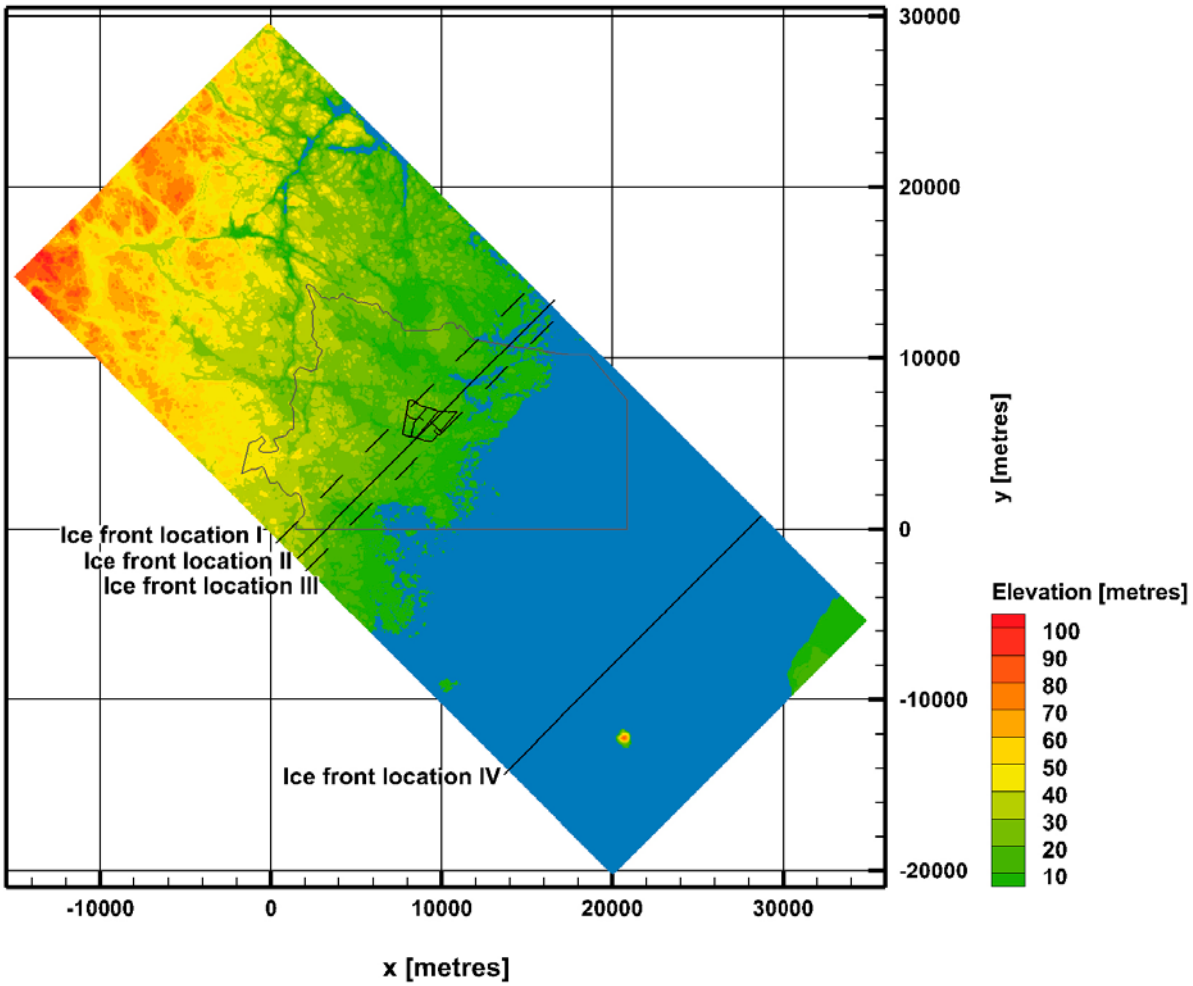

Figure 1-5. *Map showing the present-day topography at Laxemar-Simpevarp and the positions of ice front locations IFL I-IV for a NW-SE orientation of the flow model domain. The large polygon in the centre shows the model domain used for groundwater flow modelling in SDM-Site. The repository area is located in the centre part of the large polygon. The y-axis points towards north.*

1.3.4 Hydrogeological quantities and performance measures

As shown in Figure 1-2, the following hydrogeological quantities are studied in each flow simulation:

- Pressure P [$ML^{-1}T^{-2}$] (or [Pa])
- Darcy flux q [LT^{-1}] (or [m/s])
- Salinity C [MM^{-1}] (or [%])

A particle tracking algorithm is used to simulate advective transport of radionuclides. As shown in Figure 1-2, the following performance measures are studied for particles travelling from surface to repository depth (i.e. recharge, subscript R), and from repository depth back to surface (i.e. discharge, subscript D):

- Flow path lengths L [L] (or [m])
- Travel times t_w [T] (or [y])
- Flow-related transport resistances F [TL^{-1}] (or [y/m])

As briefly mentioned above, some of the results from the groundwater flow simulations reported here are used in other modelling studies, e.g. fracture water and matrix porewater salinities are exported to the hydrochemical modelling by /Gimeno et al. 2010/.

1.4 Setting of the Laxemar site

The Laxemar-Simpevarp area is located on the Swedish east coast near Oskarshamn and c. 350 km south of Stockholm.

The Laxemar-Simpevarp regional model area is dominated by a geological unit referred to as the Transscandinavian Igneous Belt (TIB). The bedrock is dominated by well preserved c. 1.8 Ga intrusive rocks varying in composition between granite-syenitoid-dioritoid-gabbroid. Although a non-uniformly distributed faint to weak foliation, is present, the most prominent ductile structures at Laxemar are discrete, low-temperature, brittle-ductile to ductile shear zones of mesoscopic to regional character, which are related to the waning stages of the Svecokarelian Orogeny. Subsequently, the rock mass has been subjected to repeated phases of brittle deformation, under varying regional stress regimes, involving reactivation along earlier formed structures. There are indications that the ductile anisotropy, including both larger ductile shear zones as well as the weak to faint foliation, minor shear zones and mylonites, has had an influence on the later brittle deformation. With a few exceptions, the deterministically modelled deformation zones at Laxemar are characterised by brittle deformation although virtually all the zones have their origin in an earlier ductile regime. The brittle history of the Laxemar-Simpevarp area is complex and involves a series of reactivation events that do not allow the construction of a consistent simple model covering their development. /Wahlgren et al. 2008/. /Söderbäck 2008/ provides a detailed description of the geological evolution of the Fennoscanian Shield in south-eastern Sweden from c. 1.91 Ga and to the Quaternary period.

The investigated area is close to the coast, cf. Figure 1-6. The topography is fairly flat (regional topographic gradient in the order of 4%; the topography corresponds to the Sub-Cambrian Peneplain /Fredén 2002/) but with relatively distinct valleys, cf. Figure 1-7 and Figure 1-8. The investigation area is located within a crystalline basement, mostly covered by a rather thin till in the elevated areas and with glaciofluvial sediments in the larger valleys. The site-average annual precipitation and specific discharge are estimated to be on the order of 600 mm and 160–170 mm, respectively /Werner et al. 2008, Larsson-McCann et al. 2002/ and the area is covered with a fairly large number of small streams indicating small local drainage basins within the regional model area, cf. Figure 1-6. The Äspö Hard Rock laboratory is an underground research facility that is located below the Äspö Island, cf. Figure 1-6, and the facility affects the groundwater flow locally in the area. The Simpevarp peninsula hosts the Clab interim facility and the nuclear power plants O1, O2 and O3. At Clab, inflows are observed to the rock caverns near the surface and the shallow shafts surrounding the foundations of the power plants, but it has a very local effect on the groundwater flow. The hydrogeology of the area is described in more detail in /Rhén and Hartley 2009/.

The regional and local model areas employed for model version SDM-Site Laxemar are shown in Figure 1-9. The *Laxemar-Simpevarp regional (scale) model area/volume* (Later in the report referenced as *Regional model area/volume*) for SDM-Site Laxemar is the same as the one used in model version Laxemar 1.2.

Laxemar local (scale) model area/volume (Later in the report referenced as *Local model area/volume*) for model version SDM-Site Laxemar and *Focused area/volume* for the *complete site investigations* is the central, southern and western parts of the local model area, cf. Figure 1-9.

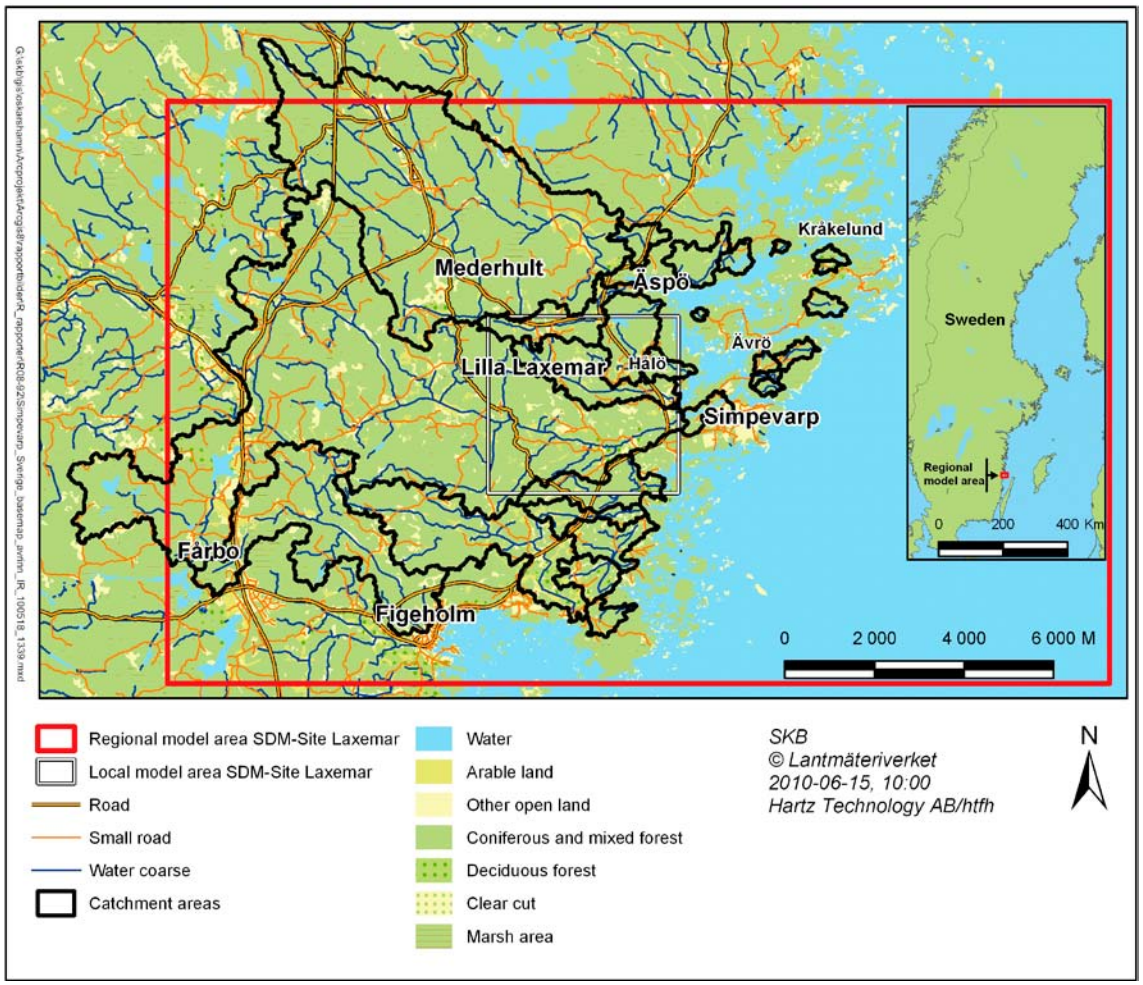

Figure 1-6. *Overview map of the Laxemar-Simpevarp regional model area with the SDM-Site Laxemar local model area indicated. The large number of small streams indicates small local drainage basins within the regional model area. /Rhén and Hartley 2009/.*

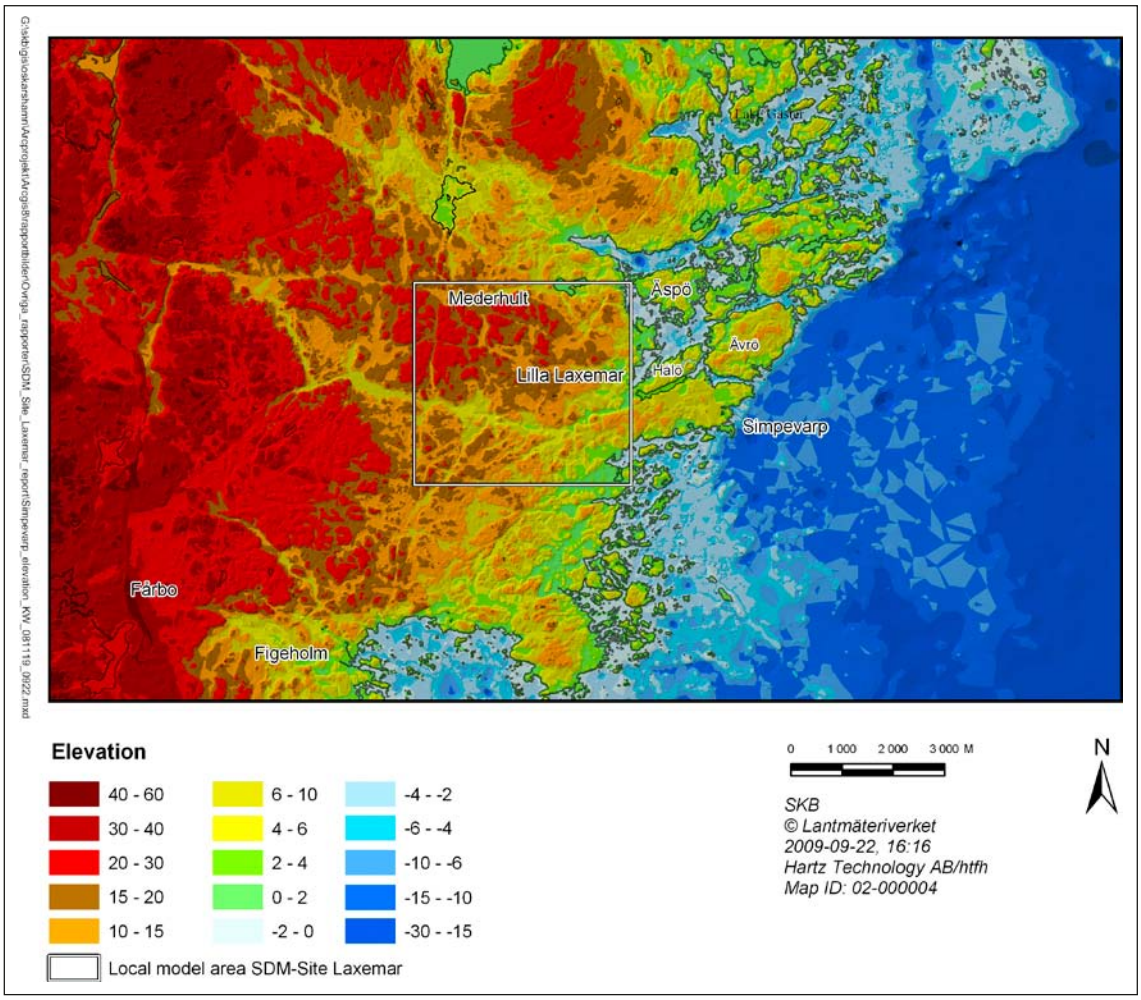

Figure 1-7. *Overview map illustrating the elevation of the ground-surface topography (m.a.s.l.) in an area corresponding to the Laxemar-Simpevarp regional model area, including the bathymetry of lakes and the sea. /Rhén and Hartley 2009/.*

Figure 1-8. *Air photographs showing the flat topography, low gradient near shore situation in the Laxemar-Simpevarp area with shallow bays, top) view from the southeast, Clab facility in the foreground, bottom) view from the west, drill site KLX05/KLX12A in the centre of the photograph. Both photographs show the outline of the focused area in Laxemar in red, cf. Figure 1-9. /Rhén and Hartley 2009/.*

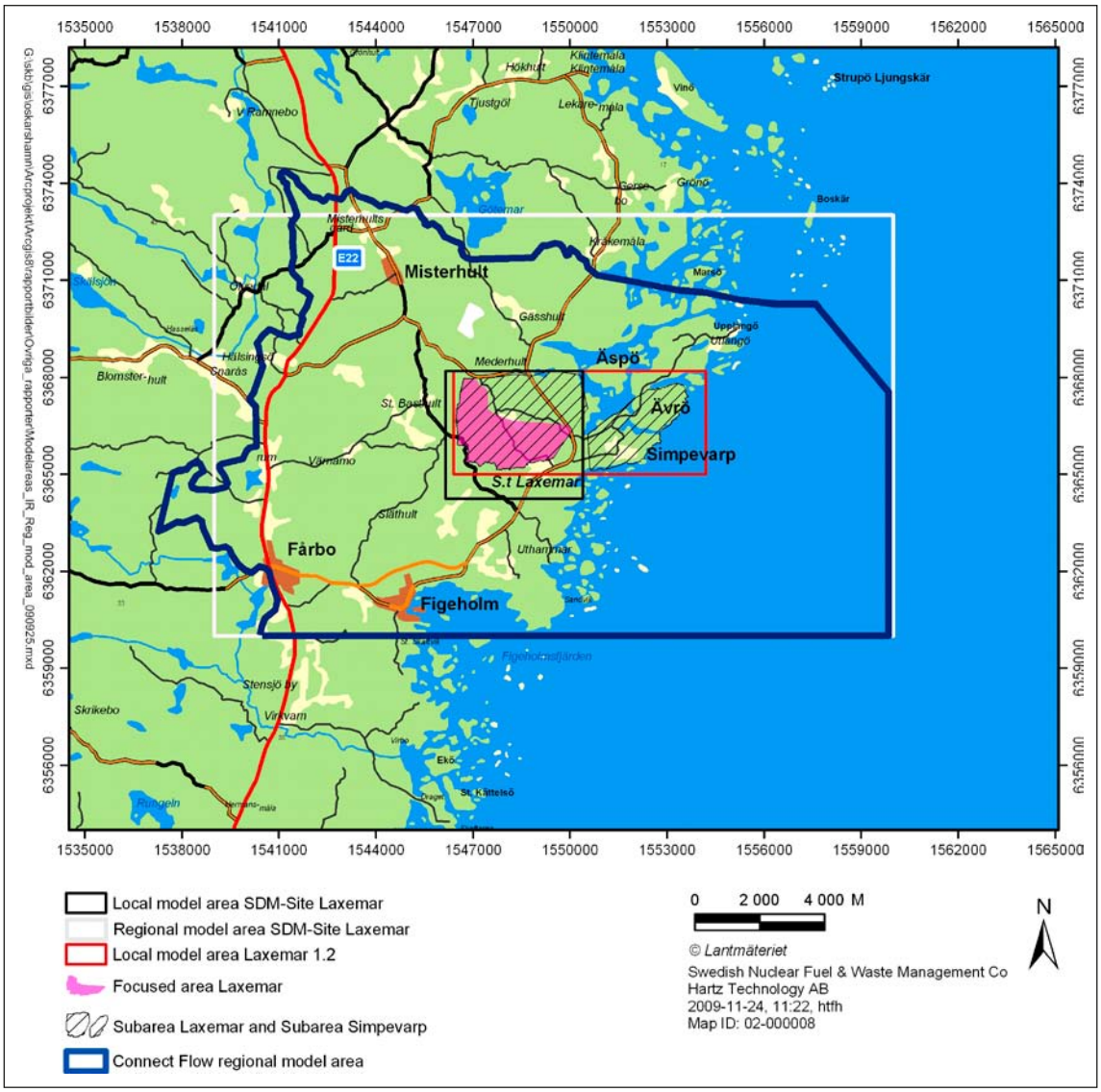

Figure 1-9. *Regional and local model areas used for model version SDM-Site Laxemar. The area coverage of the regional model is the same as that employed in previous model versions, whereas the local model area is significantly reduced compared to that employed in model version Laxemar 1.2. Laxemar subarea and Simpevarp subarea defined the investigation areas during the initial stage of the site investigations. The choice of boundaries used for the SDM-Site regional groundwater flow simulations (regional flow domain) based on surface water catchments is also shown (in this figure denoted ConnectFlow regional model area). /Rhén and Hartley 2009/.*

1.5 Studied fracture models

As explained in the work by /Joyce et al. 2010/, two hydrogeological discrete fracture network (Hydro-DFN) models are defined at Laxemar; the Hydrogeological base case and the Elaborated Hydro-DFN.

- The first model, the Hydrogeological base case, builds upon the Hydro-DFN model derived within SDM-Site /Rhén and Hartley 2009/. Besides providing a general description of the bedrock hydrogeology at Laxemar, Chapter 3 also presents the model parameters of the Hydrogeological base case.
- The second model, the Elaborated Hydro-DFN, is a refinement of the Hydrogeological base case. The model parameters of the Elaborated Hydro-DFN used herein are specified in Appendix A; but for details referred to /Joyce et al. 2010/.

The reason for the Elaboarted Hydro-DFN can be summarised as follows. During SDM-Site, the flow modelling of the palaeohydrogeological evolution at the Laxemar site showed that the derived Hydro-DFN for SDM-Site (i.e. the Hydrogeological base case) is slightly too transmissive. Reducing the permeabilities below –150 m by a factor of three improved the match to measured values. This calibration resulted in the Elaborated Hydro-DFN, see /Joyce et al. 2010/ for details.

Following the terminology used in /Joyce et al. 2010/, the Hydrogeological base case should be called Base case in the work reported here since it refers to the Hydrogeological base case studied by /Joyce et al. 2010/. Consequently, the Elaborated Hydro-DFN should be regarded as a model variant.

1.6 This report

The following chapters of the report are structured as follows.

Chapter 2 presents the choice of top boundary conditions used in this study.

Chapter 3 presents a summary of hydrogeological model derived in SDM-Site Laxemar /Rhén and Hartley 2009/.

Chapter 4 presents the primary concepts and methodology of the DarcyTools computational code /Svensson et al. 2010/.

Chapter 5 provides a description of the numerical setup, e.g. initial and boundary conditions, of the cases studied and presents the format of the figures showing the calculated performance measures.

Chapter 6 summarises the key findings.

Chapter 7 summarises the scope of the work, the applied methodology, the key assumptions made and the conclusions drawn.

In addition, the report contains six appendices, A to F .

A. This appendix presents the parameter values used in DarcyTools for the generation of hydro-geological discrete fracture network (Hydro-DFN) realisations.

B. This appendix lists the names and dates of all files that are used to parameterise the groundwater flow model.

C. This appendix discusses the support for the applied initial and boundary conditions during glaciation and deglaciation, in particular the data support for assuming a fixed (undisturbed) groundwater salinity on the bottom boundary of the model domain. Data are discussed from the perspective of both salinity and permeability data and trends with depth.

D. This appendix presents detailed results from the simulations with temperate climate conditions in a tabular format.

E. This appendix presents detailed results from the simulations of scenario A in Table 1-1 in a tabular format (Glacial climate conditions without permafrost) .

F. This appendix presents the results from the simulations of scenario B in Table 1-1 in a tabular format (Glacial climate conditions with permafrost).

2 Hydraulic conditions during glacial periods

2.1 Introduction

A literature review was made with the objective of defining and justifying hydraulic properties and top boundary conditions of a groundwater flow model intended for quantification of bounding permafrost and glacial (ice sheet) hydrogeological conditions for subsequent use within safety assessment applications. The literature review is summarised in /Vidstrand et al. 2010/. Section 2.2, below, describes details of the key boundary condition for the work reported here, i.e., the ice sheet profile.

2.2 Ice sheet profile

It is readily concluded that the key boundary condition during a glacial cycle is the thickness and the properties of the ice sheet (warm or cold based). The thickness and the properties affect all processes involved regardless of whether they are thermal (T), hydraulic (H), mechanical (M) or chemical (C). Below follows a short description of how the ice sheet profile is defined in the modelling work reported here.

Beneath the ice sheet, the pressure is specified using theoretical/empirical ice sheet thickness relationships /Paterson 1994/. This approach has been used in various earlier numerical groundwater flow simulations and is, in general, believed to overestimate the impact of an ice sheet, e.g. /Chan et al. 2005/.

/Paterson 1994/ reported two possible equations for expressing the ice sheet thickness. If the ice is assumed to be a perfectly plastic material the ice thickness adjusts to the shear stress at the base. For such conditions, the ice thickness can be expressed as:

$$h^2 = \frac{2 \cdot \tau_0}{\rho g} \cdot (L - x) \qquad (2\text{-}1)$$

where h [L] is the ice thickness at location x [L]; L [L] is the size of the ice sheet between the front and its centre (origin of x). Hence, (L-x) is the distance backward from the ice sheet margin. τ_0 [$MT^{-2}L^{-1}$] is the shear stress at the base. Values on the shear stress are reported between 0 and 100 kPa with a mean at about 50 kPa /Paterson 1994/. Adopting 50 kPa yields:

$$h = 3.4 \cdot \sqrt{L - x} \qquad (2\text{-}2)$$

Equation (2-2) has previously been assessed in hydrogeological studies by SKB either as a specified head boundary condition e.g. /Vidstrand et al. 2007/ or as a criterion for assigning a head dependent flux, e.g. /Jaquet and Siegel 2006/.

If the assumption of perfect plasticity is dropped another equation for ice thickness is obtained:

$$h = H \cdot \left(1 - \left(\frac{x}{L} \right)^{\frac{4}{3}} \right)^{\frac{3}{8}} \qquad (2\text{-}3)$$

where H [L] is the ice sheet thickness at the centre and L [L] is the maximum ice sheet horizontal extension.

Equation (2-3) is applied in the rock mechanics modelling conducted by /Lönnqvist and Hökmark 2010/, who set H to 3 km and L to 400 km. For the sake of comparison, Equation (2-3) yields an ice sheet thickness approximately twice the thickness of that obtained from Equation (2-1).

Figure 2-1 shows the three ice sheet profiles discussed in this study.

- The red graph is the so-called "theoretical maximum profile" presented in /SKB 2010/. This profile is considered valid for the pre-LGM stage (an advancing ice sheet margin) and is readily modelled by Equation (2-3). The dotted red line represents the specified pressure head curve assigned on the top boundary in the majority of the groundwater flow simulations reported here. The pressure head is set to 92% of the ice sheet thickness.
- The blue graph represents the shape of the "theoretical maximum profile" when the ice sheet margin has reach the last glacial maximum (LGM) position south of the Baltic Sea. The solid black line represents the tangent to the blue graph at a location corresponding to the Laxemar site. During the period of complete ice sheet coverage at Laxemar, the slope of the tangent (2.1 m/km) is used to model the ice sheet profile in the work reported here.
- The green graph mimics the "simulated reference climate evolution profile" presented in /SKB 2010/. This profile is considered valid for the post-LGM stage (a retreating ice sheet margin) and applicable for describing ice thickness in terrestrial areas, i.e. areas that are unaffected by the increase in the sea level caused by the abundance of meltwater.

In the work reported here, the "theoretical maximum profile" is used for both the pre-LGM and post-LGM stages.

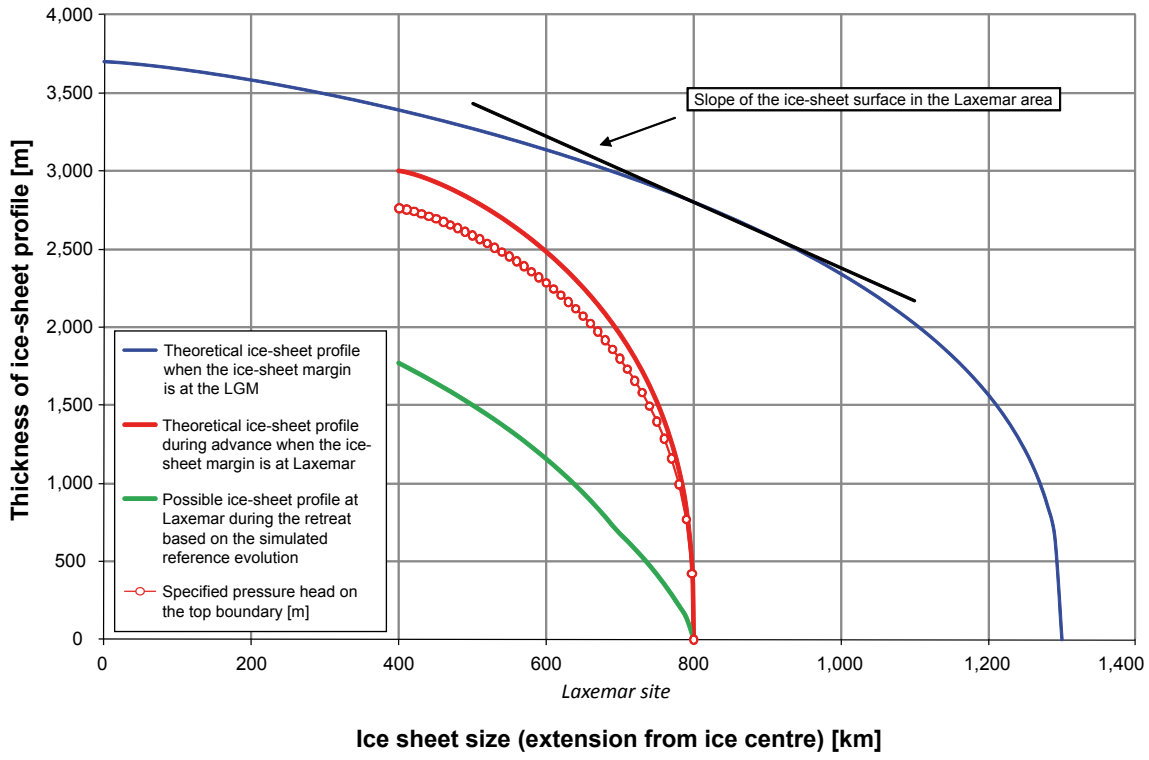

Figure 2-1. *Illustration of ice sheet profiles.*

3 Hydrogeological model of the Laxemar site

3.1 Supporting documents

The SDM-Site Laxemar hydrogeological reporting in /Rhén and Hartley 2009/ provides a detailed summary of the work described in /Rhén et al. 2008/ and in /Rhén et al. 2009/, i.e. the field investigations, the data analyses, the conceptual model development and the numerical modelling of groundwater flow and solute transport. The complete SDM-Site Laxemar site-descriptive modelling work is reported in /SKB 2009a/ and the overall confidence assessment associated with the modelling work is detailed in /SKB 2009b/.

Table 3-1 shows the cumulative number of boreholes providing hydraulic information about the bedrock in the Laxemar-Simpevarp area. The number of boreholes is shown in relation to the two investigation stages; Initial Site Investigations and Complete Site Investigations (ISI and CSI), the five model versions (Version 0, Simpevarp 1.1, Simpevarp 1.2 and Laxemar 1.2, and model version SDM-Site Laxemar) carried out during the period 2002–2008. Model version Laxemar 1.2 represents the culmination of the ISI. The current hydrogeological modelling based on data freeze Laxemar 2.3 constitutes the principal contribution to SDM-Site Laxemar, corresponding to the CSI from a hydrogeological point of view. Investigations in c. 4,000 m of deep cored boreholes (KLX01-04) provided old and new (from the ISI) hydraulic data within the Laxemar local model area for model version Laxemar 1.2. After Laxemar Stage 2.3 (CSI) hydraulic data from 16 additional deep cored boreholes within the Laxemar local model area with an approximate total length of 12,800 m were available (KLX05, KLX06, KLX07A, KLX08, KLX09, KLX10, KLX11A, KLX12A, KLX13A, KLX15A, KLX16A, KLX17A, KLX18A, KLX19A, KLX20A, KLX21B).

Table 3-1 also shows references to the major background reports in relation to each model version/stage /Follin et al. 2004, 2005, 2006, Hartley et al. 2004, 2005, 2006, 2007, Holmén 2008, Rhén et al. 1997, 2006a, b, c, 2008, 2009, SKB 2002, 2004, 2005, 2006b, c /.

Table 3-1. The cumulative new (drilled during site investigation) number of boreholes providing hydraulic information about the bedrock in the Laxemar-Simpevarp area at the end of the five model versions carried out during the period 2002 through 2008. Kxx = core-drilled boreholes, Hxx = percussion-drilled boreholes (KLX and HLX: core-drilled boreholes or percussion-drilled boreholes within the Laxemar local model area). The reports listed in italics describe the hydraulic data collected and/or the hydrogeological modelling undertaken. The reports with underlined reference numbers summarise the development of the hydrogeological modelling along with the developments achieved within the other disciplines. /Rhén and Hartley 2009/.

	Initial site investigation (ISI)			Complete site investigation (CSI)	
Desk top exercise	**Training exercise**	**Preliminary SDM**	**Preliminary SDM**	**Feedback and strategy**	**Model verification and uncertainty assessment**
Version 0	**Version 1.1**	**Simpevarp Version 1.2**	**Laxemar Version 1.2**	**Laxemar Stage 2.1**	**Laxemar Stage 2.3 (Version SDM-Site)**
0 Kxx 0 Hxx	0 Kxx [1] 0 Hxx	4 Kxx [2] 3 Hxx	9 Kxx [3] 14 Hxx 3 KLX (7%)[3] 9 HLX(26%)	11 KLX (25%)[4] 9 HLX (26%)[4]	44 KLX (100%)[5] 34 HLX (100%)
R-02-35 *TR-97-06*	R-04-25 *TR-97-06* *R-04-63* *R-04-65*	R-05-08 *R-06-20* *R-05-11* *R-05-12*	R-06-10 *R-06-21* *R-06-22* *R-06-23* *R-06-24*	R-06-110 *R-07-57* *R-08-60*	TR-09-01 *R-08-78* *R-08-91* *R-08-92*

[1] Some old data from KLX01 and KLX02 were used besides earlier interpretations from the area.

[2] Old data from KLX01, KLX02, KAV01, KAV02 and KAV03 also used besides the indicated three KSH holes and KAV01 with some new data.

[3] KLX02–04. KLX02 included as some new tests were performed in that borehole. A few data from KLX05 and KLX06 were also available but these boreholes are not included here as the large amount of data became available later. Kxx also includes three KSH holes, KAV01, KAV04A, and KAV04B. Old data from KLX01 also used but not included in the numbers in the table.

[4] KLX02–12 included but data not complete for all these boreholes at this stage. Old data from KLX01 also used. New HLX boreholes were not considered.

[5] 19 core holes longer than 300 m and 25 shorter than 300 m. KLX01 and KLX27A not included.

3.2 Systems approach in SDM-Site

In order to meet the objectives for model version SDM-Site Laxemar /Rhén and Hartley 2009/, the groundwater system is divided into different hydraulic domains. Figure 3-1 illustrates schematically SKB's systems approach as employed in the hydrogeological SDM for Laxemar. The groundwater system consists of three basic hydraulic domain types, namely HSD, HCD and HRD, where:

- HSD (Hydraulic Soil Domain) represents the Quaternary deposits.
- HCD (Hydraulic Conductor Domain) represents deformation zones.
- HRD (Hydraulic Rock mass Domain) represents the fractured bedrock between the deformation zones.

The systems approach constitutes the basis for the conceptual modelling, the site investigations and the numerical simulations carried out in support of the hydrogeological SDM /Rhén et al. 2003/.

Besides the three hydraulic domains shown in Figure 3-1, the groundwater flow (saturated flow) and solute transport modelling consists of three additional elements:

- A solute (salt) transport model for the modelling of advective transport and matrix diffusion.
- Initial conditions for groundwater flow and hydrochemistry.
- Boundary conditions for groundwater flow and hydrochemistry.

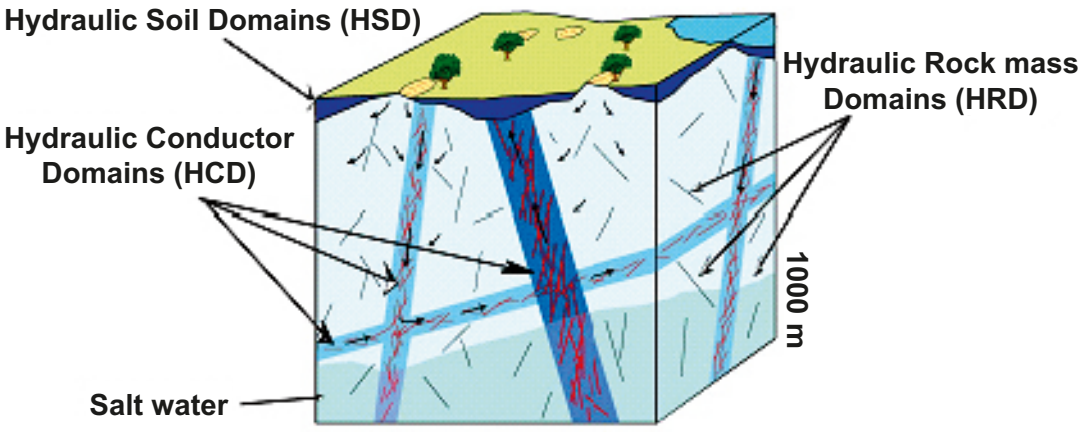

Figure 3-1. *Cartoon showing the division of the crystalline bedrock and the overburden (Quaternary deposits) into hydraulic domains. Within each domain, the hydraulic properties are represented by equivalent values, or by spatially distributed statistical distributions /Rhén et al. 2003/.*

3.3 Summary of the bedrock hydrogeological model

3.3.1 General

Single-hole hydraulic tests, interference tests, groundwater levels and hydrochemical data are the basis for the hydrogeological characterisation, together with the geological model. Investigations have essentially been made down to c. 1,000 m depth but there is also one borehole (KLX02) that has provided data down to c. 1,600 m depth. The PFL-f (PFL is short for Posiva Flow Log and f stands for fracture or feature) method is essential for the hydrogeological model. The PFL-f method constitutes a geophysical logging device developed to detect continuously flowing features in sparsely fractured crystalline bedrock by means of difference flow logging, using a 1 m test section that is moved stepwise 0.1 m. The PFL method essentially provides an estimate of the specific capacity (Q/s) [L^2T^{-1}], where s represents the drawdown and Q the flow rate. Transient injection tests with PSS (Pipe String System) have been performed using 3 different test scales: 5, 20 and 100 m with 5 m tests only being performed in the elevation interval –300 m to –700 m, covering the foreseen repository depth, cf. /Rhén and Hartley 2009/ for details.

The Laxemar-Simpevarp regional model area is in general characterised by an undulating bedrock surface with a thin cover of Quaternary deposits, mainly till on the top of the hills and thicker Quaternary deposits in the valleys made up of till overlain by postglacial deposits. The crystalline bedrock is intersected by a number of deformation zones, denoted Hydraulic Conductor Domains (HCD) in the hydrogeological model, which are mainly steeply dipping, with less fractured bedrock between these zones. The bedrock in between the HCDs is in the hydrogeological model called Hydraulic Rock mass Domains (HRD). Hydraulically, the deformation zones are generally more conductive than the bedrock in between. The general tendency within the Laxemar-Simpevarp regional model volume is that the hydraulic conductivity decreases with depth in both HCDs and HRDs. The Quaternary deposits, called Hydraulic Soil Domains (HSD) in the hydrogeological model are generally more conductive than the bedrock. Figure 3-2 shows a generalised vertical section illustrating the overall hydrological and hydrogeological conceptual model of the Laxemar-Simpevarp area. The hydrogeological characteristics of the HCDs, HRDs and HSDs are further described in sections 3.3.2 through 3.3.4 and 3.4; details are found in /Rhén et al. 2008/.

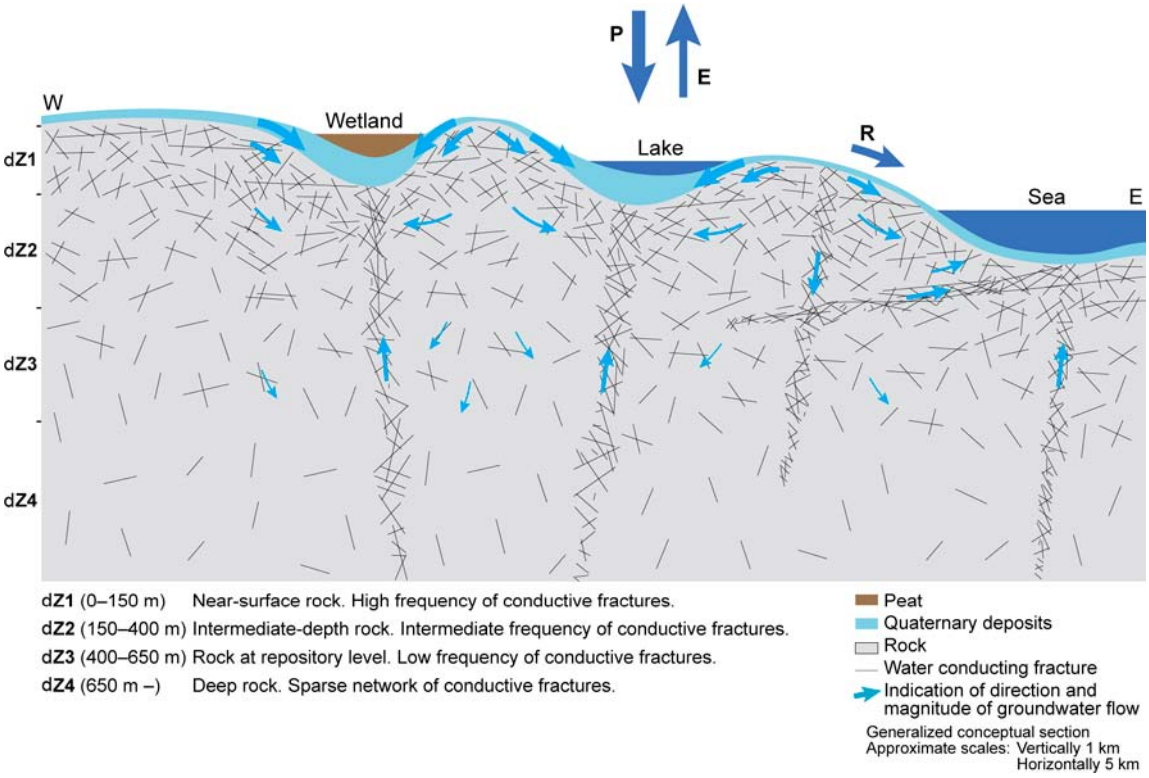

Figure 3-2. *Generalised section illustrating the conceptual model of hydrology and hydrogeology in Laxemar. Note the different horizontal (5 km) and vertical (1 km) scales. Furthermore, the thickness of the Quaternary deposits is exaggerated in the figure. /Rhén and Hartley 2009/.*

3.3.2 Hydraulic characteristics of hydraulic conductor domains (HCD)

The deformation zone model, as implemented in the SDM-Site regional flow domain, is shown in Figure 3-3.

The key interpreted characteristics are:

- A clear trend of decreasing transmissivity with depth.
- A positive correlation between interpreted deformation zone "size" and transmissivity. Size here corresponds to interpreted trace length on the surface.
- Indications that the transmissivity of HCDs is dependent on the orientation of deformation zones. E-W zones appear more conductive than zones of other orientations.
- Significant lateral variability with an estimated standard deviation of $\log_{10}(T)$ of 1.4. The standard deviation of $\log_{10}(T)$ of the entire sample of HCD transmissivities is 1.4 and standard deviation of $\log_{10}(T)$ of transmissivities within individual zones is in the range 0.5 to 2. Sample sizes within individual zones were between 2 to 14.

The data and the general models suggested for the initial assignment of hydraulic properties to HCDs in the groundwater flow modelling are presented in Figure 3-4 cf. a detailed account in /Rhén et al. 2008/. The variability in transmissivity is large but considering mean values for depth zones employed in the HRD modelling, see Figure 3-4, the transmissivity decreases with depth, cf. /Rhén et al. 2008/. There is also a tendency that the transmissivity is positively correlated to the interpreted lineament length of the HCD and also that HCDs with E-W orientations are slightly more transmissive than HCDs of other orientations, cf. /Rhén et al. 2008/.

However, some of the HCDs are intersected by several boreholes at a range of depths and it was judged that there was enough data for assessment of zone-specific trend functions for seven of the HCDs, cf. /Rhén et al. 2008/.

An exponential trend model is used for the depth trend of the transmissivity:

$$T(z)=10^{(a+B\cdot z)} \qquad (3\text{-}1)$$

z: Elevation in m (m.a.s.l.) (z defined positive up). The coefficients *a* and *B* in the exponential trend model are based on a linear regression of log10(T) data from surface down to lowermost depth zone, see /Rhén et al. 2008/ for details.

Several interference tests have shown that dolerite dykes may act as hydraulic barriers, at least locally. The best example relates to the steep N-S oriented HCD ZSMNS001C just west of the focused area, associated with a core of dolerite, cf. /Rhén and Hartley 2009/. Both interference tests and monitoring data show fairly large differences in hydraulic head on either side of two other HCDs associated with dolerite dykes, ZSMNS059A and the KLX19_DZ5-8_dolerite, are also acting as hydraulic barriers, but probably to a lesser degree where the dykes become thinner. Mapping of the cored boreholes and outcropping deformation zones has shown that fault gouge is present in some deformation zones. This implies that these HCDs can exert some hydraulic barrier effect, most likely highly localised.

The distribution of the mean transmissivity in the HCD for the *base case*[8] is shown in Figure 3-5. For stochastic realisations with lateral heterogeneity within SDM-Site, these values are used as the mean sampled value for a log-normal distribution with specified standard deviation, but truncated at ± 2 standard deviations. Equivalent plots for one example realisation of the HCD with spatial variability, standard deviation in $\log_{10}(T)$=1.4, is shown in Figure 3-6. In both cases, the heterogeneous transmissivity field is conditioned to measured values at the intercept with borehole intervals where measurements are available. Thus the local contact between the bedrock and the borehole will be as measured and not dependant on the realisation, which is important when comparing measurements and simulation results.

[8] *"Base case"* in /Rhén and Hartley 2009/ accounting for the SDM-Site Laxemar modelling corresponds to "Deterministic base model simulation" in the SDM-Site Forsmark modelling /Follin, 2008/.

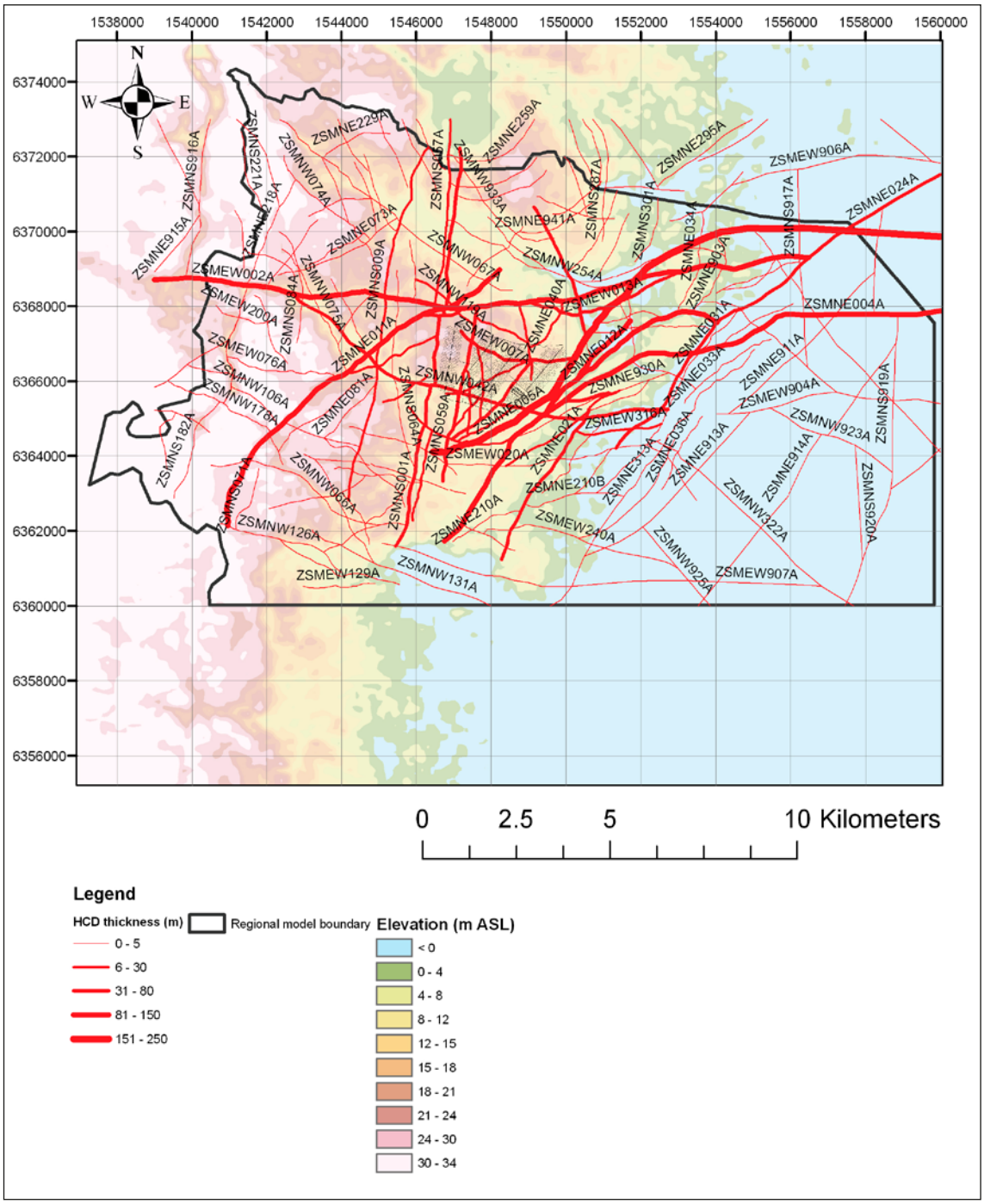

Figure 3-3. *Deformation zones included in the SDM-Laxemar deterministic deformation zone model. Colouring of zones is according to judged thickness.*

3.3.3 Hydraulic characteristics of hydraulic rock mass domains (HRD)

The hydraulic rock mass domain model, as implemented in the SDM-Site regional flow domain, is shown in Figure 3-7 though Figure 3-10. According to /Rhén et al. 2008/, four separate hydraulic rock mass domains (HRD) should be modelled in the local model area; HRD_C, HRD_EW007, HRD_N and HRD_W, that are based on the fracture domains, cf. Figure 3-9, Figure 3-10 and /Wahlgren et al. 2008/.

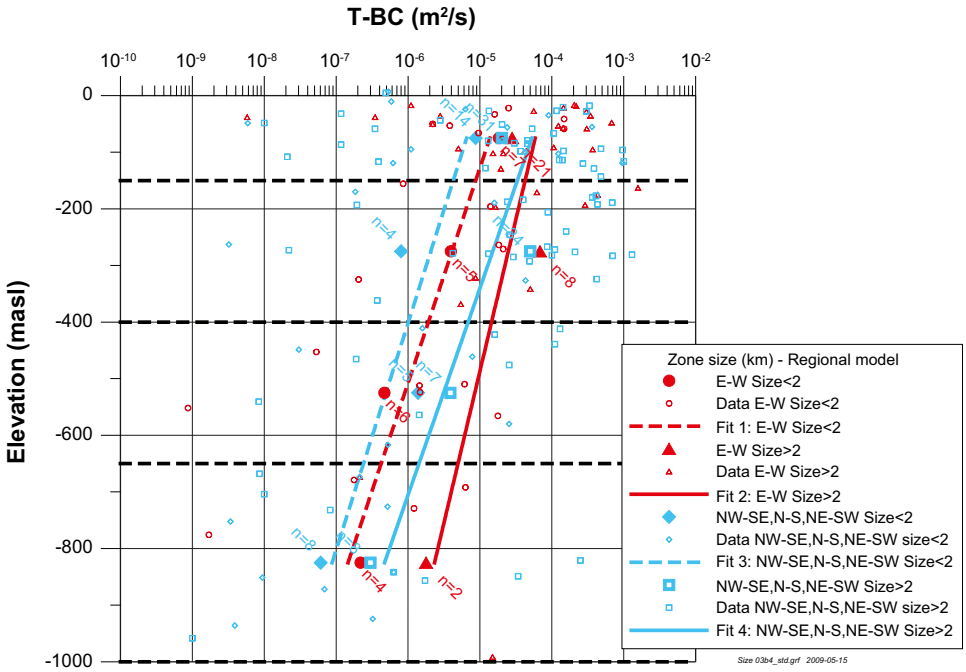

Figure 3-4. *Deformation zone transmissivity (T) related to deformation zone orientations in the horizontal plane and size, versus elevation for the regional model. Mean of $log_{10}(T)$, plotted as well as the number of observations (n). Regression line based on Mean of log10(T) /Rhén and Hartley 2009/.*

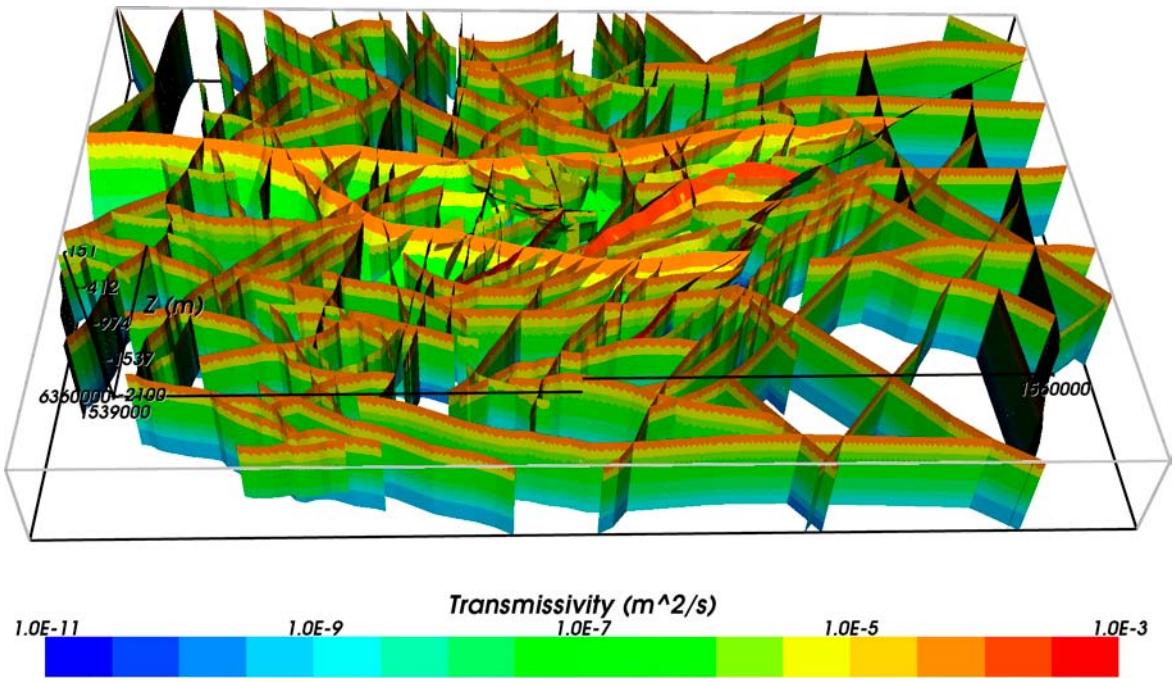

Figure 3-5. *All HCDs and their inferred depth dependent transmissivity for the deterministic base case model. Oblique view looking from the south. /Rhén and Hartley 2009/.*

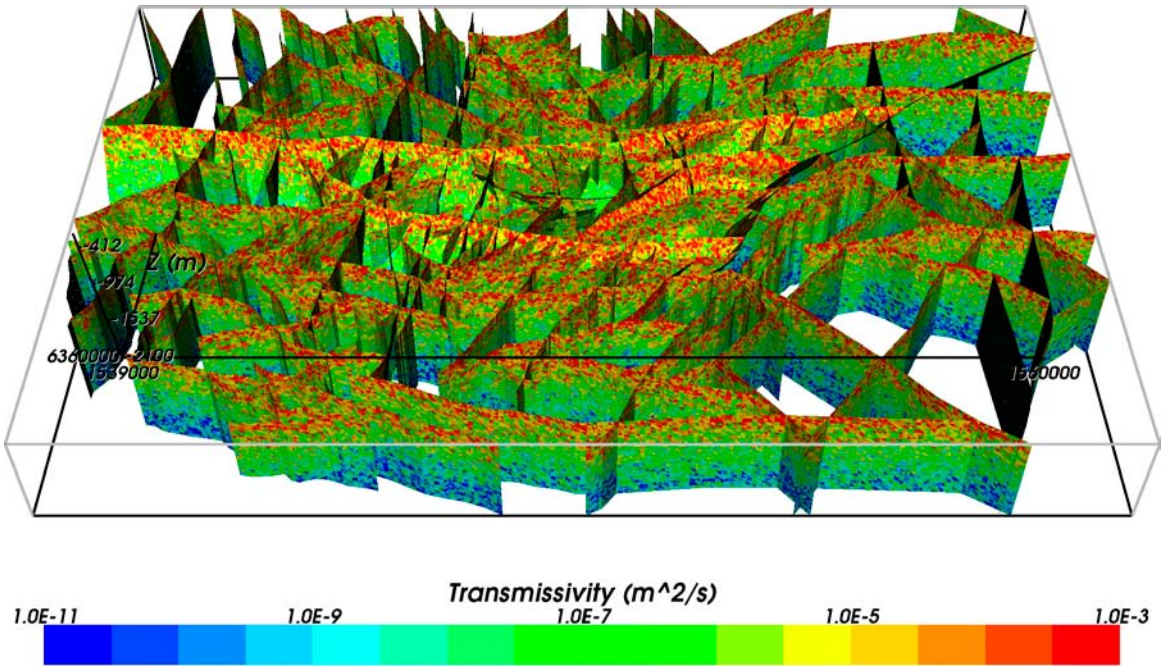

Figure 3-6. *All HCDs and their inferred depth dependent transmissivity for a case with spatial variability and a standard deviation in Log(T) of 1.4. Oblique view looking from the south. /Rhén and Hartley 2009/.*

The key interpreted characteristics are:

- The flowing features (fractures and minor deformation zones) can be grouped in four orientation sets; steep ENE, WNW, N-S and a sub-horizontal set.
- The intensity of flowing features is generally highest for the WNW set (aligned with the principal horizontal stress) with the sub-horizontal set also being important in the upper bedrock.
- A clear decreasing intensity of flowing features with depth but generally with a similar transmissivity distribution of the flowing features for the specific depth interval studied (as measured by difference flow logging; PFL-f).
- As a consequence, a resulting clear trend of decreasing hydraulic conductivity with depth, (injection tests, test scale 100 m) may be observed.
- The hydraulic conductivity is c. 10 times lower in HRDs than that of the HCDs (injection tests, test scale 100 m).

The rock mass in the regional flow domain, outside the defined four HRDs mentioned above, is based on the material property assignments made in model version Laxemar 1.2 /SKB 2006b, Rhén et al. 2006c/ (summarised in /Rhén et al. 2009/) and assessments of similarities between regional HRDs and the newly developed HRDs inside the Laxemar local model volume; HRD_C, HRD_EW007, HRD_N and HRD_W, cf. Table 3-2.

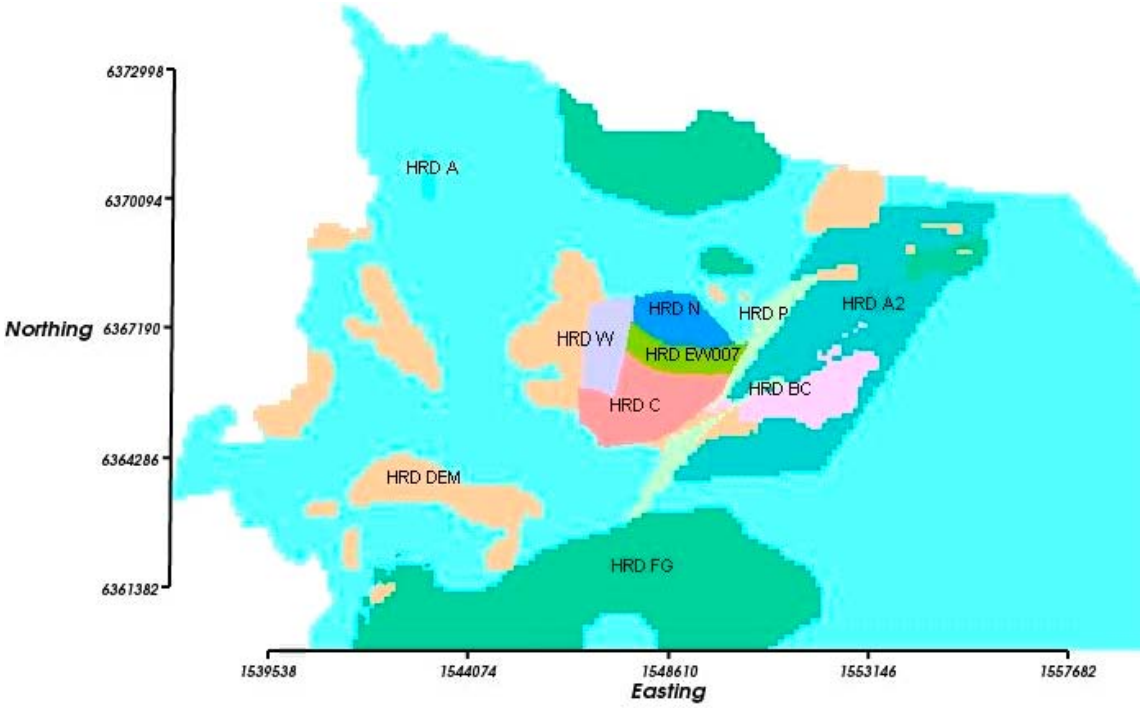

Figure 3-7. *Hydraulic rock mass domains on the top surface of the bedrock in the regional flow domain. /Rhén and Hartley 2009/.*

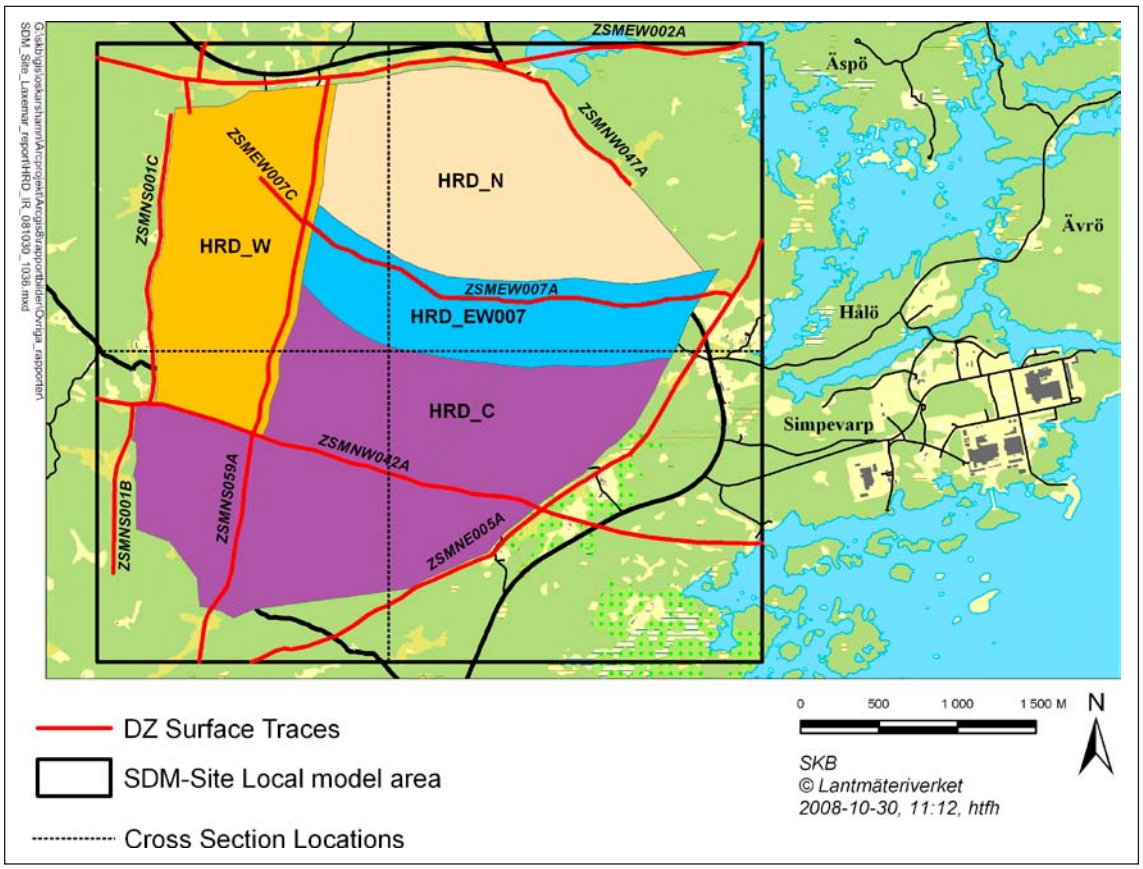

Figure 3-8. *Illustration of the SDM-Site Laxemar Hydraulic Rock Mass Domain Model. Horizontal view. DZ stands for deformation zone. /Rhén and Hartley 2009/.*

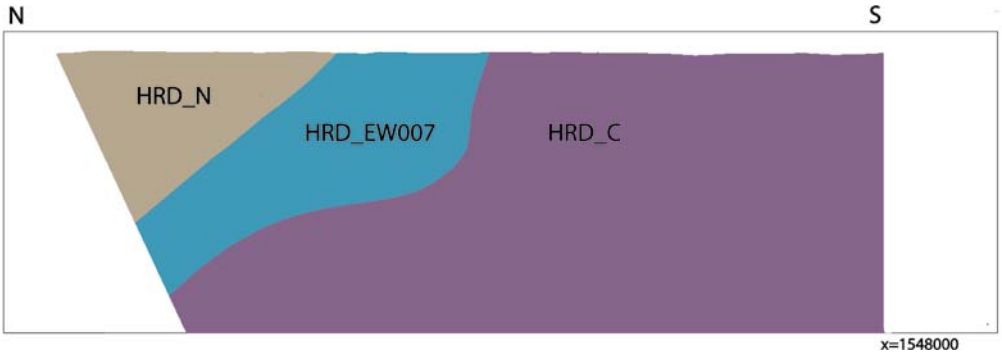

Figure 3-9. *Illustration of the SDM-Site Laxemar Hydraulic Rock Mass Domain Model. Vertical section from south (left) to north at Easting's X=154800 m, /Rhén and Hartley 2009/.*

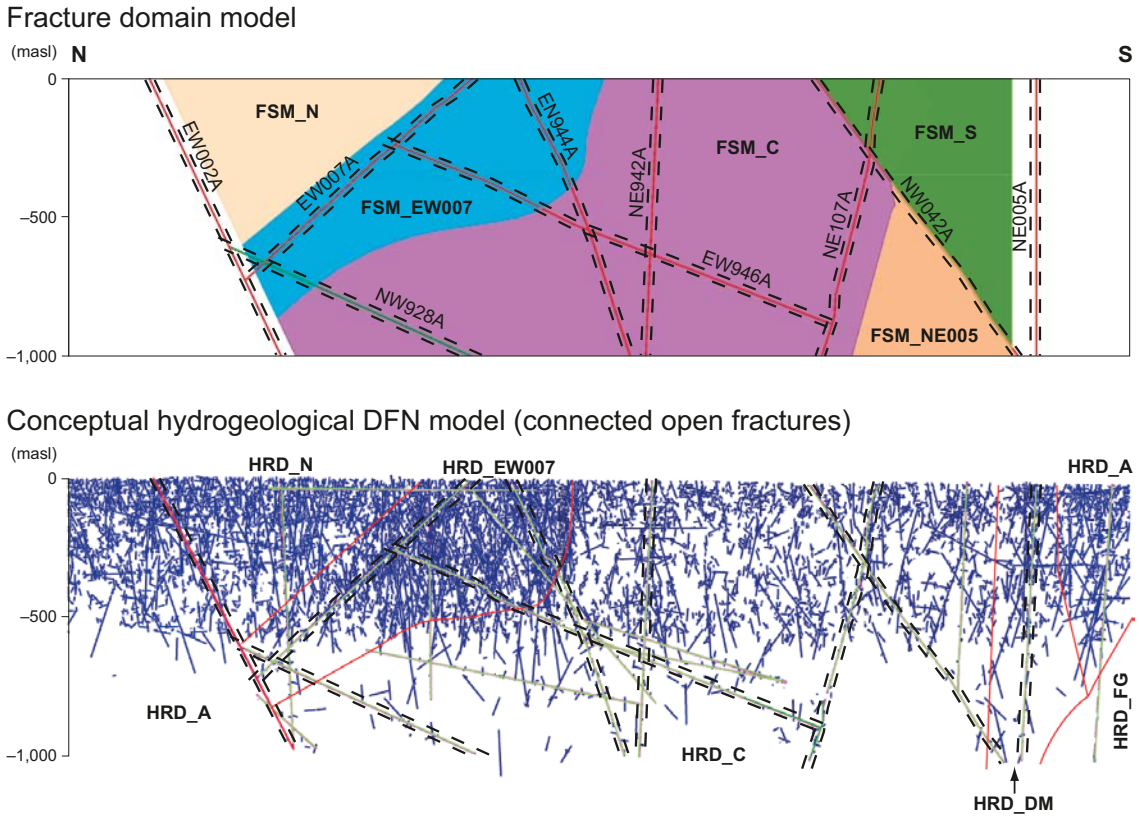

Figure 3-10. *Comparison of conceptual models for fracture domains, hydraulic DFN and associated hydraulic rock mass domains along the N-S section cf. Figure 3-8. The length of the section is ~ 4,300 m. /SKB 2009a/.*

Table 3-2. Proposed hydraulic property assignment of the regional-scale hydraulic rock mass domains to be used in SDM regional groundwater flow modelling /Rhén et al. 2008/.

Regional hydraulic rock mass domain	Suggested hydraulic properties based on hydrogeological DFN
HRD_A	HRD_N
HRD_A2	HRD_N, but rock below –650 masl is the same as –400 masl to –650 masl
HRD_D-E-M	HRD_C
HRD_B-C	HRD_C
HRD_F-G	HRD_N, but 10 times higher T
HRD_P	HRD_N

3.3.4 Hydraulic characteristics of the focused volume

The focused volume comprises HRD_C, HRD_W and the southern part of HRD_W, cf. Figure 1-9 and Figure 3-8. HRD_EW007 is more conductive compared to HRD_C and HRD_W. An example of data used for the calibration of the hydrogeological DFN model is shown in Figure 3-11. The *base case* for SDM-Site Laxemar assumes a semi-correlated transmissivity model, cf. Table 3-3. The general characteristics of the HRDs are summarised in Table 3-4 and in Table 3-5 an example of hydrogeological DFN parameters is shown.

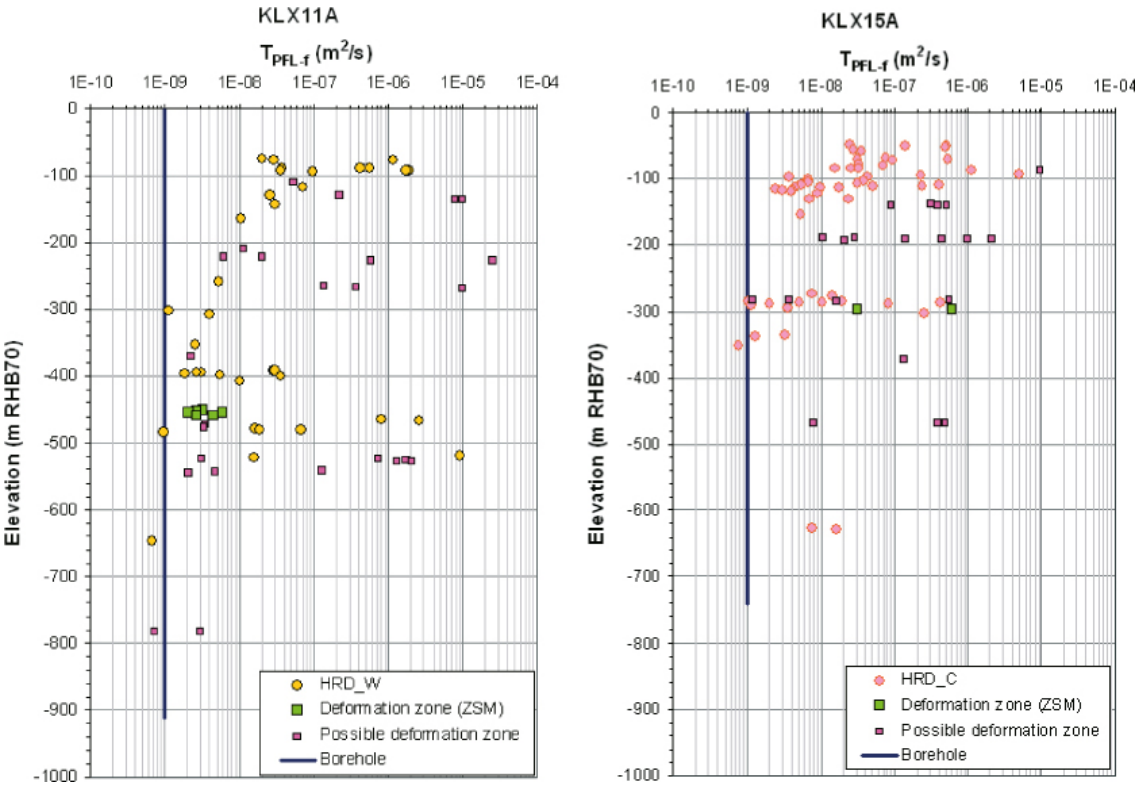

Figure 3-11. *Example of measured transmissivities (based on PFL-f) in fractures intersecting two boreholes drilled in the focused volume; KLX11A (HRD_W) and KLX15A (HRD_C) /SKB 2009a/.*

Table 3-3. Transmissivity parameters used for all sets when matching measured PFL-f flow distributions. (Log base 10) /Rhén et al. 2008/.

Type	Description	Relationship	Parameters
Correlated	Power-law relationship	$\log(T) = \log(a\, r^{b})$	a , b
Semi-correlated	Log-normal distribution about a power-law correlated mean	$\log(T) = \log(a\, r^{b}) + \sigma_{\log(T)}\, N[0,1]$	a , b, $\sigma_{\log(T)}$
Uncorrelated	Log-normal distribution about a specified mean	$\log(T) = \mu_{\log(T)} + \sigma_{\log(T)}\, N[0,1]$	$\mu_{\log(T)}$, $\sigma_{\log(T)}$

Table 3-4. Schematic summary of groundwater flow and solute transport characteristics under the current temperate climate conditions. Based on /Rhén et al. 2009/.

Depth zone	General characteristics
dZ1: > –150m	Near-surface rock, characterised by a high intensity of conductive fractures. Sub-horizontal and steeply dipping fractures striking WNW dominate. Advection dominated – high groundwater flow rates with sub horizontal fracturing giving $K_h > K_v$ in many areas. Flushed by post-glacial meteoric water. High fracture intensity implies matrix blocks 1–2 m in size, which gives equilibrium between fracture and matrix on timescales of ~1000 years.
dZ2: –150m to –400m	Intermediate-depth rock, characterised by an intermediate intensity of conductive fractures. Steeply dipping fractures striking WNW dominate except in HRD_W where no set is clearly dominant and in HRD_N and HRD_C the sub horizontal set is also important beside the WNW set. Some advection, but rock matrix diffusion (RMD) retards post-glacial meteoric penetration. Fracture intensity is generally much lower, reducing groundwater flux and increasing matrix blocks to typically ~5 m in size, such that porewater chemistry lags behind that of the fracture water by 1000s of years.
dZ3: –400m to –650m	Rock at repository level, characterised by a low intensity of conductive fractures. Steeply dipping fractures striking WNW dominate except for HRD_W where no set is clearly dominant. Low advection. RMD important because advective flow rates are small. Fracture intensity lower still, with typical matrix blocks ~10 m in size, such that porewater chemistry lags behind that of fracture water ~10,000 years.
dZ4: < –650m	Deep rock, characterised by a sparse network of conductive fractures. Steeply dipping fractures striking WNW dominate except for HRD_W where no set is clearly dominant (however rather few data occur within dZ4). Very low advection. RMD dominates. Fracture intensity very low, with typical matrix blocks ~100 m in size, such that porewater chemistry lags behind that of fracture water ~100,000 years.

Table 3-5. Description of the calibrated hydrogeological DFN input parameters for HRD_C with fixed r_0=0.038 m and intensity of open fractures based OPO (Open and Partly Open fractures). /Rhén et al. 2008/.

Depth zone (masl)	Set	Orientation set pole: (trend, plunge), conc. (°,°,-)	Fracture radius model power-law (k_r, r_0)	Intensity P_{32} (m^2/m^3) of open fractures	Transmissivity model T (m^2/s) See Table 3-3.
–150 to 0	ENE	(155.1,3.4), 9.6	(2.6, 0.038)	0.52	SC: ($6\cdot10^{-8}$, 0.5, 0.4) UC: ($2\cdot10^{-7}$, 0.6) C: ($2\cdot10^{-8}$, 0.9)
	WNW	(204,1.6), 12	(2.5, 0.038)	0.95	SC: ($2\cdot10^{-7}$, 0.6, 0.7) UC: ($1\cdot10^{-5}$, 0.9) C: ($5\cdot10^{-8}$, 1.1)
	N-S	(270.2,8.4), 7.8	(2.7, 0.038)	0.54	SC: ($2\cdot10^{-7}$, 0.6, 0.5) UC: ($1\cdot10^{-7}$, 0.7) C: ($6\cdot10^{-8}$, 1.2)
	Sub-H	(46.3,84.7), 12	(2.7, 0.038)	1.20	SC: ($1.5\cdot10^{-7}$, 0.7, 0.7) UC: ($3\cdot10^{-7}$, 0.8) C: ($6\cdot10^{-8}$, 1.0)
–400 to –150	ENE	(155.1,3.4), 9.6	(2.85, 0.038)	0.47	SC: ($1\cdot10^{-6}$, 0.7, 0.7) UC: ($2\cdot10^{-7}$, 0.7) C: ($5\cdot10^{-8}$, 1.4)
	WNW	(204,1.6), 12	(2.45, 0.038)	0.55	SC: ($8\cdot10^{-8}$, 0.3, 0.1) UC: ($3\cdot10^{-7}$, 0.6) C: ($2\cdot10^{-9}$, 1.3)
	N-S	(270.2,8.4), 7.8	(2.85, 0.038)	0.63	SC: ($1\cdot10^{-7}$, 0.7, 0.7) UC: ($2\cdot10^{-7}$, 0.4) C: ($3\cdot10^{-8}$, 1.0)
	Sub-H	(46.3,84.7), 12	(2.85, 0.038)	0.71	SC: ($1.5\cdot10^{-7}$, 0.8, 0.9) UC: ($8\cdot10^{-7}$, 1.4) C: ($3\cdot10^{8}$, 1.1)

Depth zone (masl)	Set	Orientation set pole: (trend, plunge), conc. (°,°,-)	Fracture radius model power-law (k_r, r_0)	Intensity P_{32} (m^2/m^3) of open fractures	Transmissivity model T (m^2/s) See Table 3-3.
–650 to –400	ENE	(155.1,3.4), 9.6	(2.8, 0.038)	0.38	SC: ($5{\cdot}10^{-7}$, 0.5, 0.5) UC: ($2{\cdot}10^{-6}$, 0.8) C: ($3{\cdot}10^{-8}$, 0.7)
	WNW	(204,1.6), 12	(2.5, 0.038)	0.74	SC: ($2{\cdot}10^{-8}$, 0.6, 0.4) UC: ($1{\cdot}10^{-7}$, 0.9) C: ($3{\cdot}10^{-9}$, 0.9)
	N-S	(270.2,8.4), 7.8	(2.9, 0.038)	0.47	SC: ($1{\cdot}10^{-8}$, 0.4, 0.4) UC: ($8{\cdot}10^{-8}$, 0.4) C: ($1{\cdot}10^{-8}$, 0.5)
	Sub-H	(46.3,84.7), 12	(2.9, 0.038)	0.58	SC: ($3{\cdot}10^{-7}$, 0.6, 0.6) UC: ($2{\cdot}10^{-6}$, 0.9) C: ($1.5{\cdot}10^{-7}$, 0.9)
–1,000 to –650	ENE	(155.1,3.4), 9.6	(2.9, 0.038)	0.46	SC: ($5{\cdot}10^{-9}$, 0.6, 0.4) UC: ($1{\cdot}10^{-8}$, 0.4) C: ($5{\cdot}10^{-9}$, 0.6)
	WNW	(204,1.6), 12	(2.8, 0.038)	0.73	SC: ($5{\cdot}10^{-8}$, 0.6, 0.4) UC: ($5{\cdot}10^{-7}$, 0.4) C: ($5{\cdot}10^{-8}$, 0.6)
	N-S	(270.2,8.4), 7.8	(2.95, 0.038)	0.25	SC: ($5{\cdot}10^{-9}$, 0.6, 0.4) UC: ($1{\cdot}10^{-8}$, 0.4) C: ($5{\cdot}10^{-9}$, 0.6)
	Sub-H	(46.3,84.7), 12	(2.95, 0.038)	0.35	SC: ($1{\cdot}10^{-7}$, 0.6, 0.4) UC: ($2{\cdot}10^{-7}$, 0.4) C: ($1{\cdot}10^{-7}$, 0.6)

3.4 Summary of the Quaternary deposits hydrogeological model (HSD)

The stratigraphical distribution of Quaternary deposits in the investigated area is rather uniform. Till is the oldest Quaternary deposit in the area, and is consequently resting directly upon the bedrock surface. The till in the valleys is often overlain by glacial clay, which in many valleys is overlain by a thin layer of sand followed by clay gyttja and peat.

The model developed by /Nyman et al. 2008/ contains six layers of Quaternary deposits, denoted Z1–Z6; Z1 represents the upper layer of the Quaternary deposits. These layers, illustrated in the cross section in Figure 3-12, are defined and described briefly in /Rhén et al. 2009/ and in /Nyman et al. 2008, Sohlenius and Hedenström 2008/.

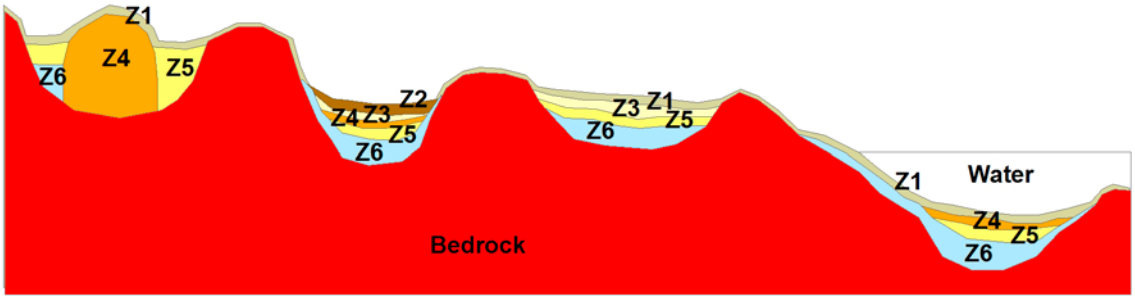

Figure 3-12. *The stratigraphical model which was used for modelling stratigraphy and total depth of Quaternary deposits in the Laxemar-Simpevarp regional model area. /Sohlenius and Hedenström 2008/. Layer Z1-6: Layer Z1 represents a thin surface(-affected) layer. Layer Z2 represents (fen or bog) peat. Layer Z3 represents postglacial clay, clay gyttja/gyttja clay, gyttja or recent fluvial sediments. Layer Z4 represents postglacial sand/gravel, glaciofluvial sediments or artificial fill. Layer Z5 represents glacial clay. Layer Z6 represents (glacial) till.*

Figure 3-13 shows the modelled distribution of total overburden depth in the Laxemar-Simpevarp regional model area. Figure 3-14 illustrates the variable depth of the Quaternary deposits along a vertical north-south section across the E-W regional deformation zone in the northern part of the local model domain; the Mederhult zone (ZSMEW002A).

This detailed Quaternary deposit model was simplified in the SDM-Site regional groundwater flow modelling representing it by four element layers vertically, each of a constant 1 m thickness, with the horizontal extent of the hydrogeological grid element (40–120 m), to represent the HSD. The same hydraulic conductivity tensor was specified for each element in a vertical stack of 4 grid elements, but varied horizontally from element-to-element, and was anisotropic with regard to horizontal and vertical components in order to represent the effective hydraulic properties of the Quaternary deposit layers. The effective hydraulic conductivity tensor for the soil package was calculated according to the actual modelled thickness of the layers of the Quaternary deposits and the hydraulic conductivities of the soil types at that location. HSD properties used in the SDM-Site *base case model* are described in Table 3-6 and illustrated in Figure 3-15. See /Rhén et al. 2009/ for details of the implementation.

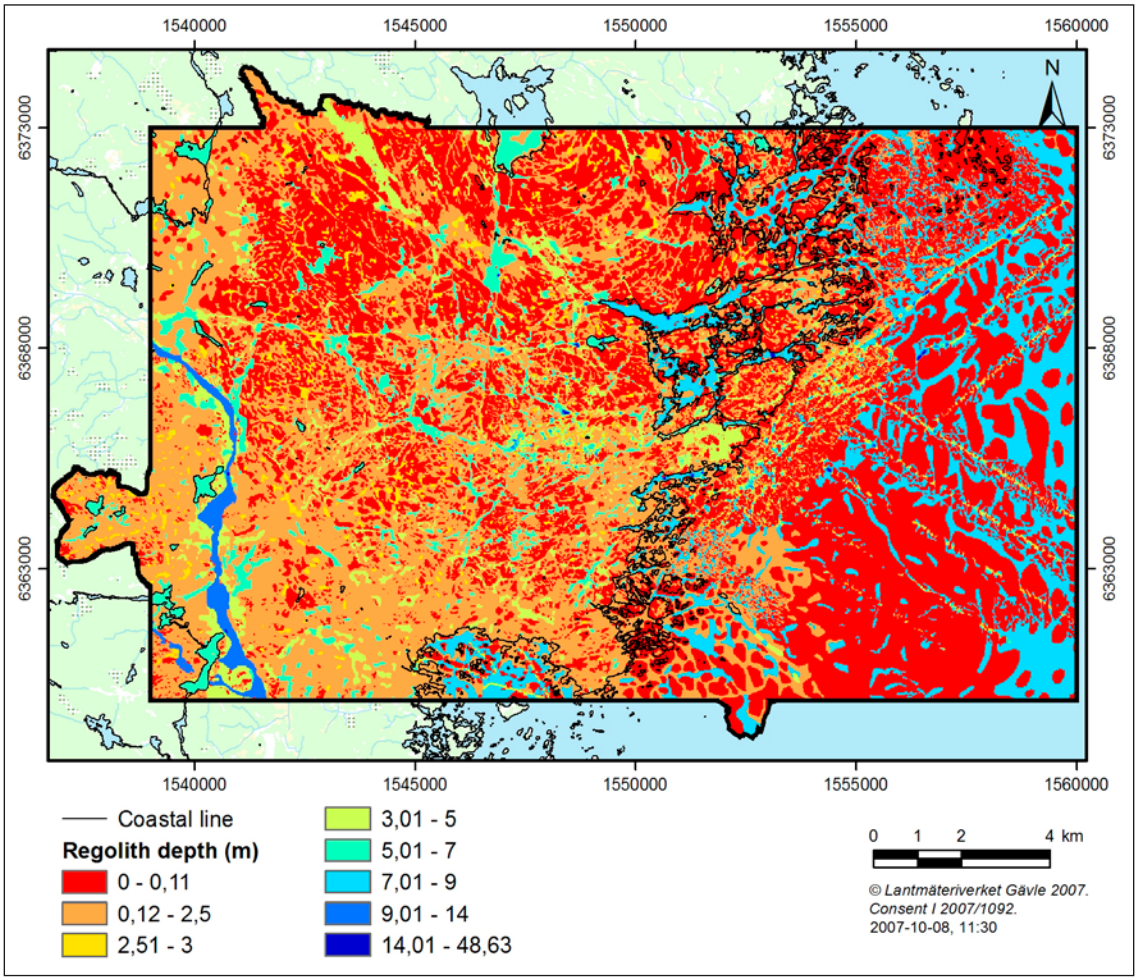

Figure 3-13. *The modelled distribution of total depths of the Quaternary deposits in the Laxemar-Simpevarp area. /Sohlenius and Hedenström 2008/.*

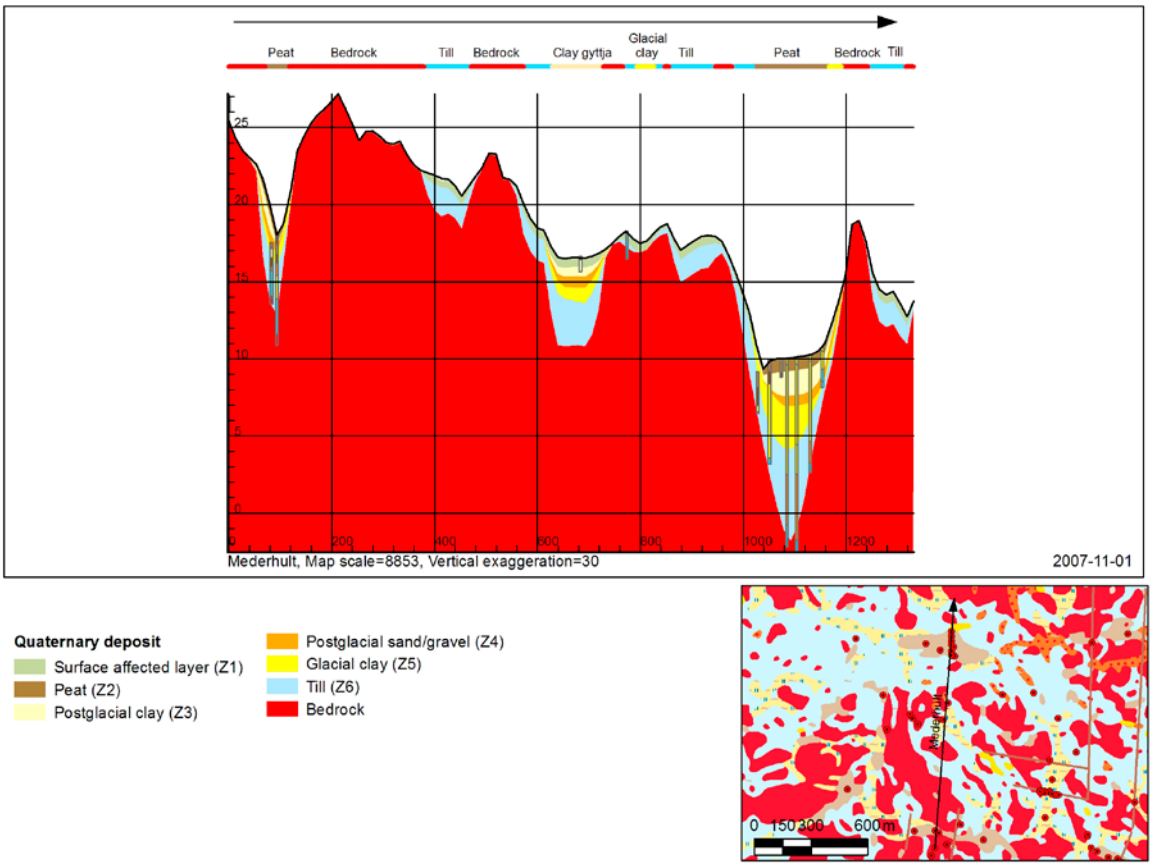

Figure 3-14. *The profile shows the total depth and stratigraphy of the Quaternary deposits in a north-south profile close to Mederhult. The valley in the right part of the profile (between 1,000 and 1,200 on the horizontal scale) is one of the largest lineaments in the model area (ZSMEW002A , cf. /Rhén et al. 2009, Figure 3-1/), /Sohlenius and Hedenström 2008/.*

Table 3-6. Prescription for hydrogeological properties of Hydraulic soil property domains used in the hydrogeological modelling (based on /Werner et al. 2008/). The relation to the model and description of the Quaternary deposits (QD type and layer) /Nyman et al. 2008, Sohlenius and Hedenström 2008, Werner et al. 2008/ is given in the second column. The modifications relative to the initial HSD assignments are highlighted in bold font, with the main change being to introduce anisotropy. Porosity is derived from specific yield /Werner et al. 2008/. /Rhén and Hartley 2009/.

Hydraulic soil property domain	QD type and layer applied to	*K* (m/s)	Porosity
Surface affected layer	Soil > 5 m thick: QD type: 1, 2, 5, 6, 7, 9, 13, 16, 17, 18, 20, 22, 24, 25, 26, 27 Layer Z1 Domain 2–24 Layer Z6	$K_h = 8 \cdot 10^{-4}$ K_h/K_v = 10:1 Original: $4 \cdot 10^{-4}$	0.15
Peat	QD type: 11, 12 Layer Z2	$K_h = 3 \cdot 10^{-6}$ K_h/K_v = 10:1	0.24
Glacial clay	QD type: 6, 8, 9, 10, 12 Layer Z3	$K_h = 1 \cdot 10^{-7}$ K_h/K_v = 10:1	0.03
Postglacial sand/gravel	QD type: 6, 7, 8, 9, 10, 12 13, 14, 15, 16, 20, 23, 24, 25, 26 Layer Z4	$K_h = 5 \cdot 10^{-3}$ K_h/K_v = 10:1	0.25
Glacial clay	QD type: 6, 8, 9, 10, 12, 13, 14, 15, 16, 17, 18, 19, 20, 21, 22, 23, 24 Layer Z5	$K_h = 1 \cdot 10^{-8}$ K_h/K_v = 2:1	0.03
Till	Soil < 5 m thick: QD type: 1, 2, 5, 6, 7, 9, 13, 16, 17, 18, 20, 22, 24, 25, 26, 27 Layer Z1 Domain 2–24 Layer Z6	$K_h = 4 \cdot 10^{-5}$ K_h/K_v = 10:1	0.05
Surface affected peat	QD type: 3,8, 21, 23 Layer Z1	$K_h = 3 \cdot 10^{-6}$ K_h/K_v = 10:1	0.24
Surface affected shingle	QD type: 4 Layer Z1	$K_h = 1 \cdot 10^{-2}$ K_h/K_v = 10:1	0.25
Surface affected sand	QD type: 10, 15 Layer Z1	$K_h = 1 \cdot 10^{-2}$ K_h/K_v = 10:1	0.25
Gyttja	QD type: 7 Layer Z3	$K_h = 1 \cdot 10^{-8}$ K_h/K_v = 2:1	0.03
Postglacial fine sand	QD type: 17 Layer Z4	$K_h = 5 \cdot 10^{-4}$ K_h/K_v = 10:1	0.25
Postglacial sand	Domain 18, 19 Layer Z4	$K_h = 1 \cdot 10^{-3}$ K_{hh}/K_v = 10:1	0.25
Postglacial gravel	QD type: 21, 22 Layer Z4	$K_h = 1 \cdot 10^{-2}$ K_h/K_v = 10:1	0.25
Artificial fill	QD type: 27 Layer Z4	$K_h = 4 \cdot 10^{-5}$ K_h/K_v = 10:1	0.05

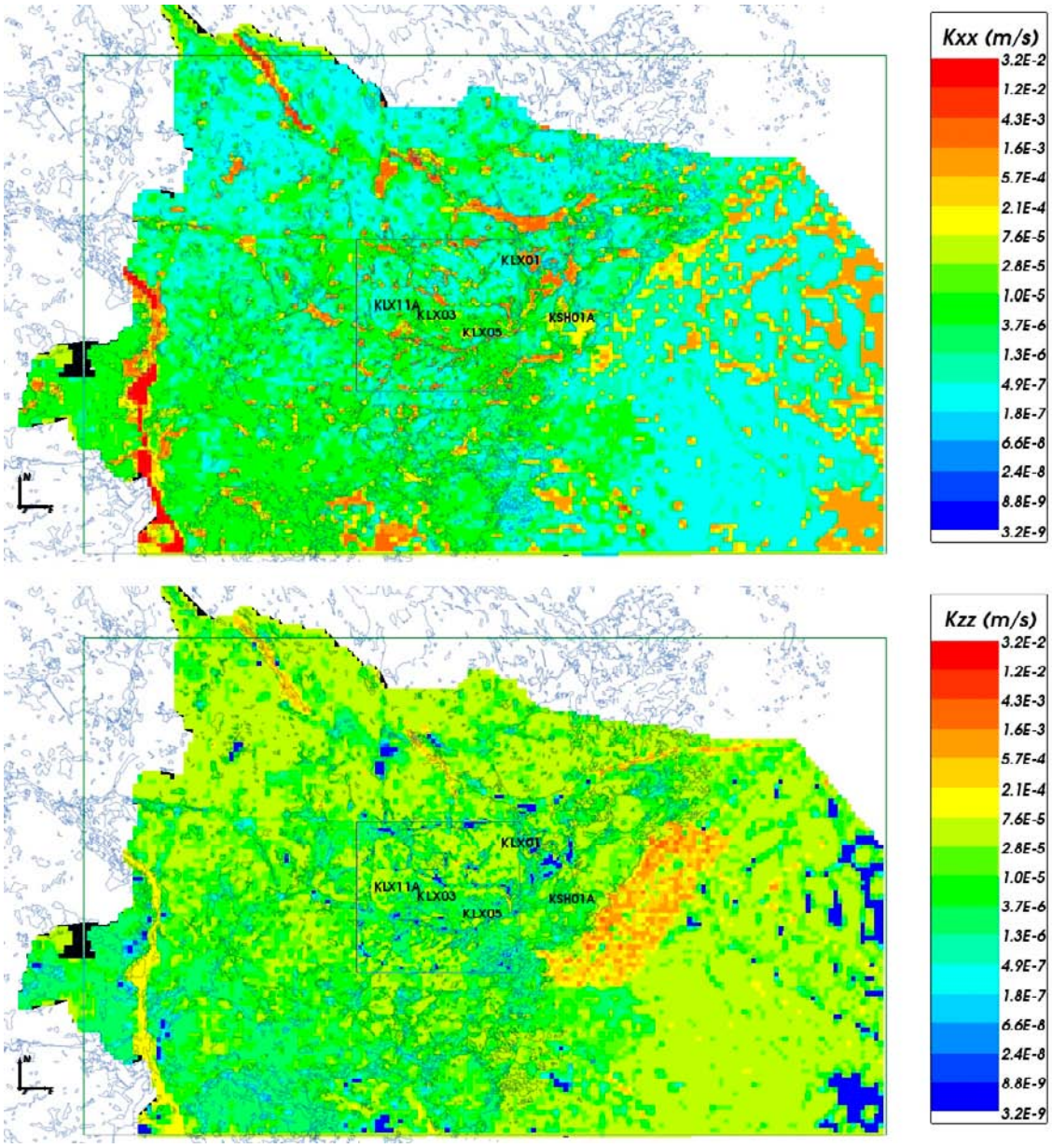

Figure 3-15. *Resulting effective hydraulic conductivity for HSD top layer based on layer thicknesses and hydraulic properties of the Quaternary deposits. Top: E-W horizontal component; Bottom: vertical component. /Rhén and Hartley 2009/.*

3.5 Groundwater flow simulations and confirmatory testing

The SDM-Site regional scale groundwater flow and solute transport simulation tests of palaeohydrogeological evolution, natural head measurements and hydraulic interference test data have confirmed that hydrogeological properties, as given by the SDM-Site hydrogeological DFN model base case /Rhén et al. 2008/ (based on all open and partly open fractures and semi-correlated transmissivity model), together with the HCD parameterisation provide an appropriate description of the hydrogeological situation in the bedrock. Only relatively minor modifications were considered necessary to obtain an acceptable match between the regional groundwater flow model results and field data.

4 Concepts and methodology

4.1 Governing equations

Coupled groundwater flow and salt transport in fractured rocks that give rise to variations in salinity and hence fluid density are modelled in DarcyTools according to the following formulation of the mass conservation equation:

$$\frac{\partial \rho\phi}{\partial t} + \frac{\partial}{\partial x}(\rho u) + \frac{\partial}{\partial y}(\rho v) + \frac{\partial}{\partial z}(\rho w) = Q \tag{4-1}$$

where ρ is fluid density [ML^{-3}], ϕ is the kinematic porosity [–], t is time [T], (u, v, w) are the directional components of the volumetric (Darcy) flux **q** [LT^{-1}] at the location (x, y, z) [L,L,L] in a Cartesian coordinate system, and Q is a source/sink term per unit volume of fluid mass [$ML^{-3}T^{-1}$]. The mass conservation equation is turned into a pressure equation by invoking the assumptions behind Darcy's law:

$$\begin{aligned} \rho u &= -\frac{K_x}{g}\frac{\partial P}{\partial x} \\ \rho v &= -\frac{K_y}{g}\frac{\partial P}{\partial y} \\ \rho w &= -\frac{K_z}{g}\frac{\partial P}{\partial z} - K_z(\rho - \rho_0) \end{aligned} \tag{4-2}$$

where K_x, K_y and K_z are the orthogonal components of the hydraulic conductivity tensor parallel to the Cartesian coordinate system [LT^{-1}], g is the acceleration due to gravity [LT^{-2}], ρ_0 is a reference fluid density [ML^{-3}], and P is the residual (dynamic) fluid pressure [$ML^{-1}T^{-2}$] at the location (x, y, z):

$$P = p + \rho_0 g z \tag{4-3}$$

where p is the gauge pressure [$ML^{-1}T^{-2}$] and $\rho_0 g z$ is the hydrostatic pressure, P_0.

The hydraulic conductivity K is related to the permeability k [L^2] through the relation:

$$K = \frac{\rho g}{\mu} k \tag{4-4}$$

where μ is the fluid dynamic viscosity [$ML^{-1}T^{-1}$]. For variable-density flow at isothermal conditions, ρ and μ are given by the following state laws:

$$\rho = \rho_0 [1 + \alpha C] \tag{4-5}$$

$$\mu = \mu_0 \tag{4-6}$$

where α and μ_0 are constants and C represents the salinity (mass fraction) [–]:

$$C = TDS / \rho \tag{4-7}$$

The migration of salt is modelled in DarcyTools in terms of advection and dispersion processes in the mobile (fracture) pore system and as a diffusion process in the immobile (rock matrix) pore system. The advection-dispersion equation for the mobile pore system is modelled in DarcyTools according to the following equation:

$$\begin{aligned} \rho\phi\frac{\partial C}{\partial t} &+ \frac{\partial}{\partial x}\left(\rho u C - \rho\gamma D_x \frac{\partial C}{\partial x}\right) \\ &+ \frac{\partial}{\partial y}\left(\rho v C - \rho\gamma D_y \frac{\partial C}{\partial y}\right) \\ &+ \frac{\partial}{\partial z}\left(\rho w C - \rho\gamma D_z \frac{\partial C}{\partial z}\right) = QC + Q_C \end{aligned} \tag{4-8}$$

where D_x, D_y and D_z are the orthogonal components of the diffusion tensor parallel to the Cartesian coordinate system [L^2T^{-1}], QC and Q_C are source/sink terms per unit volume of fluid mass [$ML^{-3}T^{-1}$], where Q_C represents the diffusive exchange of salt per unit volume of fluid mass between the mobile and immobile pore volumes [$ML^{-3}T^{-1}$], and γ is a dimensionless coefficient that describes the dependency of the kinematic porosity ϕ [-] of the mobile pore system on the dynamic pressure:

$$\phi = \phi_0 \, \gamma \tag{4-9}$$

$$\gamma = 1 + \frac{S_s}{\phi_0}\frac{(P - P_0)}{\rho g} \tag{4-10}$$

where ϕ_0 [-] is the initial kinematic porosity, S_s is the specific storage of the conductive pore system [L^{-1}].

It is noted that the concept of longitudinal and transverse hydrodynamic dispersion (dispersivity) is not considered in DarcyTools, see Equation (4-8).

The heat conservation equation may be written as:

$$\begin{aligned}\rho\phi\frac{\partial c\theta}{\partial t} + \rho_r\frac{\partial(1-\phi)c_r\theta}{\partial t} + \frac{\partial}{\partial x}\left(\rho u c\theta - \lambda_x\frac{\partial\theta}{\partial x}\right) \\ + \frac{\partial}{\partial y}\left(\rho v c\theta - \lambda_y\frac{\partial\theta}{\partial y}\right) \\ + \frac{\partial}{\partial z}\left(\rho w c\theta - \lambda_z\frac{\partial\theta}{\partial z}\right) = \left(\frac{\partial\rho u}{\partial x} + \frac{\partial\rho v}{\partial y} + \frac{\partial\rho w}{\partial z}\right)c\theta + Q_T\end{aligned} \tag{4-11}$$

where θ is the temperature [K], c is the specific heat capacity of the fluid [$L^2T^{-2}K^{-1}$] (or [J/(kg K)]), c_r is the specific heat capacity of the rock [$L^2T^{-2}K^{-1}$] (or [J/(kg K)]), ρ_r is the rock density [ML^{-3}] and λ_x, λ_y, and λ_z are the orthogonal components of the equivalent (i.e. rock with fluid) thermal conductivity tensor [$MLT^{-3}K^{-1}$] (or [W/(m K)]). Q_T represents a sink/source term [$ML^{-1}T^{-3}$] ([or W/m^3]).

4.2 Methodology

4.2.1 Finite volume method

DarcyTools uses a staggered computational grid, which means that scalar quantities such as pressure, flow porosity and salinity use a cell-centred mesh, whereas directional quantities such as hydraulic conductivity, hydrodynamic diffusivity, mass flux, and Darcy flux use a mesh centred at the cell walls. This grid arrangement was first introduced by /Harlow and Welch 1965/ and is described in textbooks, e.g. /Patankar 1980/. Each variable is assumed to be representative for a certain control volume (represented as a point value), which is the volume for which the equations are formulated. DarcyTools uses the finite volume method to transform the differential equations into algebraic equations of the type:

$$a_P\Phi_P = a_W\Phi_W + a_E\Phi_E + a_S\Phi_S + a_N\Phi_N + a_B\Phi_B + a_T\Phi_T + S_\Phi \tag{4-12}$$

where Φ denotes the variable in question, a_i are direction coefficients (West, East, South, North, Bottom, and Top) and S_Φ represents source/sink terms. The equations are solved by the MIGAL multi-grid equation solver.

4.2.2 Continuum representation of hydraulic properties of discrete fractures

Principle

The principle used to represent hydraulic properties of discrete fractures as equivalent grid cell hydraulic properties in DarcyTools works as follows:

A fracture variable (P_f) contributes to the grid cell variable (P_c) by an amount which is equal to the intersecting volume of the fracture (V_f) times the value of the fracture variable. Contributions from

all fractures (N) that intersect the grid cell control volume are added and the sum is divided by the volume of the cell (V_c), i.e.:

$$P_c = \sum_{i=1}^{N} \left(V_f\, P_f\right)_i / V_c \tag{4-13}$$

The intersecting volume of the fracture *f* may be written as:

$$V_f = L_f\, W_f\, b_f \tag{4-14}$$

where L_f, W_f and b_f denote the physical dimensions (length, width and thickness) of the intersecting fracture in three orthogonal directions. For the sake of simplicity, it is assumed in the equations below that the fracture thickness b_f is much thinner than the geometrical resolution of the computational grid (the grid size).

Grid-cell hydraulic conductivity

DarcyTools assumes that fracture transmissivity (T_f) is a scalar quantity and that fracture hydraulic conductivity (K_f) may be written as:

$$K_f = T_f / b_f \tag{4-15}$$

Thus, the contribution from an intersecting fracture to the hydraulic conductivity of the intersected grid cell may be written as:

$$(K_c)_f = (L_f\, W_f\, T_f) / V_c \tag{4-16}$$

As DarcyTools uses a staggered computational grid, K_c is a directional quantity.

Grid-cell kinematic porosity and fracture aperture

The contribution from an intersecting fracture, deterministic or stochastic, to the kinematic porosity of the intersected grid cell can approximately be written as:

$$(\phi_c)_f = (L_f\, W_f\, (e_T)_f) / V_c \tag{4-17}$$

where $(e_T)_f$ [L] is the fracture transport aperture. In SDM-Site, a power-law function between the fracture aperture and the fracture transmissivity was assumed:

$$(e_T)_f = a\, (T_f)^b \tag{4-18}$$

with a = 0.46 and b = 0.5 /Dershowitz et al. 2003/.

In the work reported here, the transport apertures of the deterministically modelled deformation zones are based on Equation (4-18), whereas all stochastically modelled zones and fractures are given a constant transport aperture of $1 \cdot 10^{-4}$ m, see Appendix A for details.

Fracture transmissivity

The equations given above reveal that fracture transmissivity is the key hydraulic quantity in DarcyTools, i.e. fracture transmissivity is used to define both grid cell hydraulic conductivity and grid cell kinematic porosity.

DarcyTools assumes that a power-law function prevails between fracture transmissivity and fracture size (L_f). The power-law function may be written as /Svensson et al. 2010/:

$$\log(T_f) = \log\left[a_T \left(\frac{L_f}{100} \right)^{b_T} \right] + d_T\, U[-0.5,0.5] \tag{4-19}$$

where a_T is the transmissivity value of a fracture with L_f = 100 m and b_T is the exponent of the power-law function. d_T is a factor that scales a uniformly distributed random deviate U and is used when uncertainty in the power-law function is addressed.

For the sake of clarity it is noted that the relationship between the power-law parameters used in DarcyTools (a_T,b_T) and the corresponding power-law parameters (a,b) derived in SDM-Site can be written as:

$$b_T = b \tag{4-20}$$

$$a_T = a\left(100/\sqrt{\pi}\right)^{b_T} \tag{4-21}$$

4.2.3 Particle tracking performance assessment measures

A particle tracking algorithm is used to represent advective transport of radionuclides. In DarcyTools, particles are tracked in a deterministic way by moving along a discretised path within the local finite-element velocity-field. The particle tracking routine in DarcyTools, PARTRACK, has two modes of operation; the first is the classic way of moving the particle along the local velocity vector, whereas the second method uses the so called "flux-weighting" approach, and works as follows.

- A particle entering a scalar cell will, if no dispersion effects are activated, stay in the cell for a time that is equal to the free volume of the cell divided by the flow rate through the cell.
- When the particle is ready to leave the cell, it will leave through one of the cell walls that has an outgoing flow direction. The choice between cell walls with an outgoing flow is made with a likelihood that is proportional to the outflows. If several particles are traced, the cloud will thus split up in proportion to the flow rates. Complete mixing in a cell is assumed.

In the work reported here, we use the classic way of moving the particle along the local velocity vector. Three performance measures are calculated, see Figure 1-2:

- Flow path length L [L]
- Advective travel time t_w [T]
- Flow-related transport resistance F [TL^{-1}]

Flow path length

The flow path length L [L] is calculated as:

$$L = \sum_l \delta l \tag{4-22}$$

where δl [L] is a step length along a flow path of l steps.

Travel time

In principle, the travel time t_w [T] is calculated as:

$$t_w = \sum_l \frac{\phi\, \delta l}{q} \tag{4-23}$$

where ϕ [-] is the kinematic porosity along a flow path of l steps, δl [L] is a step length along the flow path, and q [LT^{-1}] is the Darcy flux along the flow path. Inserting Equation (4-15) and Equation (4-17) into Equation (4-23), the travel time spent in a grid cell intersected by a single fracture may be written as:

$$(t_w)_f = \frac{(\phi_c)_f\, L_f}{(K_c)_f\, J_f} = \frac{(e_T)_f\, L_f}{T_f\, J_f} \tag{4-24}$$

where J_f is the hydraulic gradient [LL^{-1}]. That is, the travel time depends largely on the relationship between the fracture aperture and the fracture transmissivity.

Flow-related transport resistance

The flow-related transport resistance F [TL^{-1}] is a measure of the potential for retention and retardation of radionuclides along a flow path through the fractured bedrock. In a continuous porous media code such as DarcyTools, the flow-related transport resistance is defined as:

$$F = \sum_{l} \frac{a_r \delta l}{q} \tag{4-25}$$

where a_r [L^{-1}] is the flow wetted fracture surface area per unit volume of rock along a flow path of l steps, δl [L] is a step length along the flow path, and q [LT^{-1}] is the Darcy flux along the flow path. The values of a_r used in the work reported here are specified in Appendix A.

4.2.4 Exchange of dissolved solids

In DarcyTools, the exchange of dissolved solids between the fracture water and the matrix porewater is modelled with a one-dimensional multi-rate diffusion model /Haggerty and Gorelick 1995/. The diffusion process is represented by a series of discrete exchange rate coefficients, α_{min}–α_{max} [T^{-1}], where the time scale of the remotest diffusive exchange is $1/\alpha_{min}$. Another parameter governing the diffusion process in the model of /Haggerty and Gorelick 1995/ is the ratio between the diffusive and advective pore spaces, β [-]. In fractured crystalline rock, the matrix porosity is approximately 10–100 times greater than the kinematic porosity /Follin et al. 2005/.

The chosen range of values of the exchange rate coefficients not only affects the time scales but also the penetration depths of the multi-rate diffusion process. In the work reported here, ten exchange rate coefficients are used. The value of α_{min} is set to $4 \cdot 10^{-12}$ s^{-1}, which implies a time scale of approximately 8,000 years for the remotest diffusive exchange, and the value of β is set to 10, i.e. ten times more pore space in the matrix than in the fractures. Both settings are regarded as provisional. A somewhat more elaborated discussion is provided in Appendix C.

5 Model specifications

5.1 Studied cases

In addition to the four glacial cases (a)–(d) listed in Table 1-1, a temperate case without ice and permafrost is also studied. This allows for relative comparisons of the defined hydrogeological quantities and performance measures. In this work, the differences in Darcy flux (q) and water salinity (C) are looked at by computing the ratios q/q_{temp} and C/C_{temp} obtained from the flow solutions. The differences in advective travel time (t_w) and flow-related transport resistance (F) are looked at by comparing the cumulative distribution (probability) plots obtained from the particle tracking.

The essence of Table 1-1 is repeated in Table 5-1 and visualised in Figure 5-1, Figure 5-2 and Figure 5-3. The key "climate events" looked at are highlighted in *italics* in Figure 5-1, Figure 5-2 and Figure 5-3. These are:

- Temperate (used to produce scaled (normalised) entities).
- Permafrost.
- Glacial case without permafrost.
- Glacial maximum.
- Glacial case with permafrost and a 2 km long permafrost tongue.
- Submerged.

Table 5-1. Overview of the two main scenarios, A and B, and the four studied cases (a)–(d). The cases are visualised in Figure 5-1 through Figure 5-3.

Case	Explanation
	A. Glacial climate conditions without Permafrost
(a)	NW-SE ice sheet movement
(b)	N-S ice sheet movement
(c)	Elaborated permeability conditions based on the Elaborated Hydro-DFN /Joyce et al. 2010, Appendix E/
	B. Glacial climate conditions with Permafrost
(d)	A 2 km long tongue of permafrost within the margin of the ice sheet

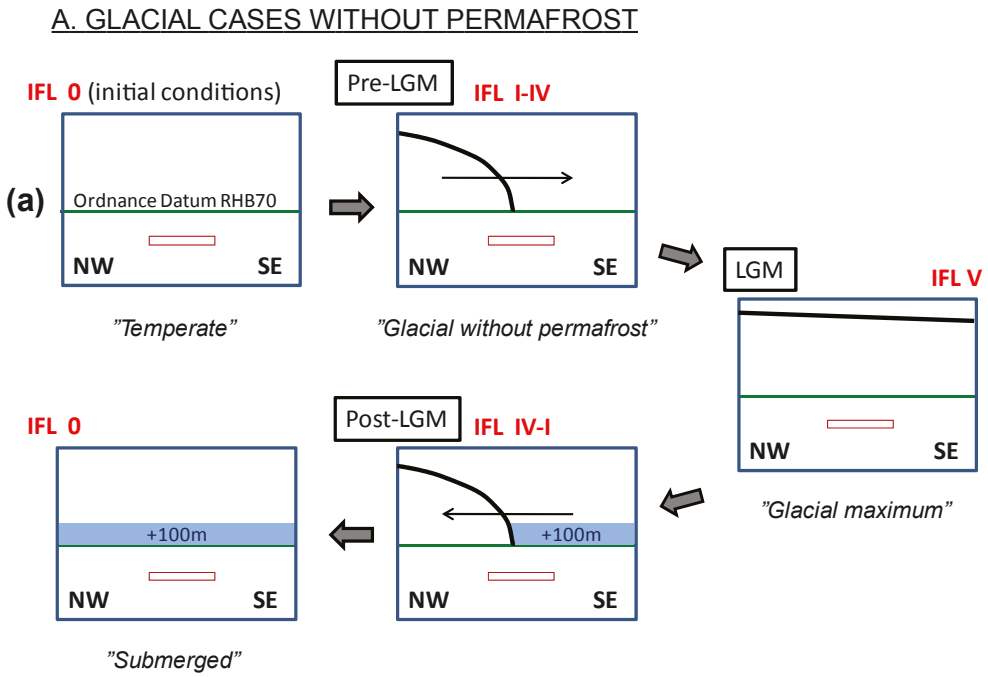

Figure 5-1. *Cartoons visualising the modelling associated with case (a), see Table 5-1. The deep repository is shown as a rectangle.*

A. GLACIAL CASES WITHOUT PERMAFROST (continued)

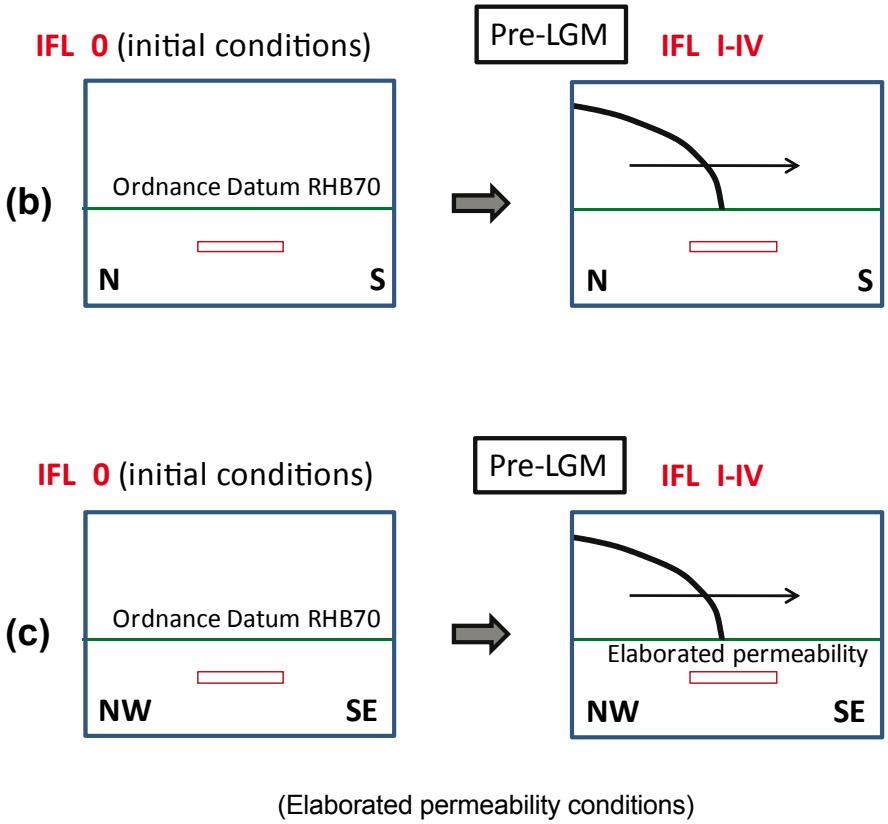

Figure 5-2. *Cartoons visualising the modelling associated with case (b) and case (c), see Table 5-1. The deep repository is shown as a rectangle.*

B. GLACIAL CASES WITH PERMAFROST

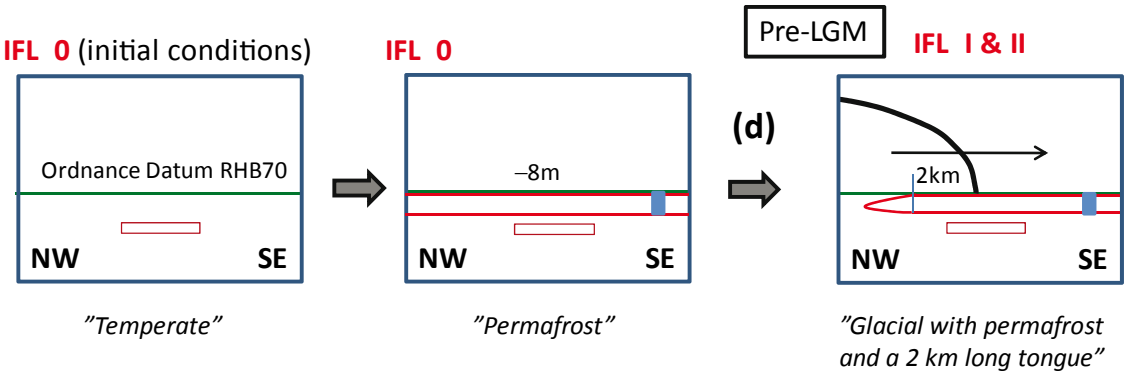

Figure 5-3. *Cartoons visualising the modelling associated with case (d), see Table 5-1. The deep repository is shown as a rectangle.*

5.2 Simulation methodology

5.2.1 Temperate case

Flow and salt transport

The governing equations for flow and salt transport are solved using fixed boundary conditions and initial conditions as applied in SDM-Site Laxemar /Rhén et al. 2009/. The initial and boundary conditions for the temperate case are shown in Table 5-2 and Table 5-3, respectively.

Transport (particle tracking)

The flow and salt transport solutions are fixed in time and particle tracking is performed. Particles are released at the 8,031 deposition hole positions.

Output

Pressure (P), Darcy flux (q), salinity (C) at the five specified measurement localities (ML 1-5) surrounding the repository. Flow path length (L), travel time (t_w), and flow-related transport resistance (F) for each particle.

5.2.2 Glacial cases without permafrost

Flow and salt transport

The flow and salt transport solutions derived for the temperate case are used as initial conditions together with the transient top boundary conditions shown in Figure 5-1, Figure 5-2 and Table 5-4. The solutions to the governing equations for flow and salt transport are saved for each ice-front location. During the LGM stage, the ice sheet profile addressed in case (a) was changed over approximately 11,000 years, see section 1.3.1. During the retreat of the ice sheet margin, the sea level was raised from the present-day elevation to +100 m above the Swedish Ordnance Datum RHB 70 causing submerged ground conditions in front of the margin, see Figure 5-1.

Transport (particle tracking)

See the corresponding paragraph in section 5.2.1.

Output

See the corresponding paragraph in section 5.2.1.

5.2.3 Glacial cases with permafrost

Flow and salt transport

First, the flow and salt transport solutions derived for the temperate case are used as initial conditions to a simulation where the sea level elevation is displaced from the present-day elevation to –8 m below the Swedish Ordnance Datum RHB 70, see Figure 5-3. Second, the flow and salt transport solutions to the shoreline displacement simulation are used as initial conditions to a simulation where a constant temperature at the ground surface of –4.2°C prevails over a period of 2,000 years. This boundary condition is applied across the entire model domain except where there are water bodies (taliks), where the temperature is set to +4°C. The topography is used to make informed judgements as to where taliks might occur. Table 5-5 and Table 5-6 show the initial and boundary conditions applied for the generation of permafrost. Third, the flow and transport solutions to the permafrost development simulation are used as initial conditions to a simulation where an ice sheet margin moves across the model domain, see Figure 5-3. The transient boundary conditions for the glacial cases with permafrost are specified in Table 5-7.

Transport (particle tracking)

See the corresponding paragraph in section 5.2.1.

Output

See the corresponding paragraph in section 5.2.1.

Table 5-2. Initial conditions of the fracture water and matrix porewater salinities. (inferred from /Rhén et al. 2009/) (cf. Appendix C)

Depth interval	Initial salinity
Ground surface to –150 m	0%
–150 m to –2,100 m	Linearly increasing to 7.2%
Below –2,100 m	7.2%

Table 5-3. Boundary conditions for the temperate case.

Boundary	Boundary conditions
Shoreline elevation	0 m RHB 70
Top boundary, land above sea	P=0 at ground surface; C=0
Top boundary, land below sea	P=g ρ_0 (sea depth); C=0%
Lateral (vertical) boundaries	$\partial P/\partial x=\partial P/\partial y=0$ and $\partial C/\partial x=\partial C/\partial y=0$
Bottom boundary at –2,496 m	$\partial P/\partial z=0$; C=7.2% by weight

Table 5-4. Boundary conditions for the glacial cases without permafrost.

Boundary	Boundary conditions
Shoreline elevation	0 m RHB 70
Top boundary, land without ice	P=0 at ground surface; C=0
Top boundary, land below sea	Hydrostatic pressure: P=g ρ_0 (sea depth); C=0%
Top boundary, land below ice	P according to Equation (2-3); C=0%
Lateral (vertical) boundaries	$\partial P/\partial x=\partial P/\partial y=0$ and $\partial C/\partial x=\partial C/\partial y=0$
Bottom boundary at –2,496 m	$\partial P/\partial z=0$; C=7.2% by weight

Table 5-5. Initial temperature conditions prior to the permafrost simulations.

Location	Temperature
At sea	0.1°C
On land	1.0°C
Depth gradient	0.015°C/m

Table 5-6. Boundary conditions for the generation of permafrost.

Boundary	Boundary condition
Shoreline elevation	–8 m RHB 70
Top boundary, land without ice	T=–4.2°C
Top boundary, taliks	T=+4°C
Top boundary, land below sea	T=+4°C
Lateral (vertical) boundaries	$\partial T/\partial x=0$; $\partial T/\partial y=0$
Bottom boundary at –2,496 m	q_{heat} = 0.0553 W/m^2

Table 5-7. Boundary conditions for the glacial cases with permafrost.

Boundary	Boundary conditions
Shoreline elevation	–8 m RHB 70
Top boundary, permafrost areas	P=0 at ground surface; C=0; T=–4.2°C
Top boundary, taliks	P=0 at talik water level; C=0; T=+4°C
Top boundary, unfrozen land Below sea: Below ice:	 P=g ρ_0 (sea depth); C=0 ; T=+4°C P according to Equation (2-3)/; C=0 ; T=+0.01°C
Lateral (vertical) boundaries	$\partial P/\partial x=0$, $\partial C/\partial x=0$, $\partial T/\partial x=0$; $\partial P/\partial y=0$, $\partial C/\partial y=0$, $\partial T/\partial y=0$
Bottom boundary at –2,496 m	$\partial P/\partial z=0$; q_{heat} = 0.0553 W/m^2 and C=7.2% by weight

5.3 Model domain, measurement localities and ice-front locations

A NW-SE orientation of the model domain is conceived to be the most appropriate orientation to study for an advancing ice sheet margin. Figure 5-4 shows the location of the NW-SE model domain studied in cases (a) and (c)–(d) and Figure 5-5 shows the location of the N-S model domain studied in case (b).

The NW-SE model domain is approximately 50 km long, 20 km wide and 2.5 km deep. The corresponding data for the N-S domain are approximately 40 km, 30 km and 2.5 km, respectively. Hence, a super-regional modelling approach is used. Examples of previous studies for SKB focusing on hydrogeological issues on a super-regional scale are, among others, /Follin and Svensson 2003, Holmén et al. 2003, Holmén 2008, Ericsson et al. 2006, Ericsson and Holmén 2010, Vidstrand et al. 2010/.

The coordinates of the cell centre of each corner cell are shown in Table 5-8. The coordinates of the five measurement locations (ML 1-5) shown in Figure 1-4 are shown in Table 5-9.

The Roman numerals shown in Figure 5-4 indicate the positions of the studied ice-front locations (IFL I–IV) for the NW-SE model domain, see Table 5-10 for coordinates. Ice-front location II (IFL II) is positioned right above the repository. The corresponding information for the N-S model domain is shown in Figure 5-5 and Table 5-11.

Table 5-8. Cell centre coordinates of the model domain corner cells.

	NW-SE model domain (Figure 5-4)		N-S model domain (Figure 5-5)	
Corner	Coordinate (x,y) (DarcyTools)	Coordinate (x,y) (RT90)	Coordinate (x,y) (DarcyTools)	Coordinate (x,y) (RT90)
NW	(–15008, 14824)	(1523992, 6374824)	(–4992, 29000)	(1534008, 6389000)
NE	(–128, 29640)	(1538872, 6389640)	(24992, 29000)	(1563992, 6389000)
SW	(20000, –20216)	(1559000, 6339784)	(–4992, –10008)	(1534008, 6349992)
SE	(34848, –5368)	(1573884, 6354632)	(24992, –10008)	(1563992, 6349992)

Table 5-9. Coordinates of the measurement localities ML 1-5.

Measurement locality	Coordinate (x,y,z) (DarcyTools local)	Coordinate (x,y,z) (RT 90, RHB 70)
1	(8000, 5500, –500)	(1547000, 6365500, –500)
2	(9250, 6000, –500)	(1548250, 6366000, –500)
3	(10500, 6500, –500)	(1549500, 6366500, –500)
4	(10200, 5700, –500)	(1549200, 6365700, –500)
5	(8000, 6500, –500)	(1547000, 6366500, –500)

Table 5-10. Coordinates of ice-front locations I–IV for the NW-SE model domain. The ice front is oriented at 45 degrees trending NE-SW.

Ice-front location	Coordinate (x,y) (DarcyTools local)	Coordinate (x,y) (RT 90)
I	(1100, 0)	(1540100, 6365500)
II	(3200, 0)	(1542200, 6365500)
III	(4400, 0)	(1543400, 6365500)
IV	(27800, 0)	(1566800, 6365500)

Table 5-11. Coordinates of ice-front locations I and II for the N-S model domain.

Ice-front location	Coordinate (x,y) (DarcyTools local)	Coordinate (x,y) (RT 90)
I	(–, 6650)	(–, 6366650)
II	(–, –5050)	(–, 6354950)

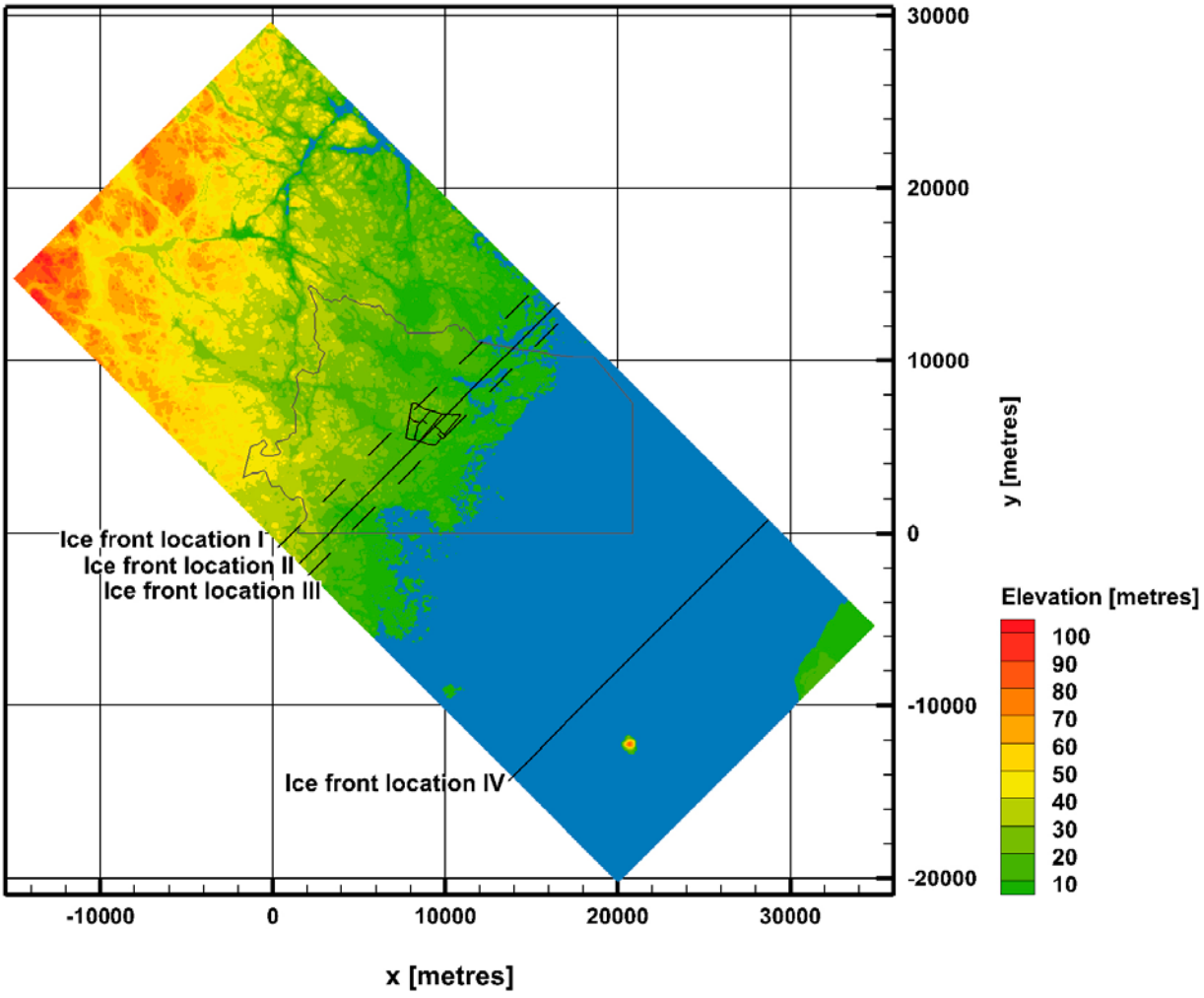

Figure 5-4. Location of the model domain in cases (a), (c), and (d) The map shows the present-day topography at Laxemar-Simpevarp and the positions of the studied ice-front locations (IFL I–IV). The large polygon in the centre is the regional flow domain used in the groundwater flow modelling for SDM-Site Laxemar /Rhén et al. 2009/. The locations of the suggested final repository for spent nuclear fuel is also shown. The y-axis points towards north.

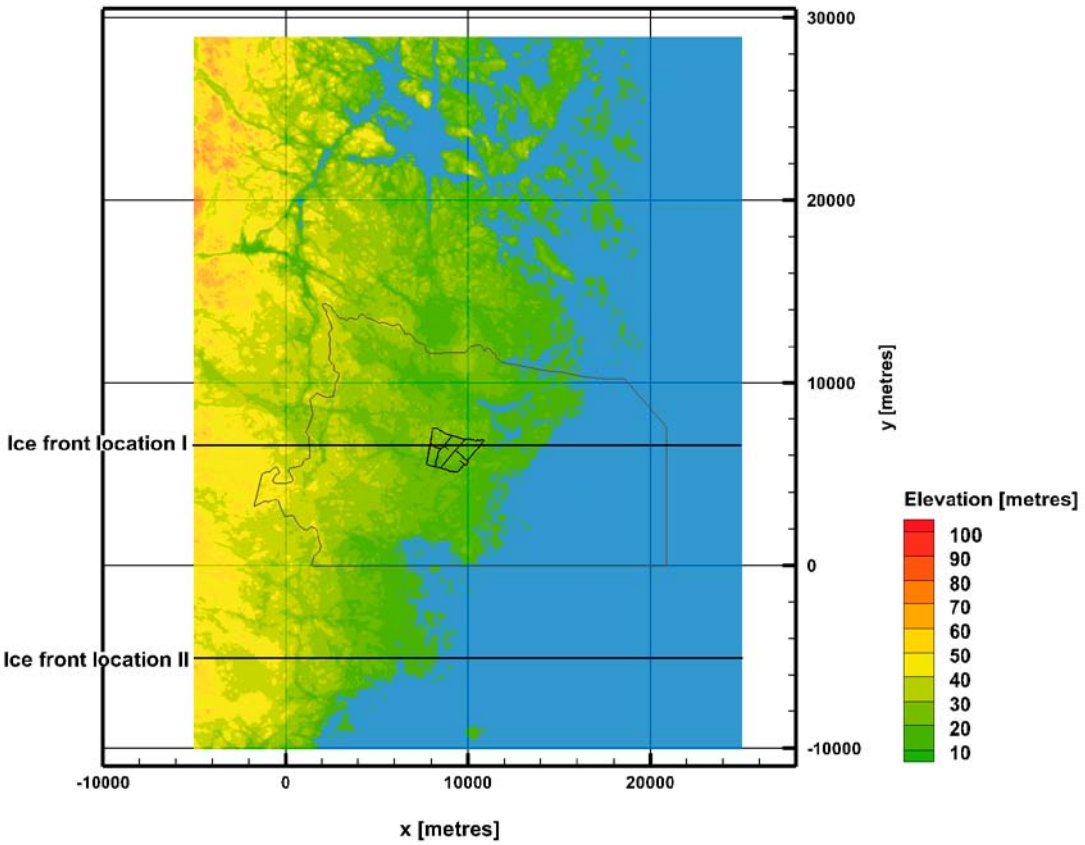

Figure 5-5. *Location of the model domain used in case (b). The map shows the present-day topography at Laxemar-Simpevarp and the positions of the studied ice-front locations (IFL I & II). The locations of the suggested final repository for spent nuclear fuel is also shown. The y-axis points towards north.*

5.4 Hydraulic properties

The geometry and hydraulic properties of discrete geological features in the bedrock such as deformation zones are the same as in SDM-Site. The data used here are imported from /Joyce et al. 2010/ and visualised in Figure 5-6.

Concerning the stochastic hydrogeological properties of the fracture domains within the focused area, the statistical distributions used here are identical to those used by /Joyce et al. 2010/. However, a single realisation is studied in the work reported here, whereas /Joyce et al. 2010/ study several realisations.

The parameters and the parameter values used to generate a hydrogeological realisation of the fracture domains within the focused area are listed in Appendix A, which also presents the hydraulic properties used for the bedrock outside the fracture domains and the deformation zones modelled deterministically in SDM-Site.

The grid cell hydraulic properties of the uppermost 20 m of the model domain and the minimum values of the hydraulic properties below 20 m depth are shown in Table 5-12 and Figure 5-7.

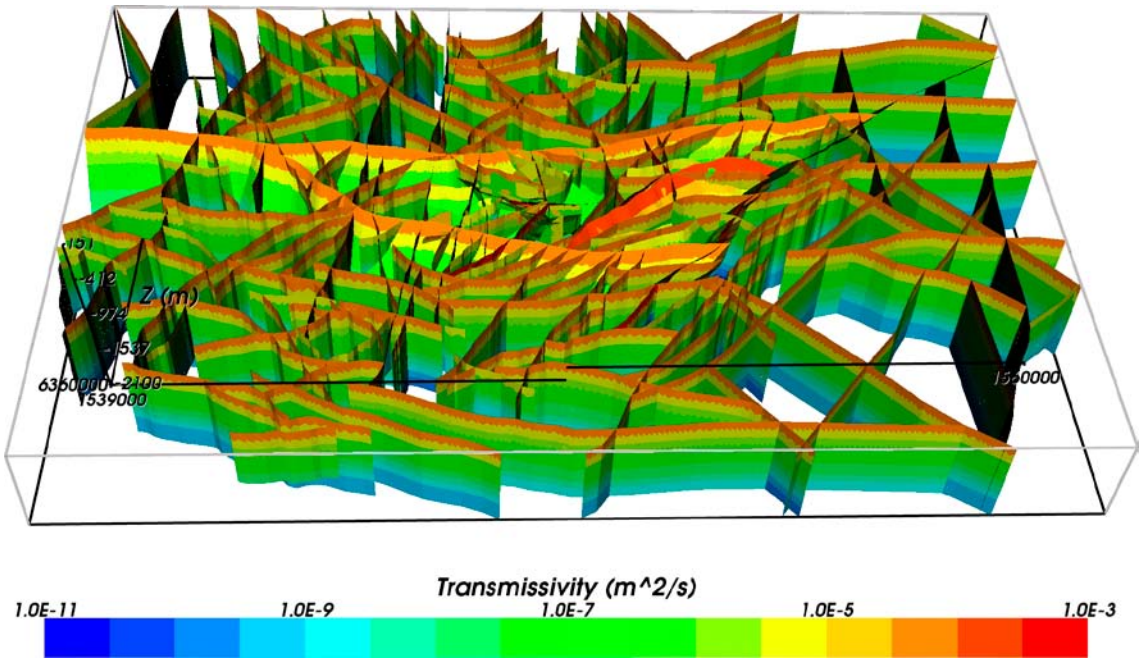

Figure 5-6. *Visualisation of regional and local scale deformation zones (HCD). Each zone is coloured by its hydraulic conductivity (cf. Figure 3-5). Oblique view looking from the south. /Rhén and Hartley 2009/.*

Table 5-12. Grid cell hydraulic properties applied in this work in the uppermost 20 m of the model domain and the minimum values allowed below this depth. (After /Vidstrand et al. 2010/.)

Grid cell property	Depth interval	Value
Hydraulic conductivity K_c [m/s]	< 20 m depth	$K_{c,h} = \max \begin{cases} 1 \cdot 10^{-7} \\ 5 \cdot 10^{-3}\, 10^{-Depth/3} \end{cases}$ $K_{c,v} = 1 \cdot 10^{-6}$
	≥ 20 m depth	$K_{c,h} \geq 3 \cdot 10^{-11}$ $K_{c,v} \geq 3 \cdot 10^{-11}$
Kinematic porosity ϕ_c [-]	< 20 m depth	$\phi_c = \max \begin{cases} 1 \cdot 10^{-3} \\ 5 \cdot 10^{-2}\, 10^{-Depth/20} \end{cases}$
	≥ 20 m depth	$\phi_c \geq 1 \cdot 10^{-5}$
Specific storage $S_{s,c}$ [m^{-1}]	≥ 0 m depth	$S_{s,c} = 1 \cdot 10^{-9}$

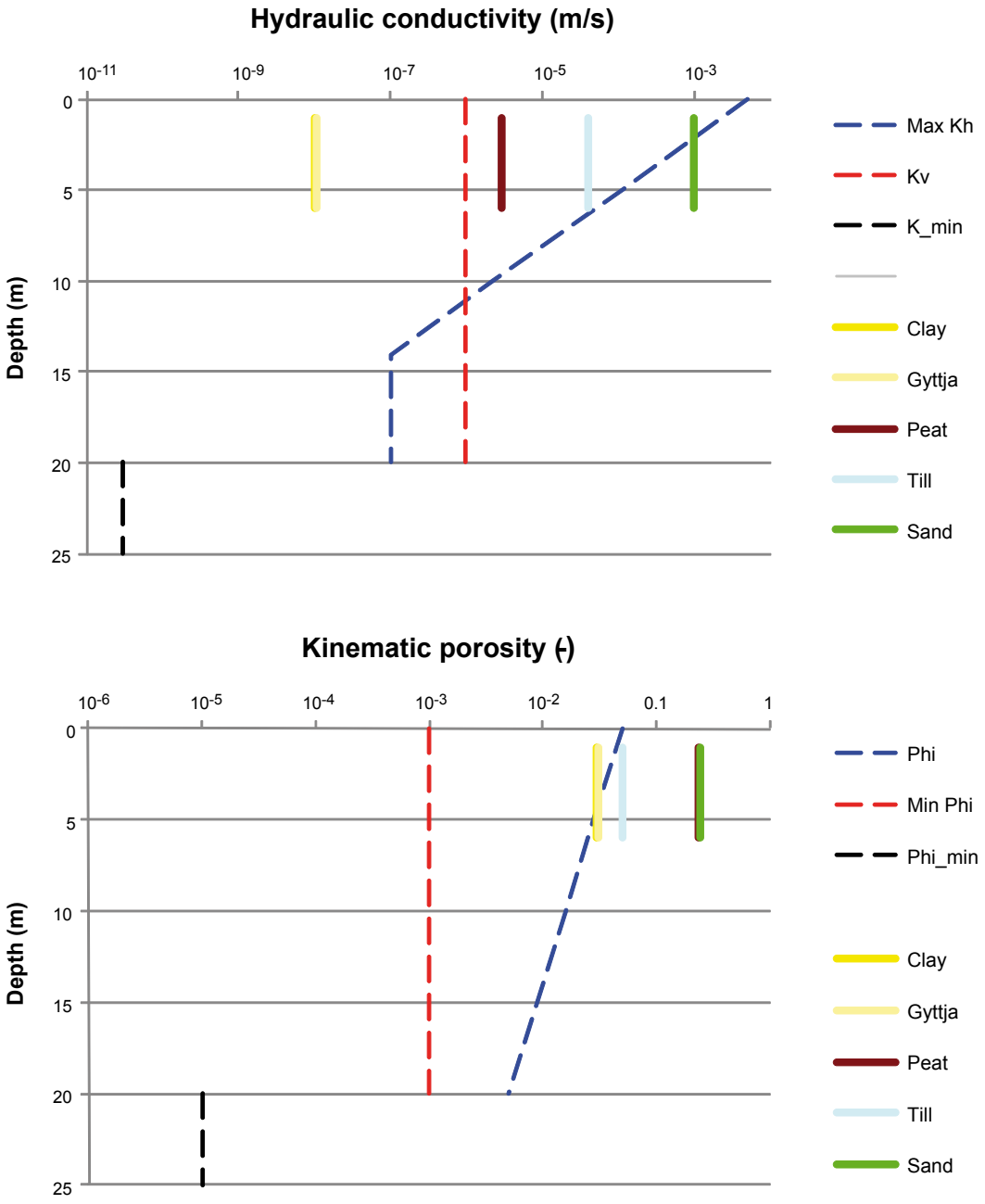

Figure 5-7. *The blue and red dashed lines show the values used in this work to simulate the hydraulic properties of the Quaternary deposits and the uppermost bedrock, i.e. above 20 m depth. The black dashed lines represent the minimum values of hydraulic properties of the non-fractured parts of the bedrock below this depth (cf. Table 5-12). The solid lines represent the values shown in Table 3-6.*

Figure 5-8 shows an example of the effect of freezing on the permeability using the algorithm described in /Vidstrand et al. 2010, Appendix A/. This range of reduction is similar to the reduction simulated by /Hartikainen et al. 2010/.

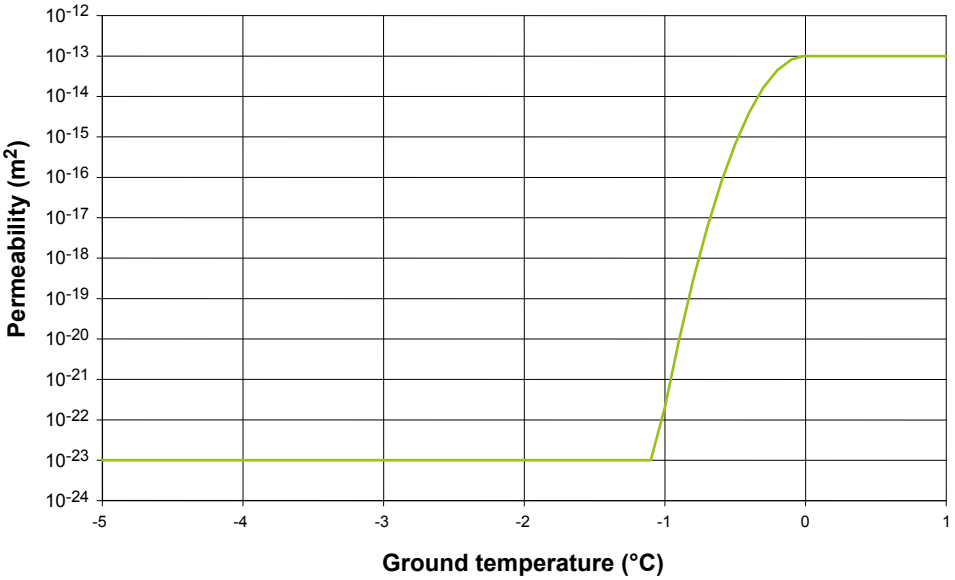

Figure 5-8. *An example of how the permeability depends on the temperature in the work reported here.*

5.5 Thermal properties

The values used in the flow simulations are shown in Table 5-13. The properties assigned are based on estimated mean values taken from /Sundberg et al. 2009/.

Table 5-13. Thermal properties.

Property	Value
Thermal conductivity [W/mK]	2.75
Heat capacity [J/m³K]	$2.23 \cdot 10^6$

5.6 Computational grid

The model domain is discretised by an unstructured grid. Close to ground surface, the 50 m digital elevation model[9] used is refined to fit a cell size of 32 m in the horizontal directions. The resolution of the topographic variations in the vertical direction is set to 2 m. The bottom of the model domain is located at an elevation of –2,560 m. The thickness of the bottom cell layer is constant throughout the model domain and set to128 m. (The elevation of the pressure node in the bottom cell layer is located at –2,496 m [= –2,560 m+(128 m/2)].)

Within the area specified in Table 5-14, the cell size is $(32\ m)^3$ (cf. the area shown in Figure 1-4). Far away from this area, the largest cell size is $(512\ m)^3$. In between, a varying cell size is used. In total, the model domain consisted of 7.4 million cells.

[9] Brydsten L, 2009. Data set delivery 50 m DEM of regional extent (see Appendix B).

Table 5-14. Corner coordinates of the area shown in Figure 1-4.

Corner	Coordinate (x,y) (DarcyTools local)	Coordinate (x,y) (RT90)
NW	(7000, 8000)	(1546000, 6368000)
NE	(11500, 8000)	(1550500, 6368000)
SW	(7000, 4500)	(1546000, 6364500)
SE	(11500, 4500)	(1550500, 6364500)

5.7 Permeability at the five measurement localities

Measurement localities ML 1-5 are located nearby the repository in regions with different hydraulic properties. Figure 5-9 shows a close-up view around measurement locality ML 2. The hydraulic properties of the grid cells containing red dots are affected by the hydraulic properties of the deformation zones nearby as a result of the chosen discretisation.

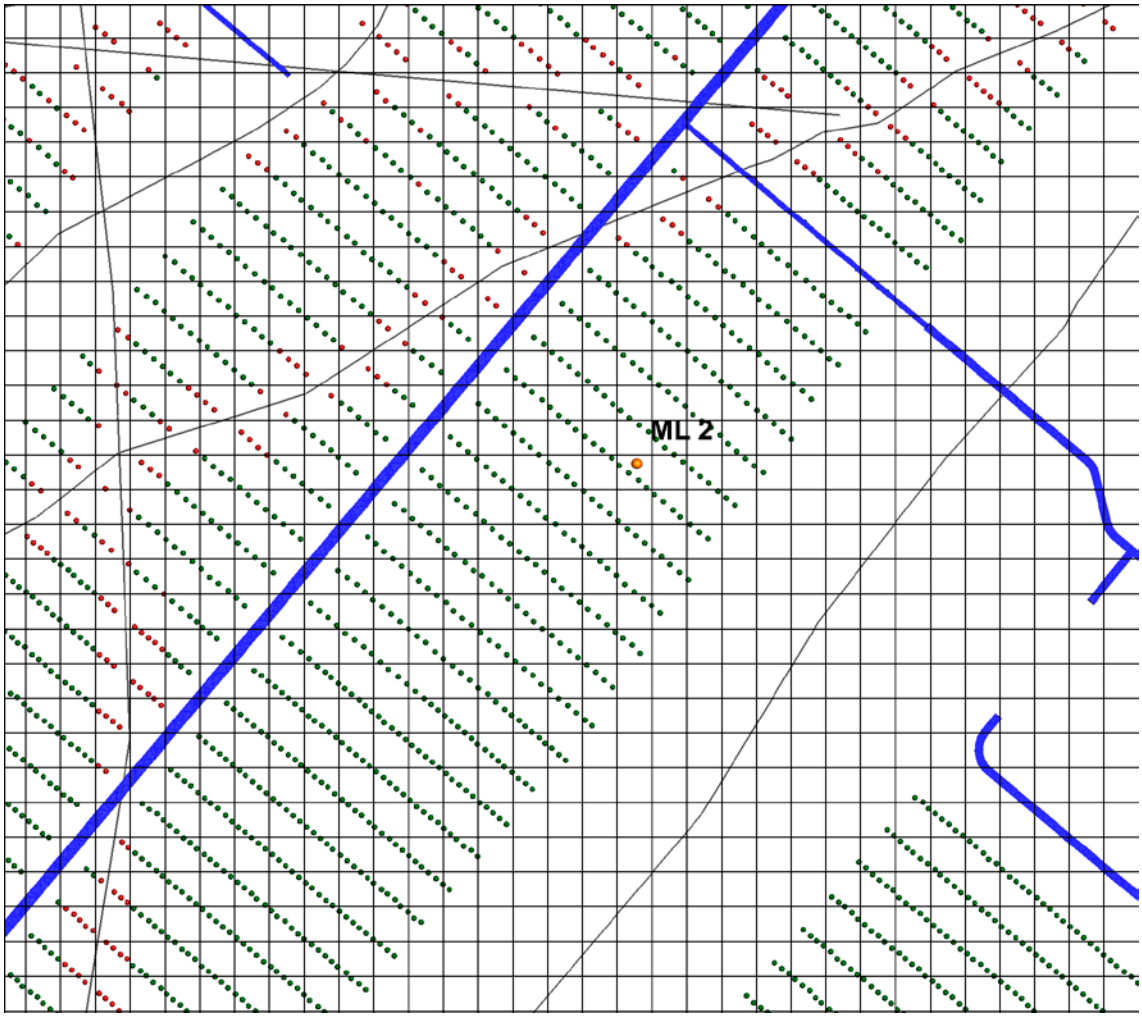

Figure 5-9. *Horizontal view of the computational grid around measurement locality number 2. The resolution of the computational grid adjacent to the repository is 32 m. The transportation tunnels are shown as blue lines and the deposition hole positions as dots. The dots are coloured red or green depending on if they are positioned within grid cells that also contain one or several intercepts with the deterministically modelled deformation zones (red dot) or not (green dot). That is, the hydraulic properties of the cells with red dots are affected by the hydraulic properties of the deformation zones as a result of the chosen discretisation. The deformation zones are here visualised as trace lines (scan lines without geological thickness).*

Figure 5-10 shows the positions of the five measurement localities (ML 1-5) and the permeability field at repository depth. Figure 5-11 shows a close-up view around each locality.

- ML 1 is placed close to the southwest corner of the repository area and found close to a north-south trending deformation zone. The maximum permeability of the grid cell hosting ML 1 is $1 \cdot 10^{-14}$ m^2.
- ML 2 is placed in the centre of the target volume and is not affected by any deformation zone. The maximum permeability of the grid cell hosting ML 2 is $5 \cdot 10^{-15}$ m^2.
- ML 3 is placed in the northeast corner of the repository area and is more or less surrounded by minor deformation zones. The maximum permeability of the grid cell hosting ML 3 is $8 \cdot 10^{-15}$ m^2.
- ML 4 is placed in the southeast corner of the repository area just west of a minor deformation zone. The maximum permeability of the grid cell hosting ML 4 is $8 \cdot 10^{-15}$ m^2.
- ML 5 is placed at the western part of the repository area. The maximum permeability of the grid cell hosting ML 5 is $7 \cdot 10^{-16}$ m^2.

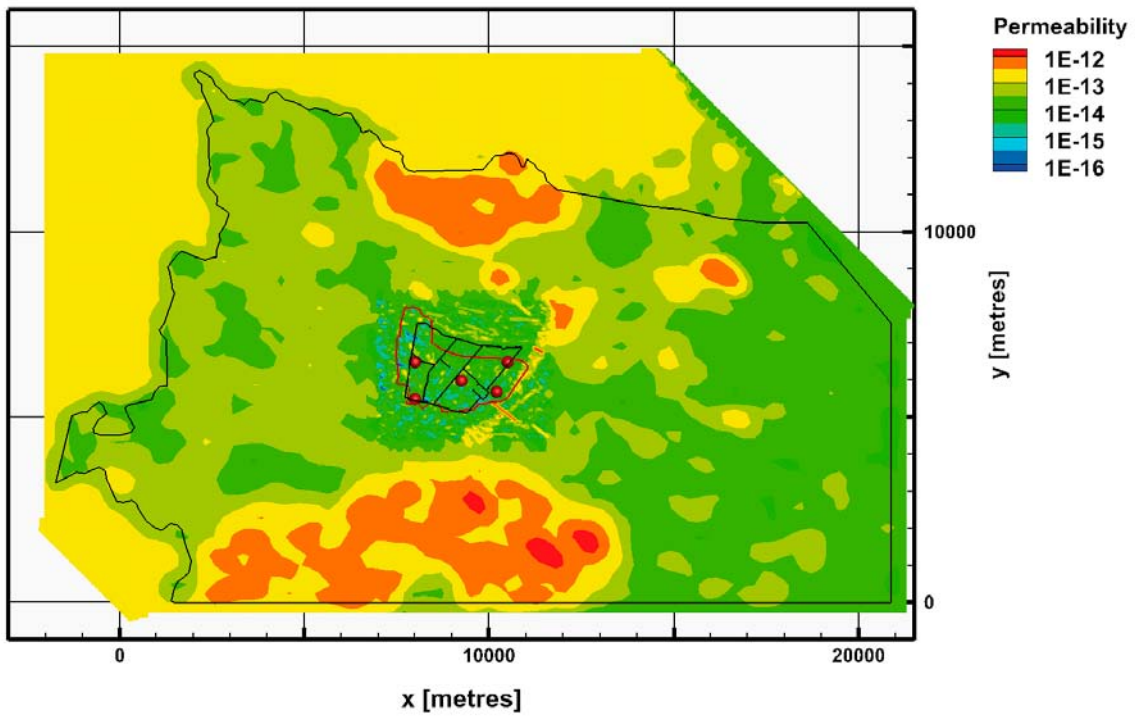

Figure 5-10. *Horizontal view showing the five measurement localities (ML 1-5) and the permeability field at repository depth (elevation –500 m). The large polygon shows the regional flow domain used in SDM-Site /Rhén et al. 2009/. The elongated polygon inside the large polygon is the focused area. The deep repository is located in the central part of the focused area. The y-axis points towards north.*

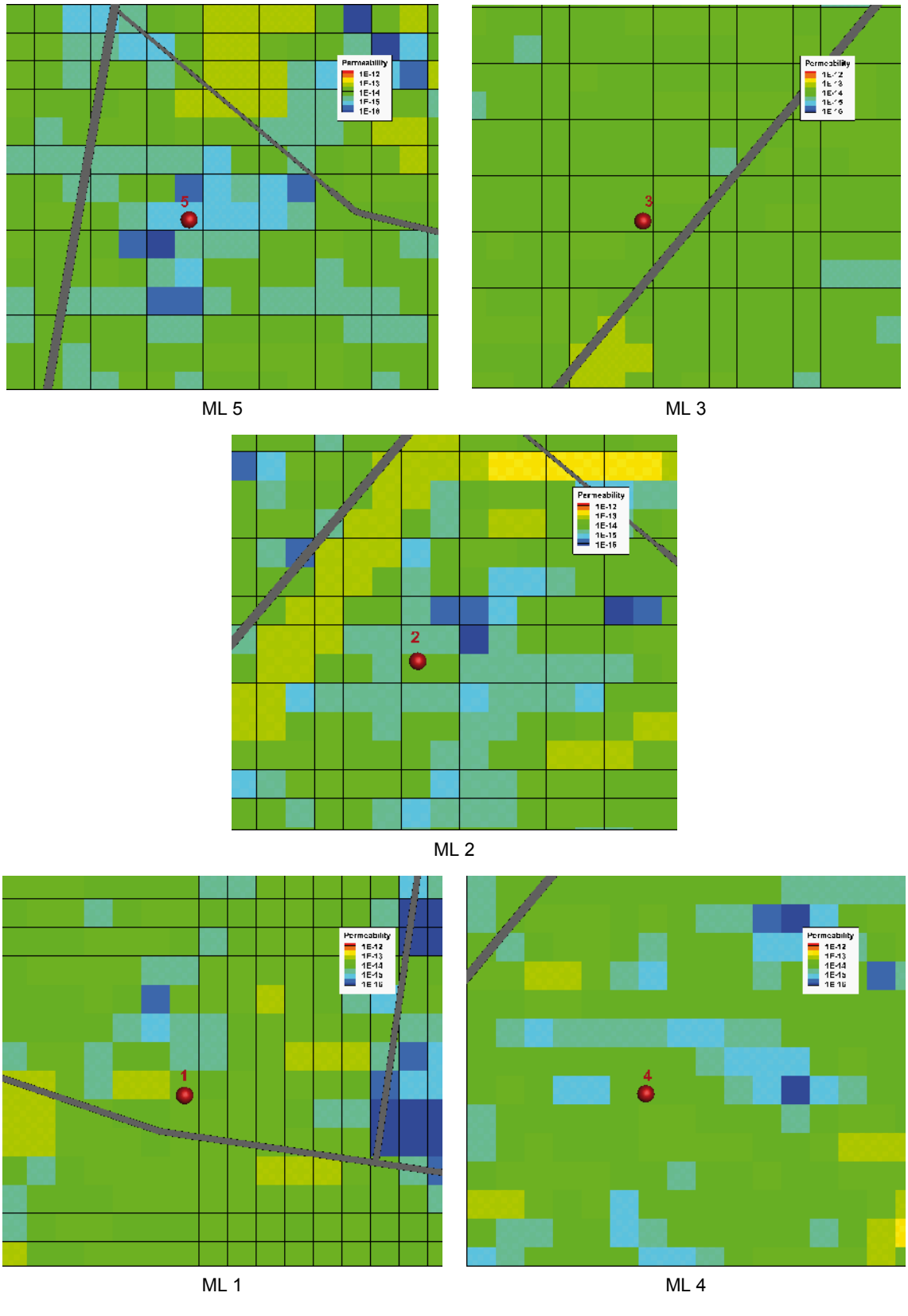

Figure 5-11. *Horizontal views of the permeability field around the five measurement localities (ML 1-5). Maximum grid cell permeability values are shown.*

Figure 5-12 shows the positions of the five measurement localities (ML 1-5) and the permeability field at repository depth for elaborated permeability conditions (case (c)). Figure 5-13 shows a close-up view around each locality also for the elaborated permeability conditions.

- ML 1 is placed close to the southwest corner of the repository area and found close to a north-south trending deformation zone. The maximum permeability of the grid cell hosting ML 1 is $3 \cdot 10^{-16}$ m^2.
- ML 2 is placed in the centre of the target volume and is not affected by any deformation zone. The maximum permeability of the grid cell hosting ML 2 is $3 \cdot 10^{-15}$ m^2.
- ML 3 is placed in the northeast corner of the repository area and are more or less surrounded by minor deformation zones. The maximum permeability of the grid cell hosting ML 3 is $1 \cdot 10^{-14}$ m^2.
- ML 4 is placed in the southeast corner of the repository area just west of a minor deformation zone. The maximum permeability of the grid cell hosting ML 4 is $4 \cdot 10^{-15}$ m^2.
- ML 5 is placed at the western part of the repository area. The maximum permeability of the grid cell hosting ML 5 is $3 \cdot 10^{-15}$ m^2.

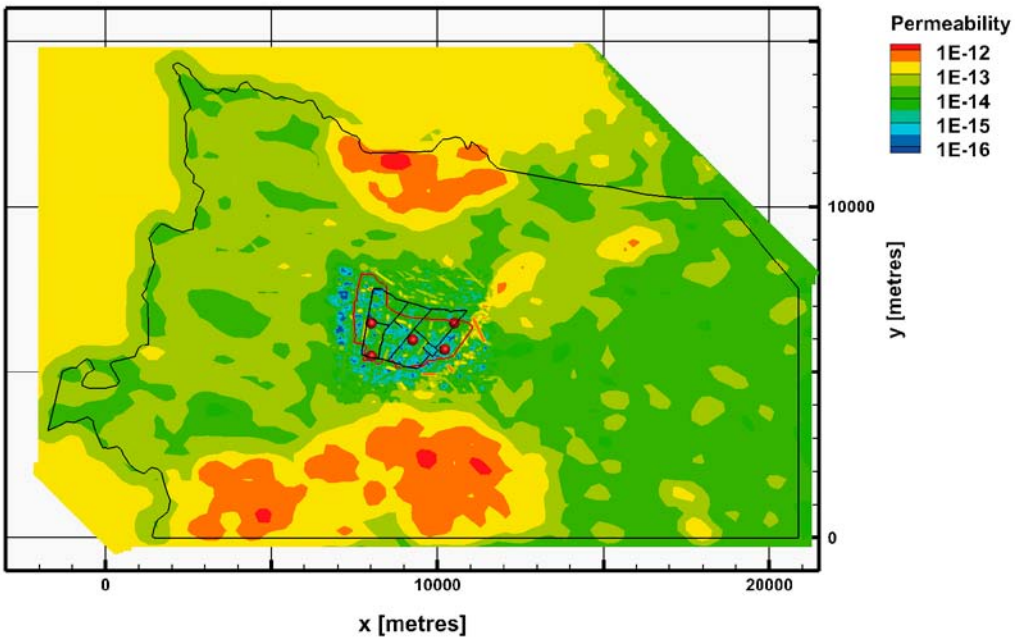

Figure 5-12. *Horizontal view showing the five measurement localities (ML 1-5) and the permeability field at repository depth (elevation –500 m) for the elaborated permeability conditions (case (c)). The large polygon shows the regional flow domain used in SDM-Site /Rhén et al. 2009/. The elongated polygon inside the large polygon is the focused area. The deep repository is located in the central part of the focused area. The y-axis points towards north.*

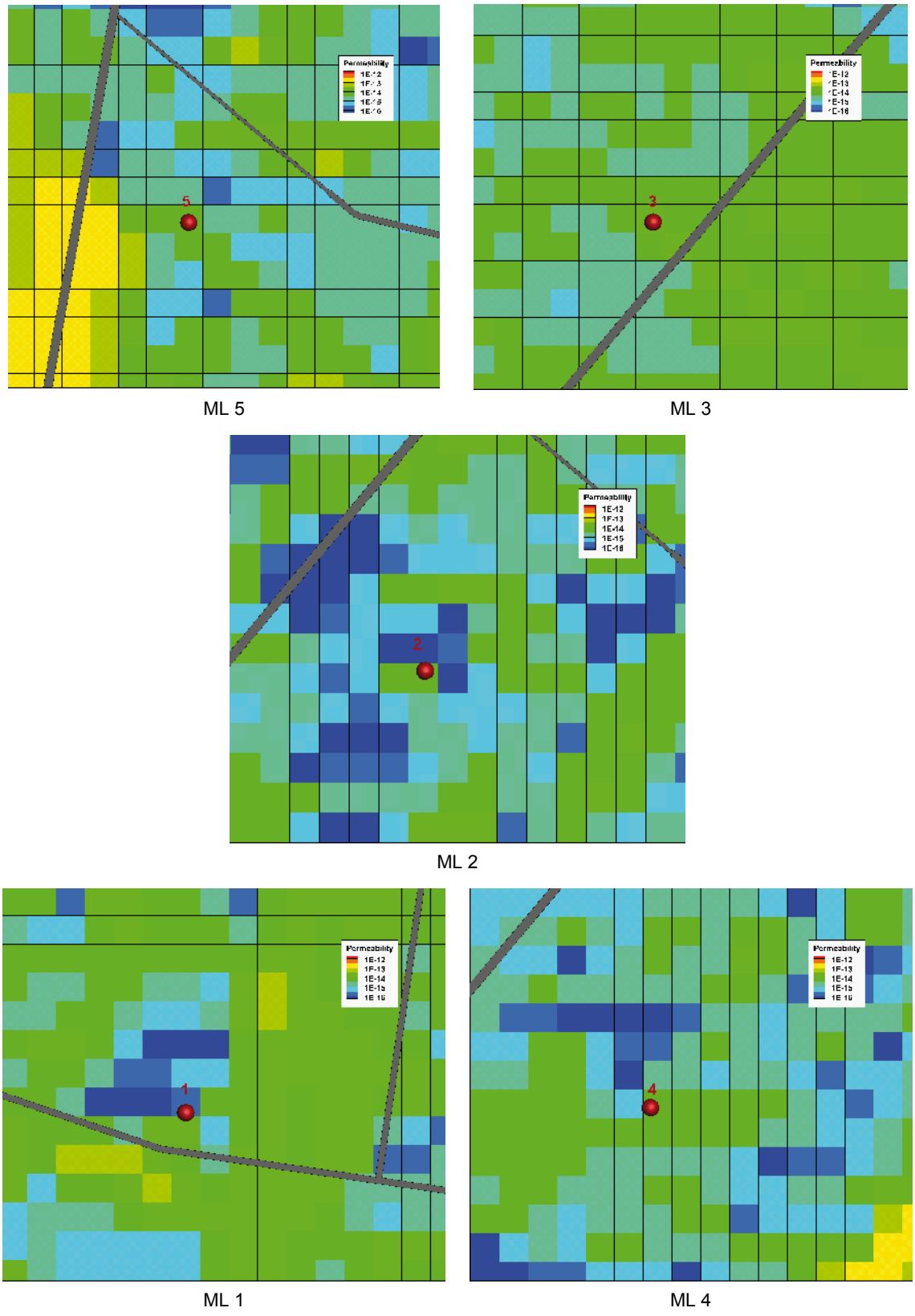

Figure 5-13. *Horizontal views of the permeability field for the elaborated permeability conditions (case (c)) around the five measurement localities (ML 1-5). Maximum grid cell permeability values are shown.*

6 Results

6.1 Introduction

Appendices D–F present detailed information from the groundwater flow simulations of the temperate case, the glacial case without permafrost and the glacial case with permafrost in a tabular format. Below, the key findings are summarised.

6.2 Temperate climate conditions

The results from the temperate case simulation reported in Appendix D are aimed at (i) providing initial conditions for the glacial simulations, and (ii) producing scaled (normalised) entities of the modelling results obtained from the glacial simulations. Further, as the results from glacial simulations are exported to other model applications, e.g. /Gimeno et al. 2010/, a judgment of the confidence that could be placed in the underpinning temperate case simulation is needed.

Figure 6-1 shows a comparison of the simulated Darcy fluxes at the 8,031 deposition hole positions during temperate climate conditions using two types of flow concepts, Discrete Fracture Network (DFN) and Equivalent Continuous Porous Medium (ECPM). The red curve shows the results obtained from the simulations conducted with DarcyTools (ECPM) on a super-regional scale, and the blue curve shows the results from the simulations conducted with ConnectFlow (DFN) on a repository scale. The results are in a reasonable agreement given the differences in flow concept and model scale.

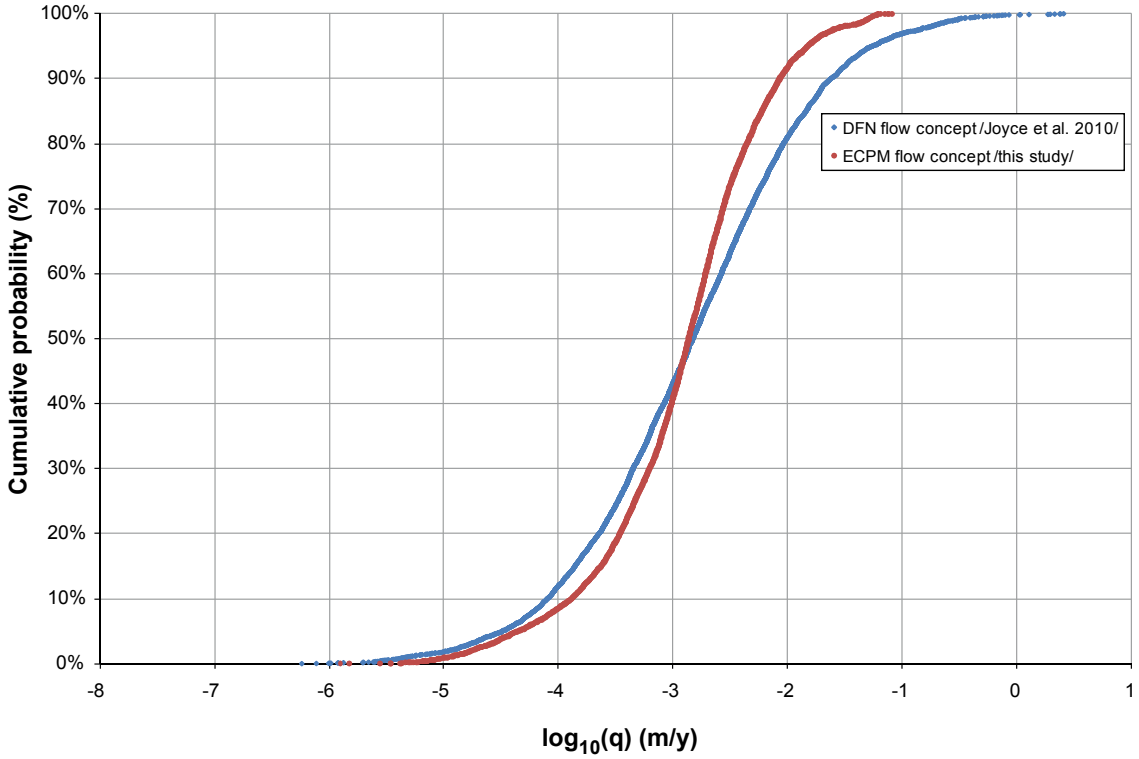

Figure 6-1. *Cumulative distribution function plot of the Darcy fluxes at 8,031 deposition hole positions (all designated deposition positions) during temperate climate condition for two different flow modelling concepts, Discrete Fracture Network (DFN) and Equivalent Continuous Porous Medium (ECPM). The result from /Joyce et al. 2010/ only includes those deposition hole positions that have particles successfully reaching the model top boundary.*

6.3 Glacial climate conditions

The key analyses are:

- **Hydrogeological evolution.** The changes in Darcy flux (q) and advective (fracture) water salinity (C) at repository depth relative to temperate climate conditions (q_{temp} and C_{temp}) are simulated on a super-regional scale. It is noted that groundwater chemistry is here represented by salinity alone.
- **Recharge and discharge locations in the biosphere.** The recharge and discharge locations are identified using forward and backward particle tracking from positions representing the deposition hole locations within the repository footprint. The particle tracking is performed for steady-state velocity fields representing different ice-front locations relative to the location of the repository.
- **Performance measures.** The hydrogeological performance measures of interest are the Darcy flux (q) at each deposition hole location, and the flow-related transport properties along flow paths from the deposition hole locations, i.e. the advective travel time (t_w) and the flow-related transport resistance (F). In principle, these are directly obtained from the super-regional model for all ice-front locations. However, the repository structures are not explicitly included in the super-regional model, and hence results for the different release paths from a repository are not obtained from the work reported here. For the sake of comparisons, the cumulative density function plots of the Darcy flux and flow-related transport resistance obtained from the super-regional model are shown here for the glacial case without permafrost.
- **Site related variants.** Some properties of the site, with specific relevance to glacial conditions, as well as the glacial conditions related to the glacial climate are uncertain. The impacts of alternative parameterisations related to these issues are assessed in order to judge their importance.

Hydrogeological evolution

Permafrost is a key process to consider as it reduces the permeability of subsurface materials to water flux. Permafrost does not develop instantaneously, but its development is a transient process. The performance of the freezing algorithm used to modify Holocene hydraulic conductivity values as a function of temperature was illustrated in /Vidstrand et al. 2010/. The input to the permafrost model is obtained from the ground surface temperature time series described in /SKB 2006a/.

A discontinuous permafrost layer is considered in the work reported here, which implies that the permafrost layer contains more or less unfrozen sections depending on the local boundary conditions and material properties. Probable locations for taliks are estimated from the forecasted landscape development carried out based on the shoreline displacement at Laxemar.

As the speed of the ice sheet margin during glaciation (50 m/y) is greater than the rate of thawing of the permafrost layer, a tongue of trapped permafrost is created close to the ice sheet margin, cf. Figure 5-3. Results presented in /Vidstrand et al. 2010/ suggest insignificant differences in Darcy flux between the two cases of permafrost conditions studied at the ice sheet margin /Vidstrand et al. 2010, case (d) and (e)/.

Figure 6-2 shows Darcy fluxes for a NW-SE vertical cross-section through the potential repository area. Three cases are shown. The upper most cross-section represents temperate conditions (IFL 0). The cross-section in the middle represents an advancing ice sheet margin at IFL II without permafrost in the periglacial area. The bottom most cross-section represents an advancing ice sheet margin at IFL II with permafrost conditions in the periglacial area.

Figure 6-3 shows the salinity field for a NW-SE vertical cross-section through the potential repository area. Three cases are shown. The upper most cross-section represents temperate conditions (IFL 0). The cross-section in the middle represents an advancing ice sheet margin at IFL II without permafrost in the periglacial area. The bottom most cross-section represents an advancing ice sheet margin at IFL II with permafrost conditions in the periglacial area. Figure 6-4 shows the same salinity fields but on a horizontal plane placed at –500 m through the target volume.

In summary, Figure 6-2 and Figure 6-3 show that the hydraulic pressures at the bottom of the ice sheet distort the temperate conditions and causes glacial meltwater to recharge and flush the advective system. In effect, the more saline water in the fractures is pushed forwards and upwards (upconing).The reason for the, in general, lower salinity near the ground surface for the glacial case with permafrost is that the permafrost hinders discharge at the top boundary (cf. the bottom most image in Figure 6-2), except where taliks (unfrozen ground) occur. In Figure 6-2 and Figure 6-3 the discharge within the closest talik location (the shore line) is seen clearly at about three quarters of the transect length.

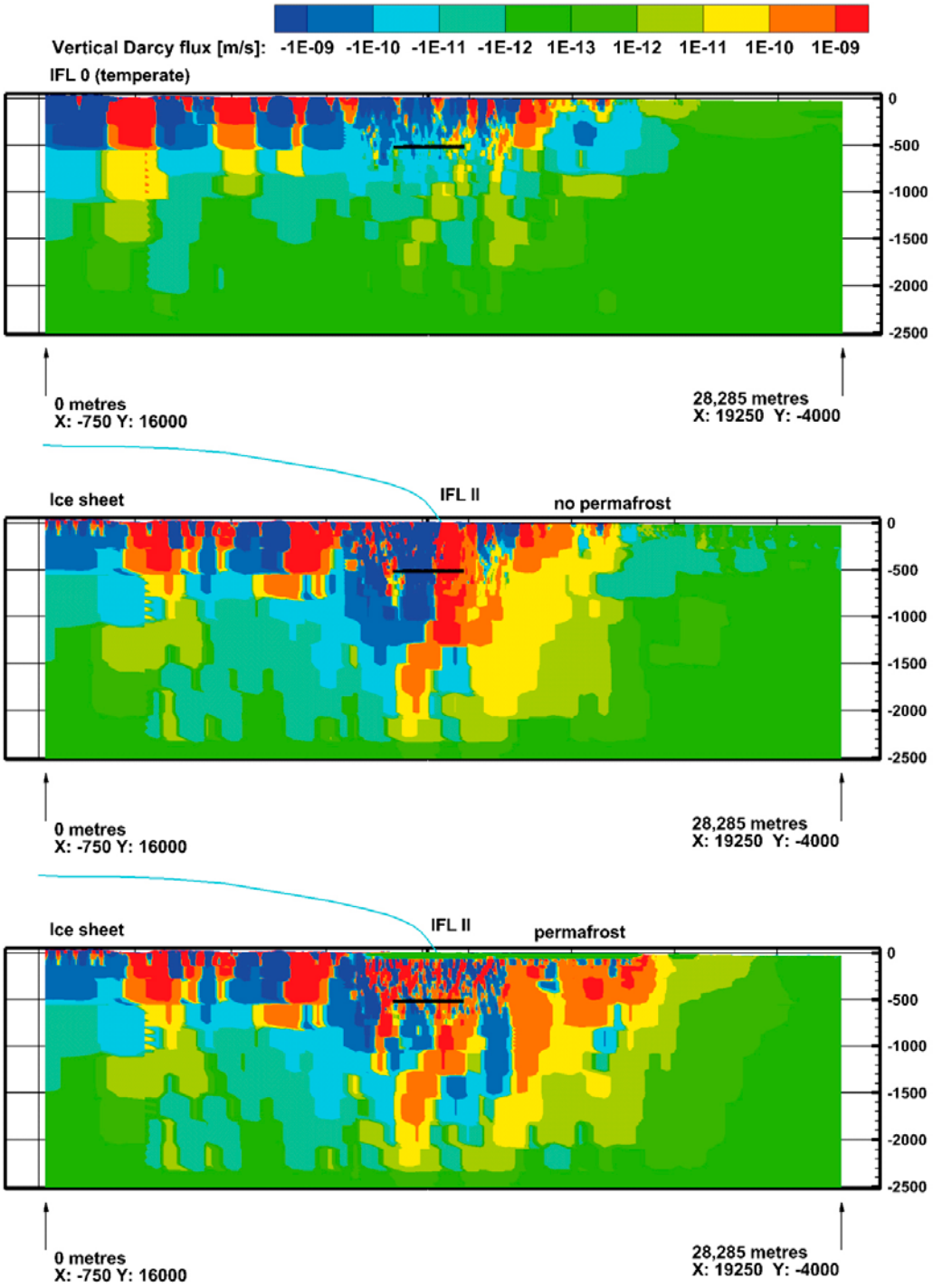

Figure 6-2. *Top: Darcy flux during temperate conditions mapped on a cross-section parallel to the direction of the ice sheet movement during glaciation. The images in the middle and at the bottom show the Darcy fluxes when the ice sheet margin is at IFL II for the glacial case without permafrost (middle) and for the glacial case with permafrost (bottom). Negative values represent downward directed fluxes. The position of the ice sheet profile is illustrated with a blue curve.*

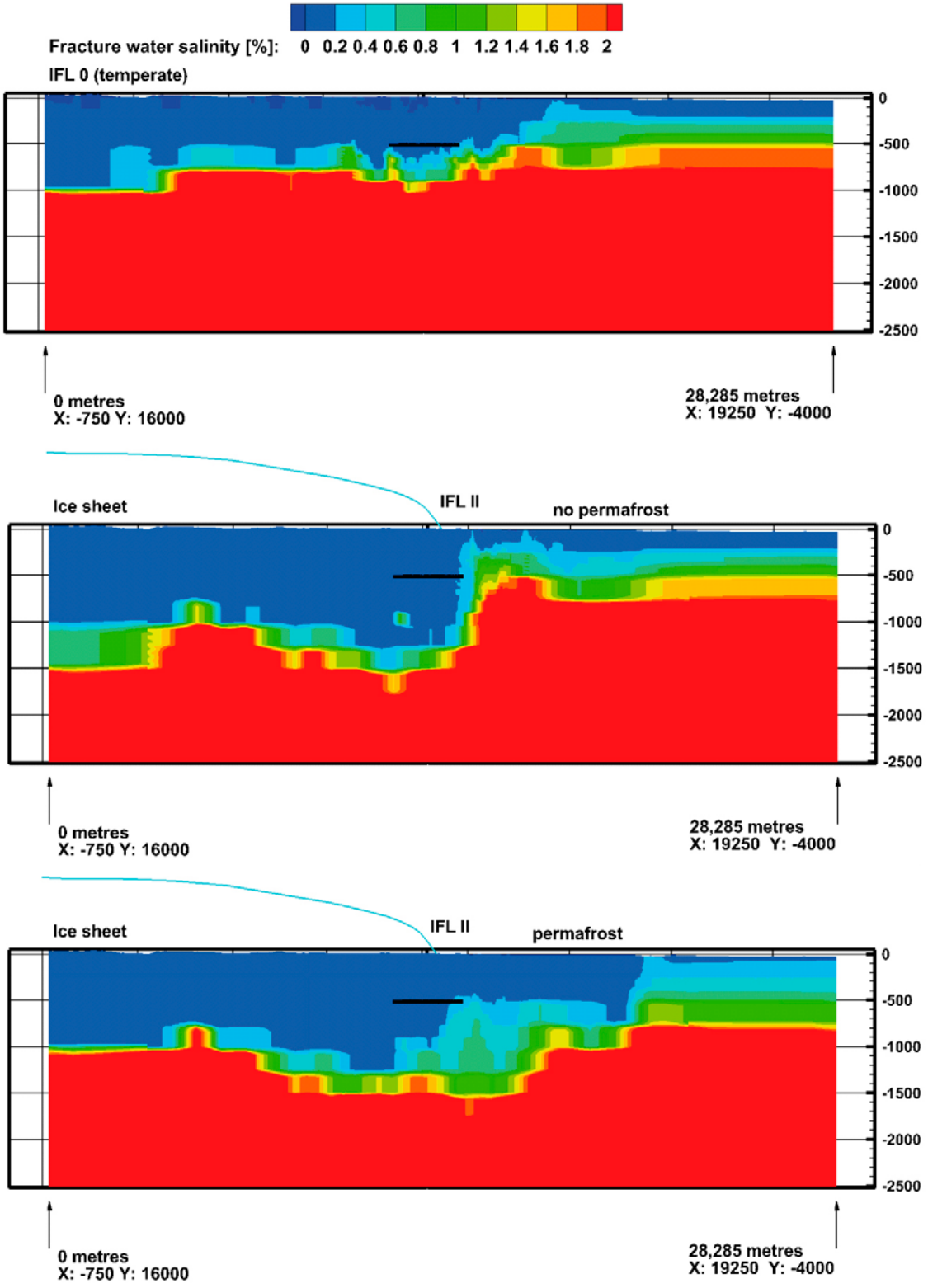

Figure 6-3. *Top: Fracture (advective) water salinity during temperate conditions mapped on a cross-section parallel to the direction of ice sheet movement during glaciation. The images in the middle and at the bottom show the fracture water salinity when the ice sheet margin is at IFL II for the glacial case without permafrost (middle) and for the glacial case with permafrost (bottom). The position of the ice sheet profile is illustrated with a blue curve.*

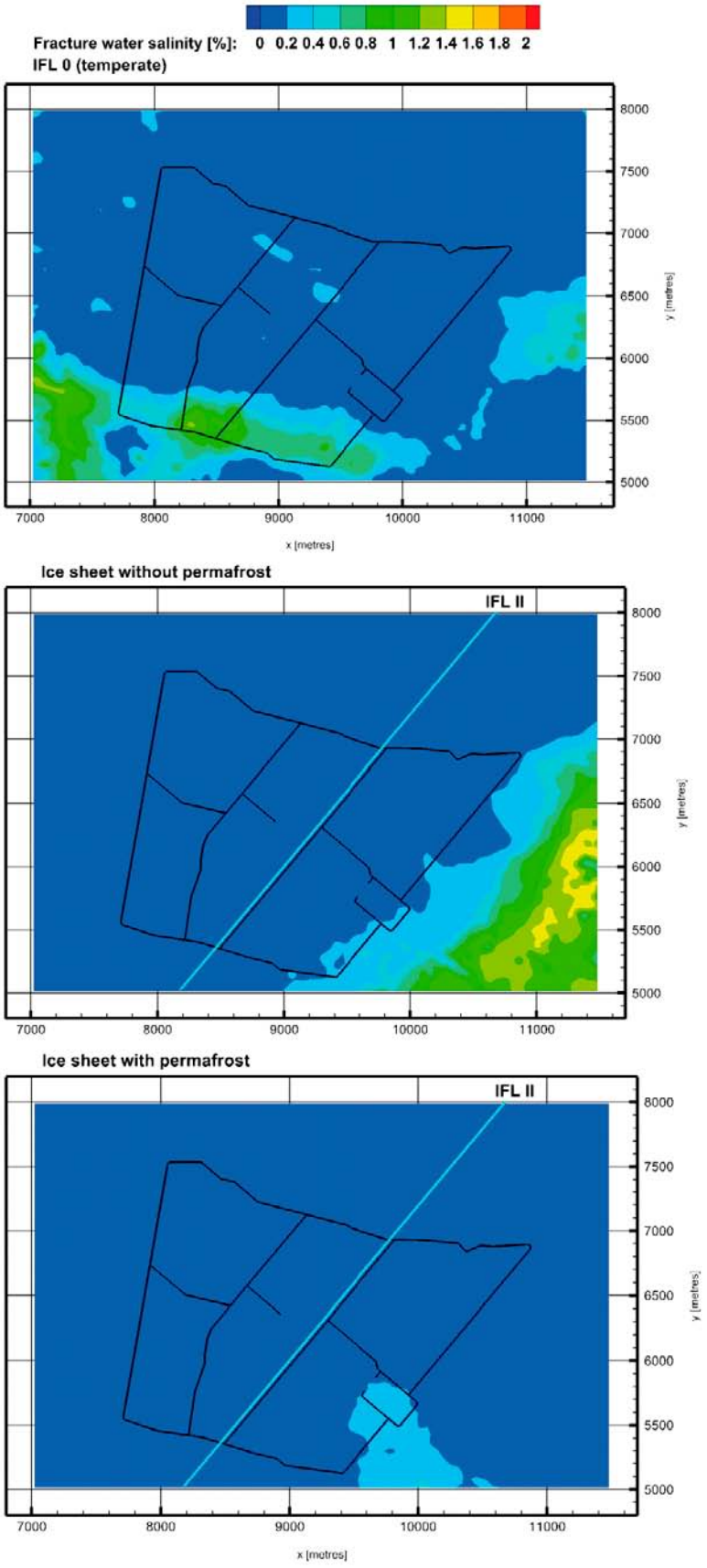

Figure 6-4. *Top: Fracture (advective) water salinity during temperate conditions mapped on a horizontal plane located at –500 m. The images in the middle and at the bottom show the fracture water salinity when the ice sheet margin is at IFL II for the glacial case without permafrost (middle) and for the glacial case with permafrost (bottom). The black thin lines represent main repository tunnels.*

The changes in Darcy flux and fracture water salinity during the simulated period (IFL 0 → IFL V → IFL 0) are monitored at the five measurement localities ML 1-5 and expressed as ratios relative to the corresponding initial, temperate values, see Figure 6-5 and Figure 6-7. It is recalled that the term temperate is not to be understood as 2000 AD, but rather as a time slot in the future when the ice sheet margin is close to, but still outside, the flow model domain, i.e. IFL 0.

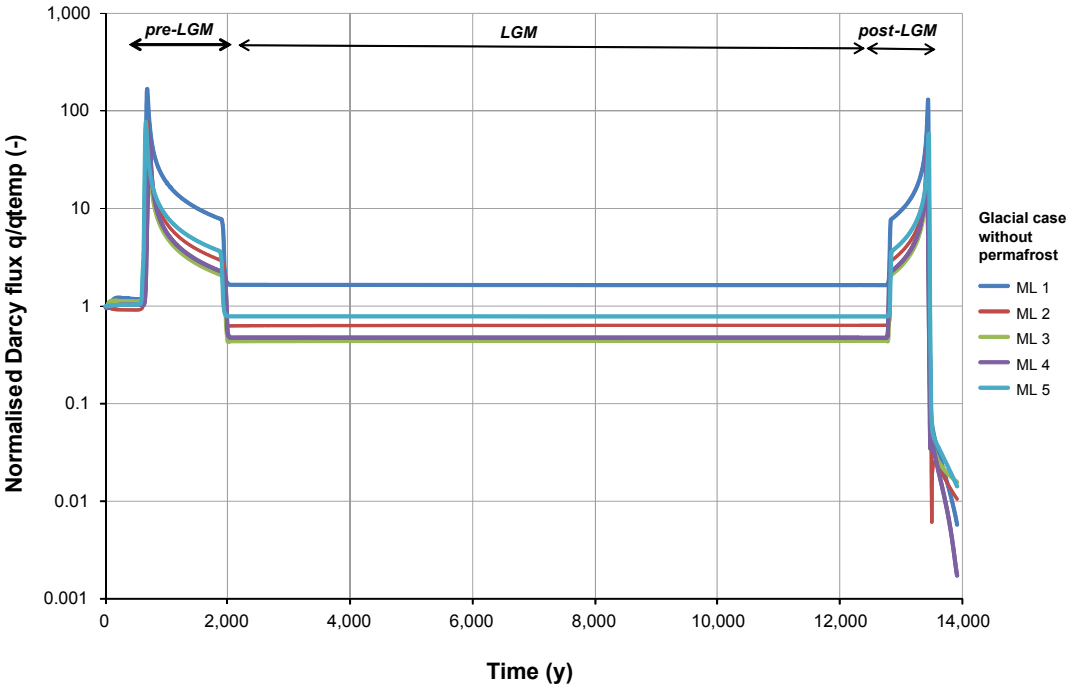

Figure 6-5. *Plot showing the normalised change in Darcy flux, (q/q_{temp}), at ML 1-5 during approximately 13,000 years for the glacial case without permafrost.*

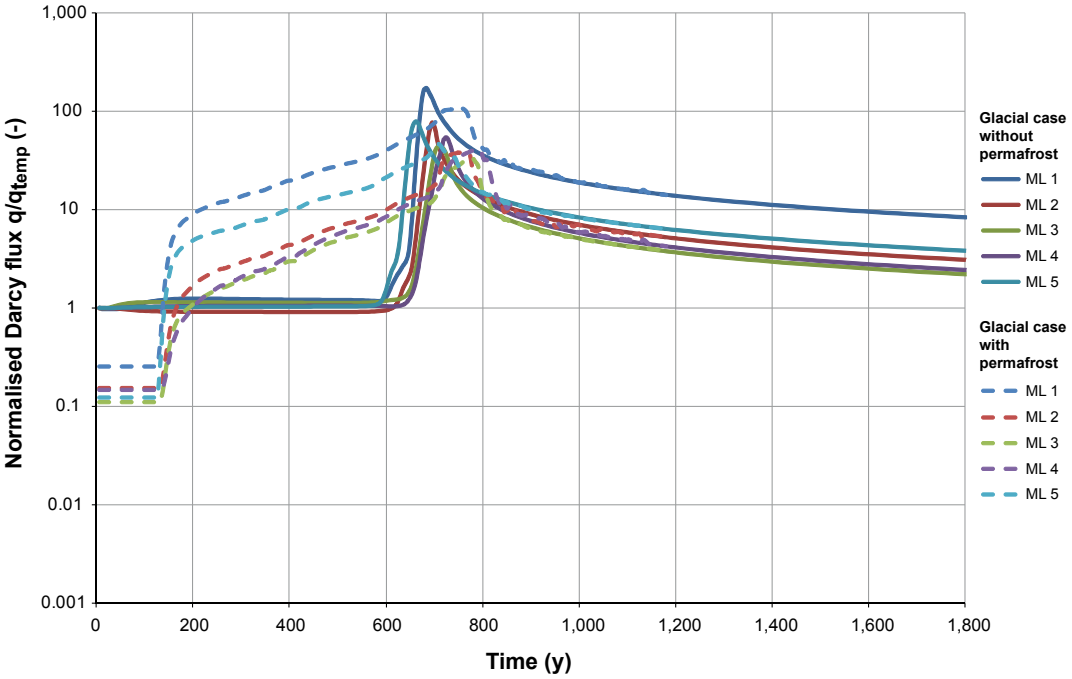

Figure 6-6. *Close-up of the plot in Figure 6-5 showing the normalised change in Darcy flux, (q/q_{temp}), at ML 1-5 during glaciation (pre-LGM). Besides the glacial case without permafrost (solid lines), the evolution of the glacial case with permafrost (dashed lines) is also shown. After approximately 700 years, the two scenarios are identical.*

In Figure 6-5, it is seen that the Darcy flux increases dramatically during the two ice front passages. The immediate shift to low and constant values at the start of the period of complete ice coverage is an artifact of the instantaneous shift in ice sheet gradient at that moment. In reality, a smoother transition is expected. For the glacial case with permafrost, slightly different shapes of the curves are obtained during glacial advance, see Figure 6-6. However, for the remaining parts of the cycle, the curves are, in principal, identical to those shown in Figure 6-5 as there is no permafrost during these periods.

The normalised change in the salinity development is shown in Figure 6-7. The glacial passage during advance (pre-LGM) is characterised by an initial upconing followed by an out flushing resulting in lower salinities than during the initial temperate conditions. However, during the initial part of subsequent stage, i.e. when the site is completely covered by the ice sheet (LGM), a gradual increase in fracture water salinity at repository depth occurs. This gain of the "salt water interface" is primary due to an out diffusion (see Figure 6-8) of the available porewater salinity and not, as in the case of the Forsmark site, due to the slow, but continuous advective transport of salt from below since this salt interface at Laxemar is significant deeper after the pre-LGM phase. (It is recalled that the fracture water salinity at great depth is assumed to be undisturbed (fixed) at all times in the flow model.)

The glacial passage during retreat (post-LGM) is also characterised by an upconing and flushing event, but the effects are considerable smaller than during the advance. The reason for this is two-fold; (i) the speed of the retreating ice sheet margin is twice as fast as the speed of the advancing ice sheet margin (100 m/y versus 50 m/y), and (ii) the area in front of the retreating ice sheet margin is submerged. These conditions reduce the duration and the magnitude of the hydraulic gradient across the ice sheet margin significantly.

It is noted that the average speed of the retreating ice sheet margin considered for the reference climate evolution in /SKB 2010/ is 300 m/y; i.e. three times the speed considered in the work reported here. The effect of this difference is was investigated and reported in /Vidstrand et a. 2010/; concluding that a lower ice front retreat rate enhance the upconing and subsequent flushing during the retreat. Secondly, the retreating ice sheet profile considered is significantly thicker and steeper at the ice sheet margin than the ice sheet profile considered for the reference climate evolution in /SKB 2006a, 2010/, see Figure 2-1 in section 2.2. Thus, the conditions considered here exaggerate the impact of the ice sheet; still the results indicate that the fracture water salinities are more or less restored at repository depth during the simulated period (IFL 0 → IFL V → IFL 0).

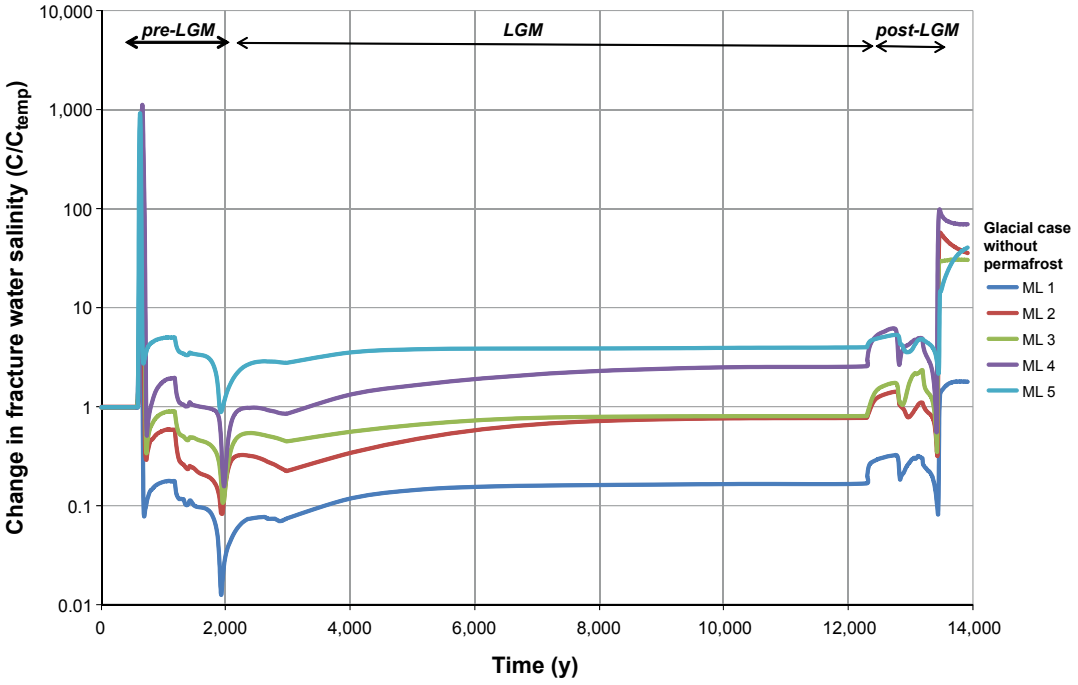

Figure 6-7. *Plot showing the normalised change in concentration, (C/C_{temp}), at ML 1-5 during approximately 13,000 years for the glacial case without permafrost.*

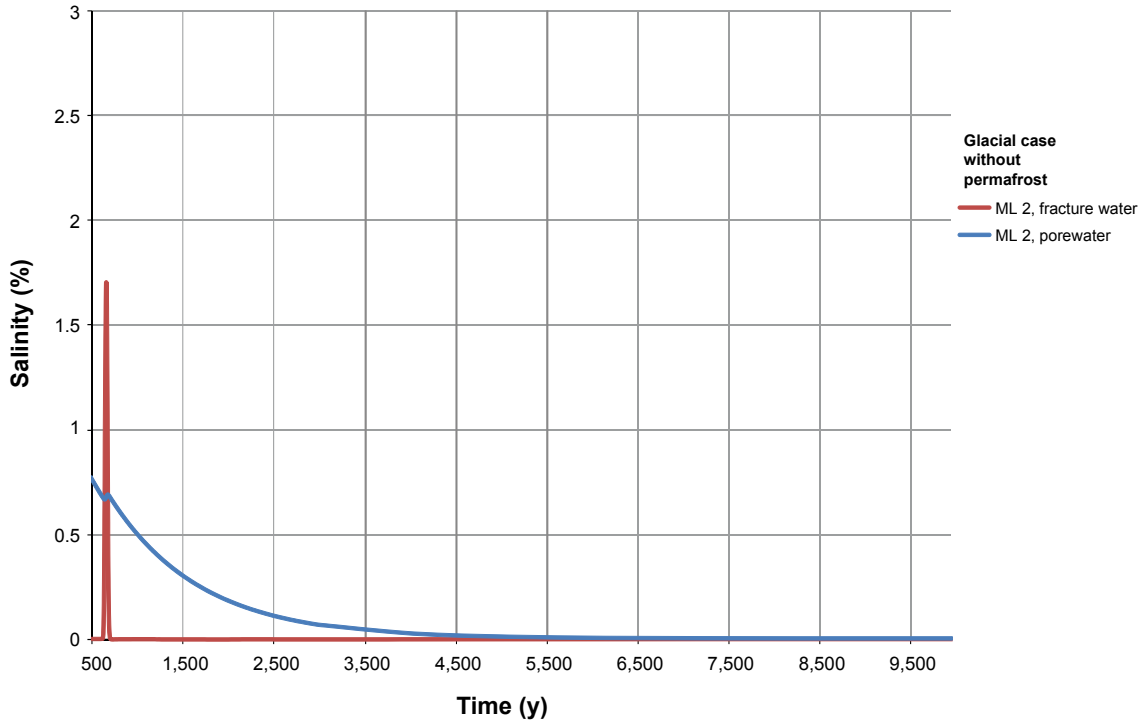

Figure 6-8. *Plot showing the concentration, (C) in the fracture water and porewater, respectively, for ML 2 during approximately 10,000 years for the glacial case without permafrost. Data for ML 2 are from the Glacial case without permafrost at repository depth.*

Recharge and discharge locations in the biosphere

The top image in Figure 6-9 shows the recharge and discharge locations when the ice sheet margin reaches ice-front location II for the glacial case without permafrost, and the bottom image in Figure 6-9 shows the corresponding results for the glacial case with permafrost. For the glacial case without permafrost a significant amount of particles recharge at the upstream boundary of the model domain. For the glacial case with permafrost even more particles recharge at the upstream boundary. This suggests that the model domain is too small to give a fully undisturbed view of all recharge locations for a fixed Darcy flux field. Nevertheless, it may be concluded that the present-day topographic water divides, which play an important role for the recharge and discharge during temperate conditions, are significantly diminished in importance during glacial conditions.

In contrast, the discharge locations are predominantly found well within the physical boundaries of the model domain and often very close to the margin of the ice sheet. The differences seen in the discharge pattern between the two glacial cases are largely caused by the varying hydraulic properties and boundary conditions. For the glacial case with permafrost there are two centres of discharge:

- The deformation zone model that exists within the regional flow domain for SDM-Site Laxemar. In this simulation approximately four percent of the released particles exit along deformation zones.
- The talik (predicted shore line of the Baltic Sea) positioned approximately 4 kilometres southeast of the repository and in front of the ice sheet margin. In this simulation, the talik catches approximately 96% of the released particles.

Performance measures

For the sake of comparisons, the Darcy flux and flow-related transport resistance are shown in Figure 6-10 and Figure 6-11, respectively, for the glacial case without permafrost when the ice sheet margin is at IFL II and IFL IV. It is observed in Figure 6-10 that the median Darcy flux of the temperate case is increased by approximately 1.5–2 orders of magnitude when the ice sheet margin is at IFL II. A corresponding but somewhat smaller decrease of the flow-related transport resistance is

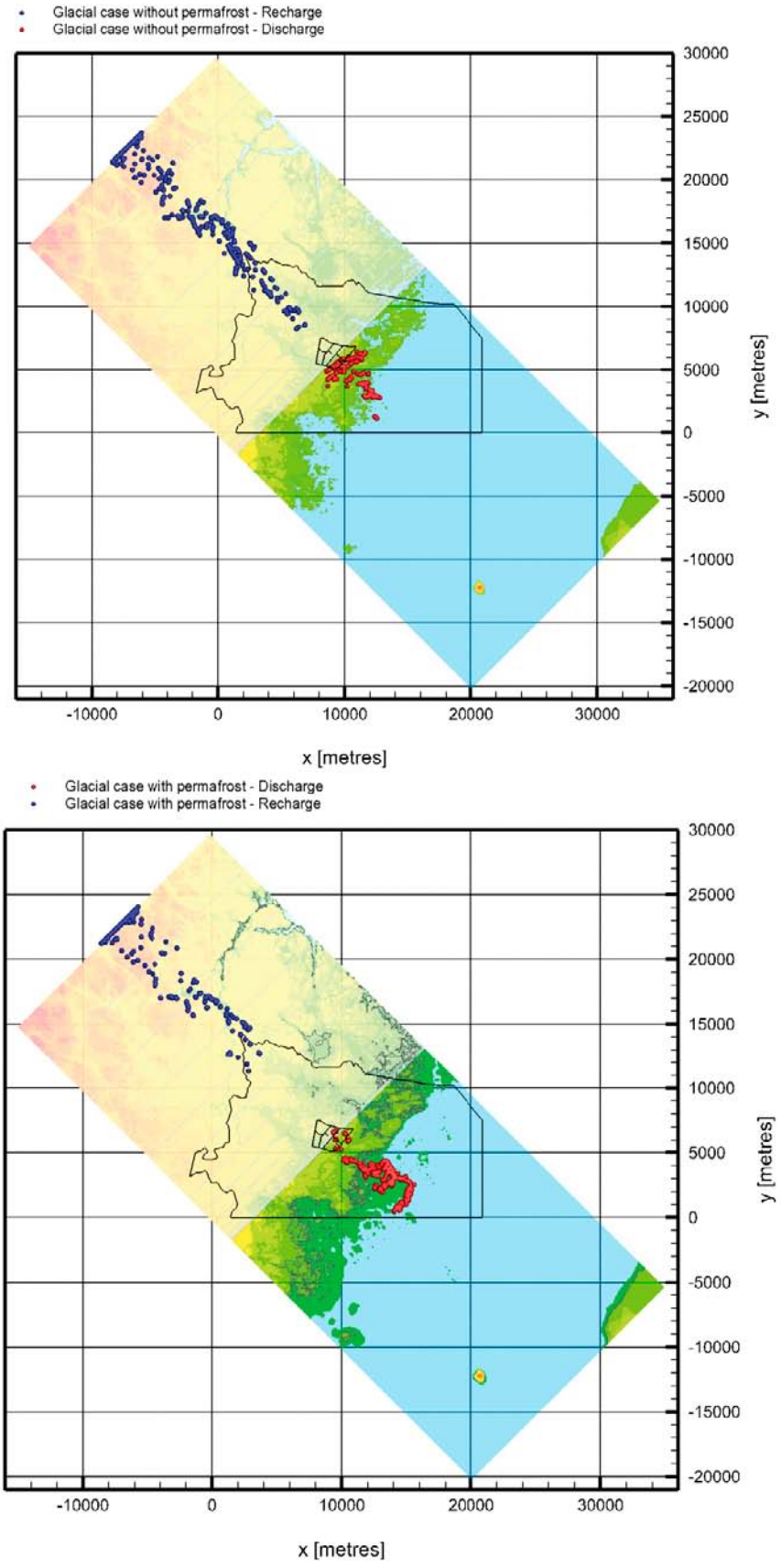

Figure 6-9. *Recharge (blue) and discharge (red) locations of the 8,031 particles released at repository depth when the advancing ice sheet margin is at ice-front location II. Top: Ice sheet without permafrost. Bottom: Ice sheet with permafrost and taliks. The talik is positioned in the predicted future shoreline in front of the ice sheet margin to the east).*

observed in Figure 6-11. Also, Figure 6-10 indicates that the Darcy fluxes are more or less uniformly influenced by the glacial boundary conditions. Thus, it appears that regions with low fluxes are equally affected by the high gradients induced by the ice sheet as regions with high fluxes. However, this result may be due to the fact that the super-regional model reported here treats the crystalline bedrock as a continuous porous medium.

Site-related variants

N-S ice advance direction

Based on the historic and modelled data described in /SKB 2006a, 2010/, a NW-SE to N-S orientation of the model domain is conceived to be the most appropriate orientation to study for an advancing ice sheet margin. The simulations carried out includes a variant sensitivity test where a N-S ice advance direction is used as an alternative to the NW-SE orientation of the base case. In conclusion, the simulation results suggest minor differences of probably insignificant importance.

Elaborated permeability conditions

The elaborated permeability conditions have a significant impact on primary the Darcy fluxes. Figure 6-12 indicate that the lower Darcy fluxes are decreased by approximately one order of magnitude whereas the larger fluxes are maintained, hence the distribution is significantly changed. Figure 6-13 shows the, in general, decrease in Darcy fluxes, here illustrated with the transient development at measurement locality 2 during the pre-LGM. The decrease is approximately a factor 3, however the flow field is also significantly more heterogeneous in the elaborated permeability case as compared to the base case, see Figure 6-14.

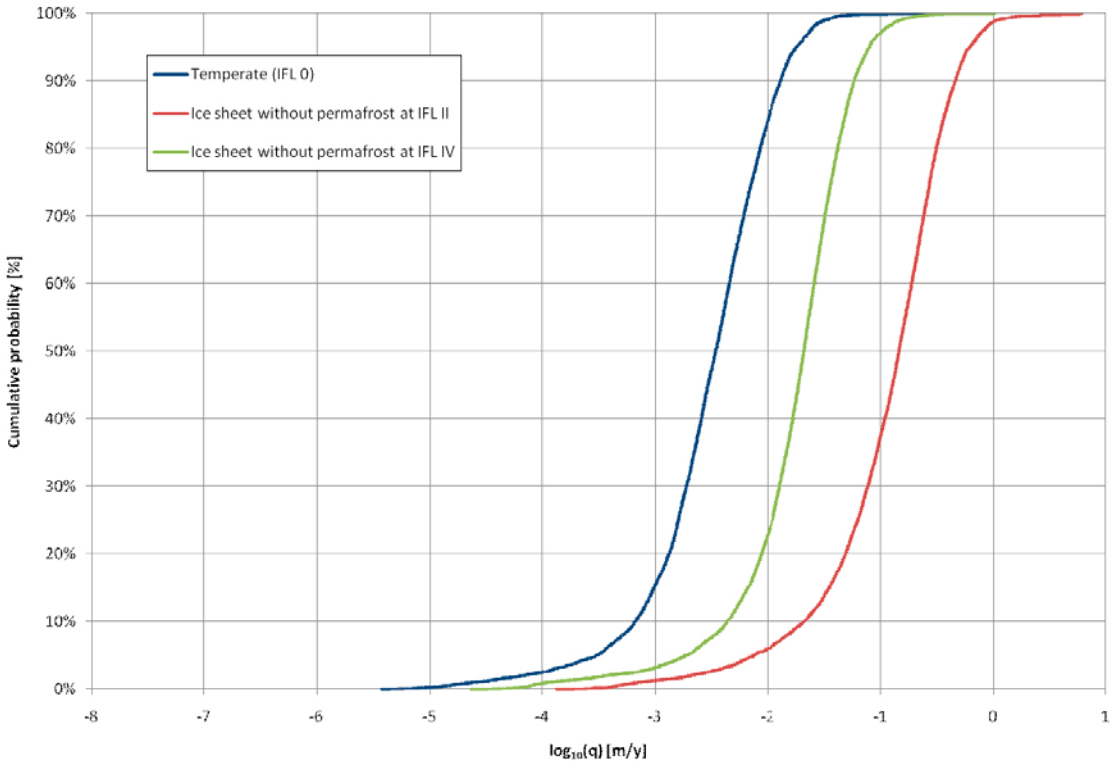

Figure 6-10. *Cumulative distribution function plot of Darcy fluxes for the temperate case (IFL 0) and the glacial case without permafrost when the ice sheet margin is at IFL II and IFL IV, respectively.*

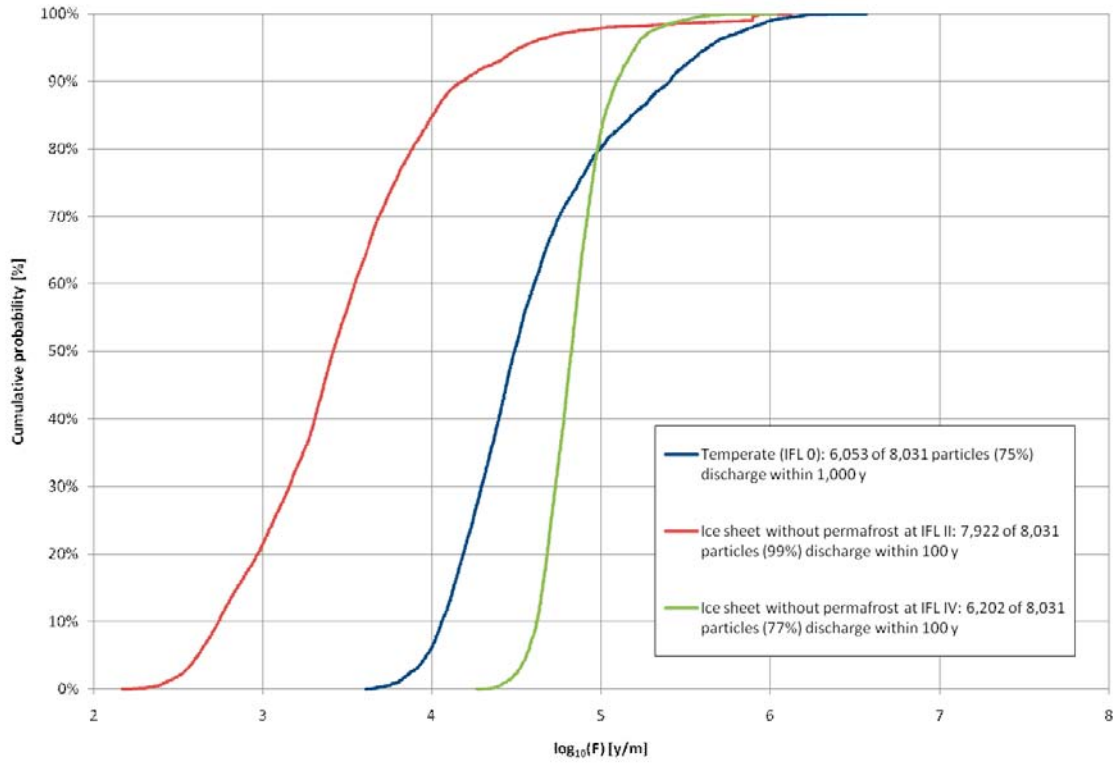

Figure 6-11. *Cumulative distribution function plot of flow-related transport resistances for the temperate case (IFL 0) and the glacial case without permafrost when the ice sheet margin is at IFL II and IFL IV, respectively.*

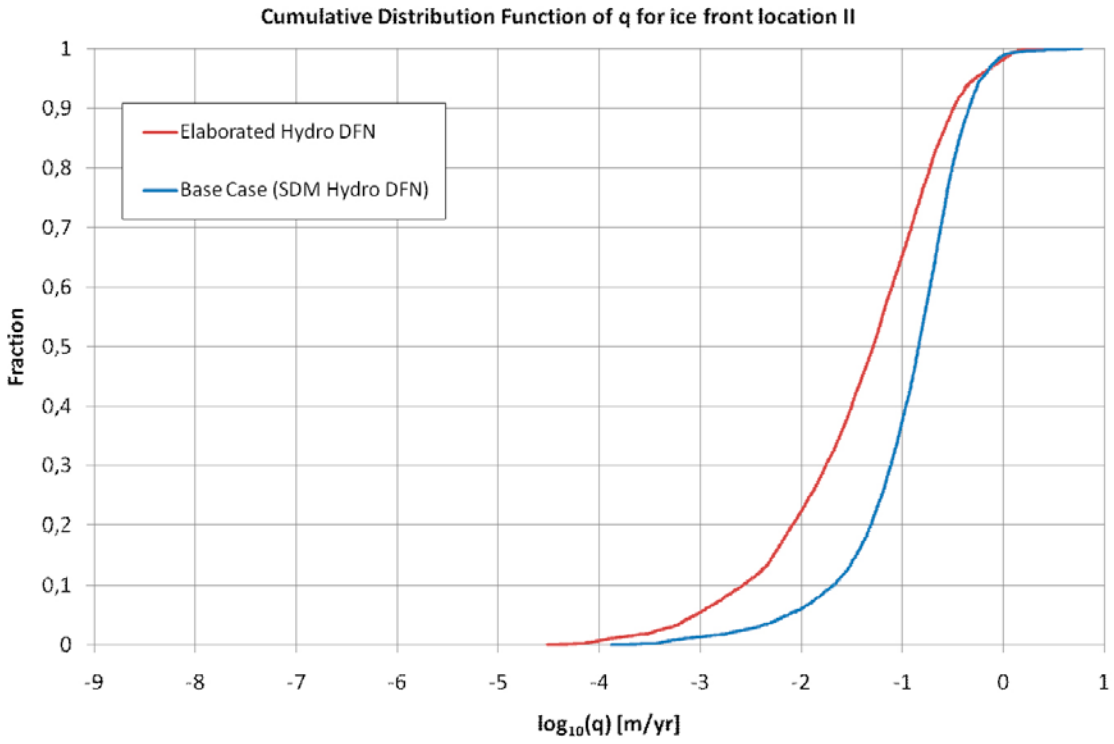

Figure 6-12. *Comparison of the cumulative distribution function plot of Darcy fluxes for the glacial case without permafrost when the ice sheet margin is at IFL II for the base case (SDM Hydro DFN) and IFL II for the elaborated permeability conditions (case (c))(Elaborated Hydro DFN).*

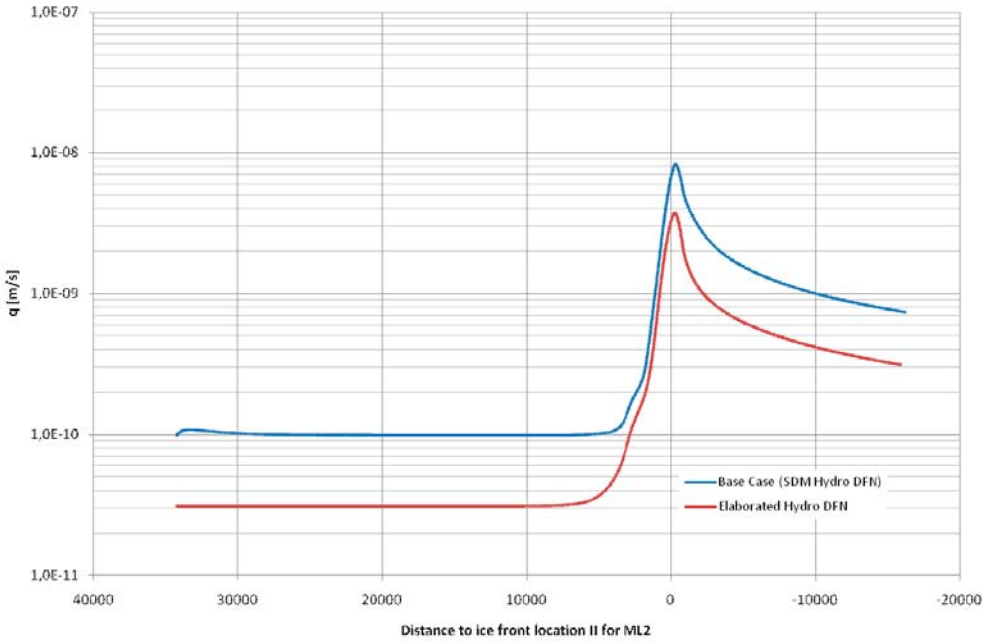

Figure 6-13. *Comparison of the Darcy fluxes at the ML 2 for the glacial case without permafrost during pre-LGM for the base case (SDM Hydro DFN) and for the elaborated permeability conditions (case (c)) (Elaborated Hydro DFN).*

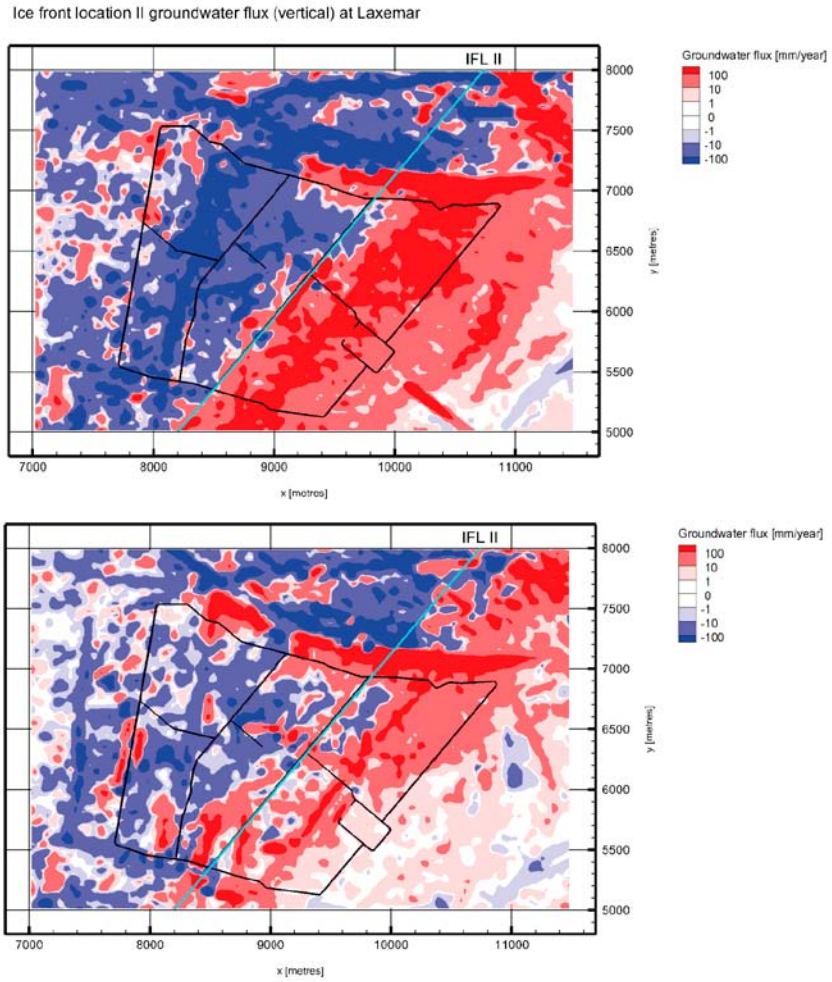

Figure 6-14. *Darcy fluxes at a plane at –500 metres depth for the glacial case without permafrost when the ice sheet margin is at IFL II for (top) the base case (SDM Hydro DFN) and for (bottom) the elaborated permeability conditions (case (c))(Elaborated Hydro DFN).*

6.4 Overview of performance measures

6.4.1 Temperate climate conditions

The recharge locations of the particle traces that pass through the 8,031 deposition hole positions coincide with topographic highs inside the boundary of the regional model domain for groundwater flow as depicted in SDM-Site Laxemar /Rhén et al. 2009/. In practice, all particles recharge above the repository area, hence local and short recharge pathways dominate.

The Darcy fluxes at the investigated 8,031 deposition hole positions vary between $1 \cdot 10^{-13}$ and $9 \cdot 10^{-9}$ m/s with a median value around $1 \cdot 10^{-10}$ m/s. The mobile fracture water salinity is close to 0%, i.e. fresh water.

Table 6-1 presents median values on some of the considered performance measures (flow path length, travel time, and flow-related transport resistance) for the five measurement localities, ML 1-5.

Table 6-1. Performance measures for the temperate case: Median flow path lengths, travel times, and flow-related transport resistances at measurement localities ML 1-5.

	Discharge			Recharge		
ML	Flow path length [m]	Travel time [y]	Flow-related transport resistance [y/m]	Flow path length [m]	Travel time [y]	Flow-related transport resistance [y/m]
1	767	1.6	$2.1 \cdot 10^4$	3,507	25.3	$4.5 \cdot 10^5$
2	1,127	1.3	$2.8 \cdot 10^4$	929	1.1	$3.3 \cdot 10^4$
3	1,431	0.8	$2.1 \cdot 10^4$	1,457	1.1	$5.6 \cdot 10^4$
4	2,070	0.7	$2.1 \cdot 10^4$	1,128	0.8	$2.0 \cdot 10^4$
5	1,415	2.1	$2.3 \cdot 10^4$	874	1.5	$1.8 \cdot 10^4$

6.4.2 Glacial climate conditions without permafrost

The recharge flow paths for the glacial case without permafrost are significantly longer than the discharge flow paths. Indeed, most of the discharge locations are found in front of the ice sheet margin or in close proximity to nearby deformation zones.

The Darcy fluxes at repository depth generally increase by two orders of magnitude during glaciation (pre-LGM) when the ice sheet margin is located right above the repository (ice-front location II). Typical Darcy fluxes are between $4 \cdot 10^{-12}$ and $2 \cdot 10^{-7}$ m/s with a median value around $5 \cdot 10^{-9}$ m/s. The salinity at repository depth varies significantly during the passage of the ice sheet margin. The salinities first increases to about 2% and then again decrease to about 0%. However, during the subsequent stage, i.e. when the site is completely covered by the ice sheet (LGM), the Darcy fluxes are low and a small but gradual increase in fracture water salinity at repository depth occurs. This recovery of the "salt water interface" is primary due to an out diffusion of the available porewater salinity and not, as in the case of the Forsmark site, due to the slow, but continuous advective transport of salt from below since this salt interface at Laxemar is significant deeper after the pre-LGM phase. Approximately 6,000 years after the ice-front passage the porewater and the fracture water is in equilibrium and no further change in the fracture salinity is observed during the LGM. In the model, the fracture water salinity at great depth is assumed to be undisturbed (fixed) at all times. The data support for this assumption is presented in SDM-Site and Appendix C.

The glacial passage during retreat (post-LGM) is also characterised by an upconing and flushing event. The results indicate that salinities in fact are more or less restored during the simulated period.

Table 6-2 presents median values on some of the considered performance measures (flow path length, travel time, flow-related transport resistance) for the five measurement localities, ML 1-5 when the ice sheet margin is at ice-front location II.

Table 6-2. Performance measures for the glacial case without permafrost: Median flow path lengths, travel times, and flow-related transport resistances at measurement localities ML 1-5 when the ice sheet margin is at ice front location IFL II.

ML	Discharge			Recharge		
	Flow path length [m]	Travel time [y]	Flow-related transport resistance [y/m]	Flow path length [m]	Travel time [y]	Flow-related transport resistance [y/m]
1	2,132	0.7	$4.8 \cdot 10^3$	24,014	0.8	$2.8 \cdot 10^4$
2	959	0.4	$1.3 \cdot 10^3$	–	–	–
3	1,173	0.2	$4.1 \cdot 10^3$	24,699	1.4	$2.7 \cdot 10^4$
4	720	0.2	$1.5 \cdot 10^3$	25,622	1.1	$3.0 \cdot 10^4$
5	4,783	1.4	$1.2 \cdot 10^4$	23,672	0.9	$3.1 \cdot 10^4$

6.4.3 Glacial climate conditions with permafrost

The recharge flow paths for the glacial case with permafrost are significantly longer than the discharge flow paths though discharge flow paths may be of significant length in a permafrost region depending on the location of taliks. At Laxemar, the closest talik is the predicted future shoreline some 4–8 kilometres downstream the repository.

The Darcy fluxes at repository depth generally increase by 1–1.5 orders of magnitude during glaciation (pre-LGM) when the ice sheet margin is located right above the repository (ice-front location II). Typical Darcy fluxes are between $3 \cdot 10^{-12}$ and $9 \cdot 10^{-8}$ m/s with a median value around $2 \cdot 10^{-9}$ m/s. The salinity variations during glaciation, complete ice coverage and deglaciation resemble the variations obtained from the simulation of the glacial case without permafrost, however significantly smaller increases occur (maximum values around 0.5%). However, as the permafrost prevents discharge of the upconing saline water near the ice sheet margin, the upconing saline water is pushed forward beneath the permafrost towards more distant discharge locations, i.e. taliks.

Table 6-3 presents median values of some of the considered performance measures (flow path length, travel time, flow-related transport resistance) for the five measurement localities, ML 1-5 when the ice sheet margin is at ice-front location II.

Table 6-3. Performance measures for the glacial case with permafrost: Median flow path lengths, travel times, and flow-related transport resistances at measurement localities ML 1-5 when the ice sheet margin is at ice front location IFL II.

ML	Discharge			Recharge		
	Flow path length [m]	Travel time [y]	Flow-related transport resistance [y/m]	Flow path length [m]	Travel time [y]	Flow-related transport resistance [y/m]
1	8,287	2.1	$1.7 \cdot 10^4$	23,514	0.6	$2.6 \cdot 10^4$
2	6,701	1.7	$2.3 \cdot 10^4$	24,280	1.8	$3.0 \cdot 10^4$
3	5,736	0.5	$6.1 \cdot 10^3$	24,481	0.9	$2.6 \cdot 10^4$
4	5,016	0.9	$1.2 \cdot 10^4$	24,996	1.1	$4.1 \cdot 10^4$
5	8,263	1.1	$1.9 \cdot 10^4$	22,789	1.1	$3.1 \cdot 10^4$

6.4.4 Comparison of the Darcy flux at different time slots

Figure 6-15 shows the minimum, median and maximum values of the Darcy flux at all deposition hole positions during the main "climate events" during the simulated period (IFL 0 → IFL V → IFL 0) of periglacial and glacial climate conditions.

- Temperate (used to produce normalised quantities, see Figure 6-16) (IFL 0)
- Permafrost (IFL 0), and
- Glacial case without permafrost (IFL II),
- Glacial maximum (IFL V),
- Glacial case with permafrost and a 2 km long tongue (IFL II), and
- Submerged (IFL 0).

The climate condition "Glacial case without permafrost" provides the highest maximum as well as highest median value of all simulated climate events. Relative to the median temperate period value, the median Glacial without permafrost value is almost two orders of magnitude higher. The maximum Glacial without permafrost value is also almost two orders of magnitude higher than the maximum Temperate period value. Conditions of complete ice coverage, or when only permafrost prevails, provide Darcy fluxes slightly larger than those of Temperate conditions. When the domain is completely submerged, the Darcy fluxes are the smallest over all climate conditions.

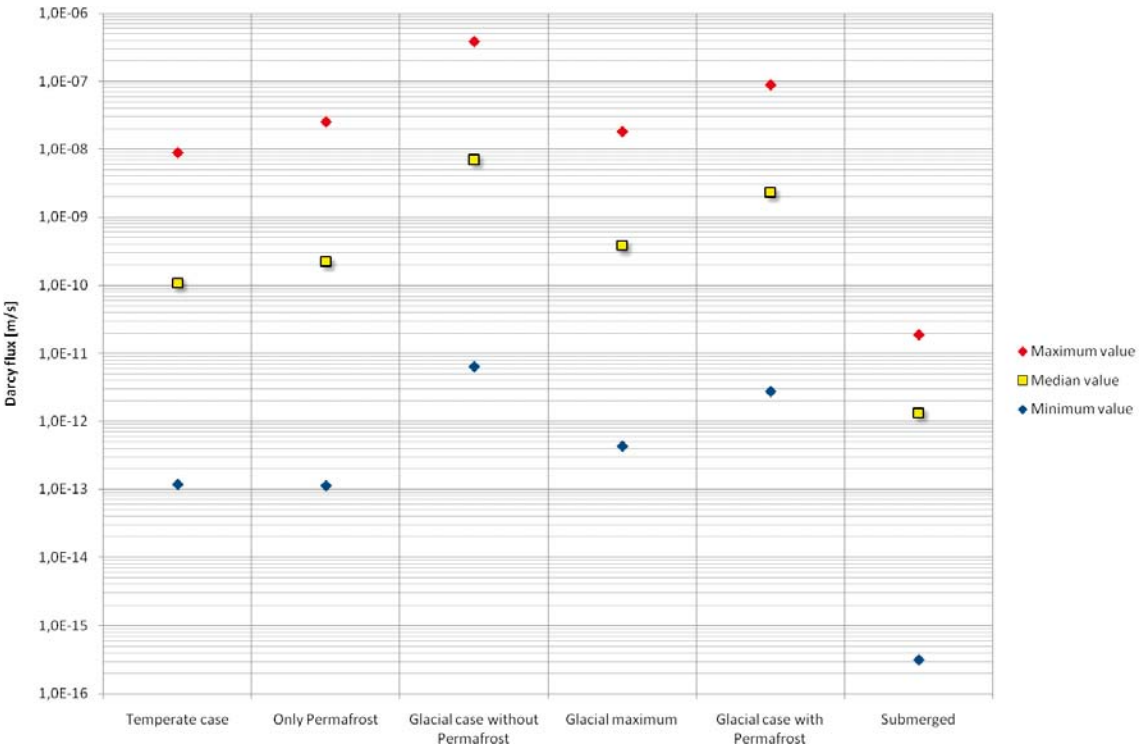

Figure 6-15. *Darcy flux at repository depth for the main climate events considered during the simulated period of periglacial and glacial climate conditions.*

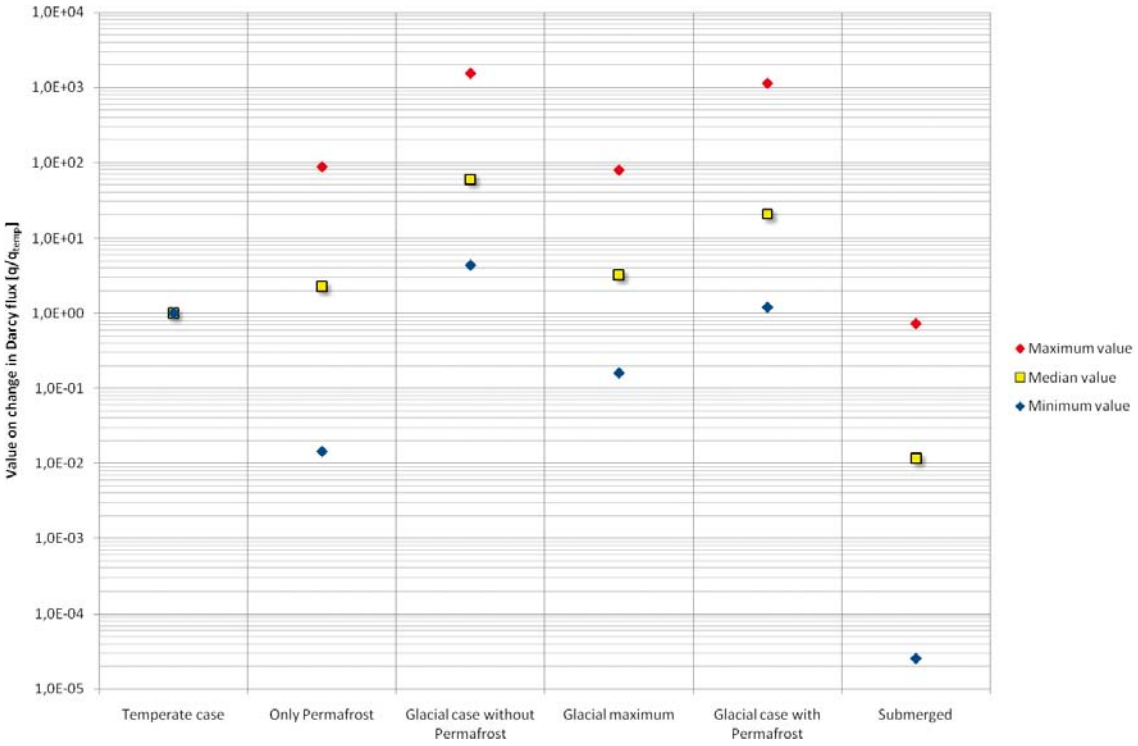

Figure 6-16. *Normalised Darcy flux (q/q_{temp}) at repository depth for the main climate events considered during the simulated period of periglacial and glacial climate conditions.*

7 Summary and conclusions

7.1 Scope of work

The primary driving force for groundwater flow at repository depth during periods of periglacial (permafrost) and glacial climate conditions is the difference in hydraulic pressure below the ice sheet and in front of the ice sheet margin. The expected effects of this gradient with relevance for long-term safety are related to the groundwater chemistry, the performance measures of groundwater flow at repository depth, and the flow-related transport parameters. In order to assess the magnitude of these impacts, groundwater flow simulations, based on the hydrogeological models developed as part of SDM-Site Laxemar, have been performed. The overall objective of these simulations has been to assess the effects of periglacial and glacial climate conditions on site hydrogeological and hydrogeochemical conditions.

The study aims at providing bounding hydrogeological estimates for the Laxemar site during periglacial and glacial climate conditions.. The study is coordinated with the present-day conditions at Laxemar as defined in SDM-Site as well the future conditions considered for the reference climate evolution in /SKB 2006a/.

7.2 Methodology

The groundwater flow modelling conducted during temperate climate conditions by /Joyce et al. 2010/ considers the evolution between 8,000 BC and 12,000 AD. To a large extent the setup of the temperate flow modelling of /Joyce et al. 2010/ follows the specifications of the groundwater flow modelling considered in SDM-Site, which dealt with the evolution between 8,000 BC and 2,000 AD, a time period known as the Holocene.

In comparison, the groundwater flow modelling during periglacial and glacial climate conditions reported here is less specific with regard to time although the flow modelling as such encompasses periglacial and glacial climate conditions during a time period of approximately 13,000 years. That is, there is no particular start time associated with the flow simulations conducted during periglacial and glacial climate conditions. Furthermore, it is noted that the work reported here focuses on studying the effects of a number of bounding hydraulic assumptions rather than striving for realism in every detail. Although some of the studied assumptions create overly pessimistic premises for the flow simulations, as compared to the reference climate evolution presented in /SKB 2006a, 2010/, they are useful for safety assessment applications as they provide bounds on the uncertainties involved.

Based on the reference climate evolution described in /SKB 2006a, 2010/, the flow modelling is divided into three stages referred to as pre-LGM[10], LGM, and post-LGM. During the pre-LGM stage, the ice sheet grows and the ice sheet margin moves across the site in a forward (advancing) direction. During the LGM stage, the model domain is completely covered by ice for thousands of years. During the post-LGM stage, the ice sheet melts and its margin moves across the site in a backward (retreating) direction. The three stages implies transient top boundary conditions.

The groundwater flow modelling uses a coupled thermal-hydraulic-chemical analysis of the different periods of a glacial cycle. The simulations are based on version 3.2 of the DarcyTools code. This version of DarcyTools contains an algorithm that can account for changes in permeability as a function of temperature, which is considered necessary in order to simulate transient and spatially varying hydrological and hydraulic conditions during the evolution of permafrost and ice sheets. The flow modelling did not consider changes in groundwater salinity due to freezing and thawing. Nor did it consider any heat flux from the repository to the surface nor any hydraulic-mechanical issues.

The flow simulation results comprise fluid pressures (P), Darcy fluxes (q), and water salinities (C), as well as advective transport performance measures obtained by particle tracking such as flow

[10] LGM is a standard acronym used to denote the glacial maximum of the last glaciation (Weichsel), cf. /SKB 2010/.

path lengths (L), travel times (t_w), and flow-related transport resistances (F). The Darcy fluxes, the water salinities and the flow-related transport resistances constitute the primary output quantities. Pressures, travel times and flow path lengths constitute second-order performance measures.

Pressures, Darcy fluxes, and water salinity values are captured in increments of six years at five measurement locations for an advancing and retreating ice sheet margin. Advective flow path lengths, travel times, and flow-related transport resistances are calculated for all (8,031) deposition hole positions at four specified ice-front locations. The modelling is accompanied by a sensitivity study, which among other matters, investigated the impact of different ice sheet flow directions and different hydraulic properties.

It is noted that a repository is not included in the work reported here. However, the influence of the hydraulic characteristics of the backfilled tunnels on the performance measures during periods with periglacial and glacial climate conditions could be accounted for by exporting the simulation results to be used as input (boundary conditions) in the groundwater flow modelling conducted by /Joyce et al. 2010/.

In summary, the following stages are considered in the work reported here:

- **Pre-LGM stage.** Two different azimuth directions of ice sheet movement:
  1. Advance from north-west, and 2. Advance from north; Two types of periglacial conditions:
  1. No permafrost and 2. Permafrost in front of the ice sheet margin as well as extending 2 km within the margin of the ice sheet (permafrost tongue); Three types of permeability conditions:
  1. Undistorted conditions, i.e. present-day conditions, 2. Elaborated permeability conditions (based on an Elaborated Hydro-DFN), i.e. variant of present-day conditions, and 3. Distorted conditions due to freezing and thawing.
- **LGM stage.** The model domain is completely covered by a thick ice sheet during approximately 11,000 years.
- **Post-LGM stage.** One azimuth direction of ice sheet movement (retreat from south-east); submerged ground conditions in front of the ice sheet margin; undistorted permeability conditions.

The flow simulations are listed in Table 1-1. There are two main scenarios, without permafrost and with permafrost, and four cases, see Figure 5-1 to Figure 5-3.

7.3 Assumptions

The study is based on several assumptions and simplifications. The most important ones are listed below.

1. The size of the model domain used in the work reported here is much larger than the model domain used for SDM-Site. Hence, simplifying assumptions are made regarding the hydraulic properties away from the focused area. Although the size of the chosen model domain is sufficiently large to address many issues of relevance for performance of a repository, the model domain is still not large enough to encompass recharge areas especially under permafrost conditions.
2. Permafrost is a key process to consider as it reduces the permeability of sub-surface materials (hydraulic conductivity). Permafrost does not develop instantaneously, but is a transient process. A freezing algorithm is used to modify reported Holocene hydraulic conductivity values in a transient fashion. The thermal input to the permafrost model comes from the temperature time series described in /SKB 2006a/.
3. Permafrost reduces mainly the permeability of sub-surface materials to water flow (hydraulic conductivity). Other flow and transport parameters were assumed to be unaffected in the work reported here due to the paucity of data, e.g. the kinematic porosity.
4. A discontinuous permafrost layer is modelled, where probable locations of taliks are estimated from the forecast landscape development and the projected shoreline displacement.
5. The ice sheet margin is set to advance with an average speed of 50 m/y and retreat with an average speed of 100 m/y. During the retreat, the height of the ice sheet profile is the same as during the advance. In addition, the sea level is raised to +100 m above the Ordnance Datum causing submerged ground conditions in front of the ice sheet margin.
6. An infinite source of meltwater with a hydraulic head at the base of the ice sheet equal to 92% of the ice sheet thickness is assumed at all times in all simulations. This value is assigned to all parts

below the ice sheet that are not affected by permafrost. Elsewhere, the hydraulic head is assumed to follow the topography in all terrestrial parts. In effect, subglacial meltwater that infiltrates into the subsurface will flow from areas with high hydraulic heads to areas with lower hydraulic heads.

7. The classic hydraulic mass balance equation for transient density and viscosity-dependent groundwater flow is favoured over the hydro-mechanical mass balance equation considered in the literature. That is, a one-dimensional loading efficiency of zero is taken to be more relevant for the objectives of this report as it enhances the gradients and thereby the fluxes at repository depth.
8. Isostasy is not accounted for.
9. The abundance of eskers in the Fennoscandian Shield demonstrates the frequency of major meltwater tunnels during the retreat of the Weichselian ice sheet. The eskers occur on top of crystalline bedrock, which reveals that it was here that the bulk of the meltwater runoff took place during the deglaciation. The role of meltwater tunnels for groundwater flow during deglaciation has been interpreted in different ways in the literature. In the work reported here, the transient boundary conditions on the top boundary of the model domain are coordinated with those considered in /SKB 2010/, i.e. meltwater tunnels are not taken into account during glaciation and their impact on the groundwater flow at repository depth during deglaciation is considered insignificant.
10. The structural-hydraulic properties of the sparsely fractured bedrock between the deterministically modelled deformation zones are modelled stochastically. However, the variability between realisations is not addressed.

7.4 Temperate climate conditions

The temperate case is represented by a flow and salt transport solution using the SDM-Site hydrogeological model as input information /Rhén et al. 2009/.

The groundwater flow is primary controlled by the local gradient over and surrounding the repository area. However, local differences due to variations in geological conditions are encountered with flow directions dependent on the transmissivity values of major conductive deformation zones.

The recharge locations of the particle traces that pass through the 8,031 deposition hole positions all coincide with topographic highs inside the boundary of the regional model domain for groundwater flow as depicted in SDM-Site Laxemar /Rhén et al. 2009/.

7.5 Glacial climate conditions without permafrost

The recharge flow paths are significantly longer than the discharge flow paths for the glacial cases without permafrost. Indeed, most of the discharge locations are found in front of the ice sheet margin or in close proximity to nearby deformation zones.

The Darcy fluxes at repository depth generally increase by two orders of magnitude during glaciation (pre-LGM) when the ice sheet margin is located right above the repository (ice-front location II). The salinity at repository depth varies significantly during the passage of the ice sheet margin. The salinity first increases and then decreases. During the initial part of the period of complete ice coverage (LGM), the Darcy fluxes are low and a small but gradual increase in fracture water salinity occurs. This gain of the “salt water interface” is primary due to an out diffusion of the available porewater salinity and not, as in the case of the Forsmark site, due to the slow, but continuous advective transport of salt from below since this salt interface at Laxemar is significant deeper after the pre-LGM phase. In the model, the fracture water salinity at great depth is assumed to be undisturbed (fixed) at all times.

The glacial passage during retreat (post-LGM) is also characterised by an upconing and flushing event. The simulations indicate that salinities are more or less restored during the simulated period.

7.6 Glacial climate conditions with permafrost

The recharge flow paths for the glacial case with permafrost are significantly longer than the discharge flow paths, though discharge flow paths may be of significant length in a permafrost region depending on the location of taliks.

The Darcy fluxes at repository depth generally increase by two orders of magnitude during glaciation (pre-LGM) when the ice sheet margin is located right above the repository (ice-front location II). The salinity variations during glaciation, complete ice coverage and deglaciation resembles the variations obtained from the simulation of the glacial case without permafrost but the increase is significantly lower. Also, as the permafrost prevents discharge of the upconing saline water near the ice sheet margin, the upconing saline water is pushed forward beneath the permafrost towards more distant discharge locations, i.e. taliks.

7.7 Conclusions

The results reached in this study are the Darcy fluxes and fracture water salinities at repository level. These and other quantities are reported in Appendices D–F. Chapter 6 summarises the key simulation results.. The report refrains from commenting on their safety implications, however. Such safety implications can only be evaluated when the results have been propagated through the safety assessment process.

In respect of the assumptions listed in section 7.3, the following observations are made in the groundwater flow simulations reported here:

- The primary hydraulic driving force for groundwater flow during periods of periglacial and glacial conditions is the difference in hydraulic pressure below the ice sheet and the hydraulic pressure in front of the ice sheet margin, i.e. in the periglacial area. The present-day topographic water divides are significantly diminished in significance during periglacial and glacial climate conditions.
- It is during the passages of the ice sheet margin that the hydraulic gradients and the Darcy fluxes at a repository reach their maximum values during a glacial cycle. It is also then that the interface between fresh water and saline water is distorted the most.
- The hydraulic and hydrochemical disturbances during the advance stage (pre-LGM) are probably greater than the disturbances during the retreat phase (post-LGM). The reason for this is threefold; during the retreat phase, the ice profile at the ice sheet margin is probably thinner and less steep, the average speed of the ice sheet margin is probably higher, and the periglacial area in front of the ice sheet margin is probably submerged.
- During the period of complete ice coverage (LGM), the hydraulic gradients are probably smaller and more uniform than during temperate conditions. Initially a small but gradual increase in fracture water salinity at repository depth is observed in the simulations.
- In this study, the model that simulates permafrost decreases the permeability values of the major deformation zones to around 10^{-20} m^2. Still, the particle tracking performed suggests that the permafrost layer is not impervious, and hence allows a few particles to discharge where the hydraulic gradient is high. If this is an imperfection of the particle tracking algorithm used, or a physical phenomenon to be expected, e.g. due to high hydraulic gradients, is unclear.
- The discharge locations of released particles are predominantly found well within the physical boundaries of the model domain and often very close to the ice sheet margin. The differences seen between the two glacial cases studied depend on the handling of permafrost. If permafrost is included, the majority of the discharge occurs in taliks located in the periglacial area.

8 References

Bath A, Lalieux P, 1999. Technical summary of the SEDE Workshop on the use of hydrogeochemical information in testing groundwater flow models. In: Use of hydrogeochemical information in testing groundwater flow models: technical summary and proceedings of a workshop organised by the NEA Co-ordinating Group on Site Evaluation and Design of Experiments for Radioactive Waste Disposal (SEDE) and hosted by the Swedish Nuclear Fuel and Waste Management Company (SKB), Borgholm, Sweden, 1–3 September 1997. Paris: OECD, pp 13–30.

Chan T, Christiansson R, Boulton G S, Ericsson L O, Hartikainen J, Jensen R M, Mas Ivars D, Stanchell W F, Vidstrand P, Wallroth T, 2005. DECOVALEX III BMT3/BENCHPAR WP4: The thermo-hydro-mechanical responses to a glacial cycle and their potensial implication for deep geological disposal of nuclear fuel waste in a fractured crystalline rock mass. International Journal of Rock Mechanics and Mining Science, 42, pp 805–827.

Dershowitz W, Winberg A, Hermanson J, Byegård J, Tullborg E-L, Andersson P, Mazurek M, 2003. Äspö Hard Rock Laboratory. Äspö Task Force on modelling of groundwater flow and transport of solutes. Task 6c. A semi-synthetic model of block scale conductive structures at the Äspö HRL. SKB IPR-03-13, Svensk Kärnbränslehantering AB.

Dverstorp B, Strömberg B, 2008. SKI's and SSI's review of SKB's safety report SR-Can. SKI Report 2008:23, Statens kärnkraftinspektion (Swedish Nuclear Power Inspectorate), SSI Report 2008:04 E, Statens strålskyddsinstitut (Swedish Radiation Protection Authority).

Ericsson L O, Holmén J, 2010. Storregional grundvattenmodellering – en känslighets-studie av några utvalda konceptuella beskrivningar och förenklingar. SKB R-10-43, Svensk Kärnbränslehantering AB.

Ericsson L O, Holmén J, Rhén I, Blomquist N, 2006. Storregional grundvattenmodellering – fördjupad analys av flödesförhållanden i östra Småland. Jämförelse av olika konceptuella beskrivningar. SKB R-06-64, Svensk Kärnbränslehantering AB.

Follin S, 2008. Bedrock hydrogeology Forsmark. Site descriptive modelling, SDM-Site Forsmark. SKB R-08-95, Svensk Kärnbränslehantering AB.

Follin S, Svensson U, 2003. On the role of mesh discretisation and salinity for the occurrence of local flow cells. Results from a regional-scale groundwater flow model of Östra Götaland. SKB R-03-23, Svensk Kärnbränslehantering AB.

Follin S, Stigsson M, Berglund S, Svensson U, 2004. Variable-density groundwater flow simulations and particle tracking – numerical modelling using DarcyTools. Preliminary site description of the Simpevarp area – version 1.1. SKB R-04-65, Svensk Kärnbränslehantering AB.

Follin S, Stigsson M, Svensson U, 2005. Variable-density groundwater flow simulations and particle tracking – numerical modelling using DarcyTools. Preliminary site description, Simpevarp subarea – version 1.2. SKB R-05-11, Svensk Kärnbränslehantering AB.

Follin S, Stigsson M, Svensson U, 2006. Hydrogeological DFN modelling using structural and hydraulic data from KLX04. Preliminary site description, Laxemar subarea – version 1.2. SKB R-06-24, Svensk Kärnbränslehantering AB.

Follin S, Hartley L, Jackson P, Roberts D, Marsic N, 2008. Hydrogeological conceptual model development and numerical modelling using CONNECTFLOW, Forsmark modelling stage 2.3. SKB R-08-23, Svensk Kärnbränslehantering AB.

Fredén C (ed), 2002. Sveriges nationalatlas. Berg och jord (in Swedish). Stockholm: SNA publishing.

Gimeno M J, Auqué L F, Gómez J B, Salas J, Molinero J, 2010. Hydrogeochemical evolution of the Laxemar site. SKB R-10-60, Svensk Kärnbränslehantering AB.

Haggerty R, Gorelick S M, 1995. Multiple-rate mass transfer for modeling diffusion and surface reactions i media with pore-scale heterogeneity. Water Resources Research, 31, pp 2383–2400.

Harlow F H, Welsch J E, 1965. Numerical calculations of time-dependent viscous incompressible flow of fluid with free surface. Physics of Fluids, 8, pp 2182–2189.

Hartikainen J, Kouhia R, Wallroth T, 2010. Permafrost simulations at Forsmark using a numerical 2D thermo-hydro-chemical model. SKB TR-09-17, Svensk Kärnbränslehantering AB.

Hartley L, Worth D, Gylling B, Marsic N, Holmén J, 2004. Preliminary site description: Groundwater flow simulations. Simpevarp area (version 1.1) modelled with CONNECTFLOW. SKB R-04-63, Svensk Kärnbränslehantering AB.

Hartley L, Hoch A, Hunter F, Jackson P, Marsic N, 2005. Regional hydrogeological simulations – numerical modelling using ConnectFlow. Preliminary site description, Simpevarp subarea – version 1.2. SKB R-05-12, Svensk Kärnbränslehantering AB.

Hartley L, Hunter F, Jackson P, McCarthy R, Gylling B, Marsic N, 2006. Regional hydrogeological simulations using CONNECTFLOW. Preliminary site description, Laxemar subarea – version 1.2, SKB R-06-23, Svensk Kärnbränslehantering AB.

Hartley L, Jackson P, Joyce S, Roberts D, Shevelan J, Swift B, Gylling B, Marsic N, Hermanson J, Öhman J, 2007. Hydrogeological pre-modelling exercises. Assessment of impact of the Äspö Hard Rock Laboratory. Sensitivities of palaeo-hydrogeology. Development of a local near-surface Hydro-DFN for KLX09B-F. Site descriptive modelling, SDM-Site Laxemar. SKB R-07-57, Svensk Kärnbränslehantering AB.

Holmén J G, 2008. Premodelling of the importance of the location of the upstream hydraulic boundary of a regional flow model of the Laxemar-Simpevarp area. Site descriptive modelling, SDM-Site Laxemar. SKB R-08-60, Svensk Kärnbränslehantering AB.

Holmén J G, Stigsson M, Marsic N, Gylling B, 2003. Modelling of groundwater flow and flow paths for a large regional domain in northeast Uppland. A three-dimensional, mathematical modelling of groundwater flows and flow paths on a super-regional scale, for different complexity levels of the flow domain. SKB R-03-24, Svensk Kärnbränslehantering AB.

Jaquet O, Siegel P, 2006. Regional groundwater flow model for a glaciation scenario. Simpevarp subarea – version 1.2. SKB R-06-100, Svensk Kärnbränslehantering AB.

Joyce S, Simpson T, Hartley L, Applegate D, Hoek J, Jackson P, Roberts D, Swan D, Gylling B, Marsic N, Rhén I, 2010. Groundwater flow modelling of periods with temperate climate conditions – Laxemar. SKB R-09-24, Svensk Kärnbränslehantering AB.

Laaksoharju M, Smellie J, Tullborg E-L, Wallin B, Drake H, Gascoyne M, Gimeno M, Gurban I, Hallbeck L, Molinero J, Nilsson A-C, Waber N, 2009. Bedrock hydrogeochemistry Laxemar. Site descriptive modelling, SDM-Site Laxemar. SKB R-08-93, Svensk Kärnbränslehantering AB.

Larsson-McCann S, Karlsson A, Nord M, Sjögren J, Johansson L, Ivarsson M, Kindell S, 2002. Meteorological, hydrological and oceanographical data for the site investigation program in the community of Oskarshamn. SKB TR-02-03, Svensk Kärnbränslehantering AB.

Lönnqvist M, Hökmark H, 2010. Assessment of potential for glacially induced hydraulic jacking at different depths. SKB R-09-35, Svensk Kärnbränslehantering AB.

NEA-OECD, 1993. Paleohydrogeological methods and their application: proceedings of a NEA workshop, Paris, 9–10 November 1992. Paris: Nuclear Energy Agency, Organisation for Economic Co-operation and Development.

Nyman H, Sohlenius G, Strömgren M, Brydsten L, 2008. Depth and stratigraphy of regolith. Site descriptive modelling, SDM-Site Laxemar. SKB R-08-06, Svensk Kärnbränslehantering AB.

Patankar S V, 1980. Numerical heat transfer and fluid flow. New York: Hemisphere.

Paterson WSB, 1994. The physics of glaciers. Elsevier Science Ltd. Third edition.

Påsse T, 1997. A mathematical model of past, present and future shore level displacement in Fennoscandia. SKB TR 97-28, Svensk Kärnbränslehantering AB.

Rhén I, Hartley L, 2009. Bedrock Hydrogeology Laxemar. Site descriptive modelling, SDM-Site Laxemar. SKB R-08-92, Svensk Kärnbränslehantering AB.

Rhén I (ed), Gustafson G, Stanfors Roy, Wikberg P, 1997. Äspö HRL – Geoscientific evaluation 1997/5. Models based on site characterization 1986–1995. SKB TR 97-06, Svensk Kärnbränslehantering AB.

Rhén I, Follin S, Hermanson J, 2003. Hydrological site descriptive model – a strategy for its development during site investigations. SKB R-03-08, Svensk Kärnbränsle hantering AB.

Rhén I, Forsmark T, Forssman I, Zetterlund M, 2006a. Hydrogeological single-hole interpretation of KSH01A, KSH02, KSH03A, KAV01, KLX02 and HSH01–03. Simpevarp subarea – version 1.2. SKB R-06-20, Svensk Kärnbränslehantering AB.

Rhén I, Forsmark T, Forssman I, Zetterlund M, 2006b. Hydrogeological single-hole interpretation of KLX02, KLX03, KLX04, KAV04A and B, HAV09–10 and 9 HLXxx boreholes. Laxemar subarea – version 1.2. SKB R-06-21, Svensk Kärnbränslehantering AB.

Rhén I, Forsmark T, Forssman I, Zetterlund M, 2006c. Evaluation of hydrogeological properties for Hydraulic Conductor Domains (HCD) and Hydraulic Rock Domains (HRD). Laxemar subarea – version 1.2. SKB R-06-22, Svensk Kärnbränslehantering AB.

Rhén I, Forsmark T, Hartley L, Jackson C P, Roberts D, Swan D, Gylling B, 2008. Hydrogeological conceptualisation and parameterisation. Site descriptive modelling, SDM-Site Laxemar. SKB R-08-78, Svensk Kärnbränslehantering AB.

Rhén I, Forsmark T, Hartley L, Joyce S, Roberts D, Gylling B, Marsic N, 2009. Bedrock hydrogeology. Model testing and synthesis. Site descriptive modelling, SDM-Site Laxemar. SKB R-08-91, Svensk Kärnbränslehantering AB.

SKB, 2002. Simpevarp – site descriptive model version 0. SKB R-02-35, Svensk Kärnbränslehantering AB.

SKB, 2004. Preliminary site description. Simpevarp area – version 1.1. SKB R-04-25, Svensk Kärnbränslehantering AB.

SKB, 2005. Preliminary site description. Simpevarp subarea – version 1.2. SKB R-05-08, Svensk Kärnbränslehantering AB.

SKB, 2006a. Climate and climate-related issues for the safety assessment SR-Can. SKB TR-06-23, Svensk Kärnbränslehantering AB.

SKB, 2006b. Preliminary site description. Laxemar subarea – version 1.2. SKB R-06-10, Svensk Kärnbränslehantering AB.

SKB, 2006c. Preliminary site description Laxemar Stage 2.1. Feedback for completion of the site investigation including input from safety assessment and depository engineering. SKB R-06-110, Svensk Kärnbränslehantering AB.

SKB, 2008. Site decription of Forsmark at completion of the site investigation phase. SDM-Site Forsmark. SKB TR-08-05, Svensk Kärnbränslehantering AB.

SKB, 2009a. Site description of Laxemar at completion of the site investigation phase. SDM-Site Laxemar. SKB TR-09-01, Svensk Kärnbränslehantering AB.

SKB, 2009b. Confidence assessment. Site descriptive modelling, SDM-Site Laxemar. SKB R-08-101, Svensk Kärnbränslehantering AB.

SKB, 2010. Climate and climate-related issues for the safety assessment SR-Site. SKB TR-10-49, Svensk Kärnbränslehantering AB.

Sohlenius G, Hedenström A, 2008. Description of regolith at Laxemar-Simpevarp. Site descriptive modelling, SDM-Site Laxemar. SKB R-08-05, Svensk Kärnbränslehantering AB.

Sundberg J, Back P-E, Ländell M, Sundberg A, 2009. Modelling of temperature in deep boreholes and evaluation of geothermal heat flow at Forsmark and Laxemar. SKB TR-09-14, Svensk Kärnbränslehantering AB.

Svensson U, Rhén I, 2010. Groundwater flow modelling of the excavation and operational phases – Laxemar. SKB R-09-23, Svensk Kärnbränslehantering AB.

Svensson U, Ferry M, Kuylenstierna H-O, 2010. DarcyTools, Version 3.4. Concepts, methods, and equations. SKB R-07-38, Svensk Kärnbränslehantering AB.

Söderbäck B (ed), 2008. Geological evolution, palaeoclimate and historic development of the Forsmark and Laxemar-Simpevarp areas. Site descriptive modelling, SDM-Site. SKB R-08-19, Svensk Kärnbränslehantering AB.

Vidstrand P, Näslund J-O, Hartikainen J, Svensson U, 2007. Hydrogeological flux scenarios at Forsmark. Generic numerical flow simulations and compilation of climatic information for use in the safety analysis SFR1 SAR-08. SKB R-07-63, Svensk Kärnbränslehantering AB.

Vidstrand P, Follin S, Zugec N, 2010. Groundwater flow modelling of periods with periglacial and glacial climate conditions – Forsmark. SKB R-09-21, Svensk Kärnbränslehantering AB.

Vilks P, 2007. Oskarshamn site investigation. Rock matrix permeability measurements on core samples from borehole KLX03. SKB P-07-204, Svensk Kärnbränslehantering AB.

Wahlgren C-H, Curtis P, Hermanson J, Forssberg O, Öhman J, Fox A, La Pointe P, Drake H, Triumf C-A, Mattsson H, Thunehed H, Juhlin C, 2008. Geology Laxemar. Site descriptive modelling, SDM-Site Laxemar. SKB R-08-54, Svensk Kärnbränslehantering AB.

Werner K, Öhman J, Holgersson B, Rönnback K, Marelius F, 2008. Meteorological, hydrological and hydrogeological monitoring data and near-surface hydrogeological properties data from Laxemar-Simpevarp. Site descriptive modelling, SDM-Site Laxemar. SKB R-08-73, Svensk Kärnbränslehantering AB.

Appendix A

Parameters for HRD modelling

A.1 Introduction

This appendix presents the model parameters used in DarcyTools for generating stochastic hydrogeological discrete fracture network (DFN) properties of the fracture domains within the focused area. The up-scaling of these properties to equivalent continuous porous medium (ECPM) properties is performed inside the code DarcyTools, see /Svensson et al. 2010/ for details. This appendix specifies also the hydraulic continuous porous media (CPM) properties used for the fracture domains located outside the SDM-Site regional flow domain.

A.2 Fracture size-intensity relationship

In DarcyTools, the number of fractures (n) in the size range [L, L+dL] may be calculated as:

$$n = I\left[\left(\frac{L+dL}{L_{ref}}\right)^{D} - \left(\frac{L}{L_{ref}}\right)^{D}\right] / D \tag{A-1}$$

where I is the number of fractures of size L_{ref} per unit volume and D is the exponent (shape factor) of a power law size distribution. The relationships between the notation used in DarcyTools and that reported for SDM-Site Laxemar may be written as:

$$L_0 = r_0 \cdot \sqrt{\pi} \tag{A-2}$$

$$I = P_{32}[r_0, \infty] \cdot L_0^{(k_r - 2)} \cdot (k_r - 2) / L_{ref}^{k_r} \tag{A-3}$$

$$D = -k_r \tag{A-4}$$

$$\lambda_1 = \cos(90 - tr) \cdot \cos(pl) \cdot \kappa \tag{A-5}$$

$$\lambda_2 = \sin(90 - tr) \cdot \cos(pl) \cdot \kappa \tag{A-6}$$

$$\lambda_3 = -\sin(pl) \cdot \kappa \tag{A-7}$$

where L_0 [m] equals the side length of the smallest fracture generated (represented as a square), r_0 [m] is its equivalent radius and $P_{32}[r_0,\infty]$ [L^2/L^3] is the fracture surface area per unit volume for all fractures in the size range [r_0,∞]. Each fracture set is assumed to obey a Fisher distribution of its own, which is characterised by a Fisher concentration κ, a mean trend tr and a mean plunge pl. Moreover, the sizes of the generated fractures are assumed to be power-law distributed, with one shape factor k_r per fracture set. The orientations of the generated fractures are fully described by λ_1–λ_3, which are the normal vectors.

The relationship between the incremental fracture intensity, $P_{32}[r_1, r_2]$, and the total intensity, $P_{32}[r_0,\infty]$, may be written as:

$$P_{32}[r_1, r_2] = P_{32}[r_0, \infty]\left(\frac{(r_1)^{(2-k_r)} - (r_2)^{(2-k_r)}}{(r_0)^{(2-k_r)}}\right) \tag{A-8}$$

A.3 Fracture input statistics

For the detailed defined HRDs illustrated in Figure A-1 statistics described in Tables A-1 to A-24 for generation of one realisation of fractures were used.

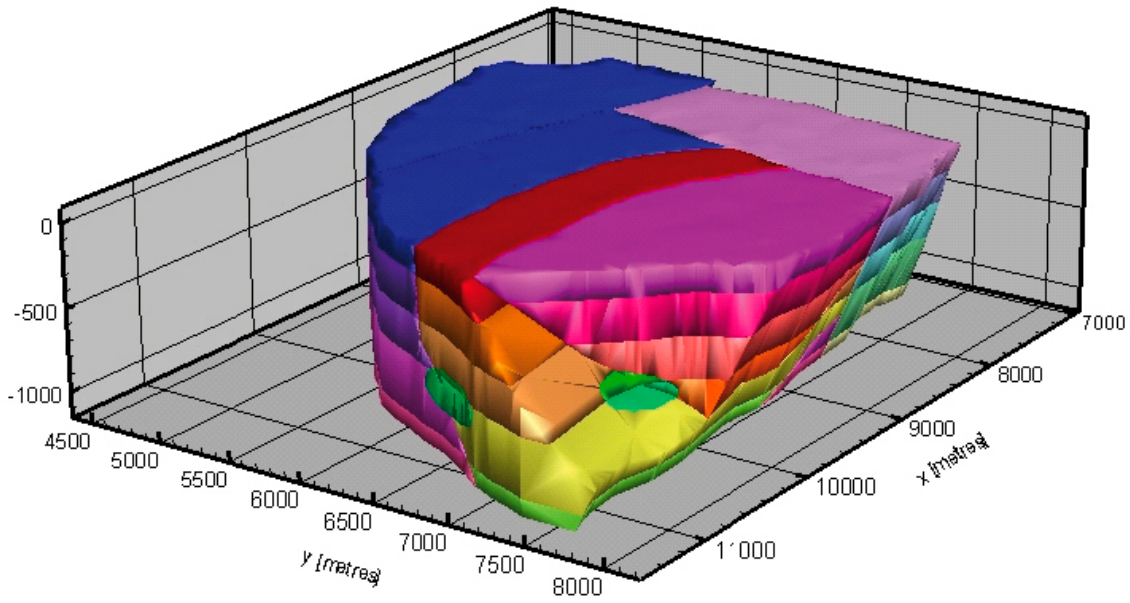

Figure A-1. *Illustrations of HRD assessed in the SDM local model. The upper layer consists of HRD_C (blue), HRD_EW007 (red), HRD_N (purple), and HRD_W (greyish purple). The layers beneath consists of the different depth intervals.*

Table A-1. Parameters values used in SDM-Site for fracture domain HRD_C. (Modified after Table 10-7 in /Rhén et al. 2008/.)

Elevation [m RHB 70]	Fracture set name	Orientation set pole: (trend, plunge), conc. κ [°,°, –]	Size model, power-law (k_r , r_0) [– , m]	Intensity, ($P_{32,open}$), valid size interval: (r_0, 564 m) [m²/m³]	Semi-correlated transmissivity model $log(T) = log(a\ r^{b}) + \sigma_{log(T)}\ N(0,1)$)
–150 to 0	ENE	(155.1,3.4), 9.6	(2.6, 0.038)	0.52	SC: ($6 \cdot 10^{-8}$, 0.5, 0.4)
	WNW	(204,1.6), 12	(2.5, 0.038)	0.95	SC: ($2 \cdot 10^{-7}$, 0.6, 0.7)
	NS	(270.2,8.4), 7.8	(2.7, 0.038)	0.54	SC: ($2 \cdot 10^{-7}$, 0.6, 0.5)
	Sub-H	(46.3,84.7), 12	(2.7, 0.038)	1.20	SC: ($1.5 \cdot 10^{-7}$, 0.7, 0.7)
–400 to –150	ENE	(155.1,3.4), 9.6	(2.85, 0.038)	0.47	SC: ($1 \cdot 10^{-6}$, 0.7, 0.7)
	WNW	(204,1.6), 12	(2.45, 0.038)	0.55	SC: ($8 \cdot 10^{-8}$, 0.3, 0.1)
	NS	(270.2,8.4), 7.8	(2.85, 0.038)	0.63	SC: ($1 \cdot 10^{-7}$, 0.7, 0.7)
	Sub-H	(46.3,84.7), 12	(2.85, 0.038)	0.71	SC: ($1.5 \cdot 10^{-7}$, 0.8, 0.9)
–650 to –400	ENE	(155.1,3.4), 9.6	(2.8, 0.038)	0.38	SC: ($5 \cdot 10^{-7}$, 0.5, 0.5)
	WNW	(204,1.6), 12	(2.5, 0.038)	0.74	SC: ($2 \cdot 10^{-8}$, 0.6, 0.4)
	NS	(270.2,8.4), 7.8	(2.9, 0.038)	0.47	SC: ($1 \cdot 10^{-8}$, 0.4, 0.4)
	Sub-H	(46.3,84.7), 12	(2.9, 0.038)	0.58	SC: ($3 \cdot 10^{-7}$, 0.6, 0.6)
below –650	ENE	(155.1,3.4), 9.6	(2.9, 0.038)	0.46	SC: ($5 \cdot 10^{-9}$, 0.6, 0.4)
	WNW	(204,1.6), 1	(2.8, 0.038)	0.73	SC: ($5 \cdot 10^{-8}$, 0.6, 0.4)
	NS	(270.2,8.4), 7.8	(2.95, 0.038)	0.25	SC: ($5 \cdot 10^{-9}$, 0.6, 0.4)
	Sub-H	(46.3,84.7), 12	(2.95, 0.038)	0.35	SC: ($1 \cdot 10^{-7}$, 0.6, 0.4)

Table A-2. DFN parameter values used in the present report for fracture domain HRD_C.

Elevation [m RHB 70]	Set	λ_1 (-)	λ_2 (-)	λ_3 (-)	D (-)	l_{ref} (m)	I (m^{-3})
–150 to 0	ENE	4.03483	–8.69230	–0.56934	–2.60	1	0.06202
	WNW	–4.87894	–10.95827	–0.33506	–2.50	1	0.12429
	NS	–7.71628	0.02693	–1.13945	–2.70	1	0.05726
	Sub–H	0.80137	0.76581	–11.94870	–2.70	1	0.12725
–400 to –150	ENE	4.03483	–8.69230	–0.56934	–2.85	1	0.04034
	WNW	–4.87894	–10.95827	–0.33506	–2.45	1	0.07450
	NS	–7.71628	0.02693	–1.13945	–2.85	1	0.05407
	Sub-H	0.80137	0.76581	–11.94870	–2.85	1	0.06094
–650 to –400	ENE	4.03483	–8.69230	–0.56934	–2.80	1	0.03514
	WNW	–4.87894	–10.95827	–0.33506	–2.50	1	0.09682
	NS	–7.71628	0.02693	–1.13945	–2.90	1	0.03732
	Sub-H	0.80137	0.76581	–11.94870	–2.90	1	0.04605
below –650	ENE	4.03483	–8.69230	–0.56934	–2.90	1	0.03653
	WNW	–4.87894	–10.95827	–0.33506	–2.80	1	0.06750
	NS	–7.71628	0.02693	–1.13945	–2.95	1	0.01831
	Sub-H	0.80137	0.76581	–11.94870	–2.95	1	0.02563

Table A-3. Transmissivity values used in Equation (4-20) for fracture domain HRD_C.

Elevation [m RHB 70]	Set	a_T (m^2/s)	b_T (-)	c_T (m^2/s)	d_T (-)
–150 to 0	ENE	$4.5068 \cdot 10^{-07}$	0.5	1	0.8
	WNW	$2.2485 \cdot 10^{-06}$	0.6	1	1.4
	NS	$2.2485 \cdot 10^{-06}$	0.6	1	1.0
	Sub-H	$2.524 \cdot 10^{-06}$	0.7	1	1.4
–400 to –150	ENE	$1.6827 \cdot 10^{-05}$	0.7	1	1.4
	WNW	$2.6824 \cdot 10^{-07}$	0.3	1	0.2
	NS	$1.6827 \cdot 10^{-06}$	0.7	1	1.4
	Sub-H	$3.7777 \cdot 10^{-06}$	0.8	1	1.8
–650 to –400	ENE	$5.6211 \cdot 10^{-08}$	0.6	1	0.8
	WNW	$5.6211 \cdot 10^{-07}$	0.6	1	0.8
	NS	$5.6211 \cdot 10^{-08}$	0.6	1	0.8
	Sub-H	$1.1242 \cdot 10^{-06}$	0.6	1	0.8
below –650	ENE	$3.7556 \cdot 10^{-06}$	0.5	1	1.0
	WNW	$2.2485 \cdot 10^{-07}$	0.6	1	0.8
	NS	$5.0185 \cdot 10^{-08}$	0.4	1	0.8
	Sub-H	$3.3727 \cdot 10^{-06}$	0.6	1	1.2

Table A-4. Parameters values used in SDM-Site for fracture domain HRD_W. (Modified after Table 10-12 in /Rhén et al. 2009/.)

Elevation [m RHB 70]	Fracture set name	Orientation set pole: (trend, plunge), conc. k [°,°, –]	Size model, power-law (k_r , r_0) [– , m]	Intensity, ($P_{32,open}$), valid size interval: (r_0, 564 m) [m^2/m^3]	Semi-correlated transmissivity model $log(T) = log(a\ r^b)+\sigma_{log(T)}\ N(0,1)$)
–150 to 0	ENE	(340.3,1.2), 15	(2.65, 0.038)	0.44	SC: ($5\cdot10^{-8}$, 0.7, 0.7)
	WNW	(208.9,2.2), 10.9	(2.5, 0.038)	0.61	SC: ($1\cdot10^{-7}$, 0.8, 0.6)
	NS	(272.8,12), 11.5	(2.65, 0.038)	0.54	SC: ($1.5\cdot10^{-7}$, 0.7, 0.7)
	Sub-H	(277.1,84.3), 11.1	(2.55, 0.038)	1.03	SC: ($1.5\cdot10^{-7}$, 0.7, 0.9)
–400 to –150	ENE	(340.3,1.2), 15	(2.65, 0.038)	0.28	SC: ($1\cdot10^{-7}$, 0.5, 0.2)
	WNW	(208.9,2.2), 10.9	(2.5, 0.038)	0.38	SC: ($3\cdot10^{-7}$, 0.5, 0.6)
	NS	(272.8,12), 11.5	(2.9, 0.038)	0.40	SC: ($1\cdot10^{-8}$, 0.5, 0.5)
	Sub-H	(277.1,84.3), 11.1	(2.7, 0.038)	0.50	SC: ($1\cdot10^{-7}$, 0.7, 1.0)
–650 to –400	ENE	(340.3,1.2), 15	(2.8, 0.038)	0.17	SC: ($3\cdot10^{-9}$, 0.6, 0.5)
	WNW	(208.9,2.2), 10.9	(2.55, 0.038)	0.33	SC: ($3\cdot10^{-8}$, 0.6, 0.5)
	NS	(272.8,12), 11.5	(2.55, 0.038)	0.30	SC: ($3\cdot10^{-8}$, 0.4, 0.4)
	Sub-H	(277.1,84.3), 11.1	(2.65, 0.038)	0.38	SC: ($5\cdot10^{-7}$, 0.4, 1.0)
below –650	ENE	(340.3,1.2), 15	(2.9, 0.038)	0.12	SC: ($5\cdot10^{-9}$, 0.6, 0.4)
	WNW	(208.9,2.2), 10.9	(2.8, 0.038)	0.09	SC: ($5\cdot10^{-8}$, 0.6, 0.4)
	NS	(272.8,12), 11.5	(2.95, 0.038)	0.14	SC: ($5\cdot10^{-9}$, 0.6, 0.4)
	Sub-H	(277.1,84.3), 11.1	(2.95, 0.038)	0.65	SC: ($1\cdot10^{-7}$, 0.6, 0.4)

Table A-5. DFN parameter values used in the present report for fracture domain HRD_W.

Elevation [m RHB 70]	Set	λ_1 (-)	λ_2 (-)	λ_3 (-)	D (-)	l_{ref} (m)	l (m^{-3})
–150 to 0	ENE	–5.05532	14.11896	–0.31414	–2.65	1	0.04962
	WNW	–5.26390	–9.53553	–0.41843	–2.50	1	0.07981
	NS	–11.23527	0.54950	–2.39098	–2.65	1	0.06090
	Sub-H	–1.09400	0.13626	–11.04512	–2.55	1	0.12912
–400 to –150	ENE	–5.05532	14.11896	–0.31414	–2.65	1	0.03158
	WNW	–5.26390	–9.53553	–0.41843	–2.50	1	0.04972
	NS	–11.23527	0.54950	–2.39098	–2.90	1	0.03176
	Sub-H	–1.09400	0.13626	–11.04512	–2.70	1	0.05302
–650 to –400	ENE	–5.05532	14.11896	–0.31414	–2.80	1	0.01572
	WNW	–5.26390	–9.53553	–0.41843	–2.55	1	0.04137
	NS	–11.23527	0.54950	–2.39098	–2.55	1	0.03761
	Sub-H	–1.09400	0.13626	–11.04512	–2.65	1	0.04285
below –650	ENE	–5.05532	14.11896	–0.31414	–2.90	1	0.00953
	WNW	–5.26390	–9.53553	–0.41843	–2.80	1	0.00832
	NS	–11.23527	0.54950	–2.39098	–2.95	1	0.01025
	Sub-H	–1.09400	0.13626	–11.04512	–2.95	1	0.04760

Table A-6. Transmissivity values used in Equation (4-20) for fracture domain HRD_W.

Elevation [m RHB 70]	Set	a_T (m^2/s)	b_T (-)	c_T (m^2/s)	d_T (-)
–150 to 0	ENE	$8.4133 \cdot 10^{-07}$	0.7	1	1.4
	WNW	$2.5185 \cdot 10^{-06}$	0.8	1	1.2
	NS	$2.524 \cdot 10^{-06}$	0.7	1	1.4
	Sub-H	$2.524 \cdot 10^{-06}$	0.7	1	1.8
–400 to –150	ENE	$7.5113 \cdot 10^{-07}$	0.5	1	0.4
	WNW	$2.2534 \cdot 10^{-06}$	0.5	1	1.2
	NS	$7.5113 \cdot 10^{-08}$	0.5	1	1.0
	Sub-H	$1.6827 \cdot 10^{-06}$	0.7	1	2.0
–650 to –400	ENE	$3.3727 \cdot 10^{-08}$	0.6	1	1.0
	WNW	$3.3727 \cdot 10^{-07}$	0.6	1	1.0
	NS	$1.5055 \cdot 10^{-07}$	0.4	1	0.8
	Sub-H	$2.5092 \cdot 10^{-06}$	0.4	1	2.0
below –650	ENE	$5.6211 \cdot 10^{-08}$	0.6	1	0.8
	WNW	$5.6211 \cdot 10^{-07}$	0.6	1	0.8
	NS	$5.6211 \cdot 10^{-08}$	0.6	1	0.8
	Sub-H	$1.1242 \cdot 10^{-06}$	0.6	1	0.8

Table A-7. Parameters values used in SDM-Site for fracture domain HRD_N. (Modified after Table 10-18 in /Rhén et al. 2009/.)

Elevation [m RHB 70]	Fracture set name	Orientation set pole: (trend, plunge), conc. κ [°,°, –]	Size model, power-law (k_r , r_0) [– , m]	Intensity, ($P_{32,open}$), valid size interval: (r_0, 564 m) [m^2/m^3]	Semi-correlated transmissivity model $log(T) = log(a\ r^b) + \sigma_{log(T)}\ N(0,1)$)
–150 to 0	ENE	(342.2,0.2), 15.8	(2.5, 0.038)	0.41	SC: ($1 \cdot 10^{-7}$, 0.6, 0.6)
	WNW	(209.8,1.6), 14.6	(2.3, 0.038)	0.92	SC: ($2 \cdot 10^{-7}$, 0.7, 0.8)
	NS	(271.3,3.8), 10.3	(2.5, 0.038)	0.46	SC: ($1 \cdot 10^{-7}$, 0.7, 1.0)
	Sub-H	(238.9,81.5), 12.7	(2.7, 0.038)	1.35	SC: ($2 \cdot 10^{-7}$, 0.7, 1.0)
–400 to –150	ENE	(342.2,0.2), 15.8	(2.8, 0.038)	0.41	SC: ($1 \cdot 10^{-7}$, 0.6, 0.8)
	WNW	(209.8,1.6), 14.6	(2.4, 0.038)	0.54	SC: ($2 \cdot 10^{-7}$, 0.6, 0.6)
	NS	(271.3,3.8), 10.3	(2.8, 0.038)	0.39	SC: ($1 \cdot 10^{-7}$, 0.4, 0.4)
	Sub-H	(238.9,81.5), 12.7	(2.75, 0.038)	1.28	SC: ($3 \cdot 10^{-7}$, 0.6, 0.6)
–650 to –400	ENE	(342.2,0.2), 15.8	(2.6, 0.038)	0.26	SC: ($1 \cdot 10^{-7}$, 0.5, 0.7)
	WNW	(209.8,1.6), 14.6	(2.4, 0.038)	0.36	SC: ($1 \cdot 10^{-7}$, 0.5, 0.5)
	NS	(271.3,3.8), 10.3	(2.6, 0.038)	0.25	SC: ($5 \cdot 10^{-8}$, 0.3, 0.3)
	Sub-H	(238.9,81.5), 12.7	(2.7, 0.038)	0.41	SC: ($5 \cdot 10^{-8}$, 0.4, 0.4)
below –650	ENE	(342.2,0.2), 15.8	(2.9, 0.038)	0.35	SC: ($5 \cdot 10^{-9}$, 0.6, 0.4)
	WNW	(209.8,1.6), 14.6	(2.8, 0.038)	0.45	SC: ($5 \cdot 10^{-8}$, 0.6, 0.4)
	NS	(271.3,3.8), 10.3	(2.95, 0.038)	0.08	SC: ($5 \cdot 10^{-9}$, 0.6, 0.4)
	Sub-H	(238.9,81.5), 12.7	(2.95, 0.038)	0.07	SC: ($1 \cdot 10^{-7}$, 0.6, 0.4)

Table A-8. DFN parameter values used in the present report for fracture domain HRD_N.

Elevation [m RHB 70]	Set	λ1 (-)	λ2 (-)	λ3 (-)	D (-)	lref (m)	l (m-3)
–150 to 0	ENE	–4.82996	15.04355	–0.05515	–2.50	1	0.05364
	WNW	–7.25299	–12.66444	–0.40766	–2.30	1	0.13016
	NS	–10.27471	0.23317	–0.68262	–2.50	1	0.06018
	Sub-H	–1.60737	–0.96963	–12.56050	–2.70	1	0.14315
–400 to –150	ENE	–4.82996	15.04355	–0.05515	–2.80	1	0.03791
	WNW	–7.25299	–12.66444	–0.40766	–2.40	1	0.07503
	NS	–10.27471	0.23317	–0.68262	–2.80	1	0.03606
	Sub-H	–1.60737	–0.96963	–12.56050	–2.75	1	0.12702
–650 to –400	ENE	–4.82996	15.04355	–0.05515	–2.60	1	0.03101
	WNW	–7.25299	–12.66444	–0.40766	–2.40	1	0.05002
	NS	–10.27471	0.23317	–0.68262	–2.60	1	0.02982
	Sub-H	–1.60737	–0.96963	–12.56050	–2.70	1	0.04348
below –650	ENE	–4.82996	15.04355	–0.05515	–2.90	1	0.02779
	WNW	–7.25299	–12.66444	–0.40766	–2.80	1	0.04161
	NS	–10.27471	0.23317	–0.68262	–2.95	1	0.00586
	Sub-H	–1.60737	–0.96963	–12.56050	–2.95	1	0.00513

Table A-9. Transmissivity values used in Equation (4-20) for fracture domain HRD_N.

Elevation [m RHB 70]	Set	a_T (m^2/s)	b_T (-)	c_T (m^2/s)	d_T (-)
–150 to 0	ENE	$1.1242 \cdot 10^{-06}$	0.6	1	1.2
	WNW	$3.3653 \cdot 10^{-06}$	0.7	1	1.6
	NS	$1.6827 \cdot 10^{-06}$	0.7	1	2.0
	Sub-H	$3.3653 \cdot 10^{-06}$	0.7	1	2.0
–400 to –150	ENE	$1.1242 \cdot 10^{-06}$	0.6	1	1.6
	WNW	$2.2485 \cdot 10^{-06}$	0.6	1	1.2
	NS	$5.0185 \cdot 10^{-07}$	0.4	1	0.8
	Sub-H	$3.3727 \cdot 10^{-06}$	0.6	1	1.2
–650 to –400	ENE	$7.5113 \cdot 10^{-07}$	0.5	1	1.4
	WNW	$7.5113 \cdot 10^{-07}$	0.5	1	1.0
	NS	$1.6765 \cdot 10^{-07}$	0.3	1	0.6
	Sub-H	$2.5092 \cdot 10^{-07}$	0.4	1	0.8
below –650	ENE	$5.6211 \cdot 10^{-08}$	0.6	1	0.8
	WNW	$5.6211 \cdot 10^{-07}$	0.6	1	0.8
	NS	$5.6211 \cdot 10^{-08}$	0.6	1	0.8
	Sub-H	$1.1242 \cdot 10^{-06}$	0.6	1	0.8

Table A-10. Parameters values used in SDM-Site for fracture domain HRD_EW007. (Modified after Table 10-15 in /Rhén et al. 2009/.)

Elevation	Fracture set name	Orientation set pole: (trend, plunge), conc. κ	Size model, power-law (k_r , r_0)	Intensity, ($P_{32,open}$), valid size interval: (r_0, 564 m)	Semi-correlated transmissivity model $log(T) = log(a\ r^b)+\sigma_{log(T)}\ N(0,1)$)
[m RHB 70]		[°,°, –]	[– , m]	[m²/m³]	
–150 to 0	ENE	(162.8,1.4), 10.7	(2.70, 0.038)	0.55	SC: ($1\cdot10^{-7}$, 0.4, 0.4)
	WNW	(25.3,0.2), 16.4	(2.3, 0.038)	1.01	SC: ($1\cdot10^{-7}$, 0.4, 0.4)
	NS	(88.9,3.9), 8.8	(2.65, 0.038)	0.33	SC: ($1\cdot10^{-6}$, 0.4, 0.4)
	Sub-H	(138.7,81.3), 9.7	(2.75, 0.038)	1.72	SC: ($3\cdot10^{-7}$, 0.5, 0.5)
–400 to –150	ENE	(162.8,1.4), 10.7	(2.8, 0.038)	0.60	SC: ($6\cdot10^{-8}$, 0.6, 0.6)
	WNW	(25.3,0.2), 16.4	(2.35, 0.038)	1.15	SC: ($2\cdot10^{-8}$, 0.6, 0.6)
	NS	(88.9,3.9), 8.8	(2.6, 0.038)	0.54	SC: ($1.5\cdot10^{-7}$,0.7,0.7)
	Sub-H	(138.7,81.3), 9.7	(2.8, 0.038)	0.82	SC: ($8\cdot10^{-8}$, 0.7, 0.9)
–650 to –400	ENE	(162.8,1.4), 10.7	(2.95, 0.038)	0.69	SC: ($3\cdot10^{-8}$, 0.4, 0.4)
	WNW	(25.3,0.2), 16.4	(2.50, 0.038)	1.43	SC: ($1\cdot10^{-7}$, 0.3, 0.3)
	NS	(88.9,3.9), 8.8	(2.95, 0.038)	0.64	SC: ($3\cdot10^{-7}$, 0.4, 0.4)
	Sub-H	(138.7,81.3), 9.7	(2.95, 0.038)	0.92	SC: ($3\cdot10^{-8}$, 0.6, 0.4)
below –650	ENE	(162.8,1.4), 10.7	(2.9, 0.038)	0.33	SC: ($5\cdot10^{-9}$, 0.6, 0.4)
	WNW	(25.3,0.2), 16.4	(2.8, 0.038)	0.89	SC: ($5\cdot10^{-8}$, 0.6, 0.4)
	NS	(88.9,3.9), 8.8	(2.95, 0.038)	0.21	SC: ($5\cdot10^{-9}$, 0.6, 0.4)
	Sub-H	(138.7,81.3), 9.7	(2.95, 0.038)	0.80	SC: ($1\cdot10^{-7}$, 0.6, 0.4)

Table A-11. DFN parameter values used in the present report for fracture domain HRD_EW007.

Elevation [m RHB 70]	Set	λ1 (-)	λ2 (-)	λ3 (-)	D (-)	lref (m)	l (m-3)
–150 to 0	ENE	3.16313	–10.21843	–0.26142	–2.70	1	0.05832
	WNW	7.00863	14.82686	–0.05725	–2.30	1	0.14289
	NS	8.77800	0.16855	–0.59853	–2.65	1	0.03721
	Sub-H	0.96837	–1.10228	–9.58839	–2.75	1	0.17068
–400 to –150	ENE	3.16313	–10.21843	–0.26142	–2.80	1	0.05548
	WNW	7.00863	14.82686	–0.05725	–2.35	1	0.16219
	NS	8.77800	0.16855	–0.59853	–2.60	1	0.06441
	Sub-H	0.96837	–1.10228	–9.58839	–2.80	1	0.07582
–650 to –400	ENE	3.16313	–10.21843	–0.26142	–2.95	1	0.05053
	WNW	7.00863	14.82686	–0.05725	–2.50	1	0.18710
	NS	8.77800	0.16855	–0.59853	–2.95	1	0.04687
	Sub-H	0.96837	–1.10228	–9.58839	–2.95	1	0.06738
below –650	ENE	3.16313	–10.21843	–0.26142	–2.90	1	0.02620
	WNW	7.00863	14.82686	–0.05725	–2.80	1	0.08229
	NS	8.77800	0.16855	–0.59853	–2.95	1	0.01538
	Sub-H	0.96837	–1.10228	–9.58839	–2.95	1	0.05859

Table A-12. Transmissivity values used in Equation (4-20) for fracture domain HRD_EW007.

Elevation [m RHB 70]	Set	a_T (m^2/s)	b_T (-)	c_T (m^2/s)	d_T (-)
–150 to 0	ENE	$5.0185 \cdot 10^{-07}$	0.4	1	0.8
	WNW	$5.0185 \cdot 10^{-07}$	0.4	1	0.8
	NS	$5.0185 \cdot 10^{-06}$	0.4	1	0.8
	Sub-H	$2.2534 \cdot 10^{-06}$	0.5	1	1.0
–400 to –150	ENE	$6.7454 \cdot 10^{-07}$	0.6	1	1.2
	WNW	$2.2485 \cdot 10^{-07}$	0.6	1	1.2
	NS	$2.524 \cdot 10^{-06}$	0.7	1	1.4
	Sub-H	$1.3461 \cdot 10^{-06}$	0.7	1	1.8
–650 to –400	ENE	$1.5055 \cdot 10^{-07}$	0.4	1	0.8
	WNW	$3.353 \cdot 10^{-07}$	0.3	1	0.6
	NS	$1.5055 \cdot 10^{-06}$	0.4	1	0.8
	Sub-H	$3.3727 \cdot 10^{-07}$	0.6	1	0.8
below –650	ENE	$5.6211 \cdot 10^{-08}$	0.6	1	0.8
	WNW	$5.6211 \cdot 10^{-07}$	0.6	1	0.8
	NS	$5.6211 \cdot 10^{-08}$	0.6	1	0.8
	Sub-H	$1.1242 \cdot 10^{-06}$	0.6	1	0.8

For all regions of the domain assessed, approximate homogeneous CPM properties of the flow-wetted fracture surface area per unit volume of rock mass (a_r) are based on the data provided by /Joyce et al. 2010 /, see Table A-13.

Table A-13. Specific flow-wetted fracture surface area per unit volume of rock applied for the fracture domains inside the focused area/volume.

Elevation [m RHB 70]	HRD_C a_r [m^2/m^3]	HRD_W a_r [m^2/m^3]	HRD_N a_r [m^2/m^3]	HRD_EW007 a_r [m^2/m^3]
> –150	1.00	1.00	1.50	1.50
–150 to -400	0.40	0.40	0.67	1.00
–400 to –650	0.22	0.12	0.33	0.40
<–650	0.02	0.02	0.16	0.04

For the region outside the detailed described HRDs, i.e. on a regional scale, the ECPM settings of hydraulic conductivity and kinematic porosity of the SDM-Site regional flow domain are established from a deterministic fracture set containing fracture geometry and fracture transmissivity (cf. Appendix B).

For the region outside the SDM-Site regional flow domain homogeneous CPM properties are assigned. These properties are based on the calculated median (cf. Figure A-3) of the overall deterministic fracture set regardless of underlying fracture domains.

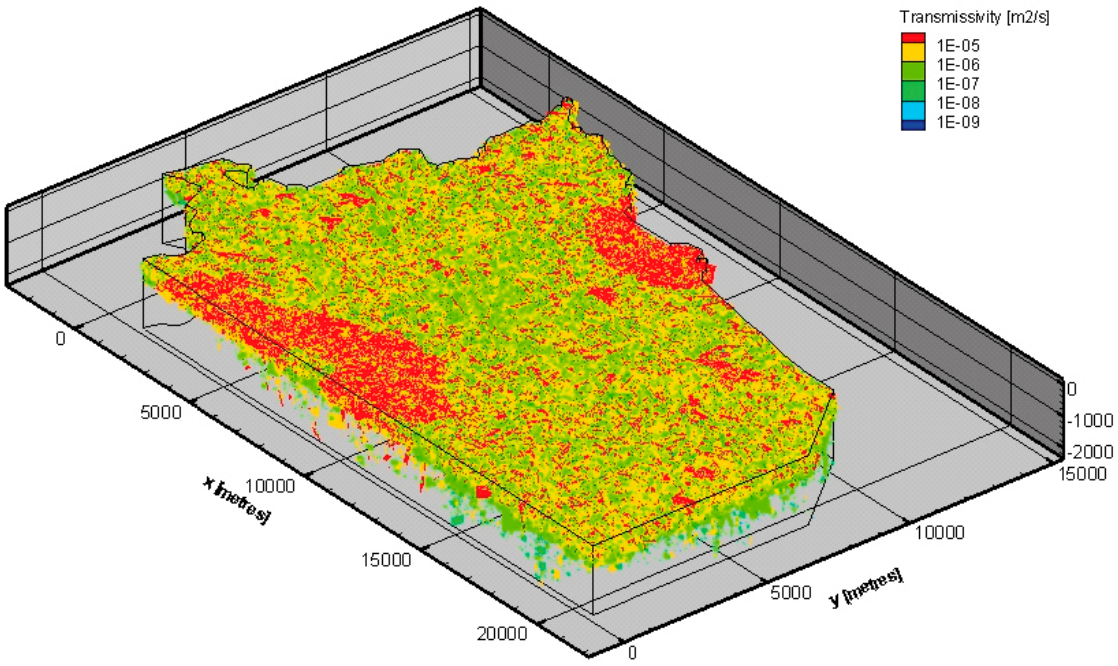

Figure A-2. *Specified deterministic fracture set used for parameterisation within the SDM-Site regional flow domain.*

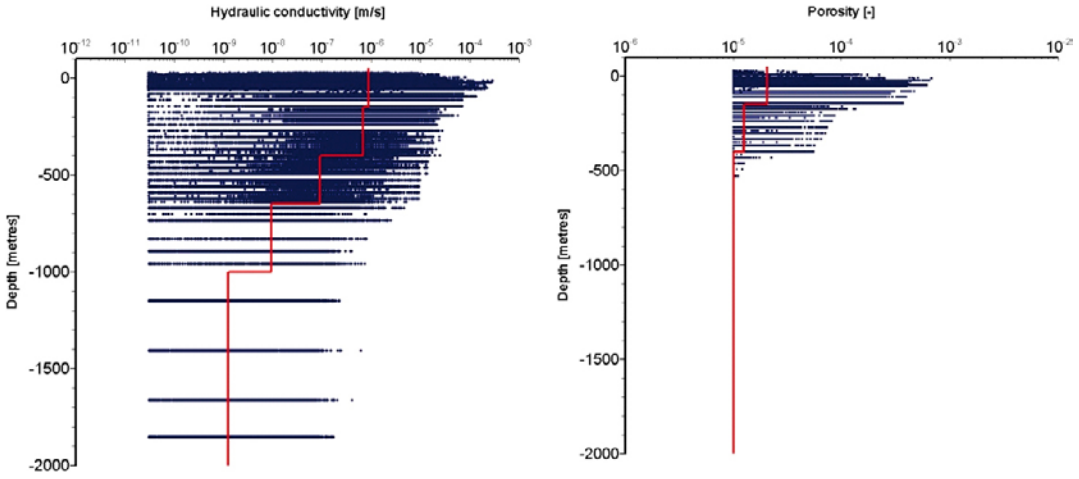

Figure A-3. *Left: Hydraulic conductivity values from all numerical cells within the SDM-Site regional flow domain. Red line represents median value within relevant depth intervals. Right: Porosity values from numerical cells within the SDM regional flow domain. Red line represents median value within relevant depth intervals.*

Table A-14. Homogeneous continuous porous media (CPM) properties applied in hydraulic rock domains outside the SDM-Site regional flow domain.

	CPM properties outside the SDM-Site regional flow domain		
Elevation [m RHB 70]	**K [m/s]**	**ϕ [-]**	**a_r [m²/m³]**
> –150	$8.9 \cdot 10^{-7}$	$2.1 \cdot 10^{-5}$	1.50
–150 to –400	$6.9 \cdot 10^{-7}$	$1.3 \cdot 10^{-5}$	0.67
–400 to –650	$9.3 \cdot 10^{-8}$	$1.0 \cdot 10^{-5}$	0.33
< –650	$9.6 \cdot 10^{-9}$	$1.0 \cdot 10^{-5}$	0.16

The general approach in DarcyTools is to specify the fracture thickness b_f [L] and the fracture kinematic porosity ϕ_f [-] of the stochastically generated fractures by fracture set and by fracture size interval. Hence, in DarcyTools there is no direct relationship between transmissivity and transport aperture similar to Equation (4-18), but the fracture transport aperture is obtained from the thickness-porosity product, i.e.

$$e_f = b_f \phi_f \tag{A-9}$$

In the work reported here all stochastically generated fractures have the same values of the fracture thickness and the fracture kinematic porosity. The values used are presented in Table A-12 together with some other fracture specifications.

Table A-15. Additional specifications used in DarcyTools.

Specification	Value	Minimum value
Generated fracture size interval	15-1,000 [m][1]	
Fracture thickness	0.1 [m]	
Fracture kinematic porosity	$1 \cdot 10^{-3}$ [-]	
Diffusion coefficient in free water	$1 \cdot 10^{-10}$ [m^2/s]	
Minimum grid cell hydraulic conductivity[2]		$3 \cdot 10^{-11}$ [m/s] (~ $4 \cdot 10^{-18}$ [m^2])
Grid cell hydraulic conductivity below –2,100m		$5 \cdot 10^{-10}$ [m/s] (~ $6.7 \cdot 10^{-17}$ [m^2])
Grid cell hydraulic conductivity below –2,300 m		$5 \cdot 10^{-11}$ [m/s] (~ $6.7 \cdot 10^{-18}$ [m^2])
Minimum grid cell kinematic porosity[3]		$1 \cdot 10^{-5}$ [-]

[1] This data range refers to square-shaped fractures. The interval for disc-shaped fractures is 8.5-564 m.
[2] Used for cells without fractures.

Table A-16. Parameter values used for fracture domain HRD_C in case (c). (based on data from /Joyce et al. 2010/).

Elevation [m RHB 70]	Fracture set name	Orientation set pole: (trend, plunge), conc. κ [°,°, –]	Size model, power-law (k_r , r_0) [–, m]	Intensity, ($P_{32,open}$), valid size interval: (r_0, 564 m) [m^2/m^3]	Semi-correlated transmissivity model $log(T) = log(a\ r^b) + \sigma_{log(T)}\ N(0,1)$)
–150 to 0	ENE	(155.1,3.4), 9.6	(2.70, 0.038)	0.52	SC: (2 10^{-7}, 0.7, 0.4)
	WNW	(204,1.6), 12	(2.49, 0.038)	0.95	SC: (2 10^{-7}, 0.9, 0.6)
	NS	(270.2,8.4), 7.8	(2.80, 0.038)	0.54	SC: (8 10^{-8}, 0.5, 0.4)
	Sub-H	(46.3,84.7), 12	(2.59, 0.038)	1.20	SC: (6 10^{-8}, 0.7, 0.5)
–400 to –150	ENE	(155.1,3.4), 9.6	(3.00, 0.038)	0.47	SC: (6 10^{-7}, 0.7, 0.9)
	WNW	(204,1.6), 12	(2.44, 0.038)	0.55	SC: (1 10^{-8}, 0.5, 0.7)
	NS	(270.2,8.4), 7.8	(2.91, 0.038)	0.63	SC: (1 10^{-8}, 0.7, 0.2)
	Sub-H	(46.3,84.7), 12	(2.87, 0.038)	0.71	SC: (3.5 10^{-8}, 1.2, 0.9)
–650 to –400	ENE	(155.1,3.4), 9.6	(2.87, 0.038)	0.38	SC: (8 10^{-8}, 0.8, 0.6)
	WNW	(204,1.6), 12	(2.54, 0.038)	0.74	SC: (3 10^{-9}, 0.8, 0.6)
	NS	(270.2,8.4), 7.8	(2.87, 0.038)	0.47	SC: (6 10^{-9}, 0.4, 0.4)
	Sub-H	(46.3,84.7), 12	(3.00, 0.038)	0.58	SC: (2 10^{-7}, 0.8, 0.7)
below –650	ENE	(155.1,3.4), 9.6	(2.96, 0.038)	0.46	SC: (1 10^{-8}, 0.7, 0.4)
	WNW	(204,1.6), 12	(3.00, 0.038)	0.73	SC: (3 10^{-7}, 0.7, 0.4)
	NS	(270.2,8.4), 7.8	(3.00, 0.038)	0.25	SC: (1 10^{-8}, 0.7, 0.4)
	Sub-H	(46.3,84.7), 12	(2.97, 0.038)	0.35	SC: (1 10^{-7}, 0.7, 0.4)

Table A-17. DFN parameter values used in the present report for fracture domain HRD_C in case (c).

Elevation [m RHB 70]	Set	λ_1 (-)	λ_2 (-)	λ_3 (-)	D (-)	l_{ref} (m)	l (m^{-3})
–150 to 0	ENE	4.03483	–8.69230	–0.56934	–2.70	1	0.05514
	WNW	–4.87894	–10.95827	–0.33506	–2.49	1	0.12524
	NS	–7.71628	0.02693	–1.13945	–2.80	1	0.04993
	Sub-H	0.80137	0.76581	–11.94870	–2.59	1	0.14463
–400 to –150	ENE	4.03483	–8.69230	–0.56934	–3.00	1	0.03166
	WNW	–4.87894	–10.95827	–0.33506	–2.44	1	0.07493
	NS	–7.71628	0.02693	–1.13945	–2.91	1	0.04923
	Sub-H	0.80137	0.76581	–11.94870	–2.87	1	0.05910
–650 to –400	ENE	4.03483	–8.69230	–0.56934	–2.87	1	0.03163
	WNW	–4.87894	–10.95827	–0.33506	–2.54	1	0.09362
	NS	–7.71628	0.02693	–1.13945	–2.87	1	0.03912
	Sub-H	0.80137	0.76581	–11.94870	–3.00	1	0.03907
below –650	ENE	4.03483	–8.69230	–0.56934	–2.96	1	0.03314
	WNW	–4.87894	–10.95827	–0.33506	–3.00	1	0.04917
	NS	–7.71628	0.02693	–1.13945	–3.00	1	0.01684
	Sub–H	0.80137	0.76581	–11.94870	–2.97	1	0.02480

Table A-18. Transmissivity values used in Equation (4-20) for fracture domains HRD_C in case (c).

Elevation [m RHB 70]	Set	a_T (m^2/s)	b_T (-)	c_T (m^2/s)	d_T (-)
–150 to 0	ENE	$3.3653 \cdot 10^{-6}$	0.7	1	0.8
	WNW	$7.539 \cdot 10^{-6}$	0.9	1	1.2
	NS	$6.009 \cdot 10^{-7}$	0.5	1	0.8
	Sub-H	$1.0096 \cdot 10^{-6}$	0.7	1	1.0
–400 to –150	ENE	$1.0096 \cdot 10^{-5}$	0.7	1	1.8
	WNW	$7.5113 \cdot 10^{-8}$	0.5	1	1.4
	NS	$1.6827 \cdot 10^{-7}$	0.7	1	0.4
	Sub-H	$4.4236 \cdot 10^{-6}$	1.2	1	1.8
–650 to –400	ENE	$2.0148 \cdot 10^{-6}$	0.8	1	1.2
	WNW	$7.5555 \cdot 10^{-8}$	0.8	1	1.2
	NS	$3.0111 \cdot 10^{-8}$	0.4	1	0.8
	Sub-H	$5.037 \cdot 10^{-6}$	0.8	1	1.4
below –650	ENE	$1.6827 \cdot 10^{-7}$	0.7	1	0.8
	WNW	$5.048 \cdot 10^{-6}$	0.7	1	0.8
	NS	$1.6827 \cdot 10^{-7}$	0.7	1	0.8
	Sub-H	$1.6827 \cdot 10^{-6}$	0.7	1	0.8

Table A-19. Parameters values used for fracture domain HRD_W in case (c). (based on data from /Joyce et al. 2010/).

Elevation [m RHB 70]	Fracture set name	Orientation set pole: (trend, plunge), conc. κ [°,°, –]	Size model, power-law (k_r , r_0) [–, m]	Intensity, ($P_{32,open}$), valid size interval: (r_0, 564 m) [m^2/m^3]	Semi-correlated transmissivity model $log(T) = log(a\ r^b)+\sigma_{log(T)}\ N(0,1)$)
–150 to 0	ENE	(340.3,1.2), 15	(2.59, 0.038)	0.44	SC: (2.1 10^{-8}, 0.7, 0.6)
	WNW	(208.9,2.2), 10.9	(2.54, 0.038)	0.61	SC: (7 10^{-8}, 0.8, 1.0)
	NS	(272.8,12), 11.5	(2.52, 0.038)	0.54	SC: (4 10^{-8}, 0.7, 0.8)
	Sub-H	(277.1,84.3), 11.1	(2.50, 0.038)	1.03	SC: (8 10^{-8}, 0.7, 0.7)
–400 to –150	ENE	(340.3,1.2), 15	(2.54, 0.038)	0.28	SC: (2.2 10^{-9}, 0.5, 0.4)
	WNW	(208.9,2.2), 10.9	(2.65, 0.038)	0.38	SC: (1.5 10^{-8}, 0.5, 1.2)
	NS	(272.8,12), 11.5	(3.00, 0.038)	0.40	SC: (5 10^{-9}, 0.4, 0.3)
	Sub-H	(277.1,84.3), 11.1	(2.72, 0.038)	0.50	SC: (1.2 10^{-7}, 0.7, 1.2)
–650 to –400	ENE	(340.3,1.2), 15	(3.00, 0.038)	0.17	SC: (3 10^{-9}, 0.6, 0.4)
	WNW	(208.9,2.2), 10.9	(2.61, 0.038)	0.33	SC: (1.5 10^{-8}, 0.5, 0.3)
	NS	(272.8,12), 11.5	(2.53, 0.038)	0.30	SC: (5 10^{-8}, 0.2, 0.2)
	Sub-H	(277.1,84.3), 11.1	(2.72, 0.038)	0.38	SC: (2 10^{-7}, 0.8, 0.8)
below –650	ENE	(155.1,3.4), 9.6	(3.00, 0.038)	0.12	SC: (1 10^{-8}, 0.7, 0.4)
	WNW	(208.9,2.2), 10.9	(3.00, 0.038)	0.09	SC: (3 10^{-8}, 0.7, 0.4)
	NS	(272.8,12), 11.5	(2.53, 0.038)	0.14	SC: (1 10^{-8}, 0.7, 0.4)
	Sub-H	(277.1,84.3), 11.1	(3.00, 0.038)	0.65	SC: (3 10^{-8}, 0.7, 0.4)

Table A-20. DFN parameter values used in the present report for fracture domain HRD_W in case (c).

Elevation [m RHB 70]	Set	λ_1 (-)	λ_2 (-)	λ_3 (-)	D (-)	l_{ref} (m)	l (m^{-3})
–150 to 0	ENE	–5.05532	14.11896	–0.31414	–2.59	1	0.05303
	WNW	–5.26390	–9.53553	–0.41843	–2.54	1	0.07717
	NS	–11.23527	0.54950	–2.39098	–2.52	1	0.06952
	Sub-H	–1.09400	0.13626	–11.04512	–2.50	1	0.13476
–400 to –150	ENE	–5.05532	14.11896	–0.31414	–2.54	1	0.03542
	WNW	–5.26390	–9.53553	–0.41843	–2.65	1	0.04285
	NS	–11.23527	0.54950	–2.39098	–3.00	1	0.02694
	Sub-H	–1.09400	0.13626	–11.04512	–2.72	1	0.05166
–650 to –400	ENE	–5.05532	14.11896	–0.31414	–3.00	1	0.01145
	WNW	–5.26390	–9.53553	–0.41843	–2.61	1	0.03894
	NS	–11.23527	0.54950	–2.39098	–2.53	1	0.03829
	Sub-H	–1.09400	0.13626	–11.04512	–2.72	1	0.03926
below –650	ENE	–5.05532	14.11896	–0.31414	–3.00	1	0.00808
	WNW	–5.26390	–9.53553	–0.41843	–3.00	1	0.00606
	NS	–11.23527	0.54950	–2.39098	–2.53	1	0.01787
	Sub-H	–1.09400	0.13626	–11.04512	–3.00	1	0.04378

Table A-21. Transmissivity values used in Equation (4-20) for fracture domain HRD_W in case (c).

Elevation [m RHB 70]	Set	a_T (m^2/s)	b_T (-)	c_T (m^2/s)	d_T (-)
–150 to 0	ENE	$3.5336 \cdot 10^{-7}$	0.7	1	1.2
	WNW	$1.7629 \cdot 10^{-6}$	0.8	1	2.0
	NS	$6.7307 \cdot 10^{-7}$	0.7	1	1.6
	Sub-H	$1.3461 \cdot 10^{-6}$	0.7	1	1.4
–400 to –150	ENE	$1.6525 \cdot 10^{-8}$	0.5	1	0.8
	WNW	$1.1267 \cdot 10^{-7}$	0.5	1	2.4
	NS	$2.5092 \cdot 10^{-8}$	0.4	1	0.6
	Sub-H	$2.0192 \cdot 10^{-6}$	0.7	1	2.4
–650 to –400	ENE	$3.3727 \cdot 10^{-8}$	0.6	1	0.8
	WNW	$1.1267 \cdot 10^{-7}$	0.5	1	0.6
	NS	$1.1201 \cdot 10^{-7}$	0.2	1	0.4
	Sub-H	$5.037 \cdot 10^{-6}$	0.8	1	1.6
below –650	ENE	$1.6827 \cdot 10^{-7}$	0.7	1	0.8
	WNW	$5.048 \cdot 10^{-7}$	0.7	1	0.8
	NS	$1.6827 \cdot 10^{-7}$	0.7	1	0.8
	Sub-H	$5.048 \cdot 10^{-7}$	0.7	1	0.8

Table A-22. Parameters values used for fracture domain HRD_EW007 in case (c). (based on data from /Joyce et al. 2010/).

Elevation [m RHB 70]	Fracture set name	Orientation set pole: (trend, plunge), conc. κ [°, °, –]	Size model, power-law (k_r , r_0) [–, m]	Intensity, ($P_{32,open}$), valid size interval: (r_0, 564 m) [m^2/m^3]	Semi-correlated transmissivity model $log(T) = log(a\ r^b) + \sigma_{log(T)}\ N(0,1)$)
–150 to 0	ENE	(162.8,1.4), 10.7	(2.77, 0.038)	0.55	SC: (3 10^{-8}, 0.6, 0.4)
	WNW	(25.3,0.2), 16.4	(2.30, 0.050)	1.01	SC: (3 10^{-8}, 0.6, 0.3)
	NS	(88.9,3.9), 8.8	(2.53, 0.038)	0.33	SC: (1 10^{-7}, 0.8, 0.3)
	Sub-H	(138.7,81.3), 9.7	(2.76, 0.038)	1.72	SC: (2.3 10^{-7},0.8,0.5)
–400 to –150	ENE	(162.8,1.4), 10.7	(2.83, 0.038)	0.60	SC: (2 10^{-7}, 0.6, 0.6)
	WNW	(25.3,0.2), 16.4	(2.41, 0.038)	1.15	SC: (3 10^{-8}, 0.6, 0.4)
	NS	(88.9,3.9), 8.8	(2.60, 0.038)	0.54	SC: (3 10^{-7},0.8, 0.4)
	Sub-H	(138.7,81.3), 9.7	(2.84, 0.038)	0.82	SC: (5 10^{-8}, 0.8, 0.4)
–650 to –400	ENE	(162.8,1.4), 10.7	(2.93, 0.038)	0.69	SC: (1 10^{-8}, 0.5, 0.2)
	WNW	(25.3,0.2), 16.4	(2.62, 0.038)	1.43	SC: (1.2 10^{-7}, 0.3, 0.2)
	NS	(88.9,3.9), 8.8	(3.00, 0.038)	0.64	SC: (8 10^{-8}, 0.4, 0.2)
	Sub-H	(138.7,81.3), 9.7	(2.99, 0.038)	0.92	SC: (1.5 10^{-7}, 0.7, 0.3)
below –650	ENE	(162.8,1.4), 10.7	(2.96, 0.038)	0.33	SC: (1 10^{-8}, 0.7, 0.4)
	WNW	(25.3,0.2), 16.4	(3.00, 0.038)	0.89	SC: (3 10^{-7}, 0.7, 0.4)
	NS	(88.9,3.9), 8.8	(3.00, 0.038)	0.21	SC: (1 10^{-8}, 0.7, 0.4)
	Sub-H	(138.7,81.3), 9.7	(2.97, 0.038)	0.80	SC: (1 10^{-7}, 0.7, 0.4)

Table A-23. DFN parameter values used in the present report for fracture domain HRD_EW007 in case (c).

Elevation [m RHB 70]	Set	λ_1 (-)	λ_2 (-)	λ_3 (-)	D (-)	l_{ref} (m)	I (m^{-3})
–150 to 0	ENE	3.16313	–10.21843	–0.26142	–2.77	1	0.05308
	WNW	7.00863	14.82686	–0.05725	–2.30	1	0.15595
	NS	8.77800	0.16855	–0.59853	–2.53	1	0.04212
	Sub-H	0.96837	–1.10228	–9.58839	–2.76	1	0.16834
–400 to –150	ENE	3.16313	–10.21843	–0.26142	–2.83	1	0.05308
	WNW	7.00863	14.82686	–0.05725	–2.41	1	0.15909
	NS	8.77800	0.16855	–0.59853	–2.60	1	0.06441
	Sub-H	0.96837	–1.10228	–9.58839	–2.84	1	0.07146
–650 to –400	ENE	3.16313	–10.21843	–0.26142	–2.93	1	0.05221
	WNW	7.00863	14.82686	–0.05725	–2.62	1	0.16689
	NS	8.77800	0.16855	–0.59853	–3.00	1	0.04311
	Sub-H	0.96837	–1.10228	–9.58839	–2.99	1	0.06303
below –650	ENE	3.16313	–10.21843	–0.26142	–2.96	1	0.02377
	WNW	7.00863	14.82686	–0.05725	–3.00	1	0.05995
	NS	8.77800	0.16855	–0.59853	–3.00	1	0.01415
	Sub-H	0.96837	–1.10228	–9.58839	–2.97	1	0.05668

Table A-24. Transmissivity values used in Equation (4-20) for fracture domain HRD_EW007 in case (c).

Elevation [m RHB 70]	Set	a_T (m^2/s)	b_T (-)	c_T (m^2/s)	d_T (-)
–150 to 0	ENE	$3.3727 \cdot 10^{-7}$	0.6	1	0.8
	WNW	$3.3727 \cdot 10^{-7}$	0.6	1	0.6
	NS	$2.5185 \cdot 10^{-6}$	0.8	1	0.6
	Sub-H	$5.7925 \cdot 10^{-6}$	0.8	1	1.0
–400 to –150	ENE	$2.2485 \cdot 10^{-6}$	0.6	1	1.2
	WNW	$3.3727 \cdot 10^{-7}$	0.6	1	0.8
	NS	$7.5555 \cdot 10^{-6}$	0.8	1	0.8
	Sub-H	1.2592·10–6	0.8	1	0.8
–650 to –400	ENE	$7.5113 \cdot 10^{-8}$	0.5	1	0.4
	WNW	$4.0235 \cdot 10^{-7}$	0.3	1	0.4
	NS	$4.0148 \cdot 10^{-7}$	0.4	1	0.4
	Sub-H	$2.524 \cdot 10^{-6}$	0.7	1	0.6
below –650	ENE	$1.6827 \cdot 10^{-7}$	0.7	1	0.8
	WNW	$5.048 \cdot 10^{-6}$	0.7	1	0.8
	NS	$1.6827 \cdot 10^{-7}$	0.7	1	0.8
	Sub-H	$1.6827 \cdot 10^{-6}$	0.7	1	0.8

Outside the detailed described HRDs, the ECPM hydraulic conductivity and kinematic porosity of the SDM-Site regional flow domain are established from a deterministic fracture set containing fracture geometry and fracture transmissivity (cf. Appendix B).

Appendix B

Compilation of input files

Name of file in DarcyTools	Date	Name of file at delivery
HCD		
HCD	2009-04-24	090423_ls_Reg_Loc_Disks_Dol_100_Cond_24_dt.zip
DET FRACTURES		
Det. Fracture set (case (a))	2009-04-07	090401_ls_mdl2_r1_sets1_64_asc.zip
Det. Fracture set (case (c))	2010-08-27	100826_ls_altdfn_r1_hrd_fractures_ascii.zip
HRD DOMAINS		
	2009-03-30	FD_LX_LOC_V23b-c_HydroVolume_2_stl.zip
DEM		
topxyz.dat	2009-03-26	Lm_50.txt
REPOSITORY LAYOUT		
(only used for visualisation)		
LX_191BD_00_8S03.stl	2009-05-03	LX_191BD_00_8S03.stl
LX_191BD_00_8S10.stl	2009-05-03	LX_191BD_00_8S10.stl
LX_191BD_00_8S15.stl	2009-05-03	LX_191BD_00_8S15.stl
LX_191BD_00_8S18.stl	2009-05-03	LX_191BD_00_8S18.stl
OTHER GEOMETRIES		
WD.dat (Water Divide)	2009-03-26	090313_Stl_filer_laxemar
PROPERTY FILE		
Case (a), (b) and (d)	2009-05-06	Laxemarproperty20090428.xlsx
Case (c)	2010-08-27	Laxemarproperty20090428_AHDFN.xlsx
ICE SHEET PROFILE		
	2009-07-03	y3a_row21_at_time_14.300BP_2.xls
DEPOSITION HOLE		
	2010-03-12	ls_Q1_2000_fpc.ptb
VELOCITIES		
Comparative result plots	2011-01-03	100820_ls_altdfn-nocalib_Q123_2000_pline_merged_ptb.zip

A list of all input files above, including storage location, is for traceability documented in the SKB data base SKBdoc under id nr 1271538.

Appendix C

Bedrock permeability and groundwater salinity

C.1 Introduction

It has been suggested that an understanding of the evolution of salinity throughout geological time is a powerful tool to predict the future development of groundwater flow and its chemical composition /NEA-OECD 1993, Bath and Lalieux 1999/. In this appendix, the data support for the applied initial and boundary conditions during periods with periglacial and glacial climate conditions is discussed, in particular the data support for assuming a fixed (undisturbed) groundwater salinity on the bottom boundary of the model domain during glaciation and deglaciation.

C.2 Invoked assumptions and their data support

C.2.1 Assumptions

The initial hydrochemical conditions used in the work reported are inferred from those used in SDM-Site, see Table 5-2; i.e. the increase in salinity with depth in the fracture water and in the matrix porewater is assumed to be in equilibrium at all depths at the start of the flow simulations. Second, during the pre-LGM, LGM and post-LGM stages, the initial fracture water salinity in the grid cells on the bottom boundary is fixed as specified in Table 5-3 and Table 5-4.

The assumption of a fixed fracture water salinity on the bottom boundary of the model domain is accompanied by an assumption a low hydraulic conductivity at depth. In the model, the grid cell hydraulic conductivity is set to $5 \cdot 10^{-10}$ m/s in all grid cells below –2,100 m elevation and to $5 \cdot 10^{-11}$ m/s in all grid cells below –2,300 m elevation, see Table A-15. Further, the minimum value of the grid cell kinematic porosity is set to $1 \cdot 10^{-5}$, implying a total fracture aperture of 1 mm/100 m of rock, see Appendix A and Table A-15.

C.2.2 Data support

The bedrock is investigated to approximately –1,600 m elevation, though most investigations are down to approximately –1,000 m at Laxemar, see Figure C-1. The measured fracture water salinity at –1,000 m elevation is approximately 2.5%. At repository depth, the fracture water salinity is approximately 1.0%.

The deepest borehole investigated by SKB is borehole KLX02 at Laxemar. The vertical depth of KLX02 is 1,660 m and the salinity at the bottom of KLX02 is approximately 8%, see Figure C-1.

Table C-1 shows the measured permeability values in fracture-free samples ranged from $7 \cdot 10^{-24}$ to $1 \cdot 10^{-19}$ m^2, corresponding to hydraulic conductivity values of $6 \cdot 10^{-17}$ to $1 \cdot 10^{-12}$ m/s, respectively. The presence of a fracture in one sample (LAX-5) increased the permeability to c. $1 \cdot 10^{-17}$ m^2.

Table C-1. Sample positions along the borehole and average matrix permeability and corresponding hydraulic conductivity for confining pressures greater than 14 MPa (Modified after /Vilks 2007/).

Sample	Core sample	Borehole length (m)	Permeability (m^2)	Conductivity (m/s)	Rock type
LAX-1*	KLX03–5	355.66	$(4\pm4)\cdot10^{-23}$	$(3\pm4)\cdot10^{-16}$	Ävrö granite
LAX-2	KLX03–8	524.63	$(8.6\pm0.9)\cdot10^{-22}$	$(7.5\pm0.8)\cdot10^{-15}$	Ävrö granite
LAX-3	KLX03–9	590.12	$(2.2\pm0.7)\cdot10^{-22}$	$(1.9\pm0.6)\cdot10^{-15}$	Ävrö granite
LAX-4	KLX03–9	590.12	$(4.1\pm1.1)\cdot10^{-21}$	$(3.6\pm0.9)\cdot10^{-14}$	Ävrö granite
LAX-5	KLX03–12	803.21	$1.45\cdot10^{-17}$	$1.27\cdot10^{-10}$	Quartz monzodiorite
LAX-6	KLX03–14	894.53	$(1.4\pm0.9)\cdot10^{-20}$	$(1.2\pm0.8)\cdot10^{-13}$	Quartz monzodiorite
LAX-7	KLX03–14	894.53	$(7.2\pm3.5)\cdot10^{-22}$	$(6.3\pm3.1)\cdot10^{-15}$	Quartz monzodiorite
LAX-8	KLX03–16	979.78	$(1.9\pm0.3)\cdot10^{-19}$	$(1.7\pm0.2)\cdot10^{-12}$	Quartz monzodiorite

* Average for confining pressures from 1.7 to 7.0 MPa.

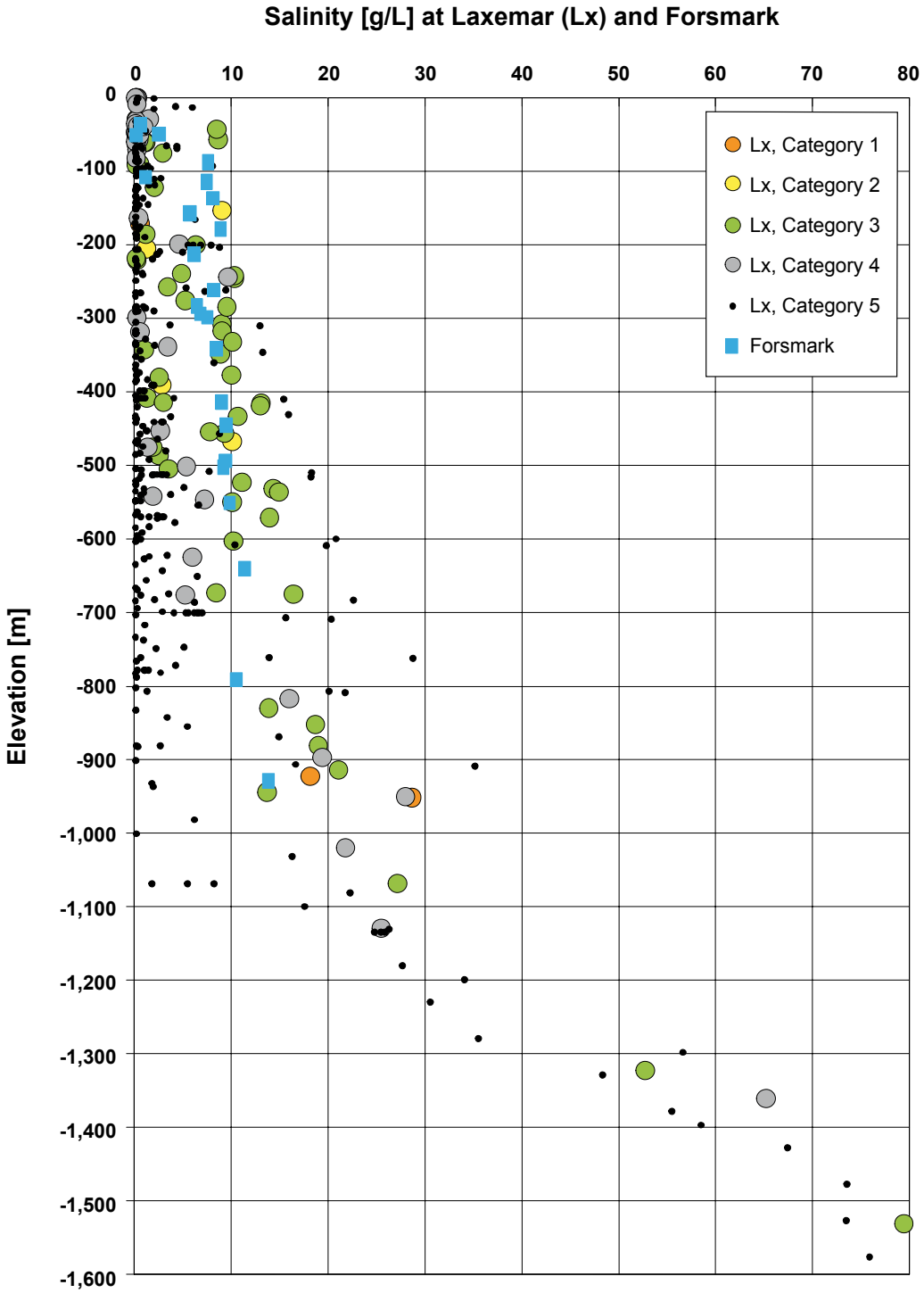

Figure C-1. *Plot of all available salinity data from the core-drilled boreholes and percussion-drilled boreholes in Laxemar sorted according to quality category and in seven boreholes at Forsmark. The data in Laxemar are classified into five categories with regard to the quality of the sampling and/or analysis method, where category 1 represent the best quality and category 5 is the poorest. The Forsmark data are all of good quality in this regard (category 3 or better). (Modified after Figure 5-15 in /Follin et al. 2008/ and Figure 5-18 in /Rhén et al. 2009/.)*

The low hydraulic conductivity observed in the laboratory samples is supported by the field data shown in Figure C-2 and Figure C-3. Figure C-2 shows a cumulative distribution plot of 631 $\log_{10}(K_{PSS})$ data measured with the Pipe String System (PSS) and a packer spacing (test scale) of 5 m[11] in the depth interval 0 to –1,000 m for rock between large deformation zones ("No-DZ"). The few data above –150 m is due to that injection tests were performed in the core-drilled part below the upper, large diameter part, of the borehole. Approximately 40% or more of the PSS data set below elevation –150 m have values below –9.9 (or $1.3 \cdot 10^{-10}$ m/s) which is the robust lower measurement limit of the PSS method /Rhén et al. 2008/. These low conductive 5 m sections represents rock with low conductive fractures or borehole sections with no conductive fractures and a large part of these low conductive sections are considered to be measurement limit values; the hydraulic conductivity values are as low or lower than the values indicated in the plot.

The fracture transmissivity data acquired with the Posiva Flow Log (PFL) shown in Figure 3-11 are repeated in Figure C-3. The data are from the focused area/volume. As can be seen in the figure, there are hardly any conductive fractures below c. –500 m elevation (the measurement limit if the PFL is c. $T=1 \cdot 10^{-9}$ m²/s). Other boreholes also indicate low frequencies of conductive fractures at depth, cf. /Rhén et al. 2008/. Figure C-4 illustrates the concepts for the by depth decreasing hydraulic conductivity and decreasing fracture frequency.

Table C-2 provides detailed statistic of Terzaghi corrected frequencies of flowing fractures (detected with the PFL method) in the Local area/volume and shows also the estimates of the fracture transmissivities, which in fact are the specific capacities of the flowing fractures. At repository depth (–400 to –650 m), the mean value of the Terzaghi corrected frequency of flowing fractures

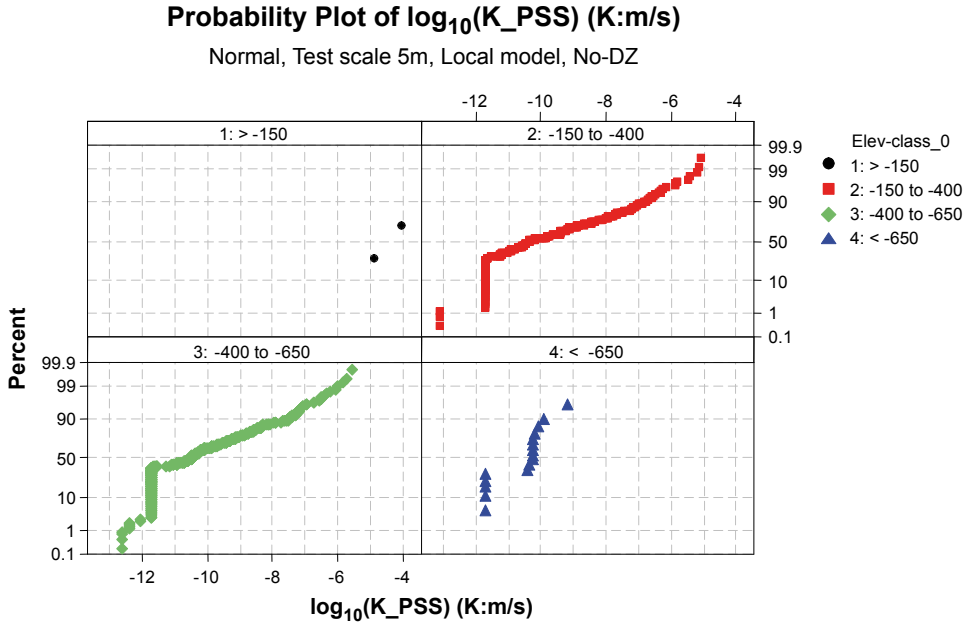

Figure C-2. *Cumulative distribution plot of 631 $\log_{10}$(K_PSS) data measured with a packer spacing (test scale) of 5 m between elevations 0 m to –1,000 m within the Local model volume in Laxemar, representing rock between deterministic deformation zones (Estimates of statistical distributions in /Rhén et al. 2008/)*

[11] A telescopic approach is used for the single-hole hydraulic testing with the PSS method at Laxemar. Each borehole is measured with consecutive 100-m long, 20-m long and 5-m long packer intervals beginning with the longest packer interval. However, non-flowing 100-m long packer intervals are not studied with 20-m long packer intervals, etc. The telescopic measurement approach saves time but it assumes that low transmissive sections are correctly characterized. To display a cumulative plot of all 5 m sections a uniform distribution of transmissivity (T) is assumed in each low-transmissive 100 m or 20 m section and the corresponding unmeasured 5 m sections respectively, are a assigned a hydraulic conductivity (K) based on the measured larger measurement scales .

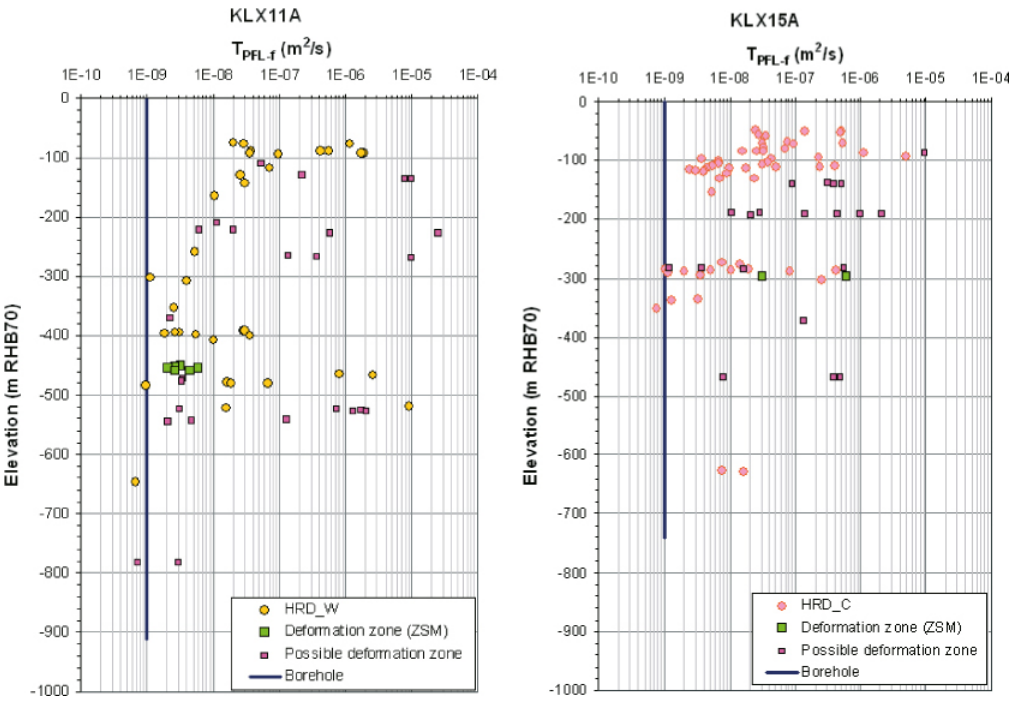

Figure C-3. *Example of measured transmissivities (based on PFL-f) in fractures intersecting two boreholes drilled in the focused volume; KLX11A (HRD_W) and KLX15A (HRD_C) /SKB 2009a/.*

detected with the PFL method is low, approximately 0.1 fractures per metre. The geometric mean of the specific capacity is also low, approximately $1{\cdot}10^{-8}$ m^3/s per metre of head change, cf. Table C-2. The product of these two values suggest an equivalent hydraulic conductivity of approximately $1{\cdot}10^{-9}$ m/s (~$1{\cdot}10^{-16}$ m^2) blocks of rock (between deterministic deformation zones) located between –400 to –650m elevation. The validity of this simple calculation is confirmed by the measurements conducted with the PSS method shown in Figure C-2.

Table C-2. Summary of transmissivity statistics of flowing features detected by PFL for the borehole intervals outside of interpreted deterministic deformation zones. MDZs (Minor Deformation Zones) are included in these statistics, but the transmissivity of individual PFL fractures are summed within an MDZ such that each is treated as a single feature. Modified after Tables 9-12 and 9-14 in /Rhén et al. 2008/).

Domain	Depth zone (m)	Min T m^2/s)	Max *T* (m^2/s)	Geometric mean (m^2/s)	PFL $P_{10,corr}$ (m^{-1})
HRD_EW007	50 to –150	4.4E–10	3.2E–05	3.58E–08	0.816
	–150 to –400	3.1E–10	3.7E–05	3.0E–08	0.550
	–400 to –650	7.9E–10	1.8E–06	2.6E–08	0.225
	–650 to –1,000	N/A	N/A	N/A	0.000
HRD_N	50 to –150	7.7E–10	6.5E–05	1.14E–07	0.773
	–150 to –400	8.3E–10	3.6E–05	7.4E–08	0.339
	–400 to –650	1.1E–09	5.2E–06	1.6E–08	0.115
	–650 to –1,000	1.3E–09	2.6E–08	4.6E–09	0.082
HRD_W	50 to –150	3.7E–10	4.6E–05	4.39E–08	0.499
	–150 to –400	1.1E–09	1.0E–05	1.4E–08	0.078
	–400 to –650	6.7E–10	9.2E–06	2.9E–08	0.060
	–650 to –1,000	3.7E–09	3.7E–09	3.7E–09	0.005
HRD_C	50 to –150	3.9E–10	3.8E–05	3.33E–08	0.564
	–150 to –400	3.7E–10	1.2E–05	1.1E–08	0.164
	–400 to –650	3.3E–10	1.1E–06	8.5E–09	0.107
	–650 to –1,000	1.5E–09	4.4E–07	2.3E–08	0.008

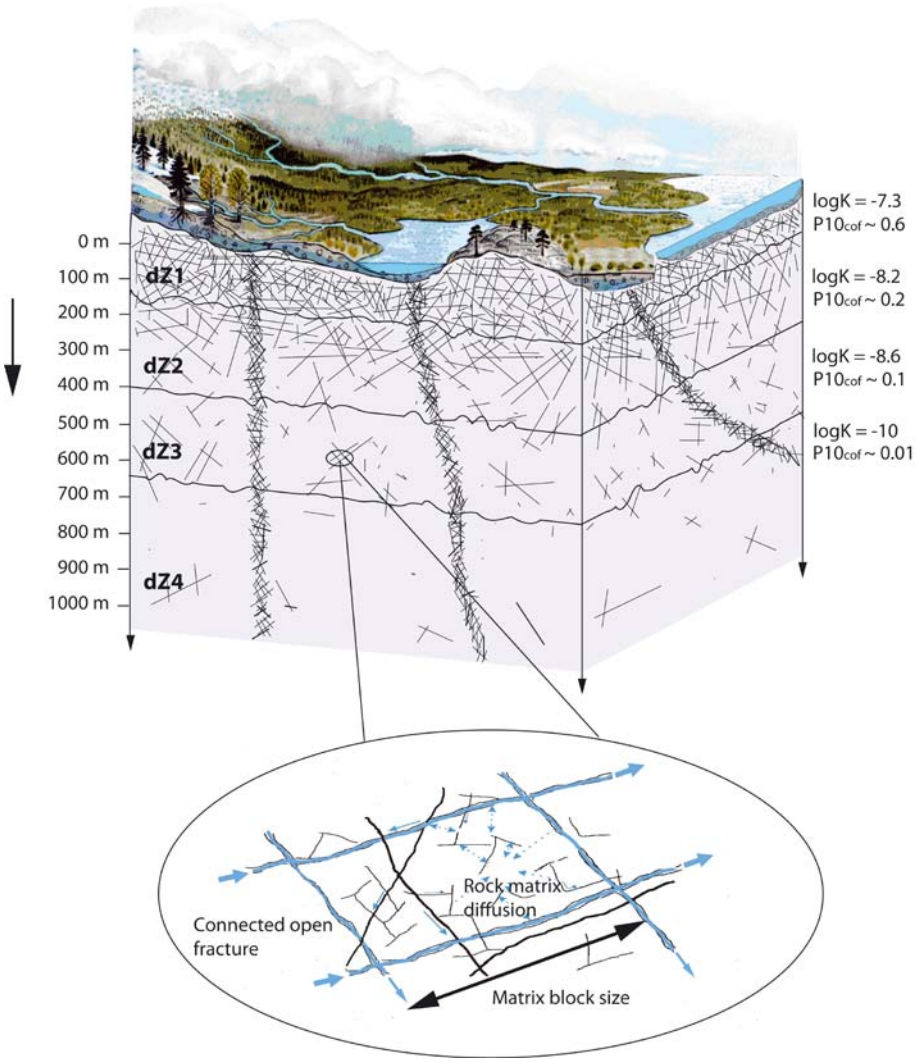

C-4. *Schematic 3D cross-section summarising the hydrogeological conceptual model of the bedrock within the focused volume in Laxemar. Flow in the uppermost depth zone dZ1 is dominated by subhorizontal and WNW fracturing. Solute transport is dominated by advection with matrix block sizes of about 2 m, and about 1,000 years for hydrochemical equilibrium between fractures and matrix. WNW fractures dominate flow in dZ2–dZ4. In dZ2, solute transport is retarded significantly by RMD with matrix block sizes of about 5 m and chemical signatures in the matrix lagging 1,000s of years behind the evolution in the fractures. RMD dominates solute transport in dZ3 with a few sparse areas of significant advection. Matrix block sizes are around 10 m, and matrix hydrochemistry lags 10,000s of years behind the evolution in the fractures. There is very little advection in dZ4 with matrix block sizes of about 100 m and 100,000s of years lag between matrix and fracture hydrochemistry. (K: hydraulic conductivity (m/s), approximate values in scale c. 100 m. P_{10cof}: Intensity (P_{32}) of connected open fractures with a transmissivity > c. 10^{-9} m^2/s.) /Rhén and Hartley 2009/.*

The porewater data shown, cf. Figure C-5 and Figure C-6, indicate a depth trend but also a distinction between bedrock characterised by high transmissivity and a high frequency of water-conducting fractures at shallow to intermediate depth, and bedrock characterised by low transmissivity and a low frequency of water-conducting fractures at greater depth, cf. Table C-2 for general trends. The frequency of flowing fractures is decreasing with depth resulting in "larger blocks" with depth and therefore longer diffusion lengths. Due to this, some water samples of porewater collected at larger depth may have a long distance to a flowing fracture and the porewater samples possibly represent a very old water that is different from the fracture groundwater at similar depth.

In boreholes KLX03 and KLX17A, generally comparable chloride contents and oxygen isotope compositions are observed for porewaters and fracture groundwaters in the transmissive shallow to intermediate depth interval down to at least about 360 m (depending on location), indicating mostly a steady-state between fracture groundwater and porewater. Two samples, however, indicate a difference between porewater and fracture groundwater and thus a transient state.

Between –360 to –430 m in boreholes KLX03 and KLX17A, porewater and fracture groundwater have almost equally negative $\delta^{18}O$ values suggesting a close to steady-state situation, whereas the chloride content of the porewater is only half that of the fracture groundwater indicating a transient state. In borehole KLX08, a similar situation is established down to at least 500 m depth. Here, the difference in chloride content between dilute porewater and moderately mineralised fracture groundwater is even more pronounced, whereas the ^{18}O isotope signature is still similar within the uncertainty band.

Towards greater depth, fracture groundwater data are limited to one single analysis in borehole KLX03 at about 920 m depth.

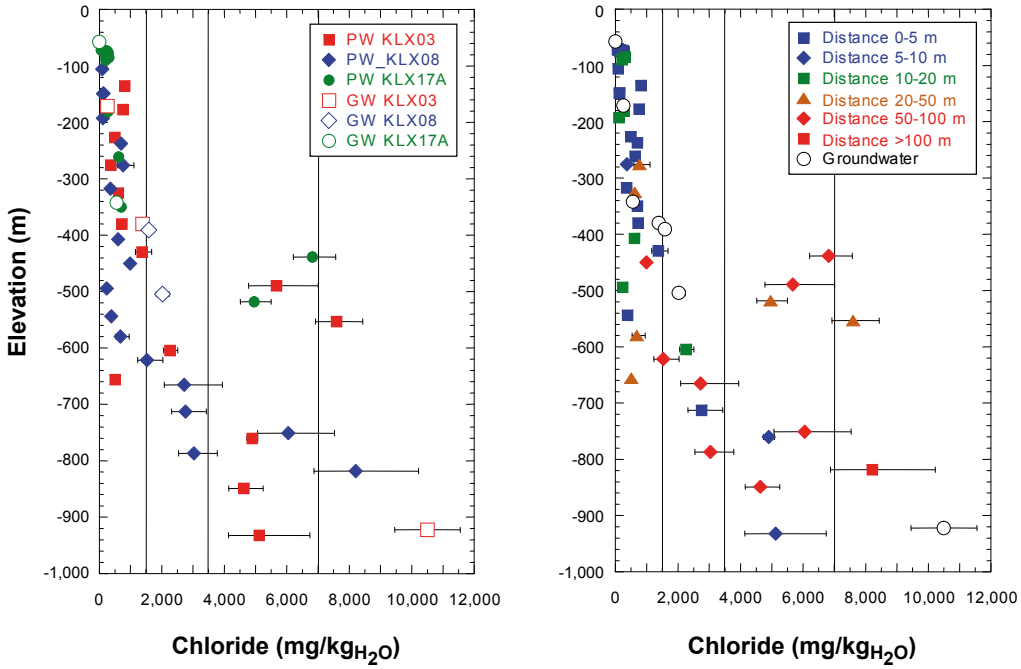

Figure C-5. *Chloride concentration in porewater (PW, closed symbols) and related. Category 1–3 groundwaters of boreholes KLX03, KLX08 and KLX17A (left), distances of the porewater samples in relation to the nearest water-conducting fracture (right), cf. /Laaksoharju et al. 2009/.*

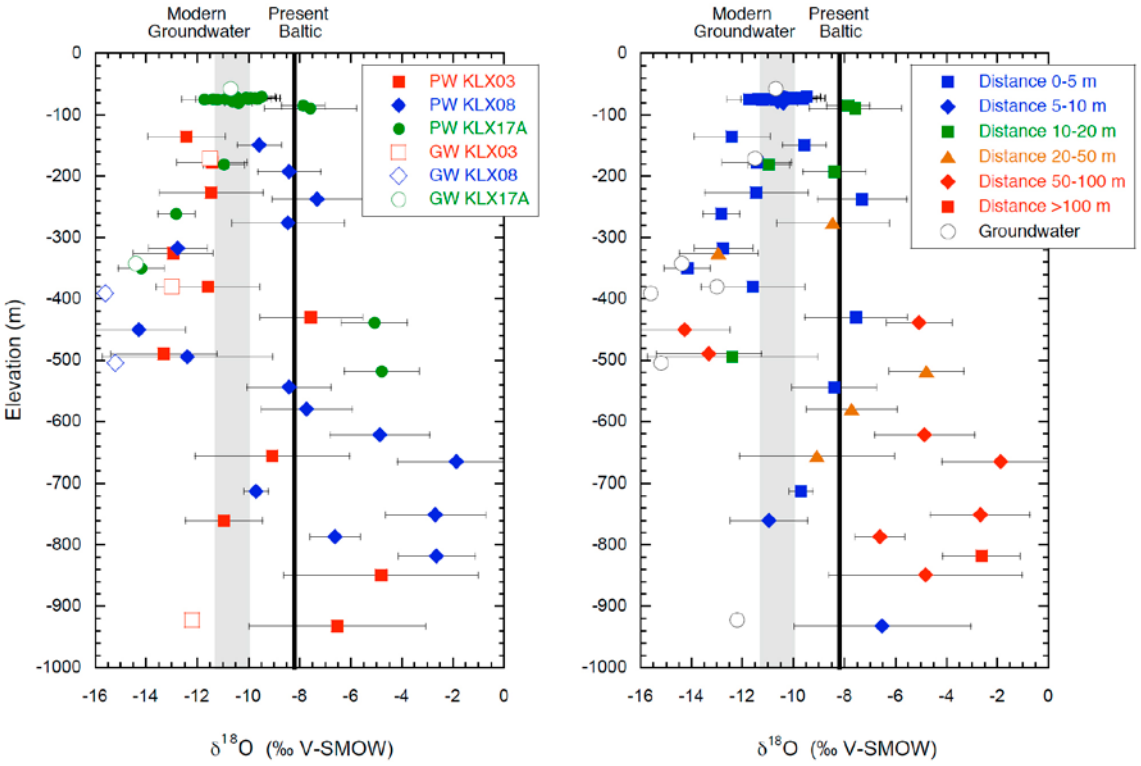

Figure C-6. *Oxygen isotope composition, $\delta^{18}O$, of porewater (PW, closed symbols) and related groundwater (GW, open symbols, Category 1–3 data) from boreholes KLX03, KLX08 and KLX17A (left), Distances of the porewater samples from the nearest water-conducting fracture on the right /Laaksoharju et al. 2009/.*

C.3 Discussion

Hydraulic data suggest that the conductive fracture frequency decreases significantly with depth at both Laxemar and Forsmark. The conductive fracture frequency is particularly low in the focused area/volume below repository depth at Laxemar. Here, hydrochemical data suggest that most of the sampled matrix porewater in deeper parts of the rock is probably very old and not easily affected by transient changes in the top boundary conditions.

Regarding the simulated exchange of dissolved solids between the fracture water and the matrix porewater, the simulation results shown in Figure 6-8 imply that it is the matrix close to the fracture surface that is included in the model rather than the matrix further away. The physical interpretation of the multi-rate diffusion model of /Haggerty and Gorelick 1995/ used in this work is briefly discussed in /Svensson et al. 2010/. In principle, the penetration depth, L_i [L], of each exchange rate coefficient, α_i [T^{-1}], may be evaluated as:

$$L_i = 2\sqrt{\left(\frac{D_e}{\phi_m \alpha_i}\right)} \qquad \text{(C-1)}$$

where D_e [L^2T^{-1}] is an effective diffusion coefficient and ϕ_m is the matrix porosity. These parameters are not used in the model of /Haggerty and Gorelick 1995/, however, and hence not specified in /Svensson et al. 2010/.

The penetration depth of the remotest diffusive exchange rate is estimated by assuming that D_e in Equation (C-1) is similar to the effective diffusion coefficients used in the temperate flow modelling by /Joyce et al. 2010/. Second, the value of the matrix porosity is estimated from the following relationship:

$$\phi_m = \beta\phi \qquad \text{(C-2)}$$

where β [-] is the ratio between the diffusive and advective pore spaces and ϕ is the grid cell kinematic porosity. Inserting $D_e = 1{\cdot}10^{-14} - 1{\cdot}10^{-13}$ m^2/s /Joyce et al. 2010, Appendix F/, $\beta = 10$ and

$\alpha_{min} = 4 \cdot 10^{-12}$ s^{-1} (section 4.2.4) and $\phi = 3 \cdot 10^{-4}$ (from the ECPM model realisation), render penetration depths of the remotest diffusive exchange rate that vary in the range of a few metres (2–6 m). These penetration depths are reached after approximately 8,000 years ($=1/\alpha_{min}$), which matches roughly the time scale of the studied problem (13,000). A value of α_{min} that matches the time span of a full glacial cycle, e.g. 100,000 years, renders penetration depths of 5–16 m. As this penetration depths are on the same order as the average spacing between the flowing fractures at repository depth, see Figure C-4, it may be concluded that the matrix porewater chemistry at repository depth is affected but still far away from flowing fractures at larger depth the matrix porewater may be unaffected by the hydrodynamics during a glacial cycle. It is the matrix porewater adjacent to the flowing fractures that is affected by matrix diffusion. The inserted numbers are conditional, of course, but the calculation does provide an explanation for the appearance of the simulated results shown in Figure 6-8.

Figure C-5 suggests that the salinities in both the fracture water and matrix porewater increase with depth. From Figure C-2 it is concluded that the fracture water salinity at Laxemar at –1,000 m elevation is probably somewhat higher than the salinity at Forsmark at this elevation, but the increase in salinity is fairly similar. A salinity of c. 7–8% by weight in both the fracture water and the matrix porewater at c. –2,000 m elevation at Laxemar appears as a reasonable assumption.

Concerning the applied top boundary conditions, the present-day shoreline (2000 AD) is used in all glacial cases without permafrost during the pre-LGM stage. This model simplification is considered appropriate from a hydraulic point of view for two reasons. First, the hydraulic gradients that occur when the ice sheet margin passes the repository area exceed by far the regional gradients caused by a distant shoreline of a low elevation. Second, the groundwater table in Sweden is close to the ground surface regardless of the shoreline elevation due to abundant precipitation and the relatively low permeability of glacial till and fractured crystalline rock. The shoreline elevation during the post-LGM stage is assumed to be at approximately +100 m, i.e. submerged conditions will prevail in front of the retreating ice sheet margin, see Figure 1-2. Figure C-7 shows the shoreline displacement between 9000 BC and 15,000 AD. Between 9000 BC and 2000 AD, the total shoreline displacement is approximately 30 m, and the top boundary condition at Laxemar changes from mostly submerged to terrestrial. During the next 10,000 years[12], the terrestrial conditions are reinforced as the expected additional total shoreline displacement is estimated to be approximately 11 m /Påsse 1997, SKB 2010/.

Discontinuities in the permafrost layer are accounted for in the groundwater flow simulations that take periglacial conditions into account. As mentioned in section 1.3, potential locations of taliks are estimated from the ongoing shoreline displacement /SKB 2006a/. Thus, the groundwater flow simulations that take permafrost into account use a different shoreline elevation. The used elevation of –8 m , cf. Table 5-6, is representative for a time period of approximately 50,000–60,000 years from today /SKB 2006a/.

Figure C-8 shows the evolution of the sea water salinity in the Laxemar area between 9000 BC and 15,000 AD. At 9000 BC, the Laxemar area was partly submerged by Lake Ancylus, which was a freshwater lake that received huge amounts of glacial meltwater from the retreating ice sheet margin. At about 6500 BC, the salinity started to increase as the Littorina Sea began to form. The Littorina Sea reached its maximum salinity between 4000 BC and 3000 BC.

[12] /SKB 2010/ considers temperate conditions for at least another 8000 years.

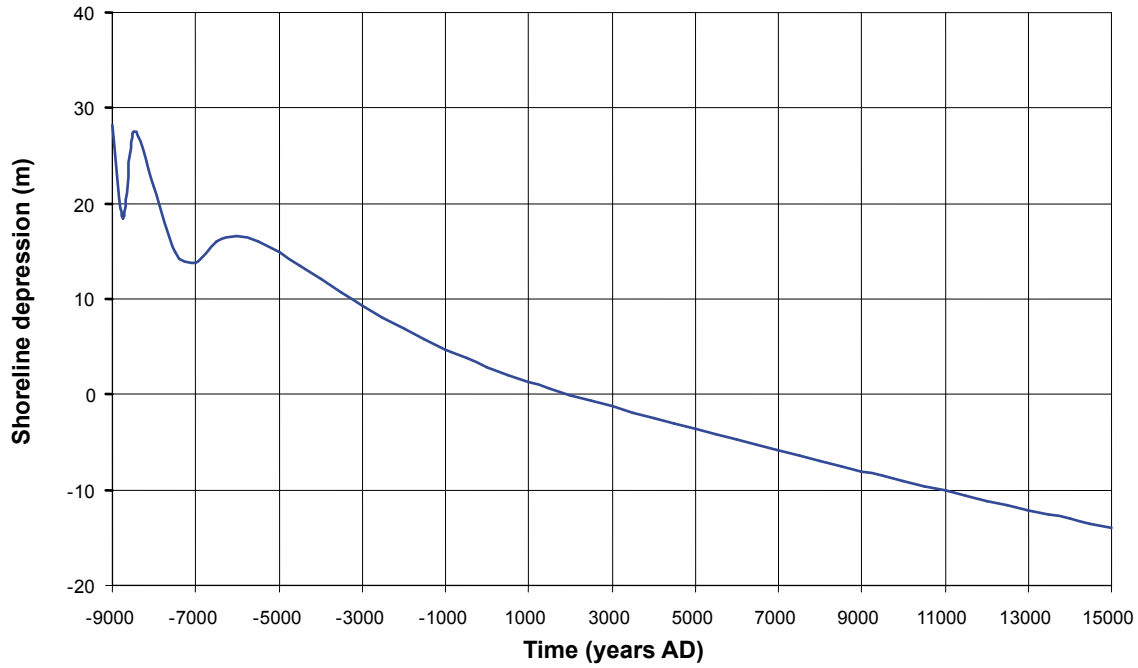

Figure C-7. *Evolution of the shoreline displacement at Laxemar during Holocene time (9000 BC to 15,000 AD). (Figure 4-6 in /Joyce et al. 2010/.)*

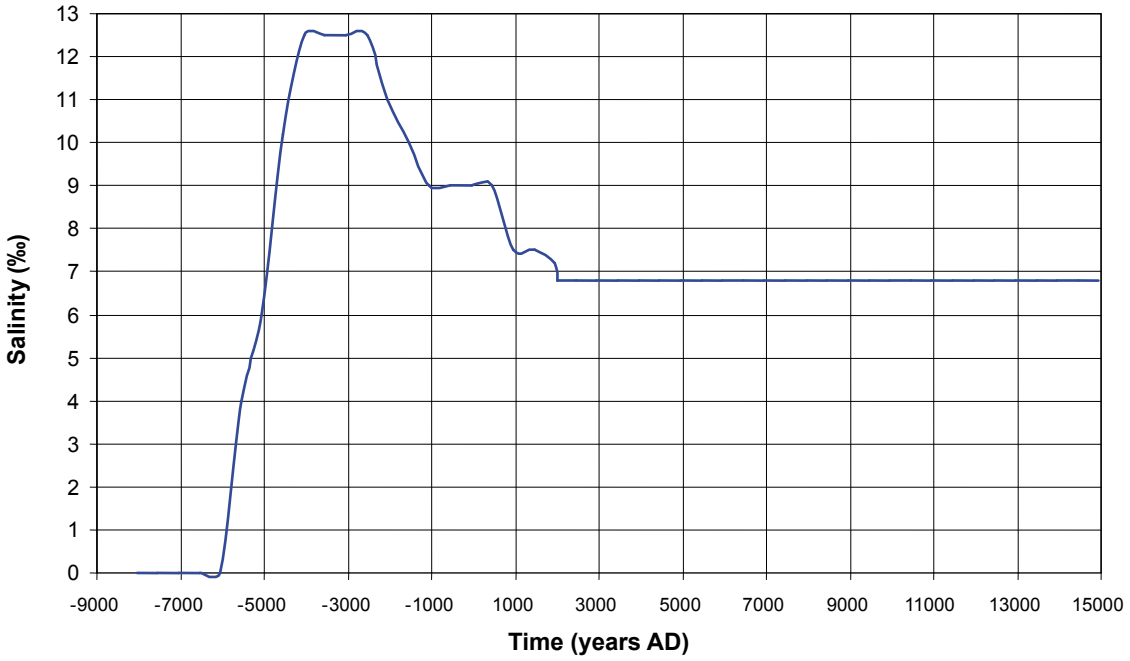

Figure C-8. *Evolution of the seawater salinity at Laxemar during Holocene time (9000 BC to 15,000 AD). (Figure 4-7 in /Joyce et al. 2010/.)*

Appendix D

Temperate case

D.1 Salinity

Figure D-1 shows the model domains assessed and the NW-SE cross-section used for visualization. Figure D-2 shows the salinity field in terms of two cross-sections. Figure D-3 shows the fracture water and the matrix porewater salinities along the NW-SE cross-section (see Figure D-1). The salinity at repository depth within the focused volume is approximately 0.0–0.2%.

The undulations in the salinity field reflect the simulated variations in the pressure field, which are affected by the spatial variability of different factors such as initial conditions and topography, resolution of the computational grid, hydraulic heterogeneity and structures, e.g. outcropping deformation zones.

D.2 Darcy flux

Figure D-4 shows the Darcy flux field along the same cross-section as shown in Figure D-3. At the repository depth within the focused volume, the Darcy fluxes are significant and directed both upward and downward.

D.3 Recharge and discharge locations

Figure D-5 shows the simulated recharge and discharge locations for particle traces that pass through the 8,031 deposition hole positions. All recharge locations coincide with topographic highs inside the regional flow domain of SDM-Site. The majority of the discharge locations are found close to the present-day coastline or in conjunction with outcropping deformation zones.

Figure D-6 shows the simulated recharge and discharge locations for particle traces that pass through the five measurement localities (ML 1-5). The recharge locations for all five measurement localities are found above the repository; typically the recharge flow path length is around 1 km. The discharge flow path lengths are typically 1–2 km.

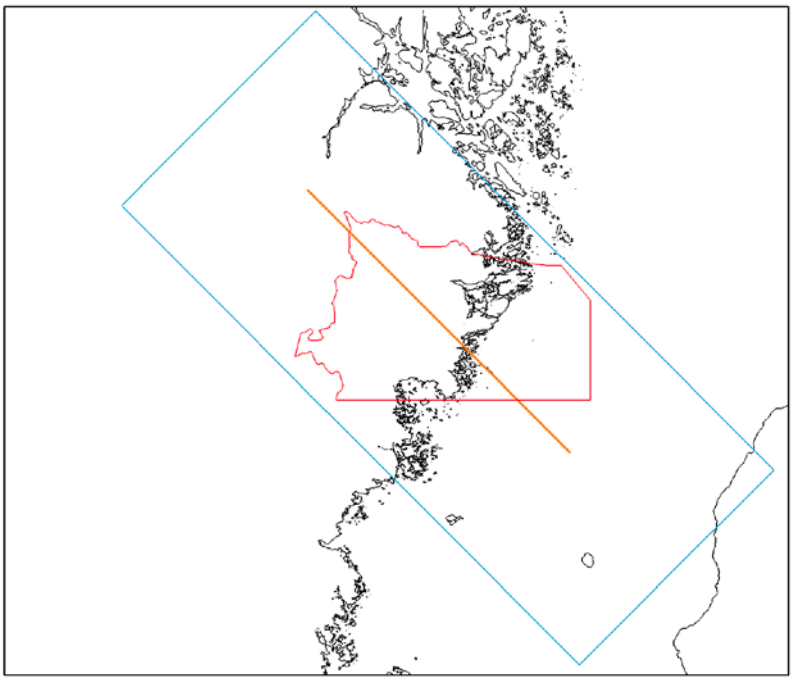

Figure D-1. *Illustration of the model domains assessed and of the NW-SE cross-section (orange line) used for visualisations. The red polygon shows the model domain used for groundwater flow modelling in SDM-Site. The larger blue polygon shows the model domain used in case (a), (c) and (d) of this study.*

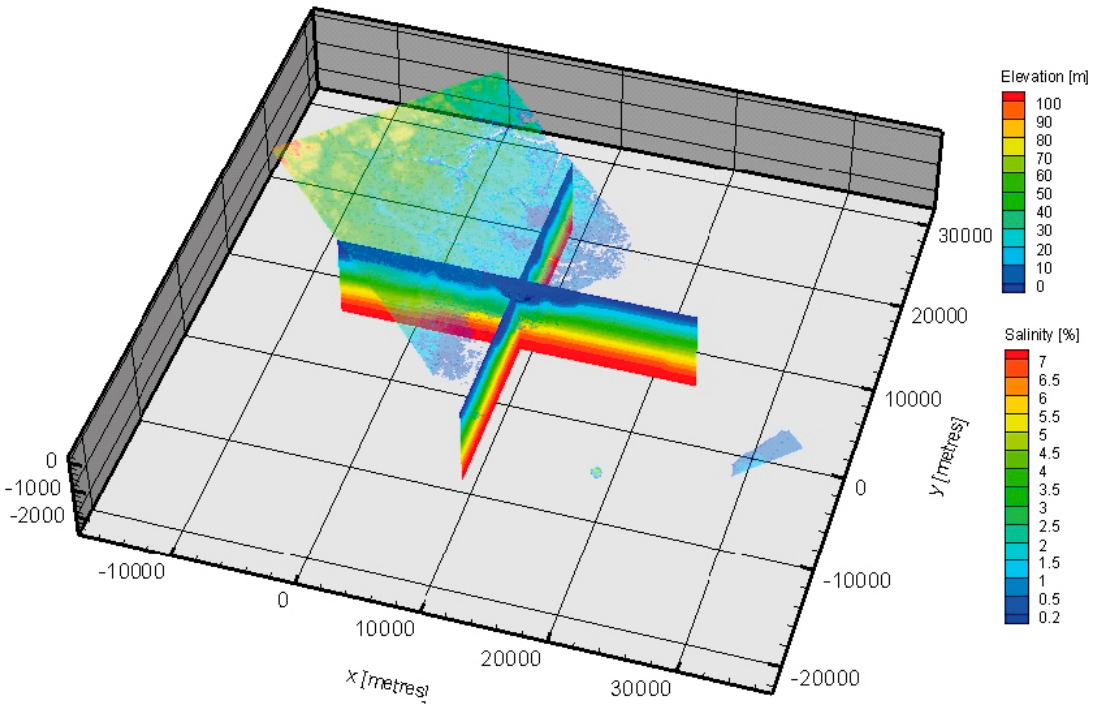

Figure D-2. *Salinity for the temperate case along two vertical cross-sections together with the present-day shoreline. The y-axis points towards north.*

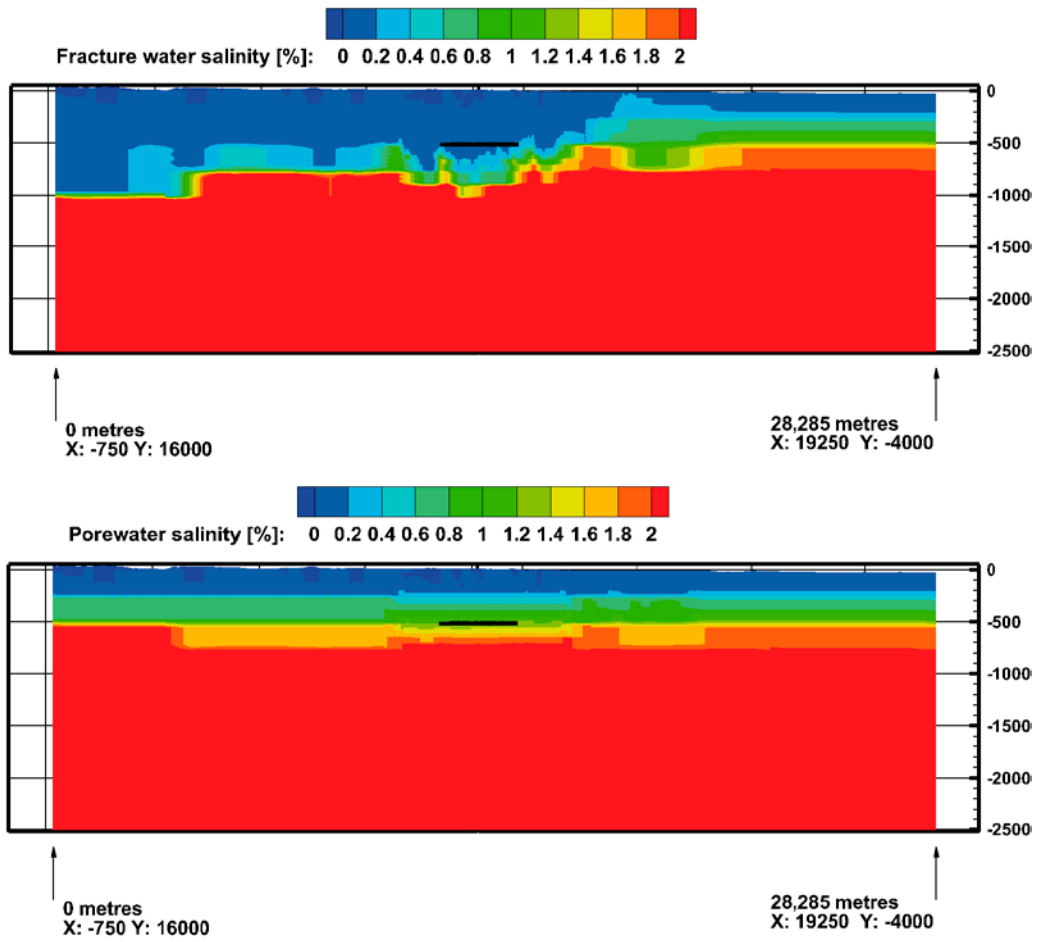

Figure D-3. *Fracture and matrix porewater salinities along the NW-SE cross-section shown in Figure D-1. The black line at –500 m elevation indicates the location of the repository.*

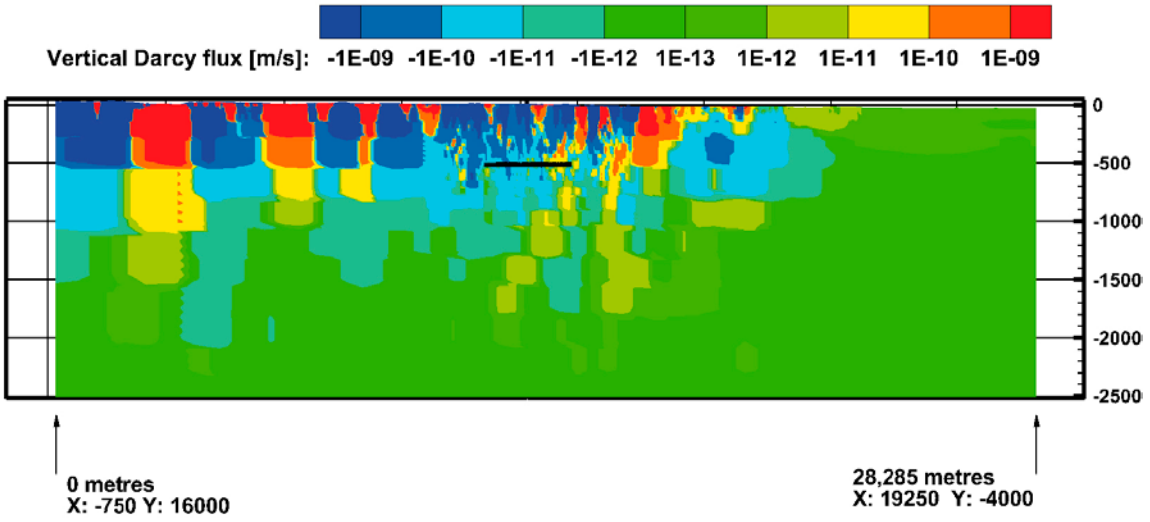

Figure D-4. *Darcy flux field along a NW-SE cross-section shown in Figure D-1. Positive values represent upward directed fluxes and negative values represent downward directed fluxes. The black line at –500 m elevation shows the location of the repository.*

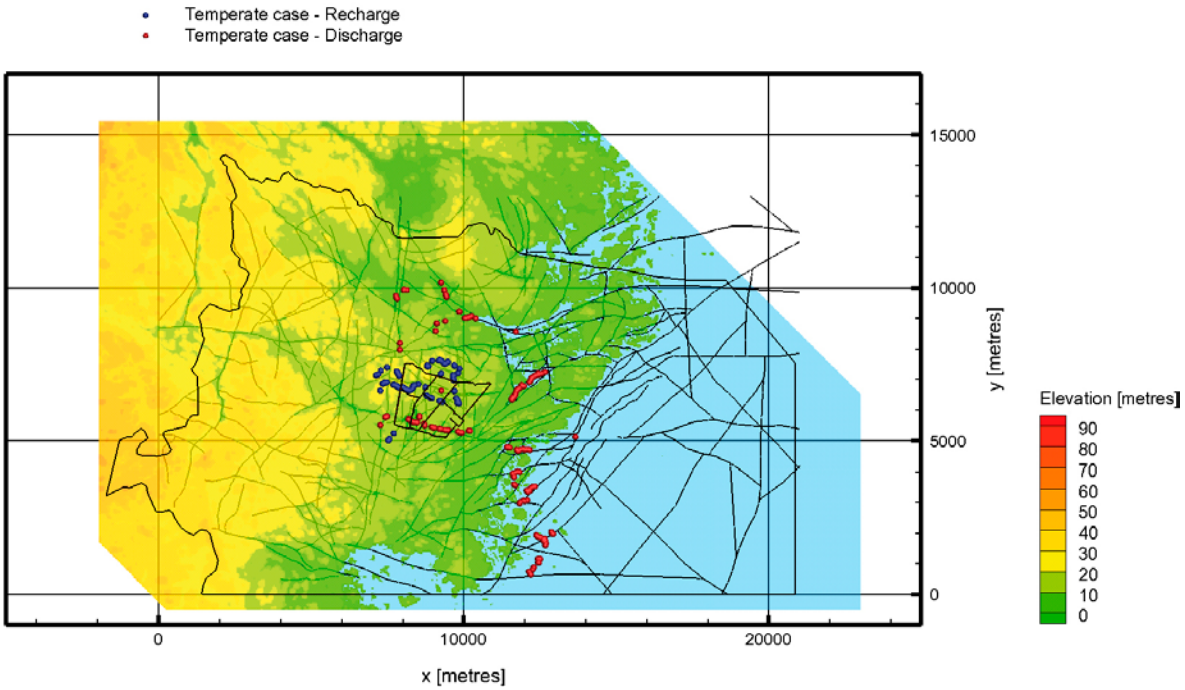

Figure D-5. *Recharge (blue) and discharge (red) locations for particle traces passing through the 8,031 deposition hole positions. The trace lines represent outcropping deformation zones. The repository is located close to the shoreline (the thicker black lines).*

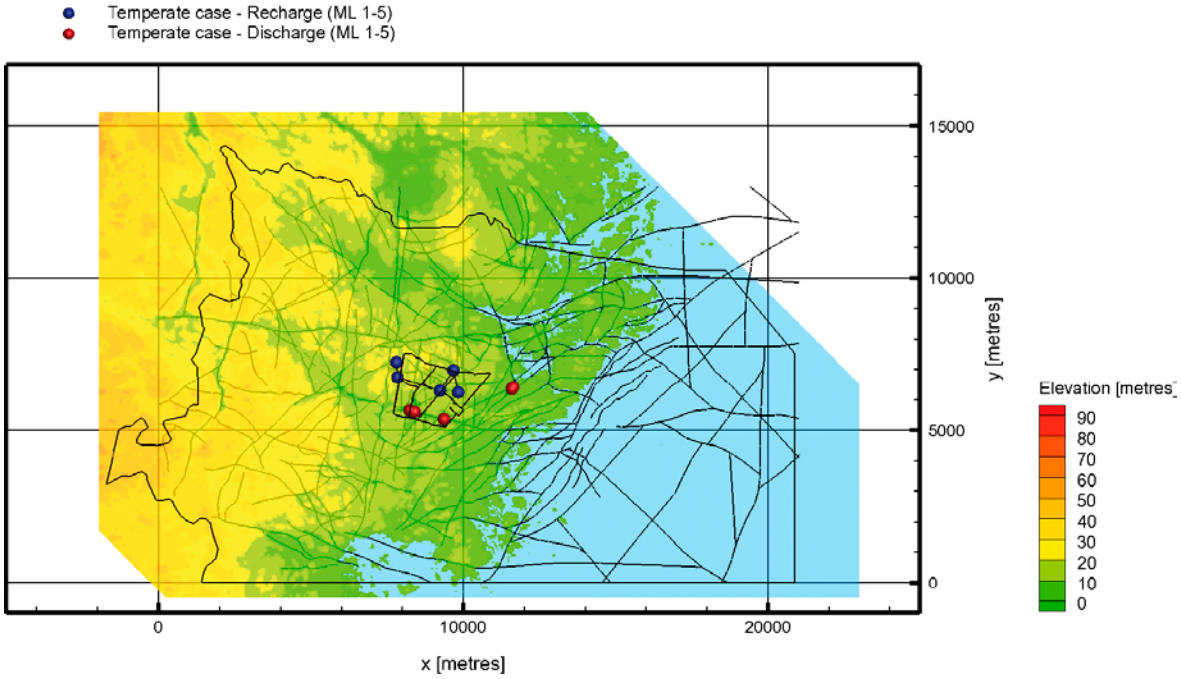

Figure D-6. *Recharge (blue) and discharge (red) locations for particle traces passing through ML 1-5. The trace lines represent outcropping deformation zones. The repository is located close to the shoreline (the thicker black lines).*

D.4 Recharge characteristics

Particles are released at the 8,031 deposition hole positions and at the five measurement localities, ML 1-5, and tracked in a backward direction for 1,000 years to investigate their recharge characteristics.

Table D-1 presents recharge flow path lengths, travel times, and flow-related transport resistances for the particles released at the measurement localities ML 1-5.

Table D-1. Temperate case recharge performance measures for ML 1-5.

Measurement locality	Flow path length [m]	Travel time [y]	Flow-related transport resistance [y/m]
1	3,507	25.3	$4.5 \cdot 10^5$
2	929	1.1	$3.3 \cdot 10^4$
3	1,457	1.1	$5.6 \cdot 10^4$
4	1,128	0.8	$2.0 \cdot 10^4$
5	874	1.5	$1.8 \cdot 10^4$

Figure D-7 to Figure D-9 show cumulative distribution (probability) plots of the recharge flow path lengths, travel times, and flow-related transport resistances for all released particles.

Figure D-7 shows the cumulative distribution of the recharge flow path lengths (L_R). The majority of recharge flow path lengths are found to be shorter than 1.5 km but some have travelled some 3–4 kilometres before reaching the deposition hole position. The values representing ML 1-5 are found distributed well within the entire ensemble.

Figure D-8 shows the cumulative distribution of the recharge travel times ($t_{w,R}$). All of the tracked particles reach repository depth in less than 1,000 years. About 90% of the deposition hole positions have a recharge travel time shorter than 10 years and only 2% have an travel time longer than 20 years. The median recharge travel time is approximately some 1.5 years. The values representing ML 1-5 are found distributed well within the entire ensemble.

Figure D-9 shows the cumulative distribution of the recharge flow-related transport resistances (F_R). About 95% of the values are greater than $1 \cdot 10^4$ y/m with a median of approximately $3 \cdot 10^4$ y/m. The values representing ML 1-5 are found distributed well within the entire ensemble.

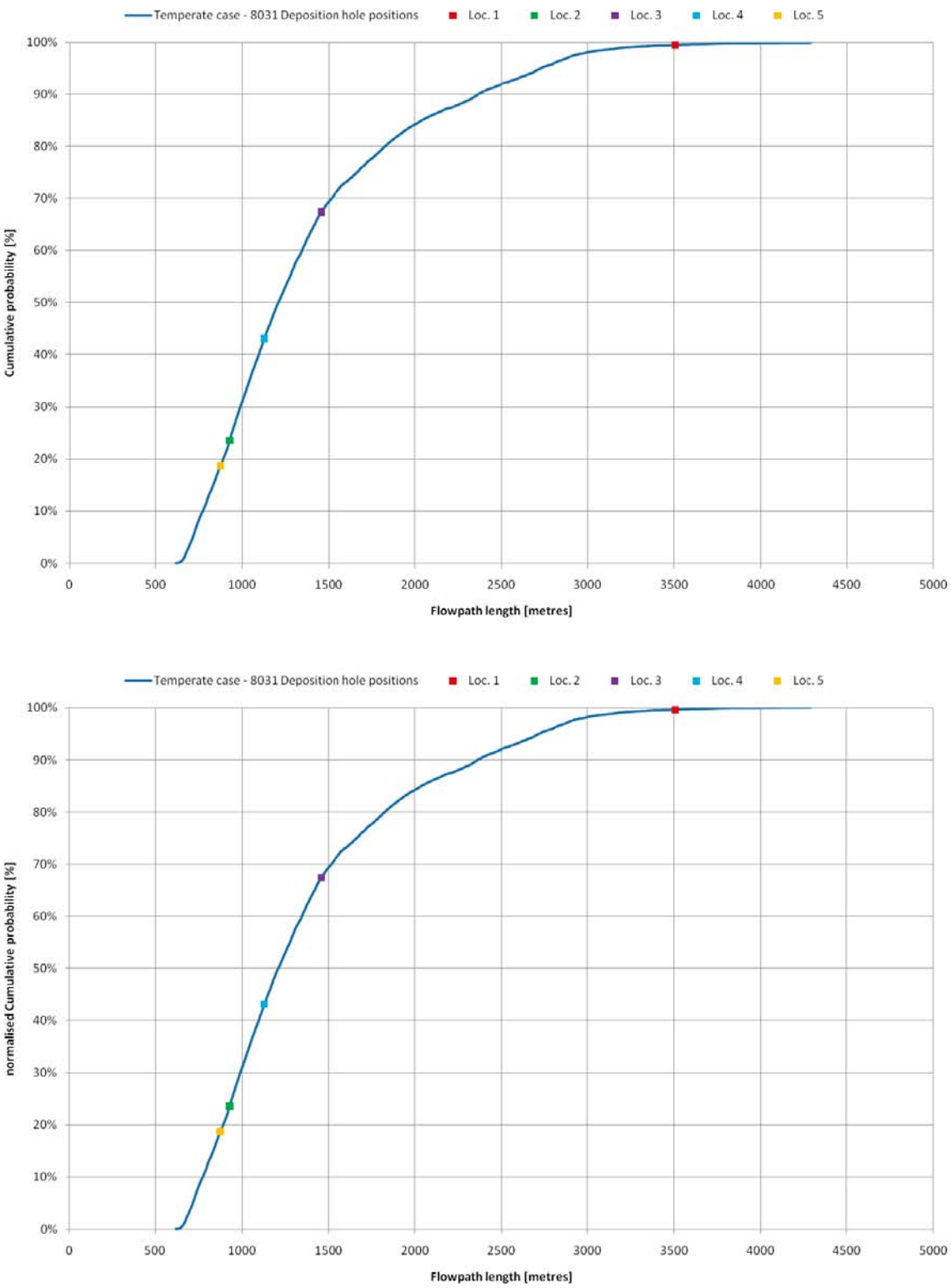

Figure D-7. *Cumulative distribution (probability) plots of the simulated recharge flow path lengths, L_R, for the temperate case. The maximum value in the upper plot is set to 100% in the lower plot.*

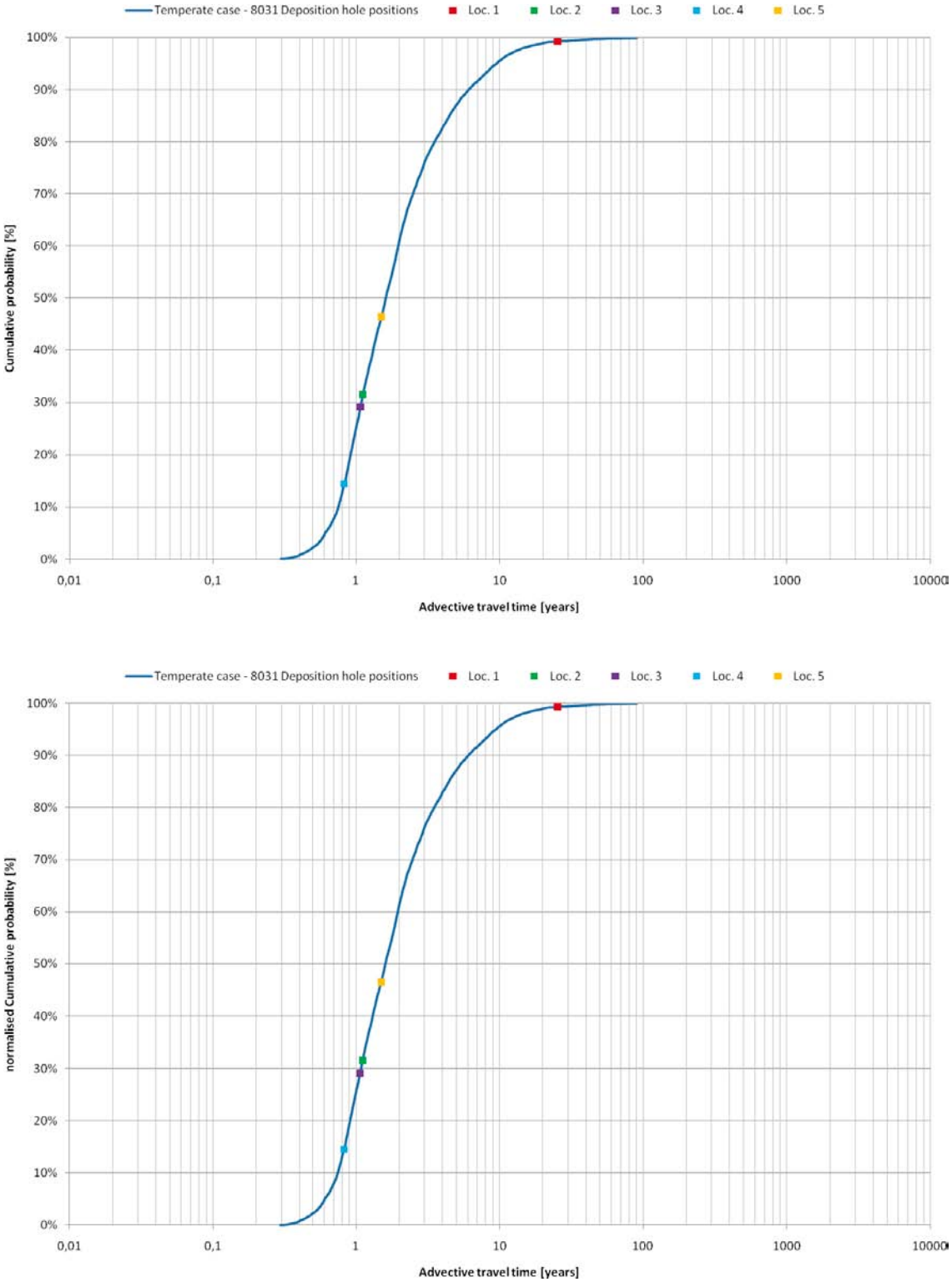

Figure D-8. *Cumulative distribution (probability) plots of the simulated recharge travel times, $t_{w,R}$, for the temperate case. The maximum value in the upper plot is set to 100% in the lower plot.*

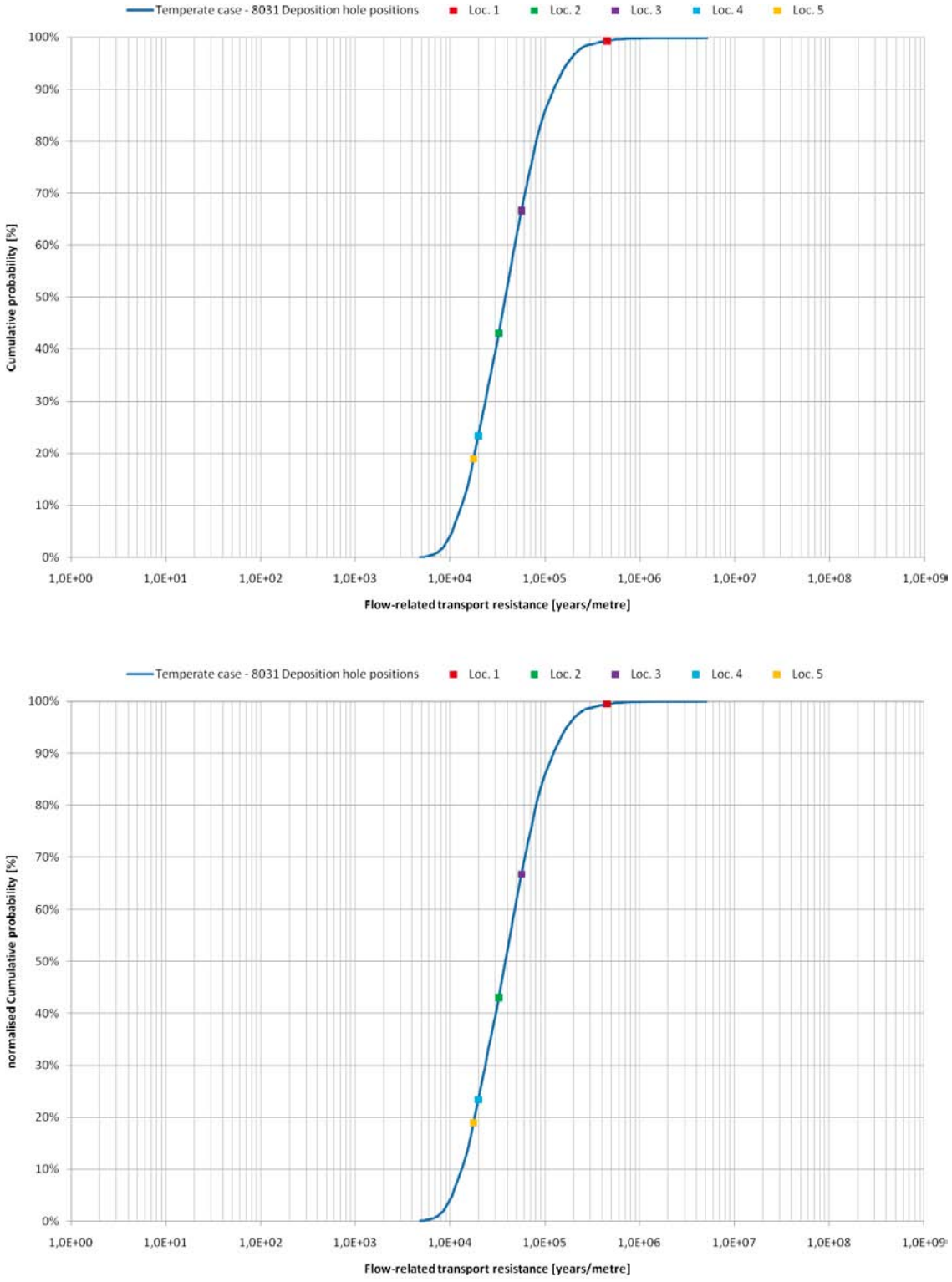

Figure D-9. *Cumulative distribution (probability) plots of the simulated recharge flow-related resistances, F_R, for the temperate case. The maximum value in the upper plot is set to 100% in the lower plot.*

D.5 Discharge characteristics

Particles are released at the 8,031 deposition hole positions and at the five measurement localities, ML 1-5, and tracked in a forward direction for 1,000 years to investigate their discharge characteristics. Not all of the released particles reached the ground surface within this period of time.

Table D-2 presents discharge flow path lengths, travel times, and flow-related transport resistances for the particles released at the measurement localities ML 1-5.

Table D-2. Discharge performance measures for ML 1-5.

Measurement locality	Flow path length [m]	Travel time [y]	Flow-related transport resistance [y/m]
1	767	1.6	$2.1 \cdot 10^4$
2	1,127	1.3	$2.8 \cdot 10^4$
3	1,431	0.8	$2.1 \cdot 10^4$
4	2,070	0.7	$2.1 \cdot 10^4$
5	1,415	2.1	$2.3 \cdot 10^4$

Figure D-10 to Figure D-12 show cumulative distribution (probability) plots of the discharge flow path lengths, travel times, and flow-related transport resistances for all released particles.

Figure D-10 shows the cumulative distribution of the discharge flow path lengths (L_R). The discharge flow path lengths are broadly distributed between approximately 1 and tens of kilometres reached in the tracked time span. Some 50% of the particles discharge with a shorter flow path length than 2 km. Some 25% of the particles do not discharge during the tracked 1,000 years. The values representing ML 1-5 are found distributed within the shorter range ensemble (shorter than 2 km).

Figure D-11 shows the cumulative distribution of the discharge travel times ($t_{w,D}$). Approximately 75% of the tracked particles reach the surface from a deposition hole position in 1,000 years or shorter. The fastest particle reaches the surface after some months (0.3 year). The median travel time indicated is roughly 2.5 years. The values representing ML 1-5 are found distributed within the faster half of the ensemble.

Figure D-12 shows the cumulative distribution of the discharge flow-related transport resistances (F_R). About 95% of the values are greater than $1 \cdot 10^4$ y/m with a median of approximately $5 \cdot 10^4$ y/m. The measurement localities ML1-5 are found well within the range of the flow-related transport resistances recorded for the 8,031 deposition hole positions.

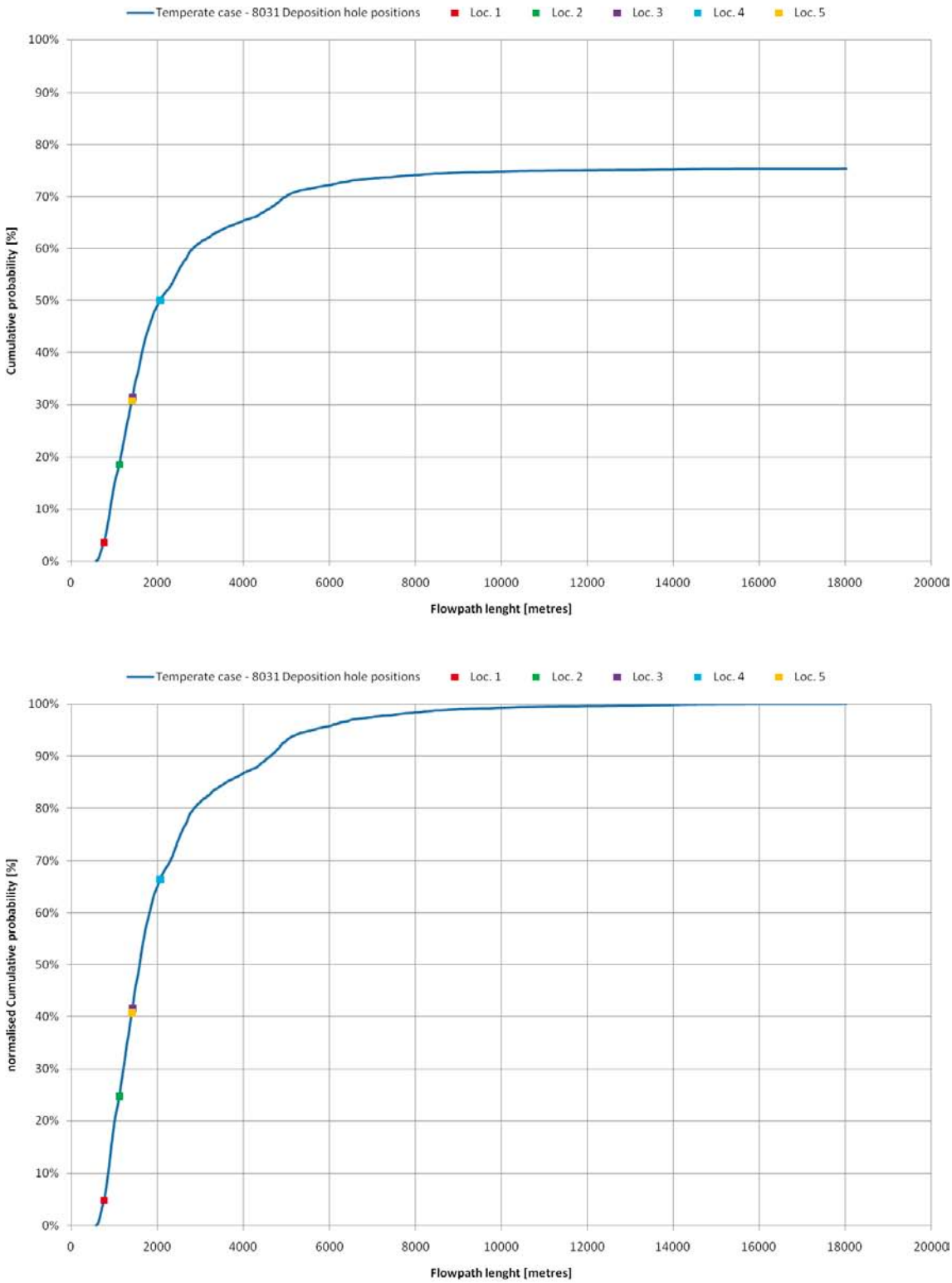

Figure D-10. *Cumulative distribution (probability) plots of the simulated discharge flow path lengths, L_R, for the temperate case. The maximum value in the upper plot is set to 100% in the lower plot.*

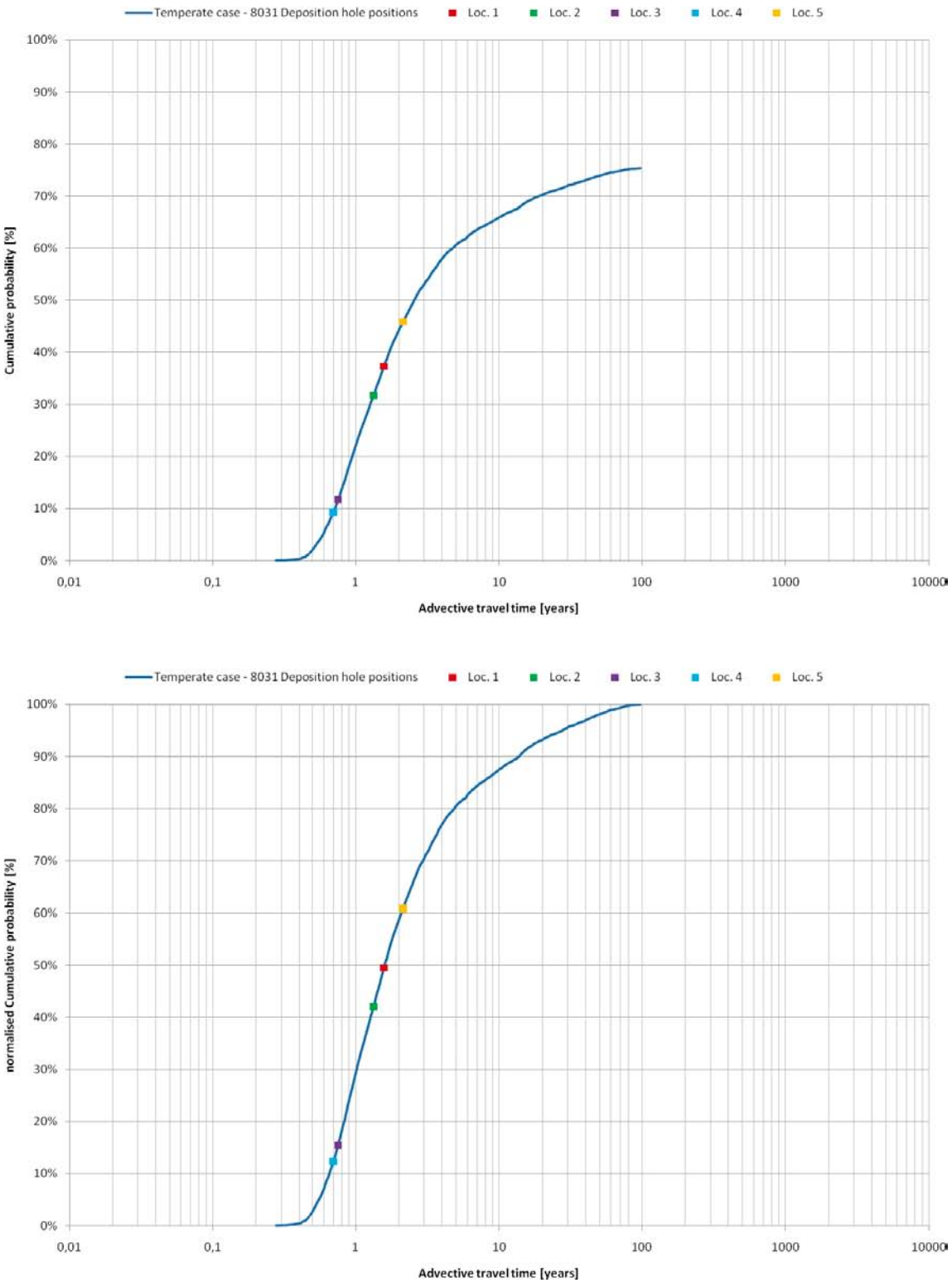

Figure D-11. *Cumulative distribution (probability) plots of the simulated discharge travel times, $t_{w,R}$, for the temperate case. The maximum value in the upper plot is set to 100% in the lower plot.*

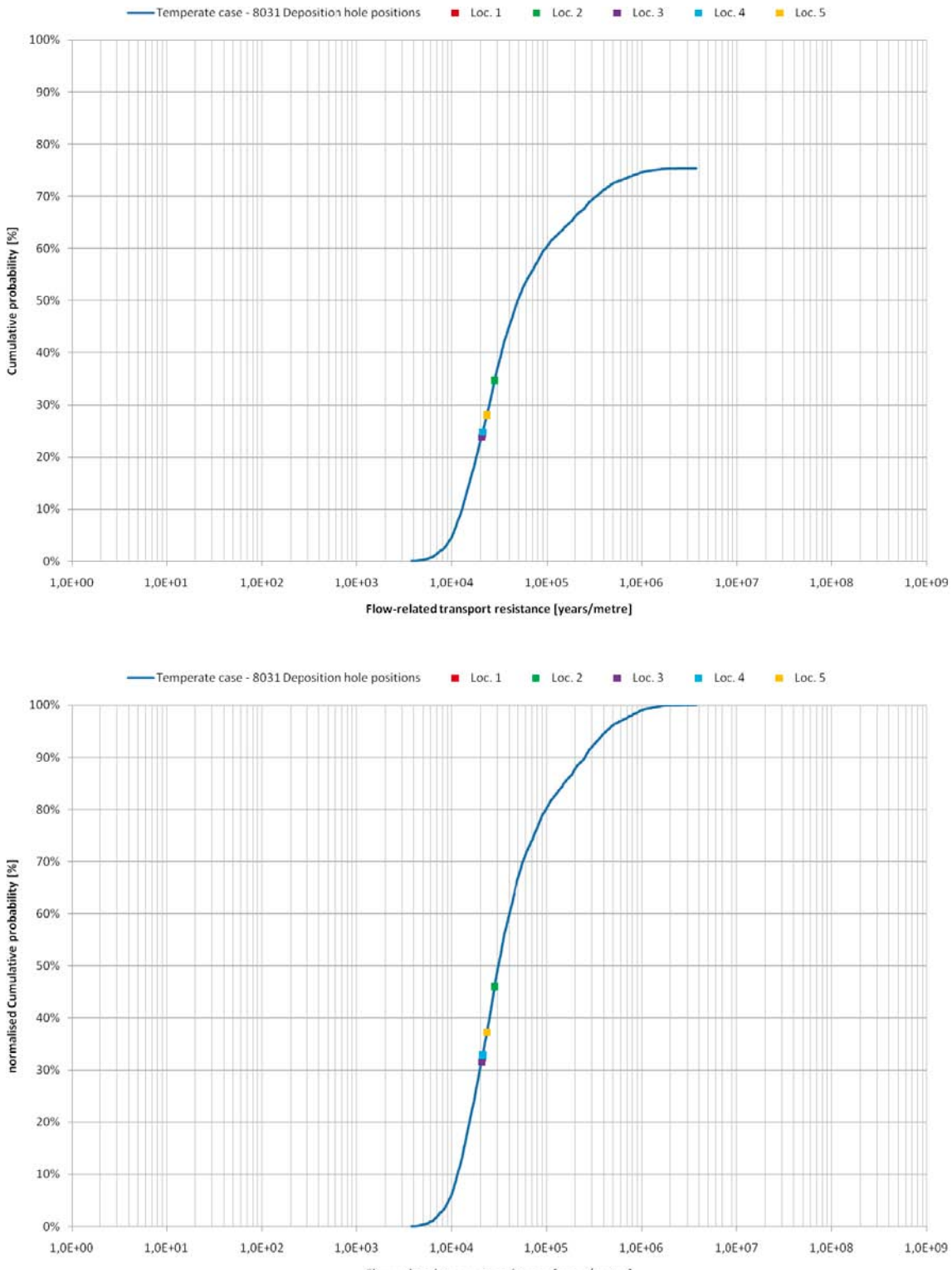

Figure D-12. *Cumulative distribution (probability) plots of the simulated discharge flow-related transport resistances, F_R, for the temperate case. The maximum value in the upper plot is set to 100% in the lower plot.*

Appendix E

Scenario A: Glacial climate conditions without permafrost

E.1 Introduction

All plots shown is this appendix refer to case (a), see Table 5-1 and Figure 5-1, except for one plot that compares case (a) with case (b) and another plot that compares case (a) with case (c). These exceptions are explicitly stated.

E.2 Top boundary conditions

Figure E-1 shows the situation during glaciation when the ice sheet margin is at ice-front location II (IFL II). The grayish area indicates the ice sheet thickness. The speed of the ice sheet margin is 50 m/y, thus IFL II is reached about 700 years after the it enters the model domain. A pressure equal to 92% of the weight of the ice sheet thickness is specified on the top boundary below the ice. Elsewhere, the pressure is set to zero in all terrestrial parts and to the hydrostatic pressure below the ice-free sea and lakes.

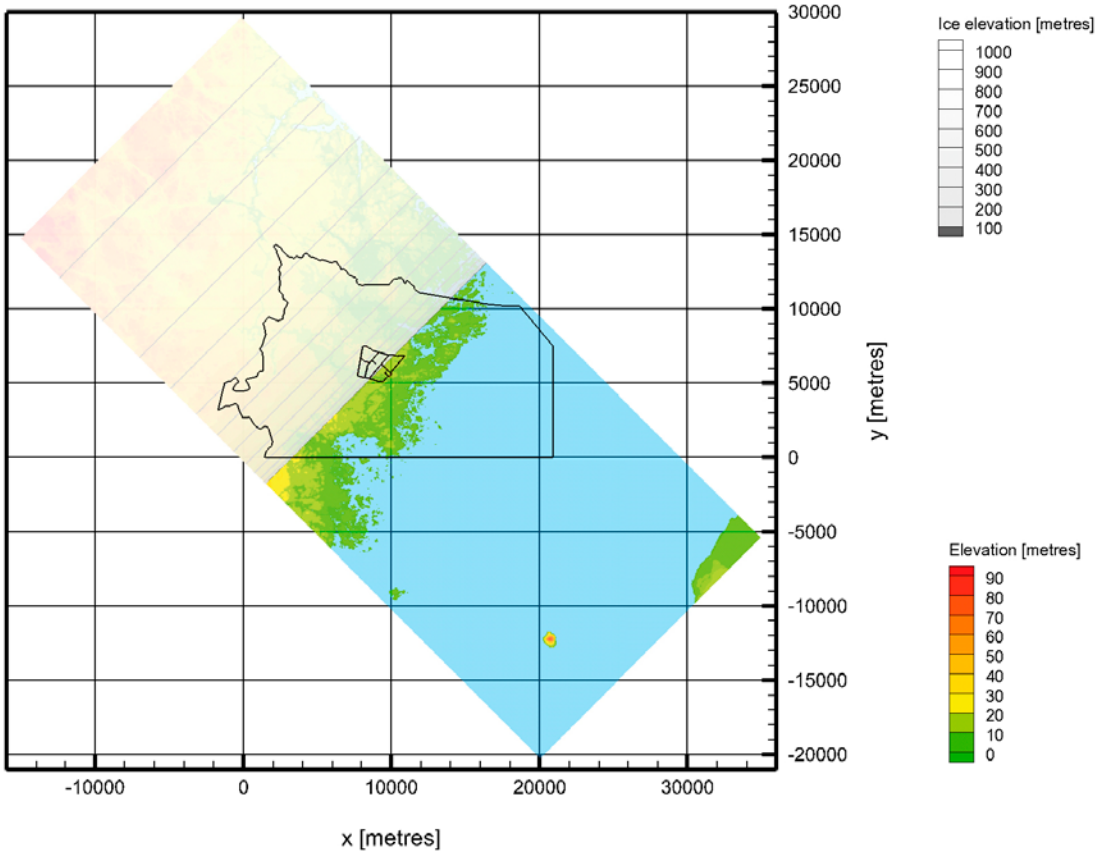

Figure E-1. *Visualisation of ice sheet thickness during glaciation when the ice sheet margin is at IFL II. The short black lines in the centre indicate the location of the repository. The y-axis points towards north.*

E.3 Pressure

Figure E-2 shows the pressure (*P)* on the NW-SE cross-section (see Figure D-1) during glaciation when the advancing ice sheet margin is at ice-front location II (IFL II).

Figure E-3 shows the simulated development of the pressure during glaciation at the five measurement localities (ML 1-5). The pressures develop similarly at these localities. The effect of the approaching ice sheet margin is not visible until the ice sheet margin is fairly close to ML 1-5.

Figure E-4 shows a comparison of the pressure developments during glaciation and deglaciation. Apart from the offset of 1 MPa during the retreat, the pressure envelopes are close to identical. The 1 MPa offset during deglaciation is due to the elevated sea level, which is set to 100 m above the Ordnance Datum during glaciation.

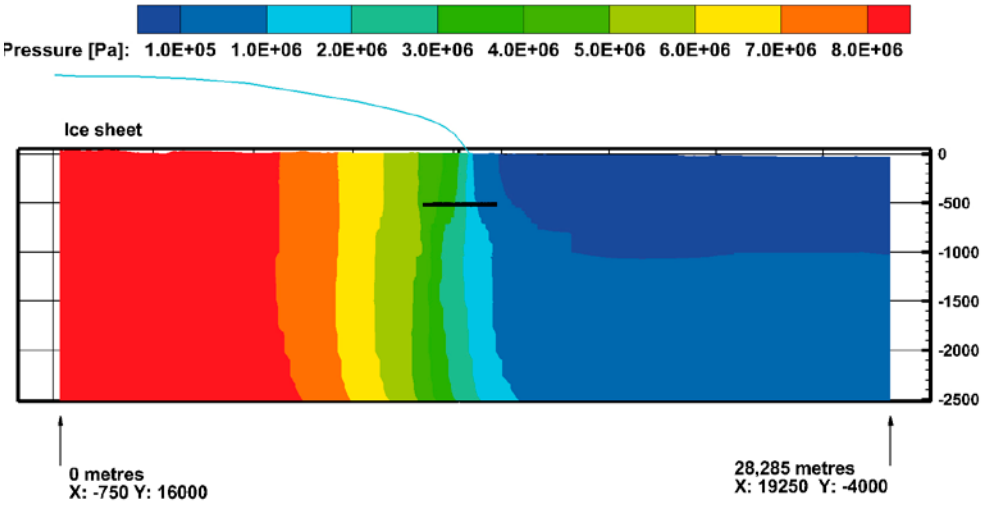

Figure E-2. *Visualisation of the pressure during glaciation when the ice sheet margin is at IFL II. The short black line in the centre indicates the location of the repository.*

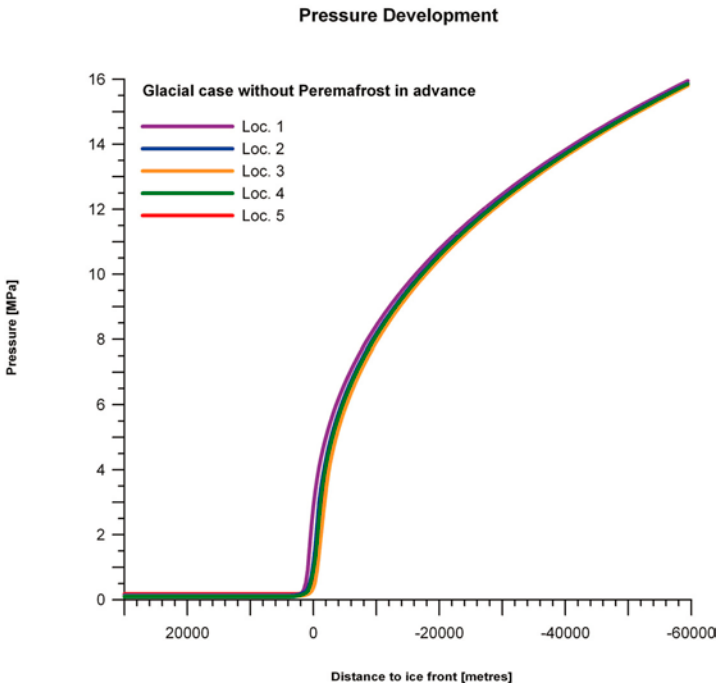

Figure E-3. *Pressure at ML 1-5 during glaciation. Positive distance values mean that the ice sheet margin has not yet arrived to the measurement locations.*

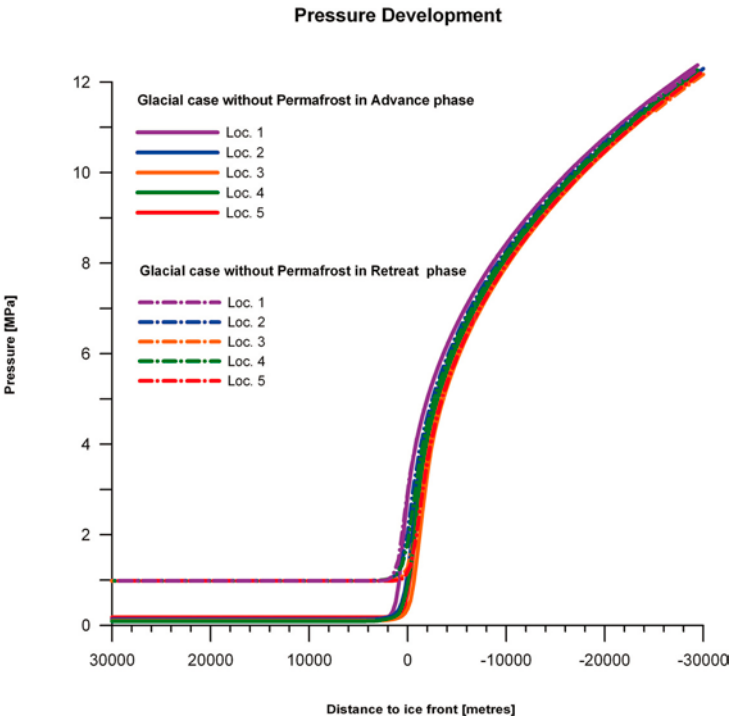

Figure E-4. *Pressure at ML 1-5 during glaciation and deglaciation. Positive distance values mean that the ice sheet margin has not yet arrived to the measurement locations.*

E.4 Darcy flux

Figure E-5 to Figure E-6 show the spatial distribution of the vertical Darcy flux (q) in a horizontal slice at –500 m elevation. The slice passes through the focused area where the repository is located.

Figure E-5 shows the vertical Darcy flux for the temperate case.

Figure E-6 shows the vertical Darcy flux during glaciation when the ice sheet margin is at ice-front location II, i.e. immediately above the repository.

Figure E-7 shows the vertical Darcy flux during glaciation mapped on a NW-SE cross-section parallel to the ice flow direction during glaciation.

Figure E-8 shows a comparison between the simulated Darcy flux at the five measurement locations during glaciation and deglaciation. The peaks and the envelopes of the Darcy fluxes are very similar.

Figure E-9 shows the normalised Darcy flux (q/q_{temp}) at ML 1-5 during the glaciation (pre-LGM), the complete ice coverage (LGM) and the deglaciation (post-LGM). During the two ice front passages, the fluxes are up to 100 times greater than those prevailing during temperate conditions. Between the two ice-front passages, the model domain is completely covered by ice for a long period of time. When the model domain is completely covered by ice for a long period of time, the simulated Darcy fluxes at ML 2 –5 are between 10–30% lower than the fluxes during temperate conditions, whereas they are approximately 30% higher at ML 1.

Figure E-10 shows the simulated Darcy flux at measurement localities 2 and 5 during the glaciations considered in cases (a) and (b). The direction of the advancing ice sheet margin does have an impact on the Darcy flux, but the overall pattern of change is similar.

Figure E-11 shows the simulated Darcy flux at ML 2 during the glaciations considered in cases (a) and (c). The elaborated permeability conditions are significant for the Darcy flux.

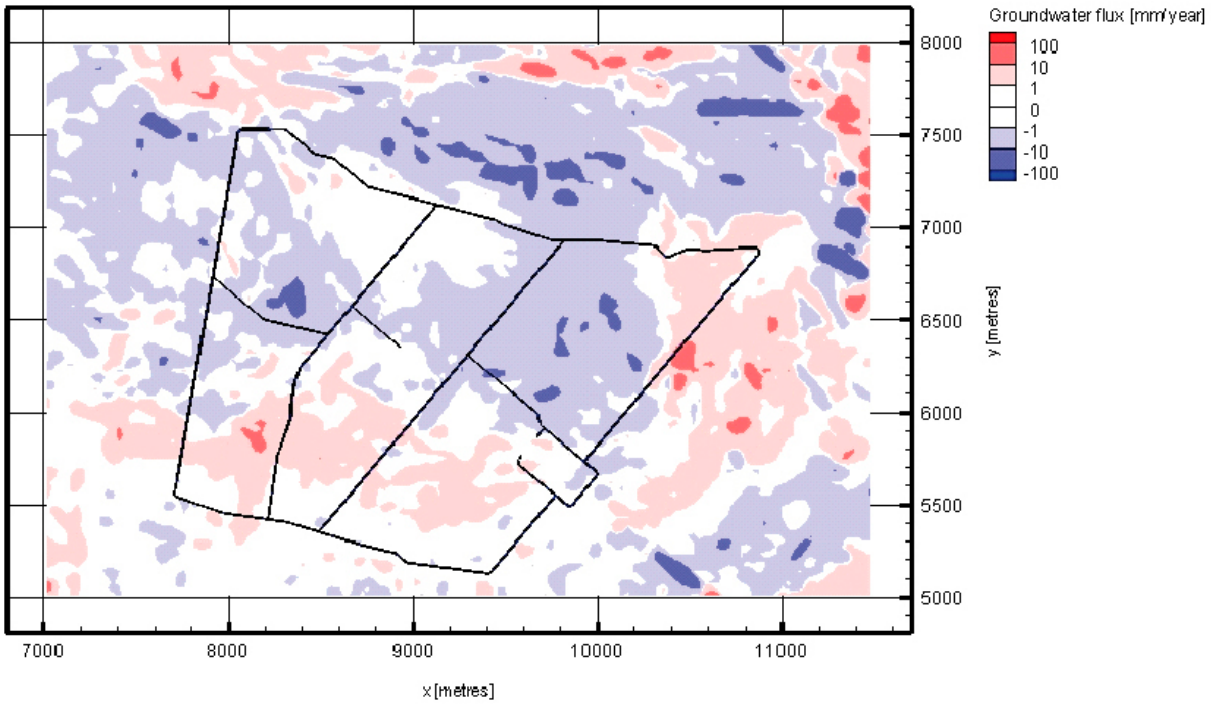

Figure E-5. *Horizontal view of the vertical Darcy flux in mm/y at –500 m elevation for the temperate case. Red colours show positive values (upward directed fluxes), whereas blue colours show negative values (downward directed fluxes). The short black lines indicate major tunnels. The y-axis points towards north.*

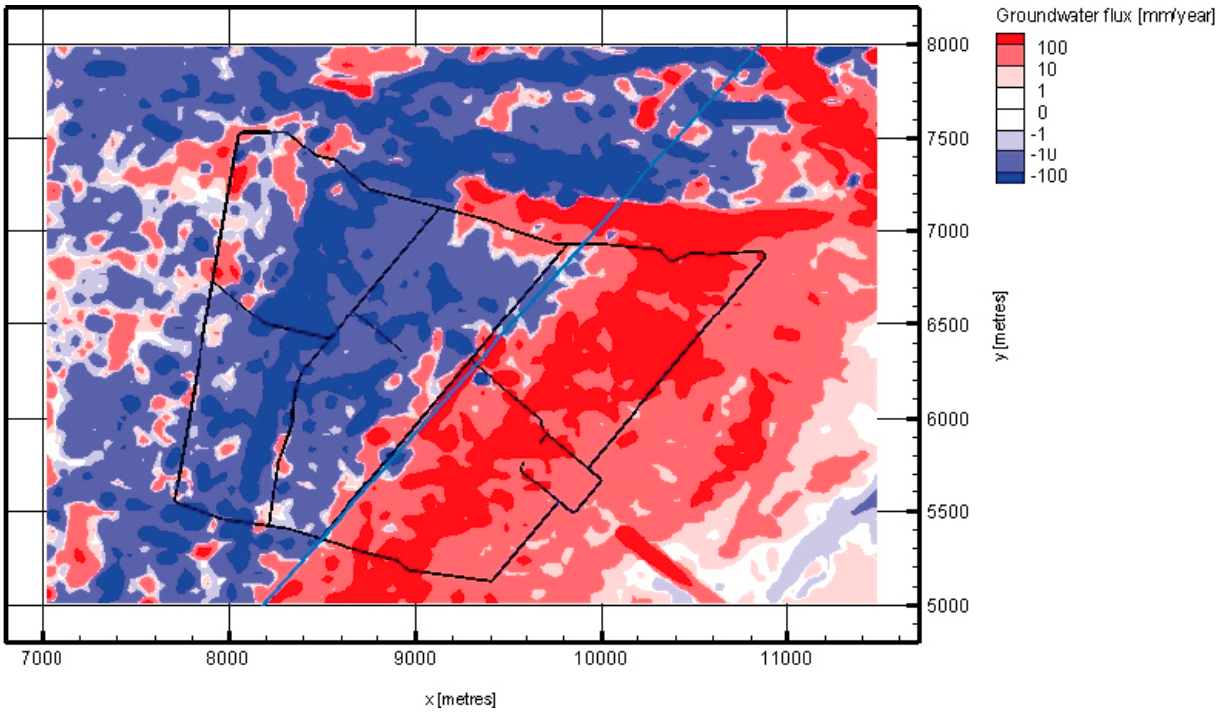

Figure E-6. *Horizontal view of the vertical Darcy flux in mm/y at –500 m elevation during glaciation when the ice sheet margin is at IFL II (blue line). Red colours show positive values (upward directed fluxes), whereas blue colours show negative values (downward directed fluxes). The short black lines indicate major tunnels. The y-axis points towards north.*

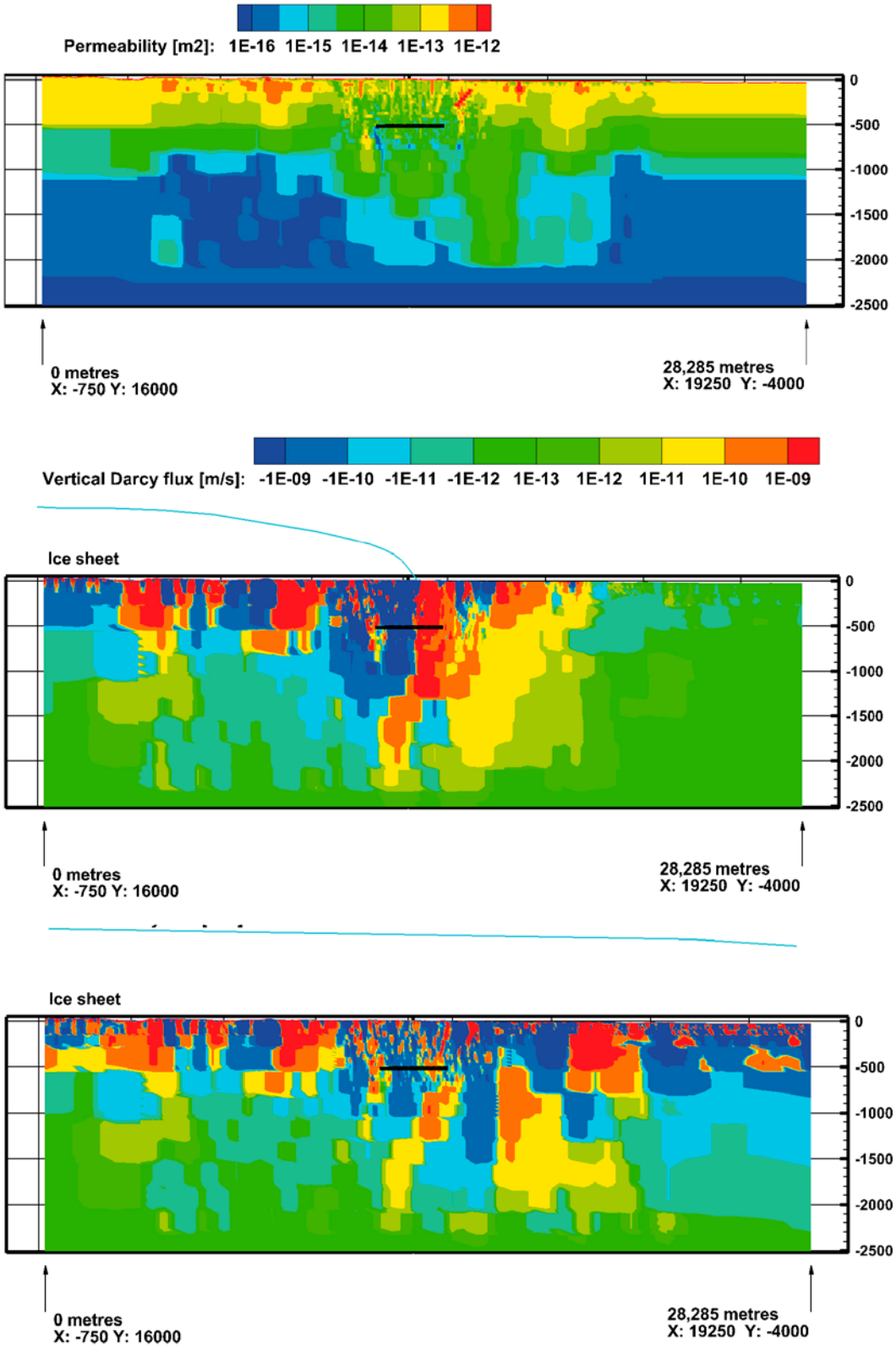

Figure E-7. *Top: Permeability field mapped on a NW-SE cross-section parallel to the ice flow direction. Middle: Vertical Darcy flux during glaciation when the ice sheet margin is at IFL II. Bottom: Vertical Darcy flux during glaciation when the ice sheet margin is at IFL IV. Positive values represent upward directed fluxes and negative values represent downward directed fluxes. The ice sheet thickness is illustrated with a blue curve. The black line at –500 m elevation shows the location of the repository.*

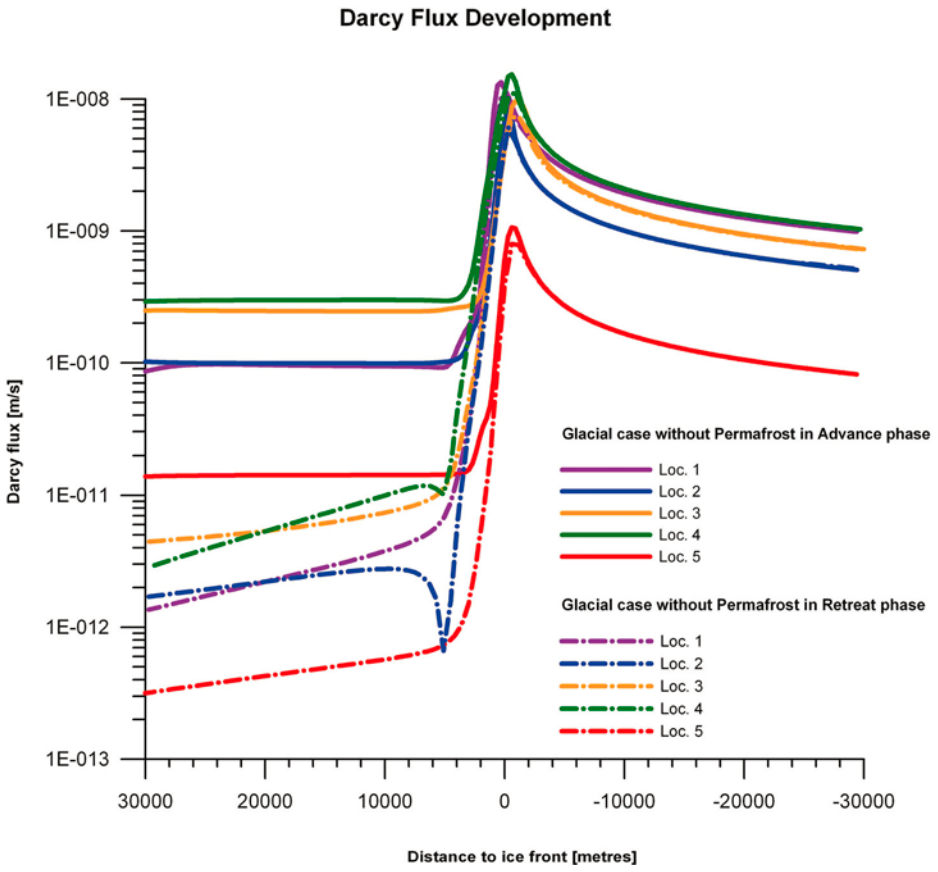

Figure E-8. *Darcy flux at ML 1-5 during glaciation and deglaciation. Positive values of "Distance to ice front" during glaciation mean that the ice sheet margin has not yet arrived to the measurement location. During the retreat, positive values indicate ice free conditions and an elevated sea level.*

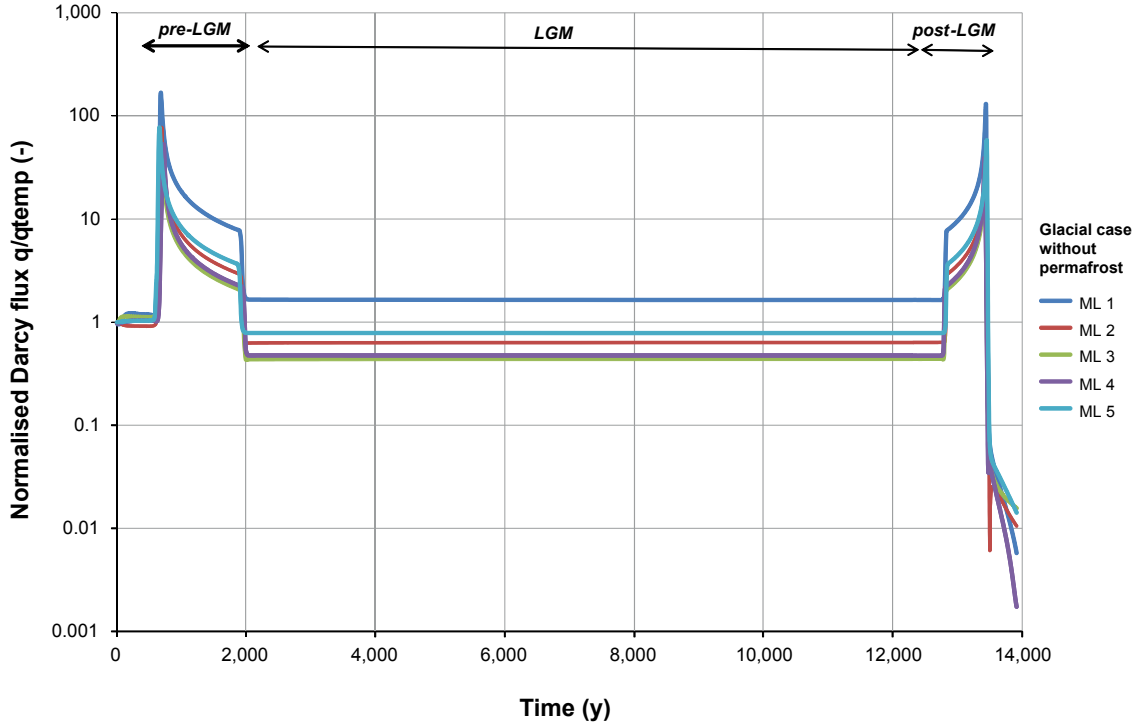

Figure E-9. *Normalised Darcy flux, q/q_{temp}, at ML 1-5 during glaciation (pre-LGM), complete ice coverage (LGM) and deglaciation (post-LGM).*

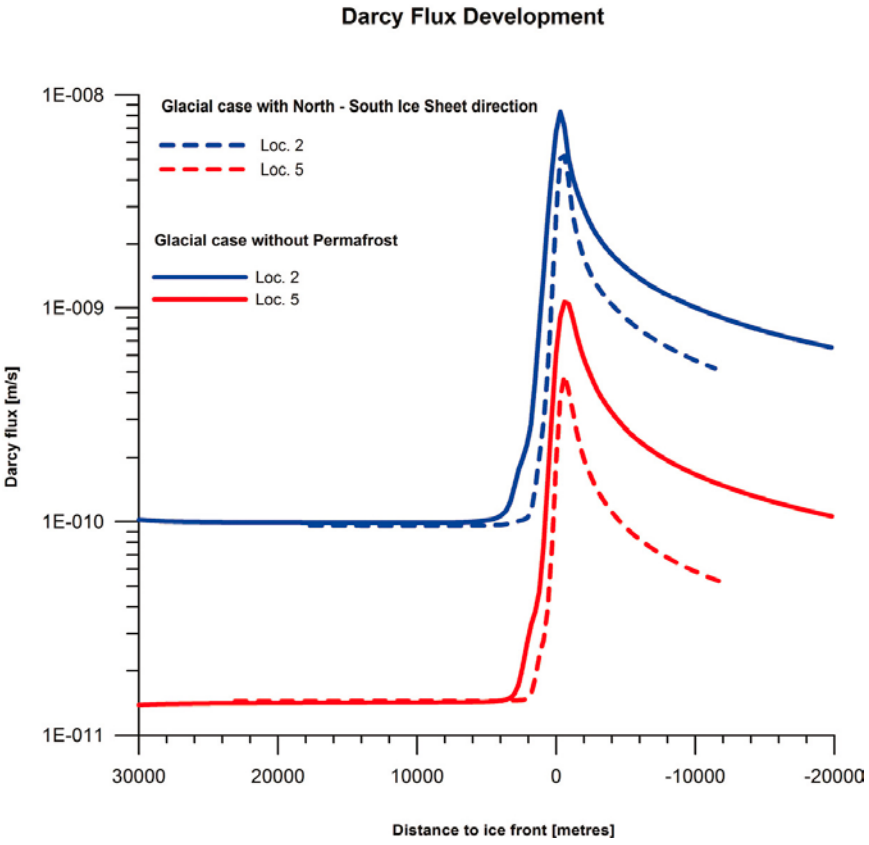

Figure E-10. *Comparison between the Darcy flux at ML 2 and ML 5 during glaciation for the conditions considered in cases (a) and (b). Positive distance values mean that the ice sheet margin has not yet arrived to the measurement locations.*

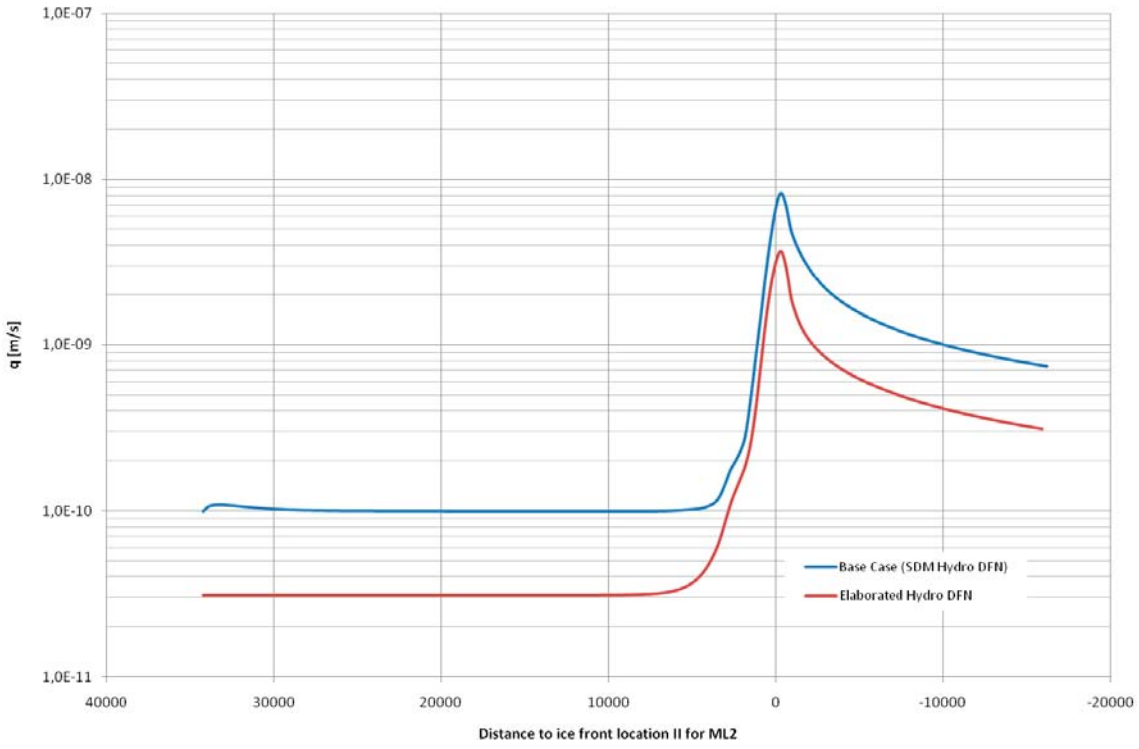

Figure E-11. *Comparison of the Darcy flux at ML 2 during glaciation for the conditions considered in cases (a) and (c). Positive distance values mean that the ice sheet margin has not yet arrived to the measurement locations.*

E.5 Salinity

The recharge of fresh meltwater during glaciation and deglaciation distorts the interface between fresh and saline groundwater. The saline groundwater is pushed forward and upward and some saline groundwater is flushed out of the model domain at the top boundary in the periglacial region in front of the ice sheet margin during the two ice sheet passages, see Figure E-12 and Figure E-13, respectively.

Figure E-14 shows the salinity field plotted on two cross-sections during glaciation when the ice sheet margin is at IFL II.

Figure E-15 shows that the distorted salinity field is weakly influenced by the transmissive deformation zones.

Figure E-16 shows the simulated fracture water salinity development at ML 1-5 during glaciation. All measurement localities experience an increase in salinity due to the upconing along the ice sheet margin. The peak salinity values at repository depth approach 1.5–2% at a time when the ice sheet margin is approximately 4 km from the site. The values shown at large x-axis numbers are illustrative of the inland flushing of the initial conditions with passing time during Temperate conditions.

Figure E-17 shows a comparison between the simulated fracture water salinity at the five measurement locations during glaciation and deglaciation.

Figure E-18 shows the normalised fracture water salinity (C/C_{temp}) at ML 1-5 during the glaciation (pre-LGM), the complete ice coverage (LGM) and the deglaciation (post-LGM). During the two ice-front passages, the salinities undulate considerably. Between the two ice front passages, the model domain is completely covered by ice for a long period of time. The observed initial recovery of the fracture water salinity during the period of complete ice coverage is primary due to an out diffusion of the available porewater salinity and not, as in the case of the Forsmark site, due to the slow, but continuous advective transport of salt from below since this salt interface at Laxemar is significant deeper after the pre-LGM phase.

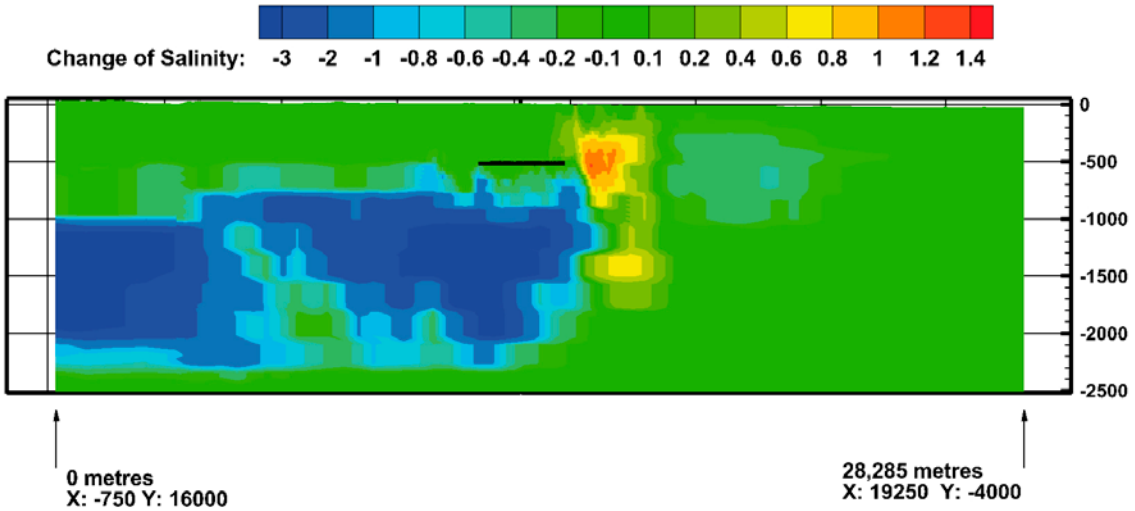

Figure E-12. *Visualisation of the change in fracture water salinity, $C–C_{temp}$, during glaciation when the ice sheet margin is at IFL II. The short black line in the centre indicates the location of the repository.*

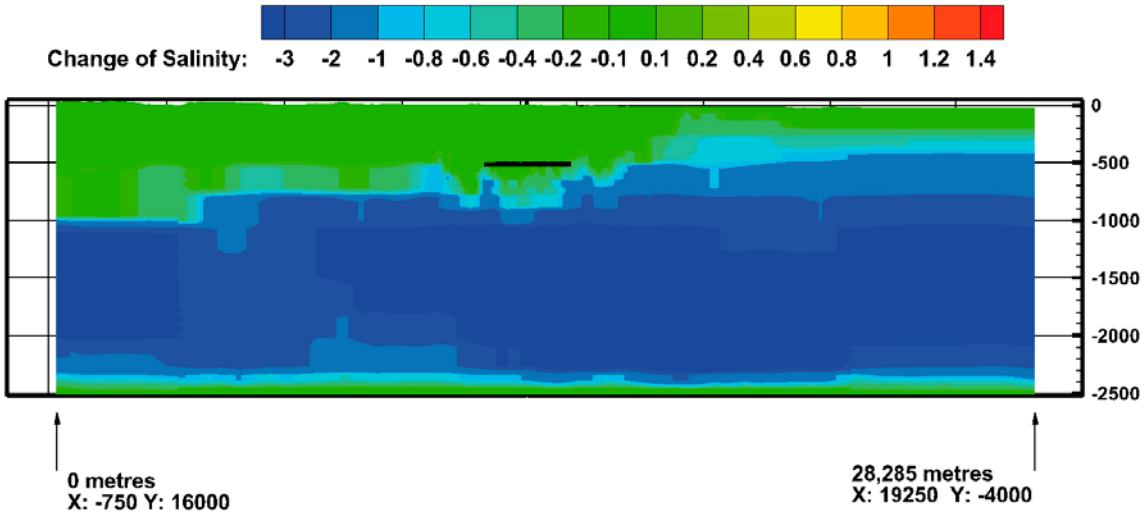

Figure E-13. *Visualisation of the change in fracture water salinity, $C–C_{temp}$, during deglaciation when the ice sheet margin is at IFL II. The short black line in the centre indicates the location of the repository.*

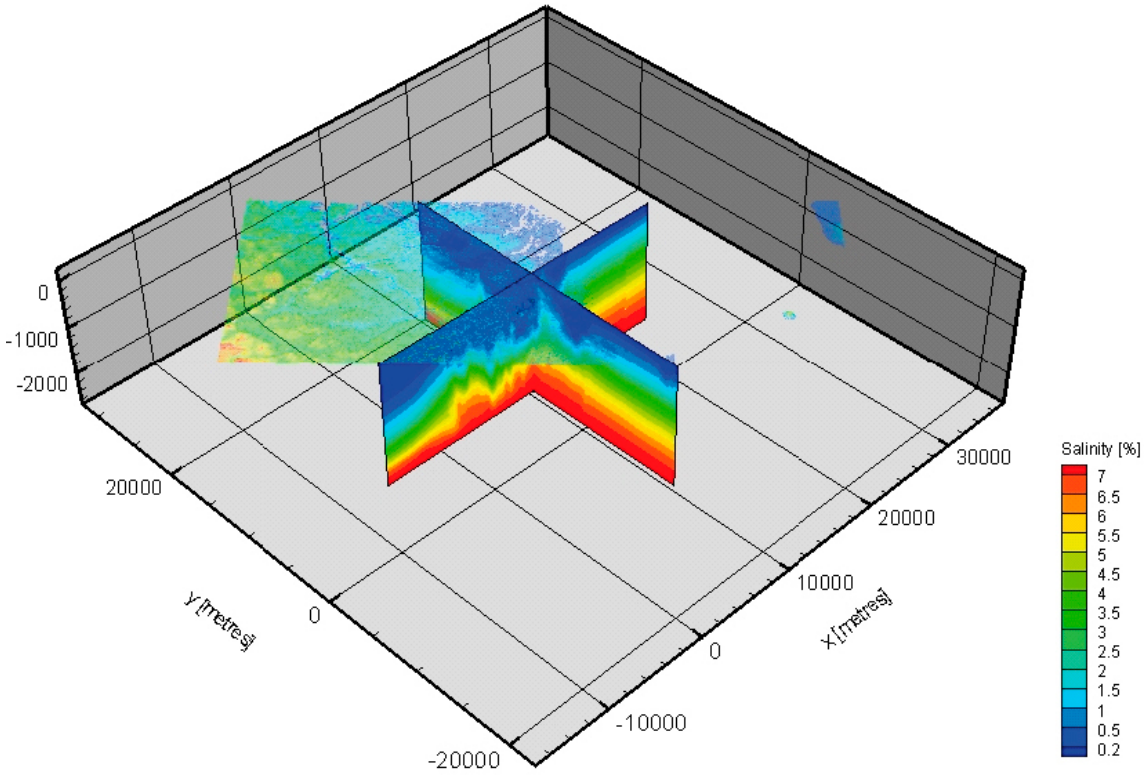

Figure E-14. *Visualisation of the salinity during glaciation when the ice sheet margin is at IFL II. The y-axis points towards north.*

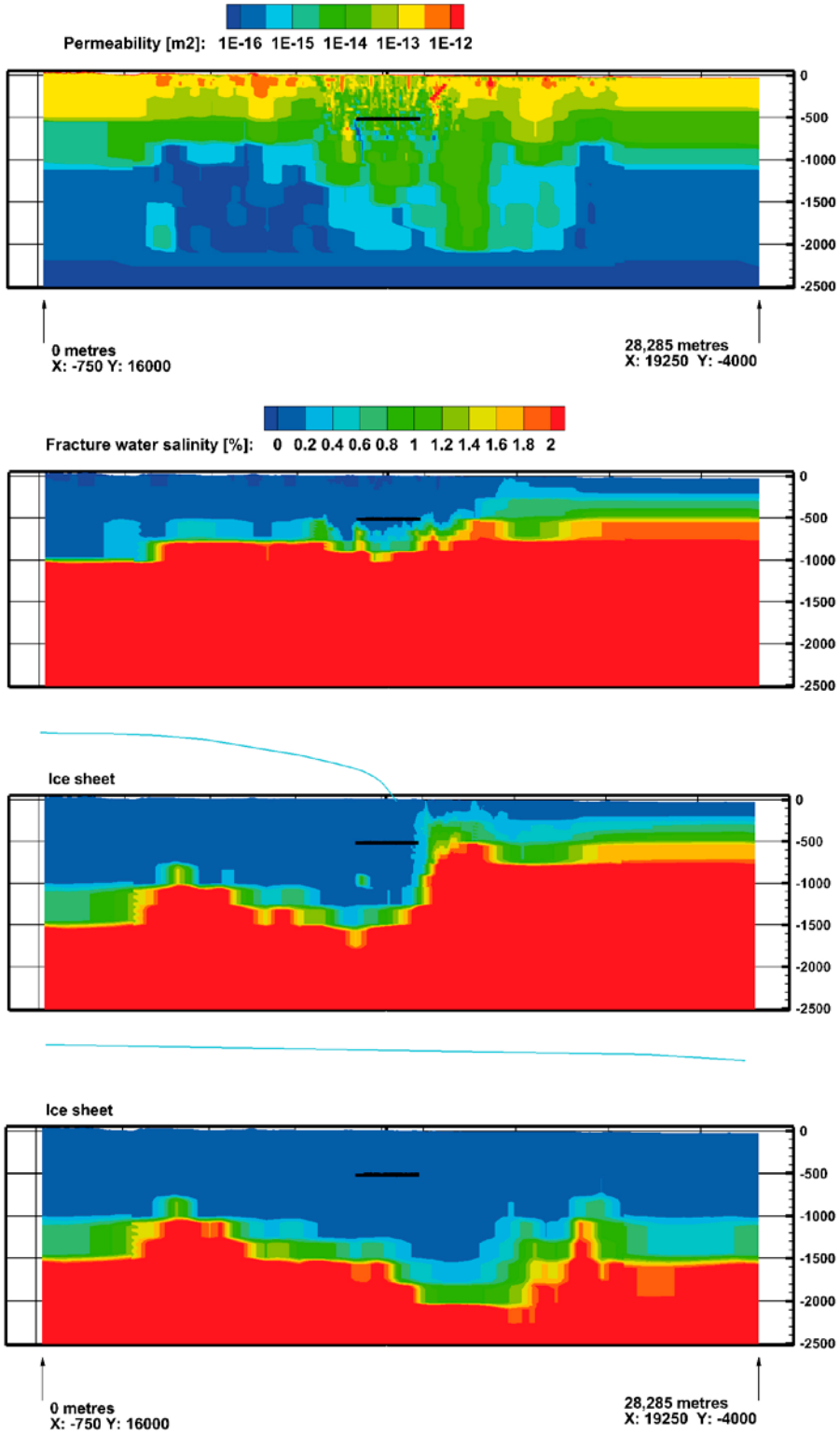

Figure E-15. *Top: Permeability field mapped on a NW-SE cross-section parallel to the ice flow direction. Upper Middle: Salinity field in the temperate case. Lower Middle: Salinity field when the ice sheet margin in case (a) is at IFL II. Bottom: Salinity field when the ice sheet margin in case (a) is at IFL IV. The ice sheet thickness is illustrated with a blue curve. The black line at –500 m elevation shows the location of the repository.*

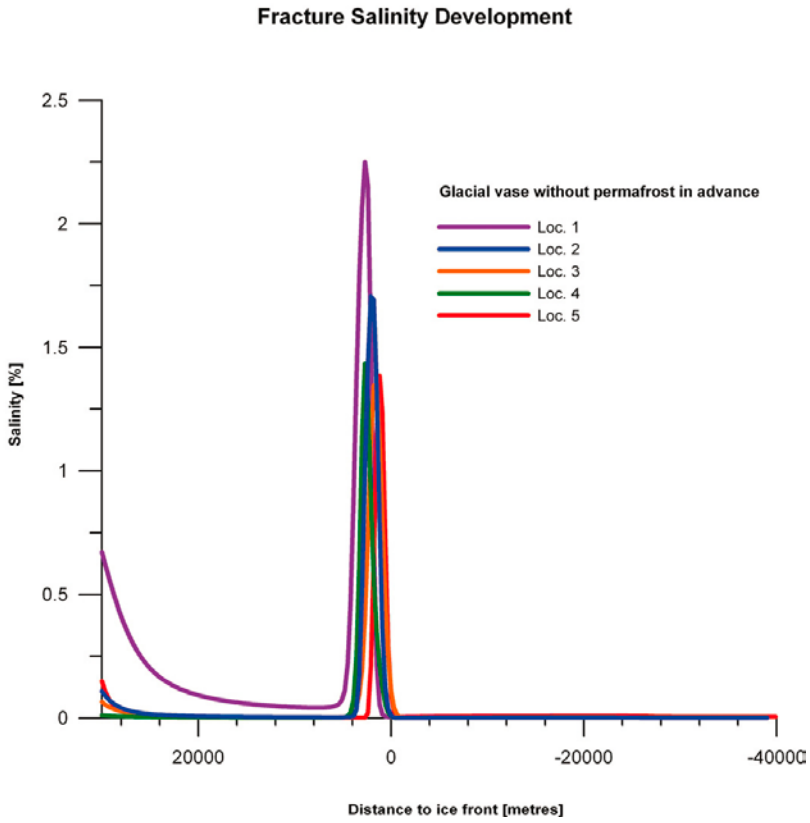

Figure E-16. *Fracture water salinity during glaciation at ML 1-5 during glaciation. Positive distance values mean that the ice sheet margin has not yet arrived at the measurement locations.*

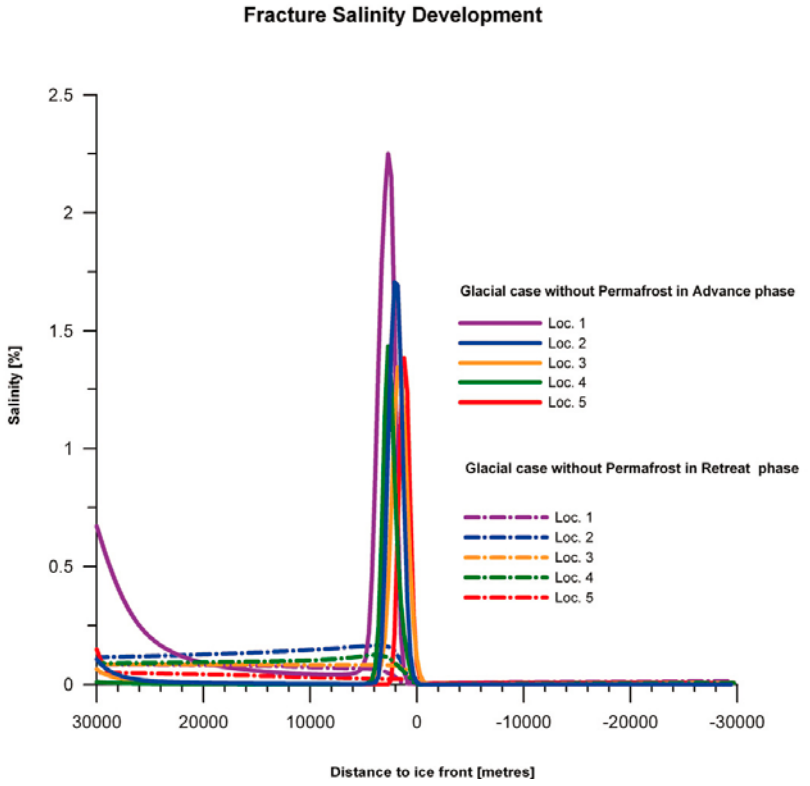

Figure E-17. *Fracture water salinity at ML 1-5 during glaciation and deglaciation in case (a). Positive values of "Distance to ice front" during glaciation mean that the ice sheet margin has not yet arrived at the measurement location. During the retreat, positive values indicate ice free conditions and an elevated sea level.*

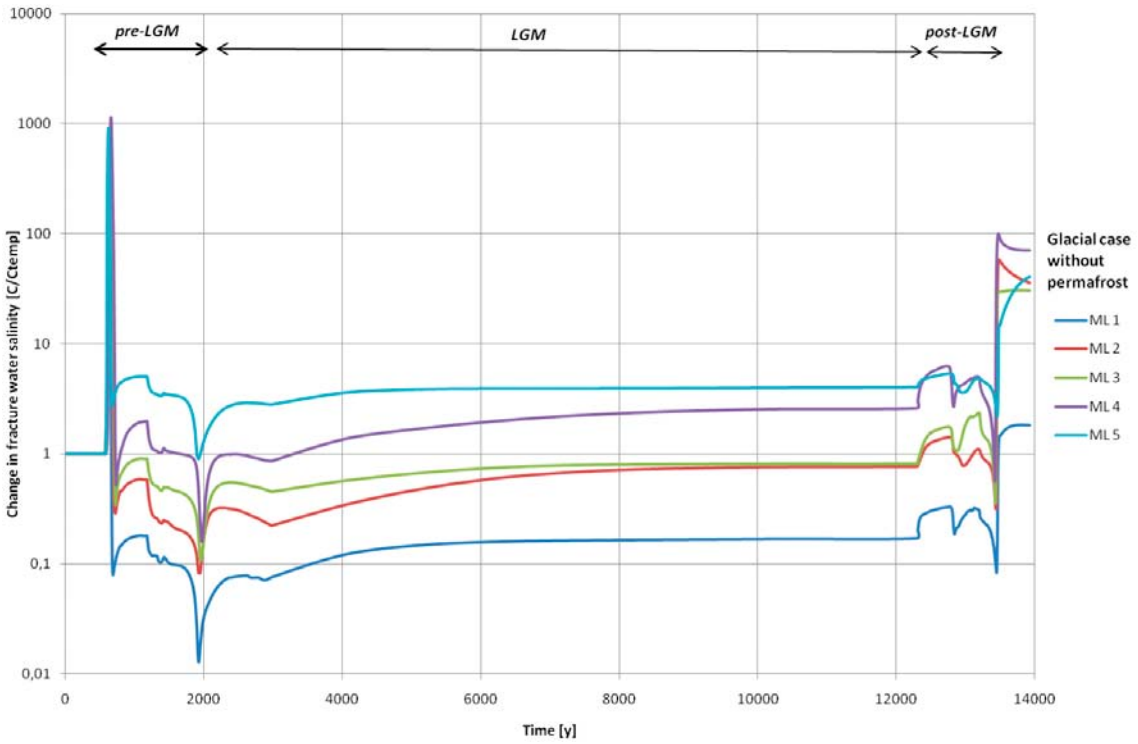

Figure E-18. *Normalised salinity, C/C_{temp}, at ML 1-5 during glaciation (pre-LGM), complete ice coverage (LGM) and deglaciation (post-LGM).*

E.6 Recharge and discharge locations

The repository contains 8,031 deposition hole positions. One particle is released at each deposition hole position and all particles are tracked backwards and forwards as a means to identify their recharge and discharge locations, respectively. It is noted that the ice sheet margin is fixed during the particle tracking, which is a simplification since the boundary conditions at the ground surface change continuously during glaciation and deglaciation.

Figure E-19 shows the results from the particle tracking when the ice-sheet margin during glaciation reached ice-front location II. Figure E-19 reveals that a number of particles recharge at the upstream boundary of the model domain, which suggests that the model domain is too small to give an undistorted view of all recharge locations for a fixed Darcy flux field. Nevertheless, it may be concluded that the present-day topographic water divides, which play an important role in recharge and discharge during temperate conditions, are of significantly diminished importance during glacial conditions.

In contrast, the majority of the discharge locations are well within the physical boundaries of the model domain and, as a matter of fact, often very close to the ice sheet margin.. At IFL II, the discharge pattern is strongly affected by the structural-hydraulic properties of the deformation zone model that exist within the regional flow domain of SDM-Site.

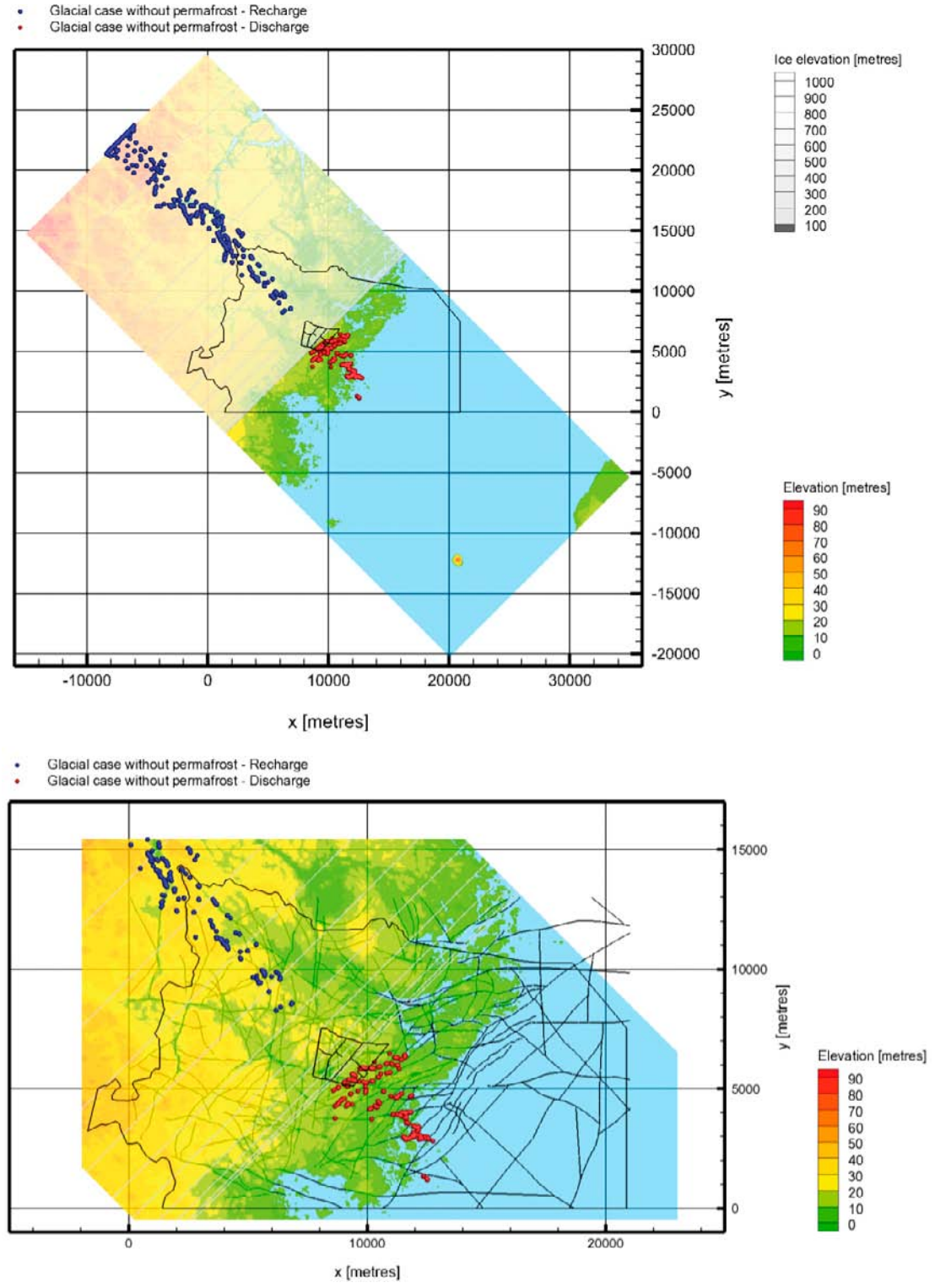

Figure E-19. *Recharge (blue) and discharge (red) locations during glaciation for 8,031 particles released at repository depth when the ice sheet margin is at IFL II. Entire domain (top) and SDM regional flow domain (bottom). The short black lines in the centre of each image indicate the location of major tunnels. The y-axis points towards north.*

E.7 Recharge performance measures

Particles are released at the 8,031 deposition hole positions and at the five measurement localities, ML 1-5, and tracked for 100 years. Not all of the released particles reach the ground surface within this period of time. Figure E-20, Figure E-21 and Figure E-22 show cumulative distribution (probability) plots of the recharge flow path lengths, travel times, and flow-related transport resistances for the particles released at the 8,031 deposition hole positions during glaciation when the ice sheet margin is at IFL II and IFL IV, respectively. For the sake of comparison, the corresponding cumulative distribution plots of these performance measures derived for the temperate case are also shown in these figures as well as the corresponding data for the particles released at ML 1-5 when the ice sheet margin is at IFL II.

Figure E-20 shows the cumulative distribution (probability) plots of the recharge flow path lengths (L_R). Typically, the presence of an ice sheet increases the recorded recharge flow path lengths compared to the temperate case. The shortest pathways are approximately 4 km, which is approximately of the same order of magnitude as the longest recharge pathway lengths during temperate conditions. During glaciation, a significant amount of particle recharge occurs at the upstream boundary. All measurement localities except ML 2 recharge in the area of the upstream boundary. The back-tracking from ML 2 does not reach the surface or boundaries within the tracked time (for ML 2 extended to 1,000 years). ML 2 is located almost straight beneath the ice front (some 100 metres downstream) where the shift between upward flow in-front of the ice sheet and downward flow beneath the tip of the ice sheet occur.

Figure E-21 shows the cumulative distribution (probability) plots of the recharge travel times ($t_{w,R}$). Typically, during the presence of an ice sheet at Laxemar the recorded recharge travel times are similar to those in the temperate case. The recharge travel times of ML 1 and ML 3-5 is are all within the range of recharge travel times recorded for the 8,031 deposition hole positions. It is worth noting that during 100 y, the ice sheet margin would have moved forward approximately 5 km if allowed to advance.

Figure E-22 show the cumulative distribution (probability) plots of the recharge flow-related transport resistances (F_R). Typically, the presence of an ice sheet decreases the recorded flow-related transport resistances compared to the temperate case. However, the smallest values recorded in the particle tracking are only slightly smaller than the smallest values recorded for the temperate case. Further, as the glaciation proceeds, as illustrated by IFL IV, the recorded recharge flow-related transport resistances increase and are somewhat greater as compared with the temperate case. The tracked measurement localities all have transport resistances clustered around the median value of the 8,031deposition hole positions.

For the sake of clarity, it is noted that the period of the ice-front passage is relatively limited and that the methodology used here for the particle tracking probably creates unduly low values of the recharge flow path lengths, advective travel times, and flow-related transport resistances.

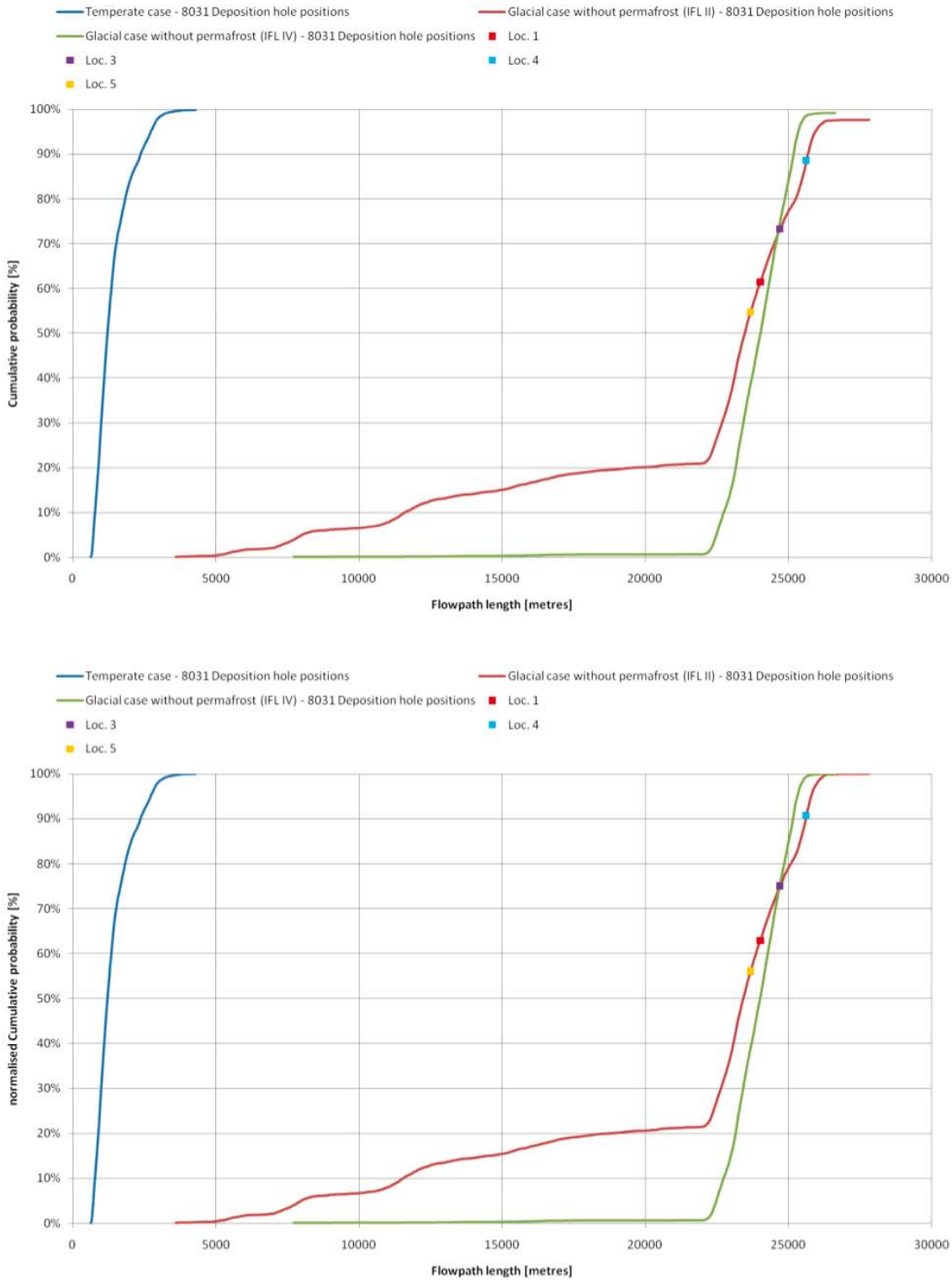

Figure E-20. *Cumulative distribution (probability) plots of the simulated recharge flow path lengths, L_R, when the ice sheet margin is at IFL II and IV, respectively. The distribution for the temperate case is also shown as well as the data for ML 1-5 at IFL II. The maximum value in the upper plot is set to 100% in the lower plot.*

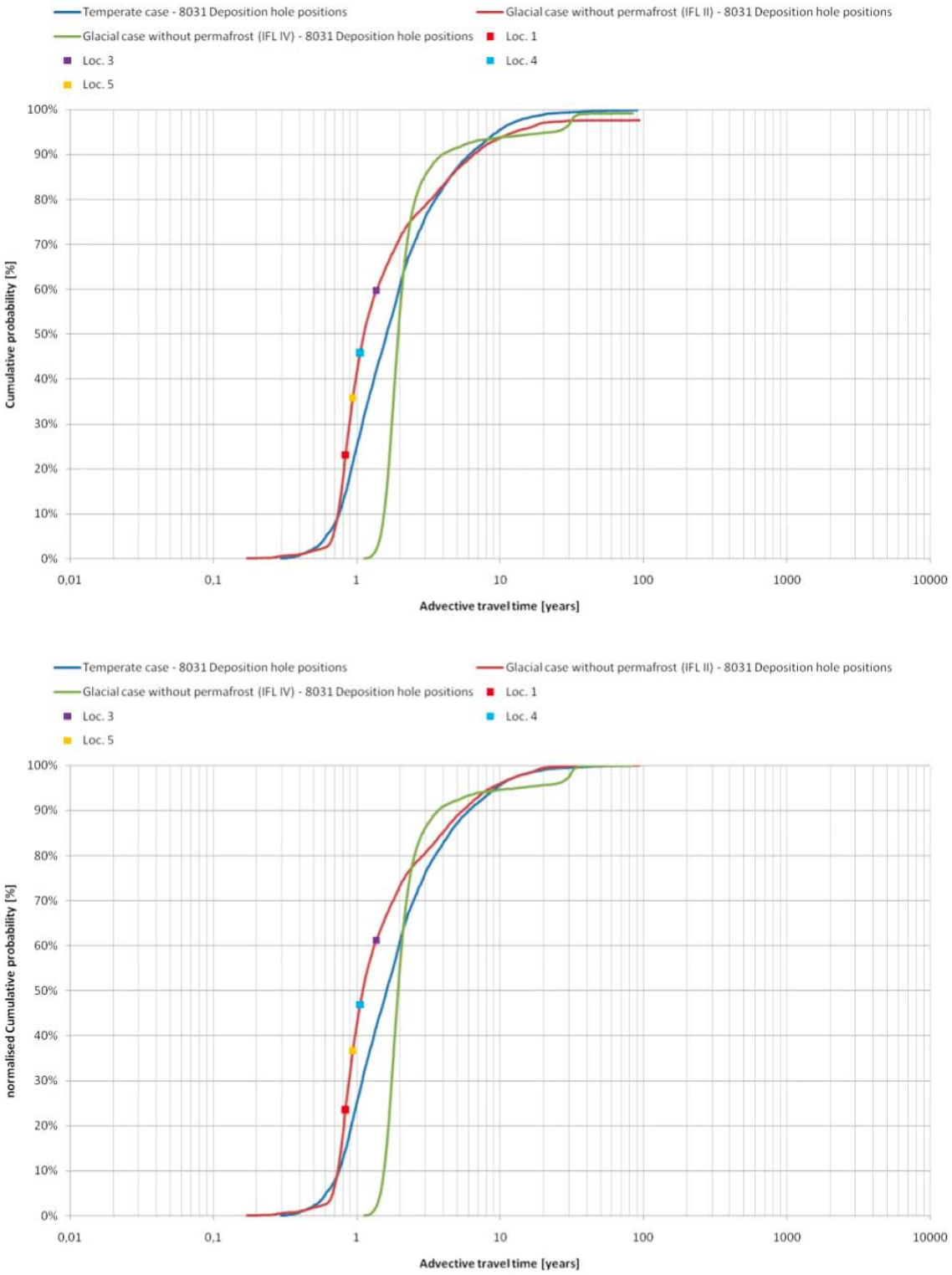

Figure E-21. *Cumulative distribution (probability) plots of the simulated recharge travel times, $t_{w,R}$, when the ice sheet margin is at IFL II and IV, respectively. The distribution for the temperate case is also shown as well as the data for ML 1-5 at IFL II. The maximum value in the upper plot is set to 100% in the lower plot.*

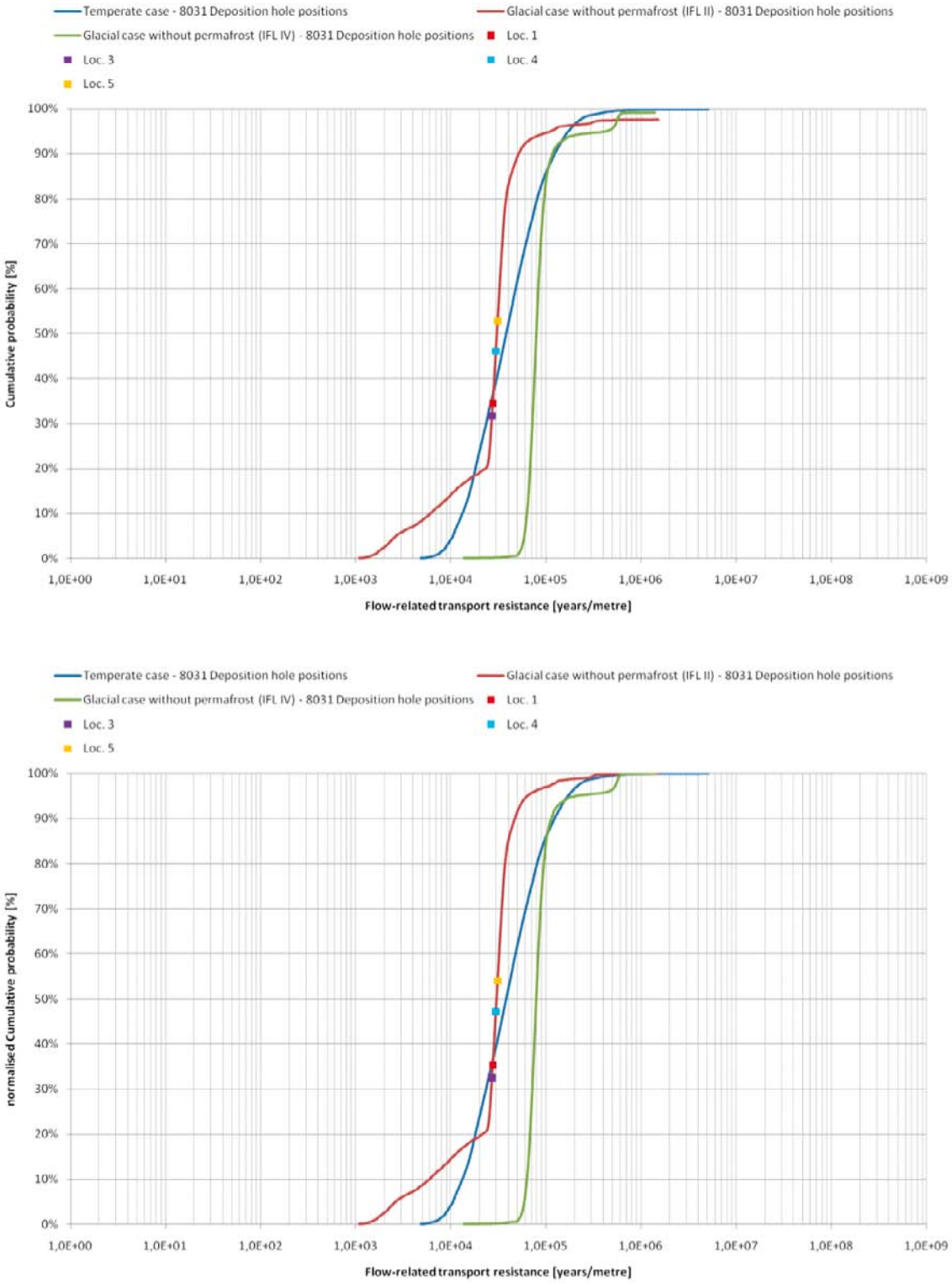

Figure E-22. *Cumulative distribution (probability) plots of the simulated recharge flow-related transport resistance. The distribution for the temperate case is also shown as well as the data for ML 1-5 at IFL II. The maximum value in the upper plot is set to 100% in the lower plot.*

E.8 Discharge performance measures

Particles are released at the 8,031deposition hole positions and at the five measurement localities, ML 1-5, and tracked for 100 years. Not all of the released particles reach the ground surface within this period of time. Figure E-23, Figure E-24 and Figure E-25 show cumulative distribution (probability) plots of the discharge flow path lengths, travel times, and flow-related transport resistances for the particles released at the 8,031 deposition hole positions when the ice sheet profile addressed is at ice-front locations II and IV, respectively. For the sake of comparison, the corresponding cumulative distribution plots of these performance measures derived for the temperate case are also shown in these figures as well as the corresponding data for the particles released at the ML 1-5 when the ice sheet margin is at IFL II.

Figure E-23 shows the cumulative distribution (probability) plots of the discharge flow path lengths (L_D). Figure E-23 shows that the passage of the ice front at IFL II does not seem to affect the minimum value of the discharge flow path length as compared with the Temperate case. However, the distribution is more affected, as 90% of the flowpaths rather than 70% have lengths of less than 5 km. As the ice moves on, the flow path lengths becomes successively larger as the majority of particles travel all the way to the ice margin before discharging. Figure E-23 shows that ML 1-5 have flow path lengths that fall within the range of the 8,031 deposition hole positions.

Figure E-24 shows the cumulative distribution (probability) plots of the discharge travel times ($t_{w,D}$). As expected, the travel times are shorter when the ice front is at IFL II than at IFL IV. In comparison with Temperate case, the discharge travel times are lowered by 0.5 to 1 orders of magnitude and approximately 98% of particles discharge within 100 y; the fastest particles discharge after some weeks. As the ice sheet margin proceeds, the sub-glacial travel times approach the values recorded for the temperate case. It is worth noting that during 100 y, the ice sheet margin would have moved forward approximately 5 km if allowed to advance.

Figure E-25 shows the cumulative distribution (probability) plots of the discharge flow-related transport resistances (F_D). The flow-related transport resistance is in general decreased by 1–1.5 orders of magnitude. As the ice sheet margin proceeds, the recorded values of the flow-related transport resistances approach and exceed the values recorded for the temperate case. The measurement localities all have values that fall quite well around the median value for the 8,031 deposition hole positions, with the possible exception of ML 5 that has a lower flow-related transport resistance as compared with the other four measurement localities, likely due to the fact that ML 5 is found well beneath the ice sheet for the time tracked.

For the sake of clarity, it is noted that the period of the ice front passage is relatively limited and that the methodology used here for the particle tracking probably creates unduly low values of the recharge flow path lengths, advective travel times, and flow-related transport resistances.

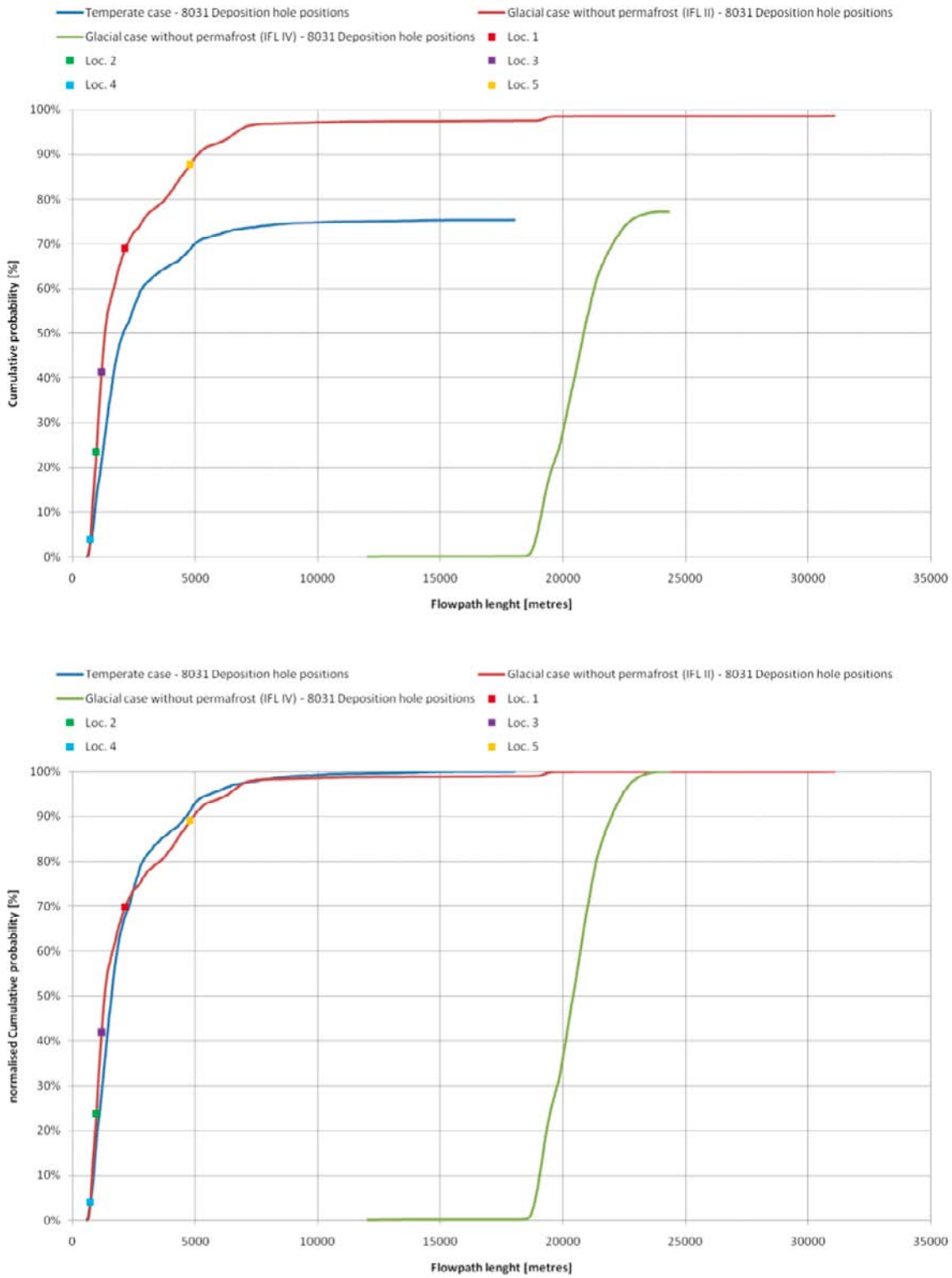

Figure E-23. *Cumulative distribution (probability) plots of the simulated discharge flow path lengths, L_D, when the ice sheet margin is at IFL II and IV, respectively. The distribution for the temperate case is also shown as well as the data for ML 1-5 at IFL II. The maximum value in the upper plot is set to 100% in the lower plot.*

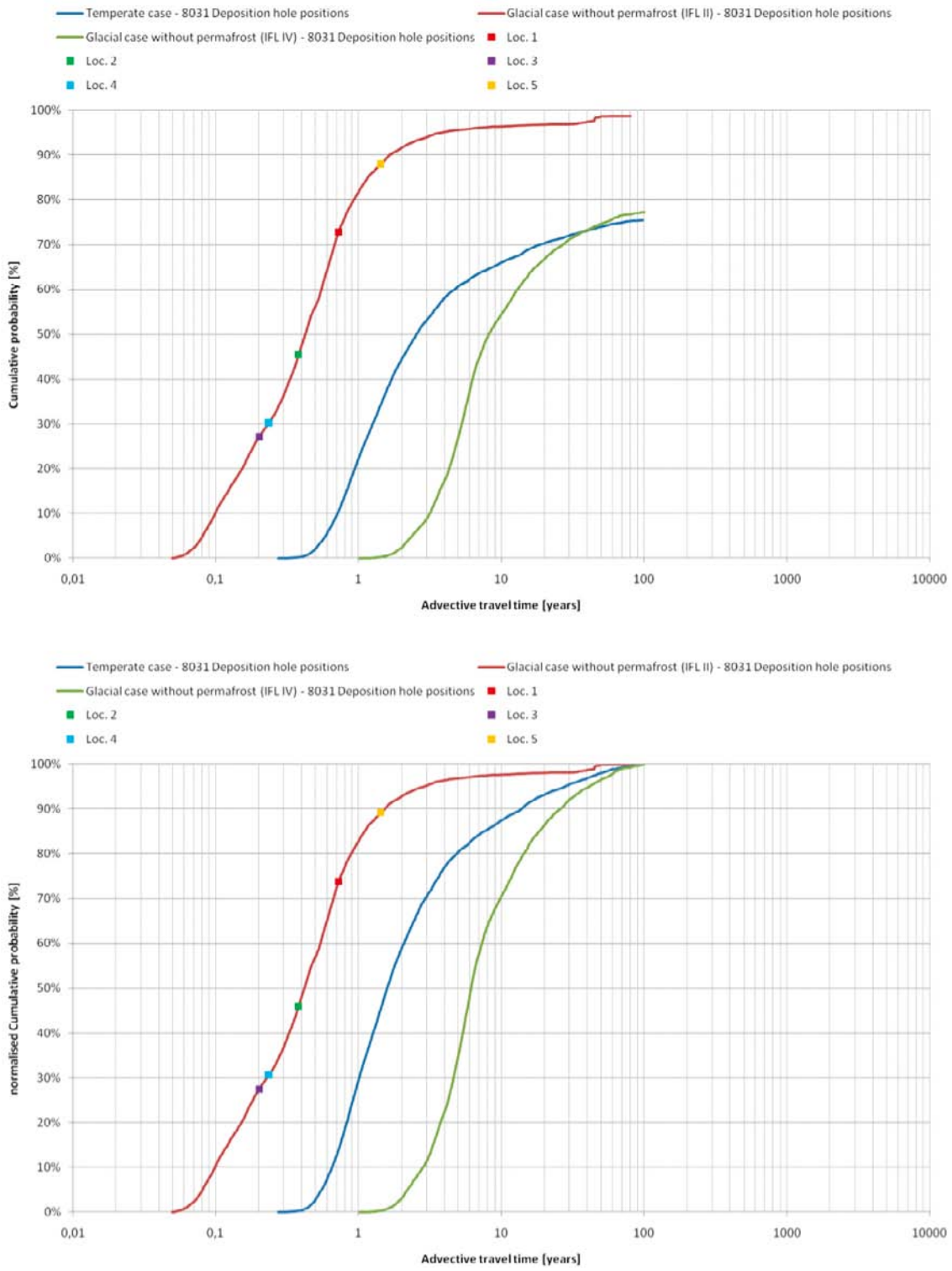

Figure E-24. *Cumulative distribution (probability) plots of the simulated discharge travel times, $t_{w,D}$, when the ice sheet margin is at IFL II and IV, respectively. The distribution for the temperate case is also shown as well as the data for ML 1-5 at IFL II. The maximum value in the upper plot is set to 100% in the lower plot.*

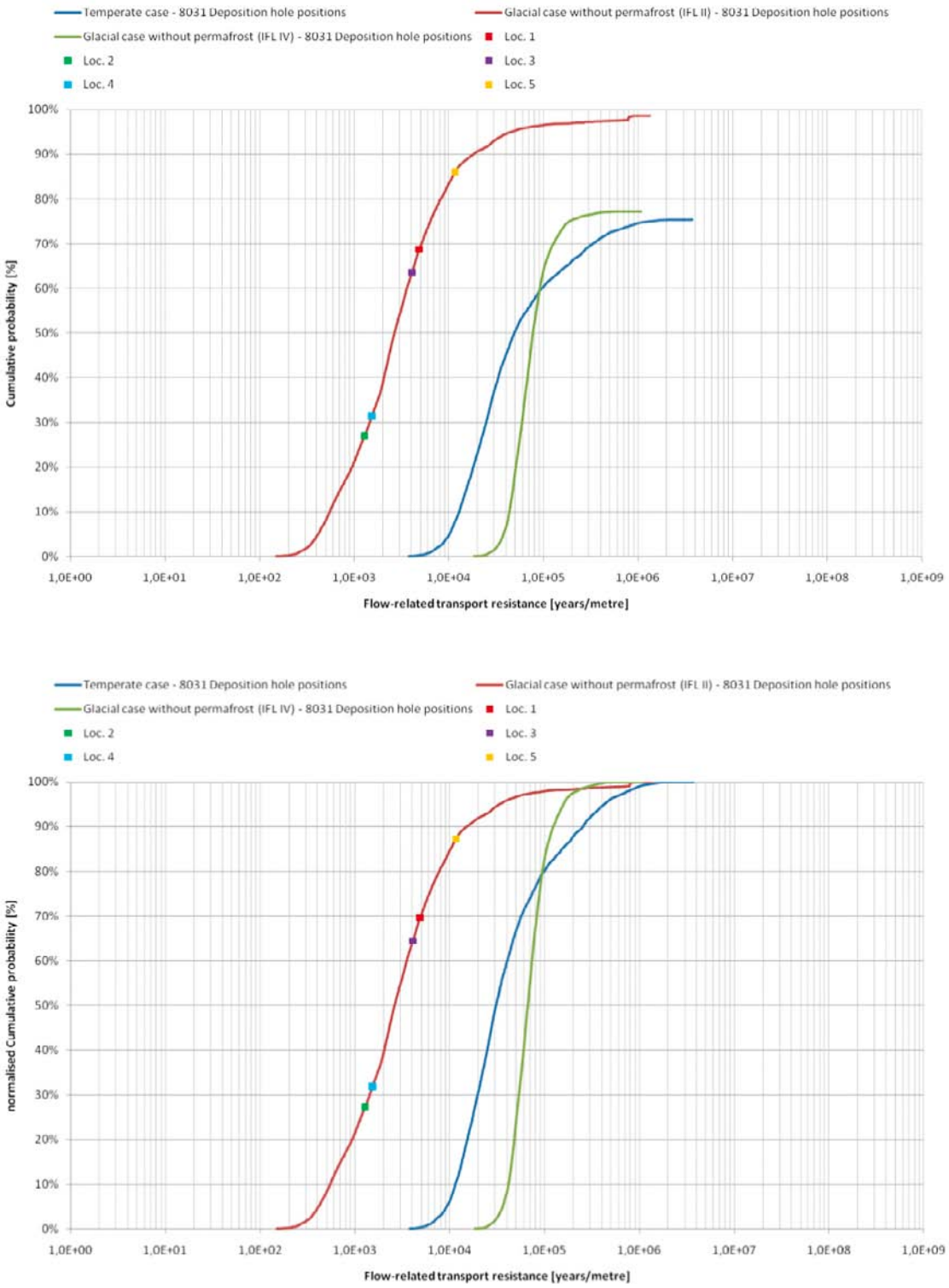

Figure E-25. *Cumulative distribution (probability) plots of the simulated discharge flow-related transport resistances, F_D, when the ice sheet margin is at IFL II and IV, respectively. The distribution for the temperate case is also shown as well as the data for ML 1-5 at IFL II. The maximum value in the upper plot is set to 100% in the lower plot.*

Appendix F

Scenario B: Glacial climate conditions with permafrost

F.1 Introduction

All plots shown is this appendix refer to case (d), see Table 5-1 and Figure 5-3.

F.2 Top boundary conditions

The grayish area in Figure F-1 indicates the ice sheet thickness when the ice sheet margin during glaciation is at ice-front location II (IFL II). The speed of the ice sheet margin is 50 m/y and it reaches IFL II after approximately 700 years in relation to the north-west boundary of the model domain.

Ice-free elevations above –8 m are subjected to permafrost; the temperature is fixed at –4.2°C. Ice-free elevations below –8 m are modeled as taliks; the temperature is fixed at +4°C. Beneath the ice sheet, the temperature is set to +0.01°C except for a 2 km long tongue behind the ice sheet margin where the temperature increases linearly from –4.2°C to +0.01°C.

A pressure equal to 92% of the weight of the ice sheet thickness is specified on the top boundary where the temperature is +0.01°C. Elsewhere, the pressure is set to zero in all terrestrial parts and to the hydrostatic pressure below the ice-free sea, lakes and taliks.

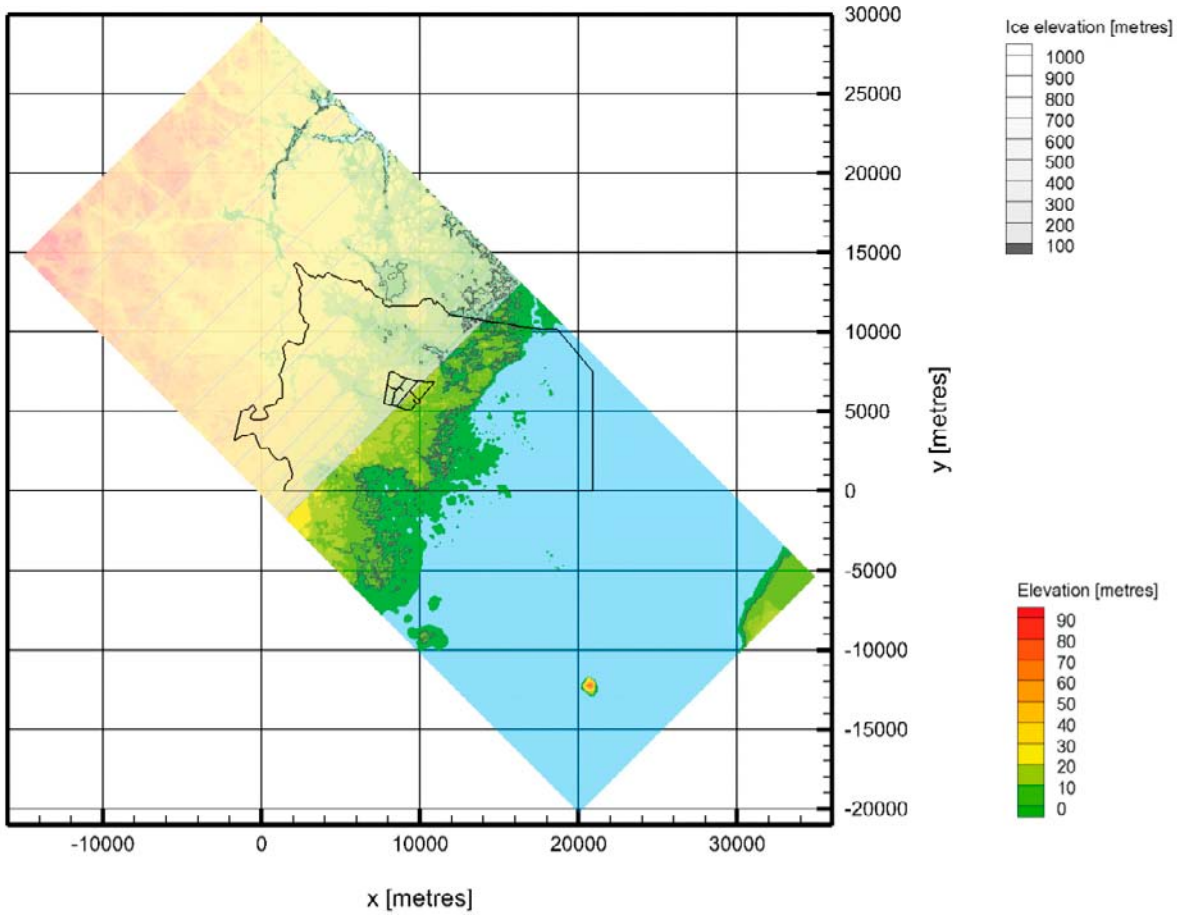

Figure F-1. *Visualisation of the ice thickness when the ice sheet margin in case (d) is at IFL II. Ice-free elevations above –8 m are subjected to permafrost and are shown in dull green (> 0 m) or green (0 to –8 m). Ice-free elevations below –8 m are shown in blue. When the ice sheet margin is at IFL II the shoreline is only some 4 kilometres downstream of the ice margin. The y-axis points towards north.*

F.3 Pressure

Figure F-2 shows the pressure (*P*) mapped on the NW-SE cross-section (see Figure D-1) when the ice sheet margin is at ice-front location II. The pressure gradient between the ice sheet and the taliks is very different from the pressure gradient shown in Figure E-2 for the glacial case without permafrost.

Figure F-3 shows the simulated development of the pressure during glaciation at the five measurement localities (ML 1-5). The pressures develop similarly at these localities. The effect of the approaching ice sheet margin is clearly visible well before the ice sheet margin is close to ML 1-5.

It is expected that a permafrost zone beneath an advancing ice sheet margin will exist, see /SKB 2010/. However, great uncertainties in the size of this zone prevail; hence in /Vidstrand et al. 2010/ a sensitivity case is used in order to see the effect of not including such a zone. The conclusion therein was that for the tested range the effects are minor.

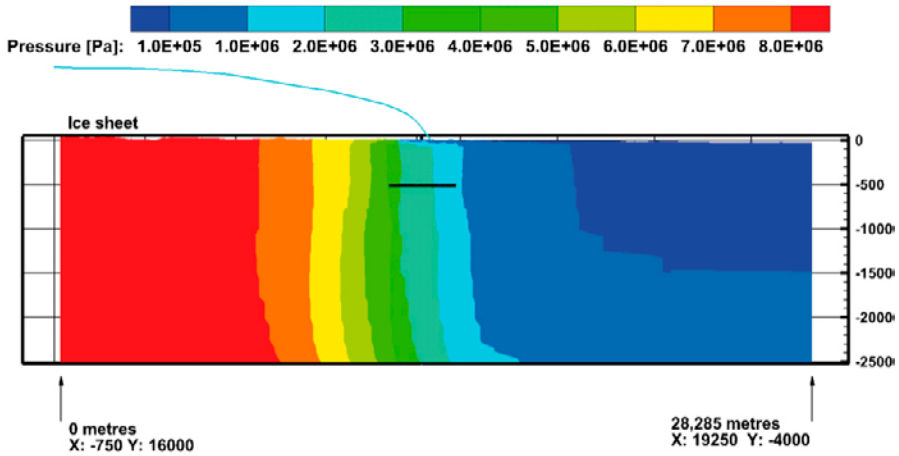

Figure F-2. *Visualisation of the pressure during glaciation when the ice sheet margin is at IFL II. The short black line in the centre indicates the location of the repository.*

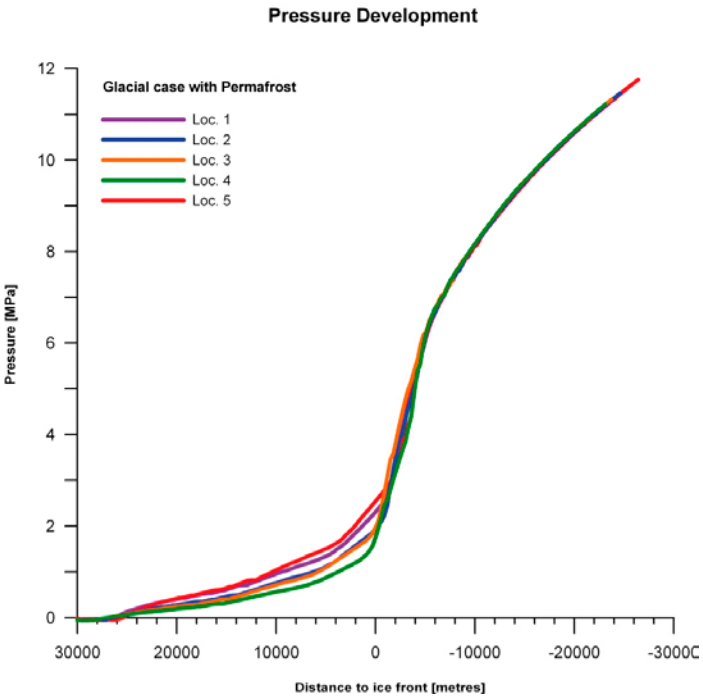

Figure F-3. *Pressure at ML 1-5 during glaciation. Positive distance values mean that the ice sheet margin has not yet arrived to the measurement locations.*

F.4 Darcy flux

Figure F-4 shows the simulated spatial distribution of the vertical Darcy flux across a plane at –500 m elevation. The plane passes through the focused area and the location of the repository. Figure F-4 shows the vertical Darcy flux when the front of the advancing ice sheet margin addressed in case (d) is at ice-front location II, i.e. immediately above the repository. Little effect of the ice sheet margin is observed due to the frozen ground "barrier" beneath, however as compared to temperate conditions the velocities are significant higher.

Figure F-5 shows the vertical Darcy flux mapped on a NW-SE cross-section parallel to the ice-flow direction addressed in case (d). Observe the "transient" permeability field due to the frozen ground conditions.

Figure F-6 shows the simulated changes in the Darcy flux, (q/q_{temp}), at the five measurement localities during an ice sheet cycle that simulates the ice sheet profile addressed in case (d). (After the passage of the ice front, the Darcy fluxes merge with that for case (a), which is copied into Figure F-12 from IFL IV and onward.). During the two ice-front passages, the fluxes are up to 100 times greater than those prevailing during temperate conditions. Between the two ice-front passages, the model domain is completely covered by ice for a long period of time. When model domain is completely covered by ice for a long period of time, the simulated Darcy fluxes at ML 2-5 are between 10–30% lower than the fluxes during temperate conditions, whereas they are approximately 30% higher at ML 1.

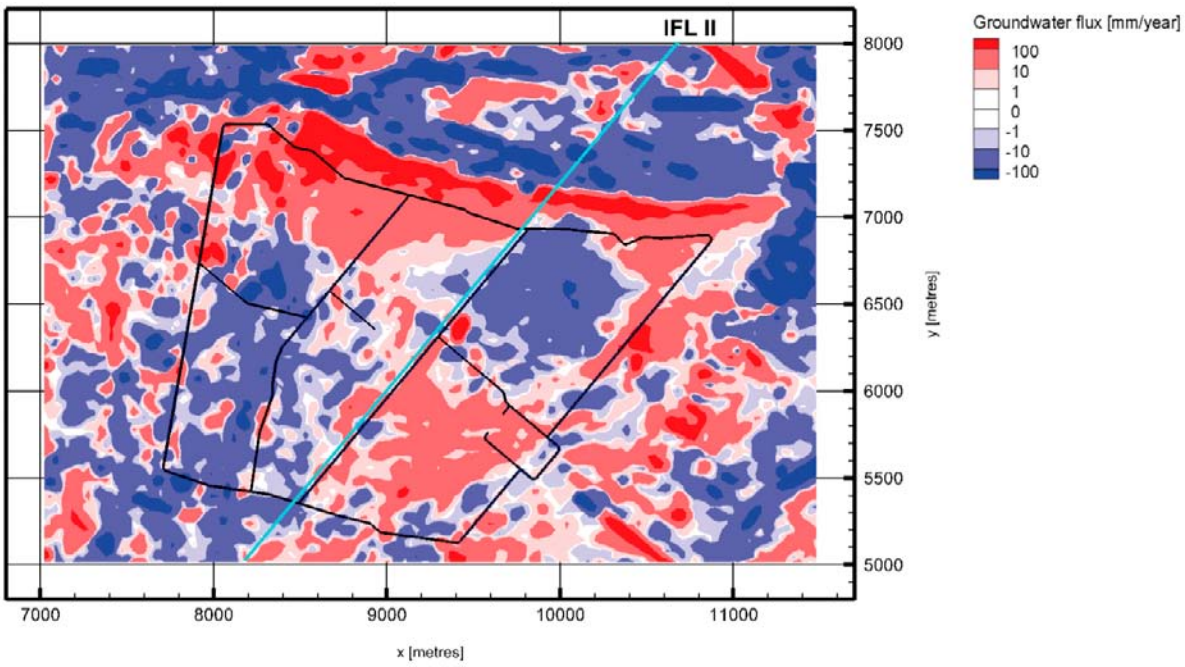

Figure F-4. *Horizontal view of the vertical Darcy flux in mm/y at –500 m elevation during glaciation when the ice sheet margin is at IFL II (ice blue line). Red colours show positive values (upward directed fluxes), whereas blue colours show negative values (downward directed fluxes). The short black lines indicate major tunnels. The y-axis points towards north.*

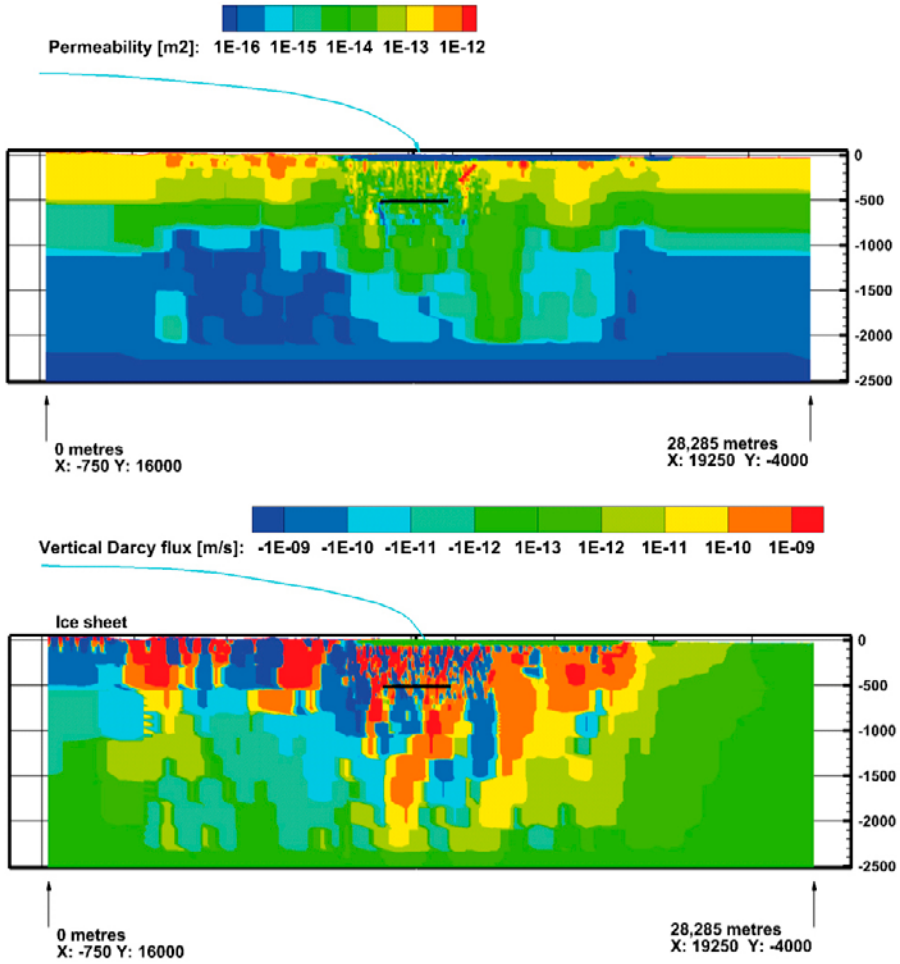

Figure F-5. *Top: Permeability field during glaciation mapped on a NW-SE cross-section parallel to the ice-flow direction when the ice sheet margin is at IFL II. Bottom: Vertical Darcy flux when the ice sheet margin is at IFL II. The ice sheet thickness is illustrated with a blue curve. The black line at –500 m elevation shows the location of the repository.*

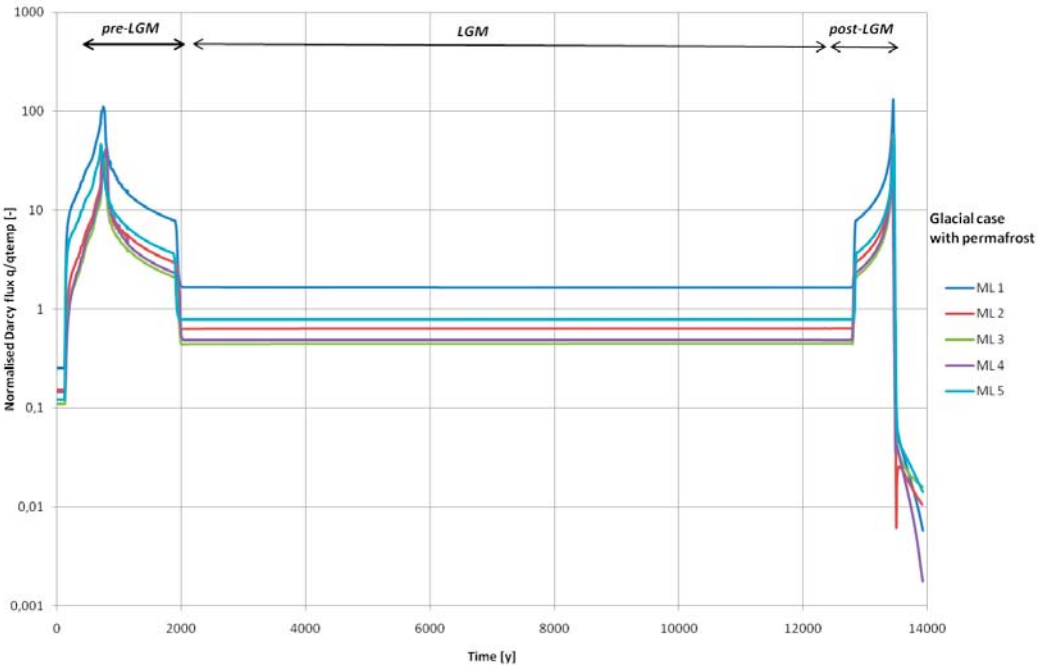

Figure F-6. *Normalised Darcy flux, q/q_{temp}, at ML 1-5 during glaciation (pre-LGM), complete ice coverage (LGM) and deglaciation (post-LGM).*

F.5 Salinity

Figure F-6 shows the salinity field in terms of a NW-SE cross-section (see Figure D-1) when the advancing ice sheet margin is at ice-front location II. The shape of the up-coning in the target volume is here mainly influenced by the presence of frozen ground inhibiting discharge at the surface along the ice margin. The permafrost layer enhances the pushing forward of the saltwater that eventually discharges in taliks occurring along the predicted future shoreline.

Figure F-7 shows the change in salinity field in terms of a NW-SE cross-section (see Figure D-1) when the advancing ice sheet margin is at ice-front location II. The most noteworthy difference with the glacial case without permafrost is the significantly smaller flushing that occurs during the glacial case with permafrost.

Figure F-8 shows the simulated fracture water salinity development at the five measurement localities during the advance of the ice sheet addressed in case (d). All measurement localities experience an increase in salinity due to up-coning caused by the approaching ice sheet margin. The salinity peak values at repository depth approach 0.3% when the ice front is some 20 km away; these values are thereafter slowly decreasing until the ice sheet margin has passed over the measurement localities. After the passage the repository depth is flushed with fresh water.

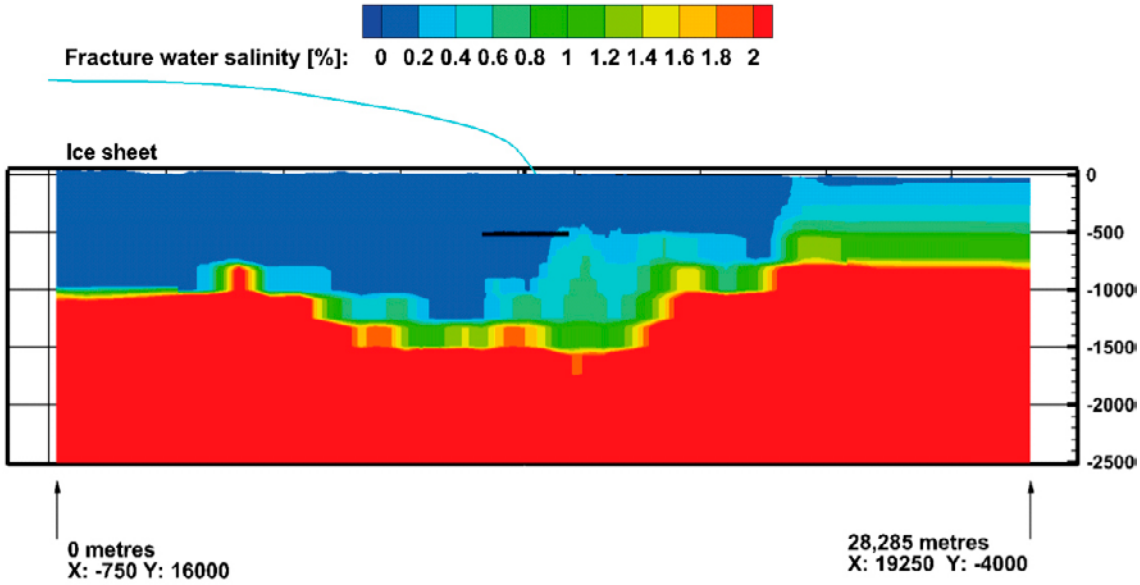

Figure F-7. *Visualisation of the salinity during glaciation when the ice sheet margin is at IFL II. The short black line in the centre indicates the location of the repository.*

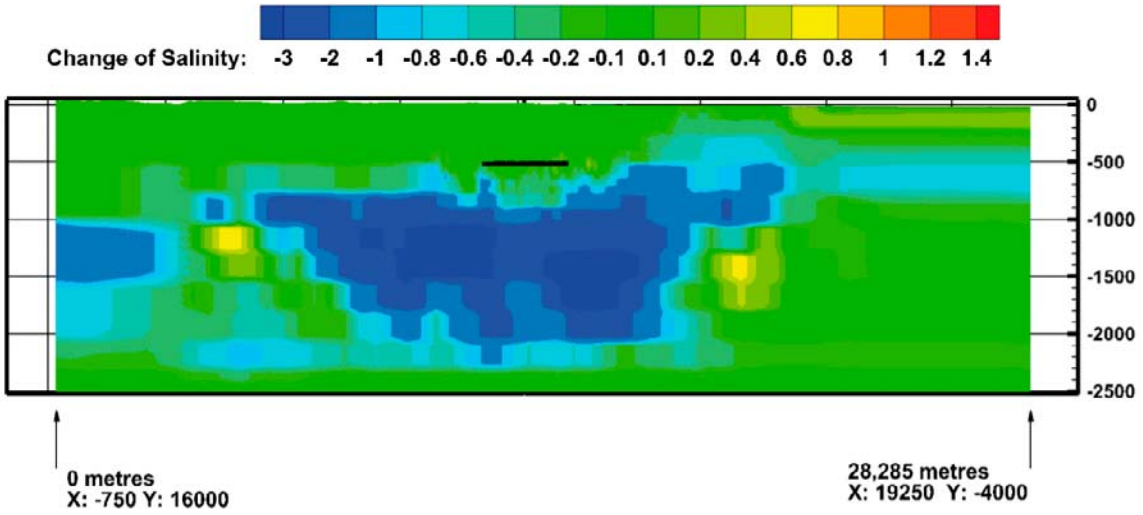

Figure F-8. *Change in the salinity field, $C_{glac,IFL\ II} - C_{glac,IFL\ 0}$, during glaciation when the ice sheet margin is at IFL II. The short black line in the centre indicates the location of the repository.*

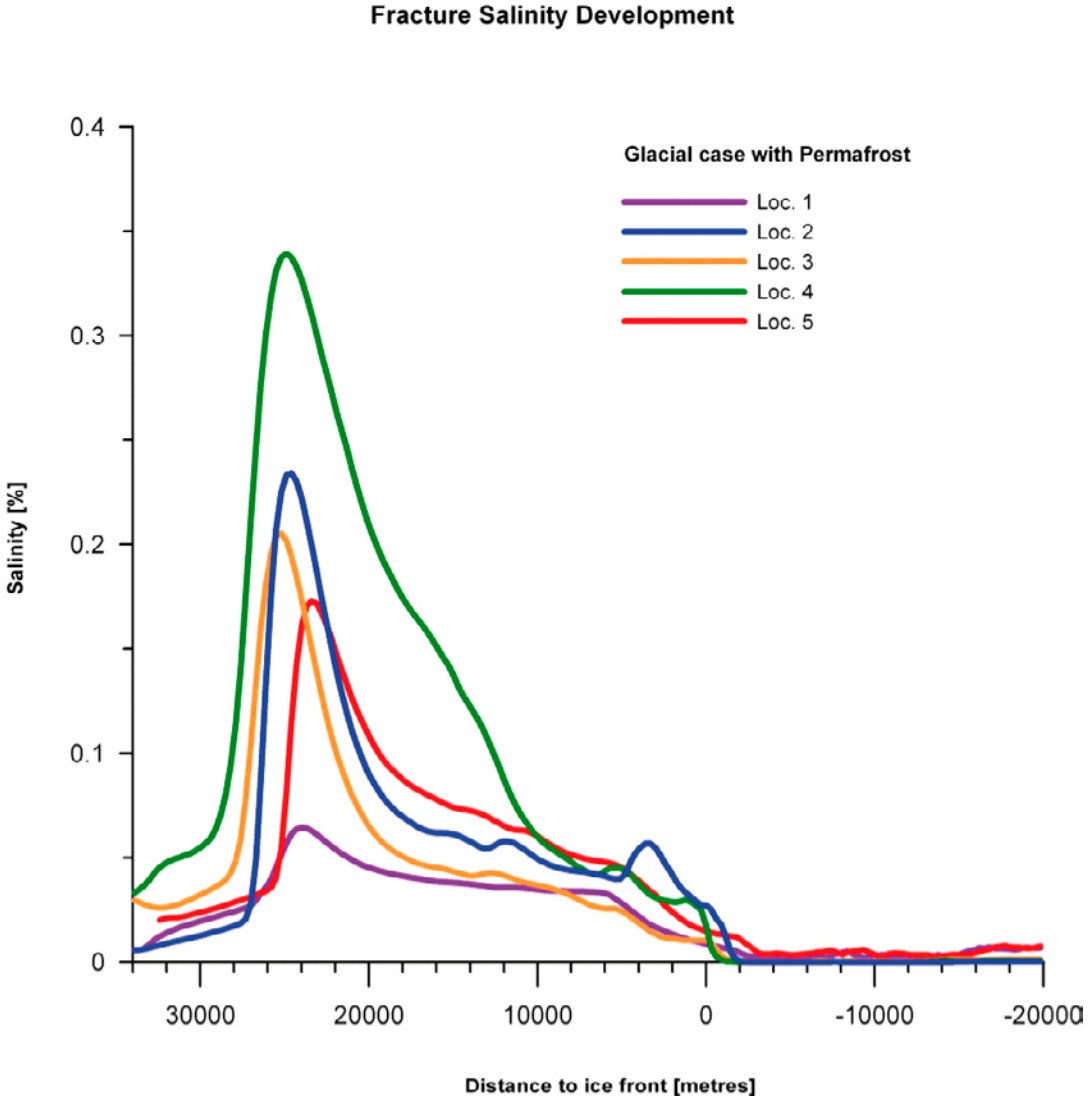

Figure F-9. *Fracture water salinity at measurement localities ML 1-5 during glacial conditions. Positive distance values mean that the ice sheet margin has not yet arrived to the measurement locations.*

F.6 Recharge and discharge locations

The repository considered for modelling contains 8,031 deposition hole positions. One particle is released at each deposition hole position and all particles are tracked backwards and forwards as a means of identifying their recharge and discharge locations, respectively. It is noted that the Darcy fluxes are fixed in space and time during the particle tracking, which is a simplification since the boundary conditions at the ground surface change with the position of the advancing ice sheet margin. Figure F-10 shows the results from the particle tracking when the ice sheet profile addressed in case (d) reached ice-front location II. Figure F-10 reveals that most particles recharge at the upstream boundary of the model domain, which strongly indicates that the model domain is too short to give a undisturbed view of the recharge locations for a fixed Darcy flux field. Nevertheless, it may be concluded that the present-day topographic water divides, which play an important role in recharge and discharge during temperate conditions, are significantly diminished in importance during glacial conditions and especially during glacial conditions together with extensive permafrost development.

In contrast, the discharge locations are predominantly found well within the physical boundaries of the model domain and, as a matter of fact, mostly along the predicted future shoreline downstream the ice margin in the domain. At ice-front location II (Figure F-10), the discharge pattern is strongly affected by the deformation zone model that exists within the regional flow domain treated in SDM-Site. In Figure F-10, 7,417 particles discharge in the taliks, whereas 347 particles discharge through the permafrost layer. That is, the permafrost has a low permeability (less than $1 \cdot 10^{-20}$ m^2), but it is not impervious with regard to the strong hydraulic gradient close to the ice sheet margin.

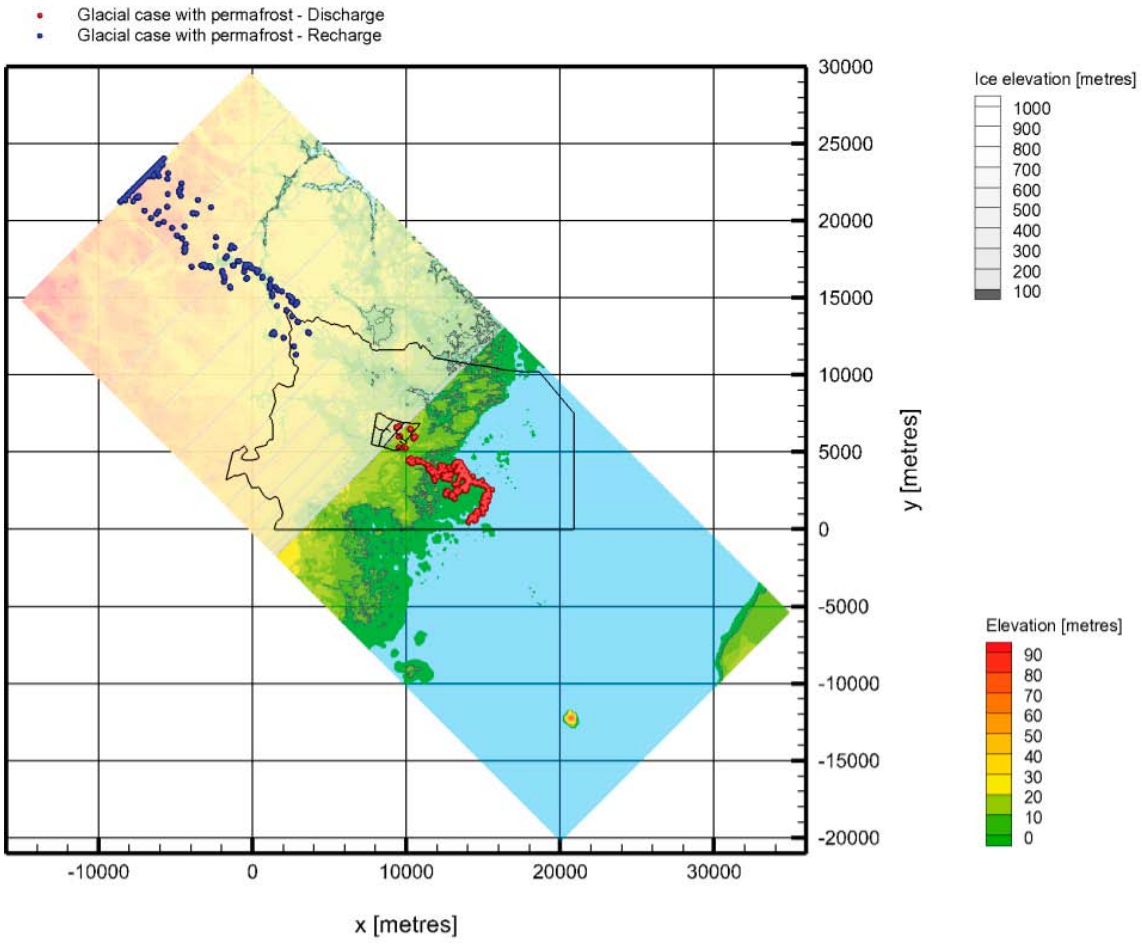

Figure F-10. *Recharge (blue) and discharge (red) locations during glaciation for 8,031 particles released at repository depth when the ice sheet margin is at IFL II. The short black lines in the centre of each image indicate the location of major tunnels.The y-axis points towards north.*

F.7 Recharge performance measures

The results from the backward particle tracking are shown in Figure F-11 to Figure F-13. It is noted that careful consideration needs to be given as to whether any quantitative conclusions can be drawn based on this information as most of the recharge locations are on the model boundary. However, the information provided here can be used for qualitative conclusions.

Particles are released at the 8,031 deposition hole positions and at the five measurement localities, ML 1-5, and tracked for 100 years. All of the released particles reach the ground surface within this period of time. Figure F-11, Figure F-12 and Figure F-13 show the cumulative distribution (probability) plots of the recharge flow path lengths, travel times, and flow-related transport resistances for the particles released at the 8,031 deposition hole positions when the ice sheet profile addressed in case (d) is at ice-front location II. The corresponding cumulative distributions of these performance measures for the temperate situation addressed in case (a) are also shown in these figures as well as the data for ML 1-5 when the ice sheet profile addressed in case (d) is at ice-front location II.

Figure F-11 shows cumulative distribution plots of the recharge flow path lengths (L_R). Typically the influence of an ice sheet with permafrost give greater flow path lengths. All measurement localities as well as deposition hole positions recharge at the upstream model boundary. Thus the assessed model domain is too small to capture the complete recharge behavior.

Figure F-12 shows cumulative distribution plots of the recharge travel times ($t_{w,R}$). The influence of an ice sheet slows up some of the fastest particles. However, in general the increase in recharge travel time is about a factor 2. The results for the measurement localities are scattered around the results for the tracked deposition hole positions. It is worth noting that during the tracked 100 years the ice sheet if allowed to continue to advance would have moved forward some 5 km.

Figure F-13 shows cumulative distribution plots of the recharge flow-related transport resistances (F_R). The flow-related transport resistance is in general localized around the mean indicating relatively similar recharge characteristics for all particles. The results for the measurement localities are scattered around the results for the tracked deposition hole positions.

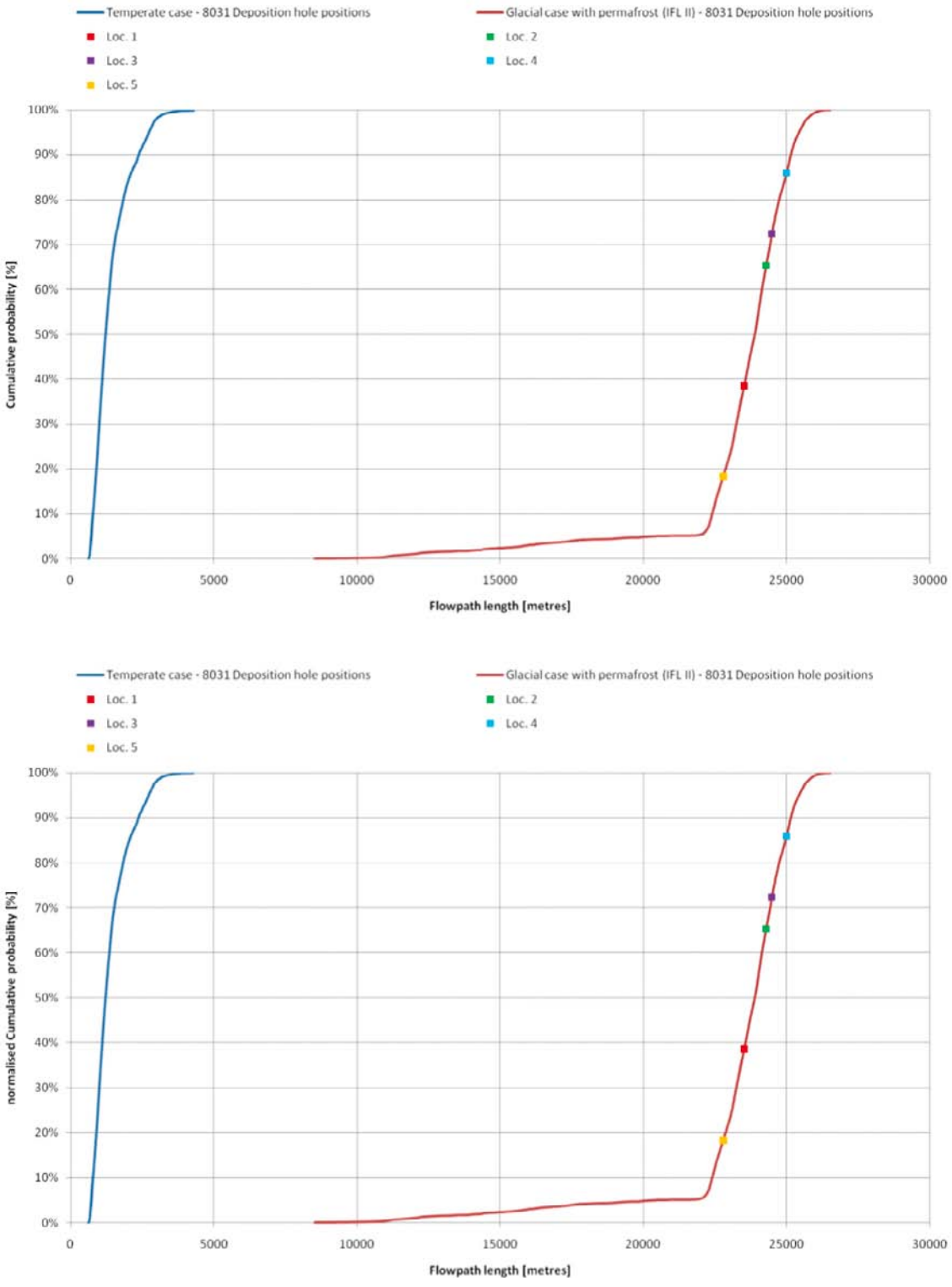

Figure F-11. *Cumulative distribution (probability) plots of the simulated recharge flow path lengths, L_R, when the ice sheet margin is at IFL II. The distribution for the temperate case is also shown as well as the data for ML 1-5 at IFL II. The maximum value in the upper plot is set to 100% in the lower plot.*

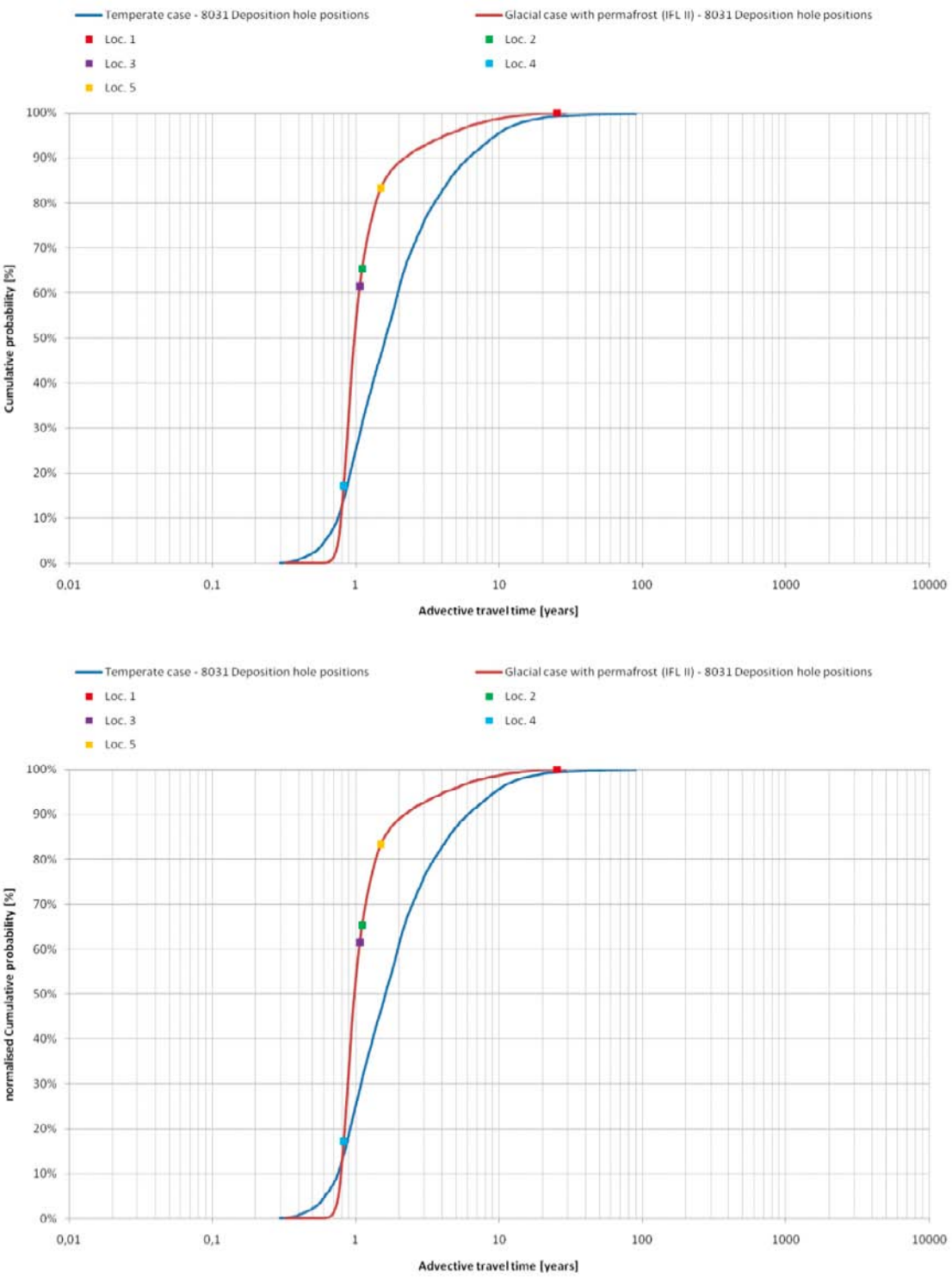

Figure F-12. *Cumulative distribution (probability) plots of the simulated recharge travel times, $t_{w,R}$, when the ice sheet margin is at IFL II. The distribution for the temperate case is also shown as well as the data for ML 1-5 at IFL II. The maximum value in the upper plot is set to 100% in the lower plot.*

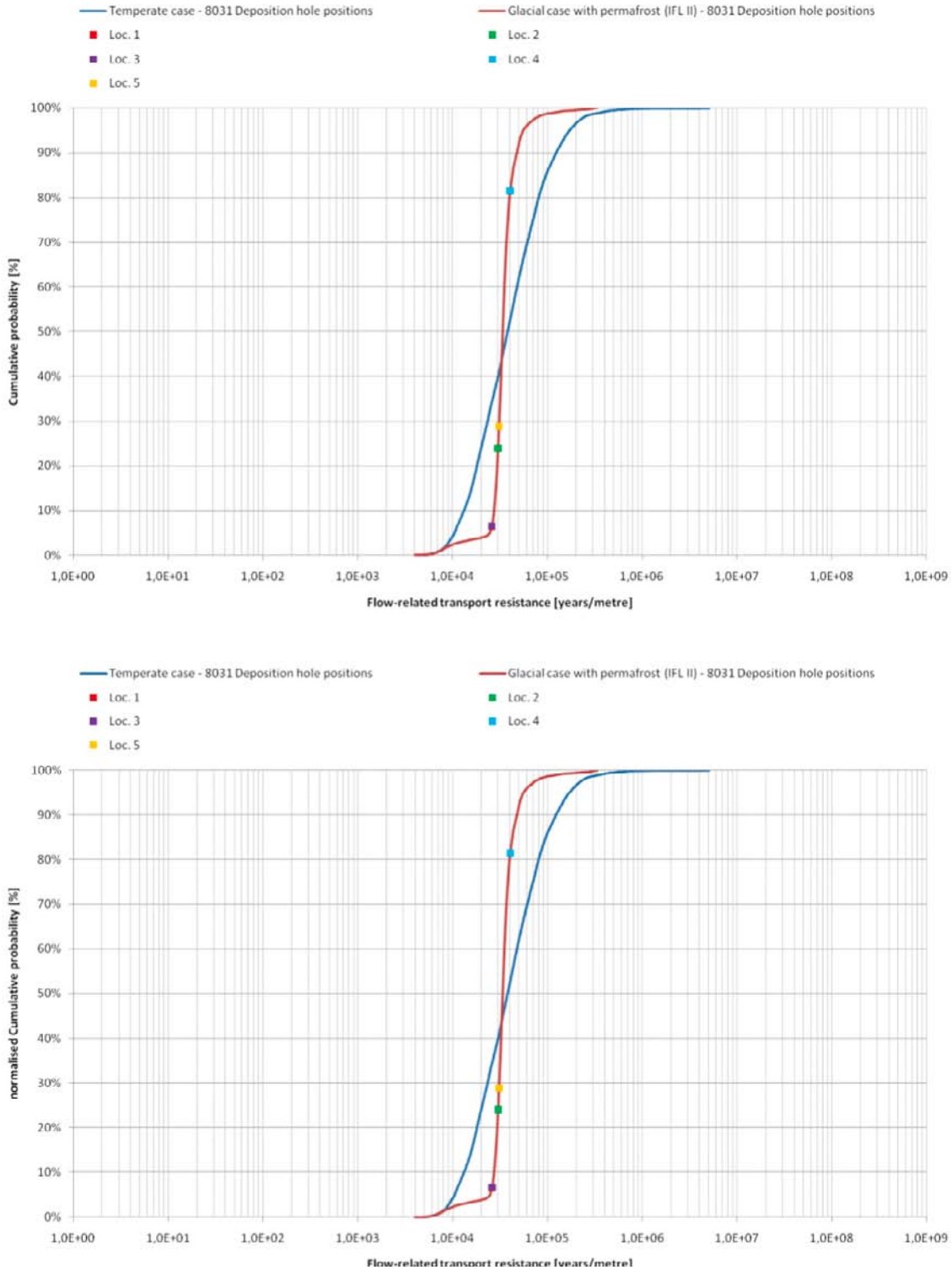

Figure F-13. *Cumulative distribution (probability) plots of the simulated recharge flow-related transport resistances, F_R, when the ice sheet margin is at IFL II. The distribution for the temperate case is also shown as well as the data for ML 1-5 at IFL II. The maximum value in the upper plot is set to 100% in the lower plot.*

F.8 Discharge performance measures

Particles are released at the 8,031deposition hole positions and at the five measurement localities, ML 1-5, and tracked for 100 years. Not all of the released particles reach the ground surface within this period of time. Figure F-14, Figure F-15 and Figure F-16 show the cumulative distribution (probability) plots of the discharge flow path lengths, travel times, and flow-related transport resistances for the particles released at the 8,031 deposition hole positions when the ice sheet profile addressed in case (d) is at ice-front location II. The corresponding cumulative distributions of these performance measures for the temperate situation addressed in case (a) are also shown in these figures as well as the data for ML 1-5 when the ice sheet profile addressed in case (d) is at ice-front location II.

Figure F-14 shows cumulative distribution plots of the discharge flow path lengths (L_D). A majority of the particles discharge in the talik represented by the predicted future shoreline. A limited number of particles discharges through the less frozen deformation zones.

Figure F-15 shows cumulative distribution plots of the discharge travel times ($t_{w,D}$). The discharge travel times are significantly shorter in case (d) as compared with temperate conditions, even though the particles have some 2–4 km longer flow path lengths. This, of course, is a result of the in general higher Darcy fluxes in case (d). The measurement localities give results within the expected range based on the deposition hole positions.

Figure F-16 shows cumulative distribution plots of the discharge flow-related transport resistances (F_D). The flow-related transport resistance is in general lowered by one order of magnitude for the few particles that result in the earliest discharge. Thereafter the flow-related transport resistance of the remaining particles in case (d) is approximately constant at $2 \cdot 10^4$ y/m, whereas for the temperate situation the flow-related transport resistance continues to increase as more particles arrive at its discharge locations.

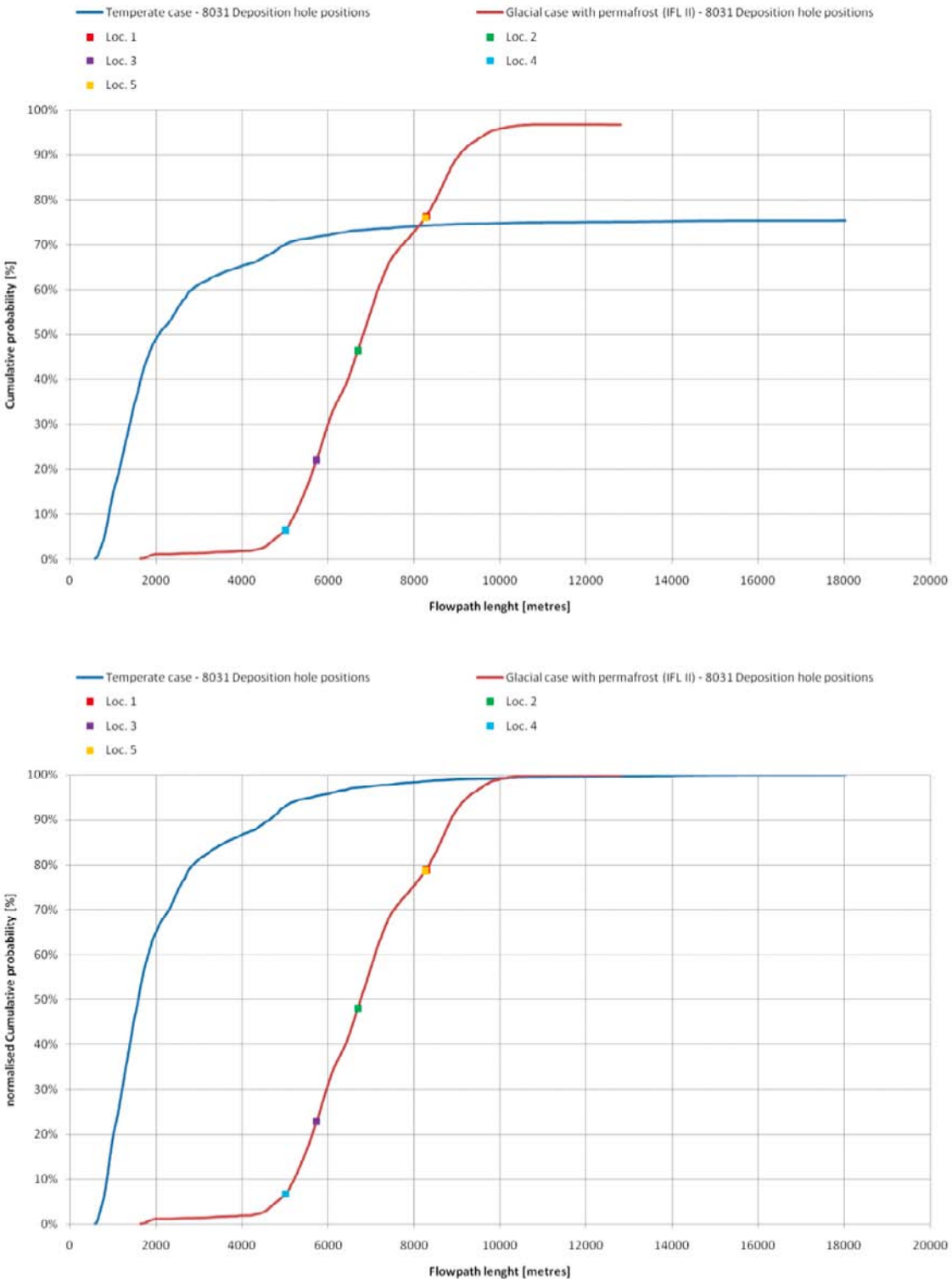

Figure F-14. *Cumulative distribution (probability) plots for the simulated discharge flow path lengths, L_D, when the ice sheet margin is at IFL II. The distribution for the temperate case is also shown as well as the data for ML 1-5 at IFL II. The maximum value in the upper plot is set to 100% in the lower plot.*

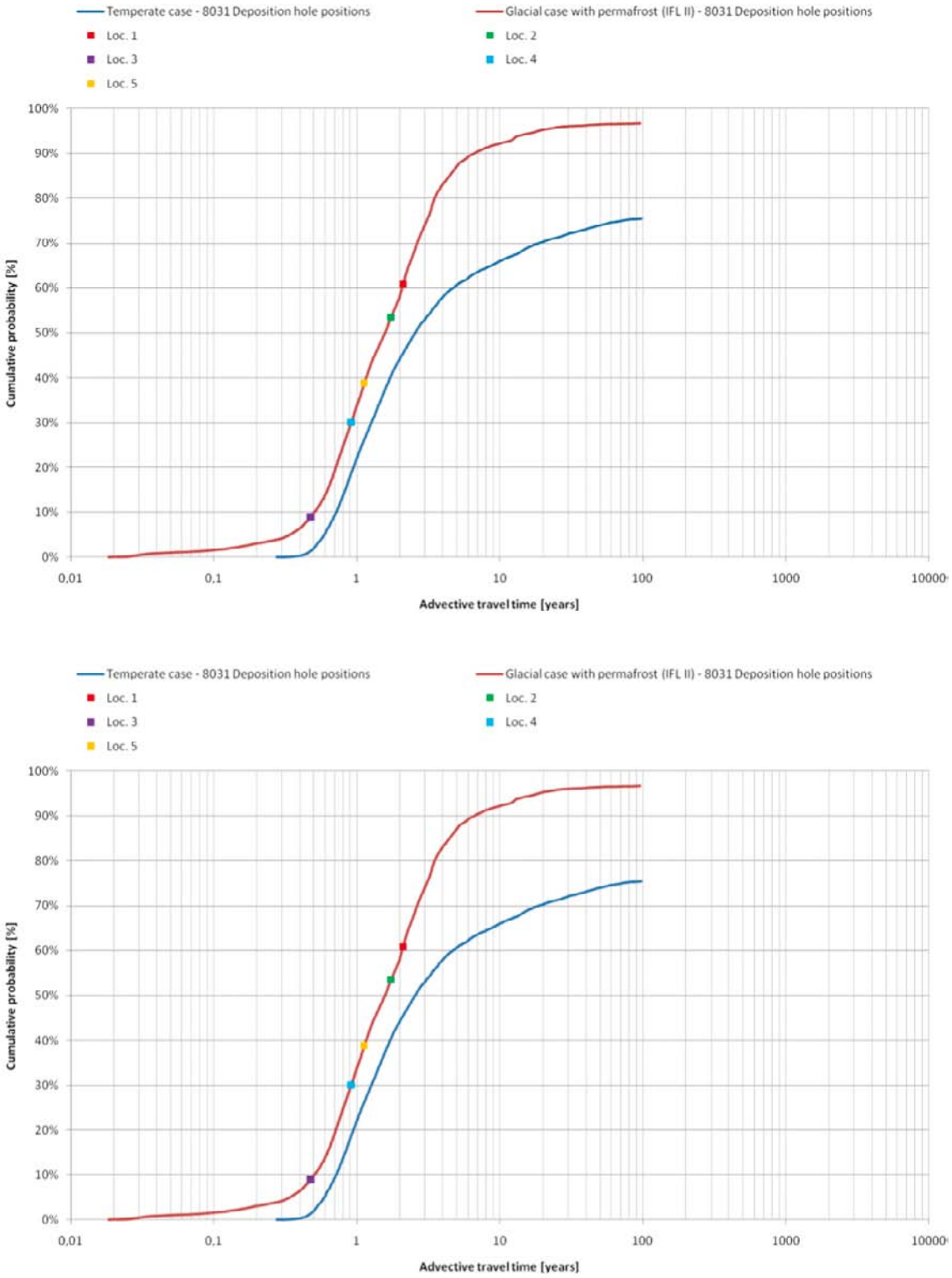

Figure F-15. *Cumulative distribution (probability) plots for the simulated discharge travel times, $t_{w,D}$, when the ice sheet margin is at IFL II. The distribution for the temperate case is also shown as well as the data for ML 1-5 at IFL II. The maximum value in the upper plot is set to 100% in the lower plot.*

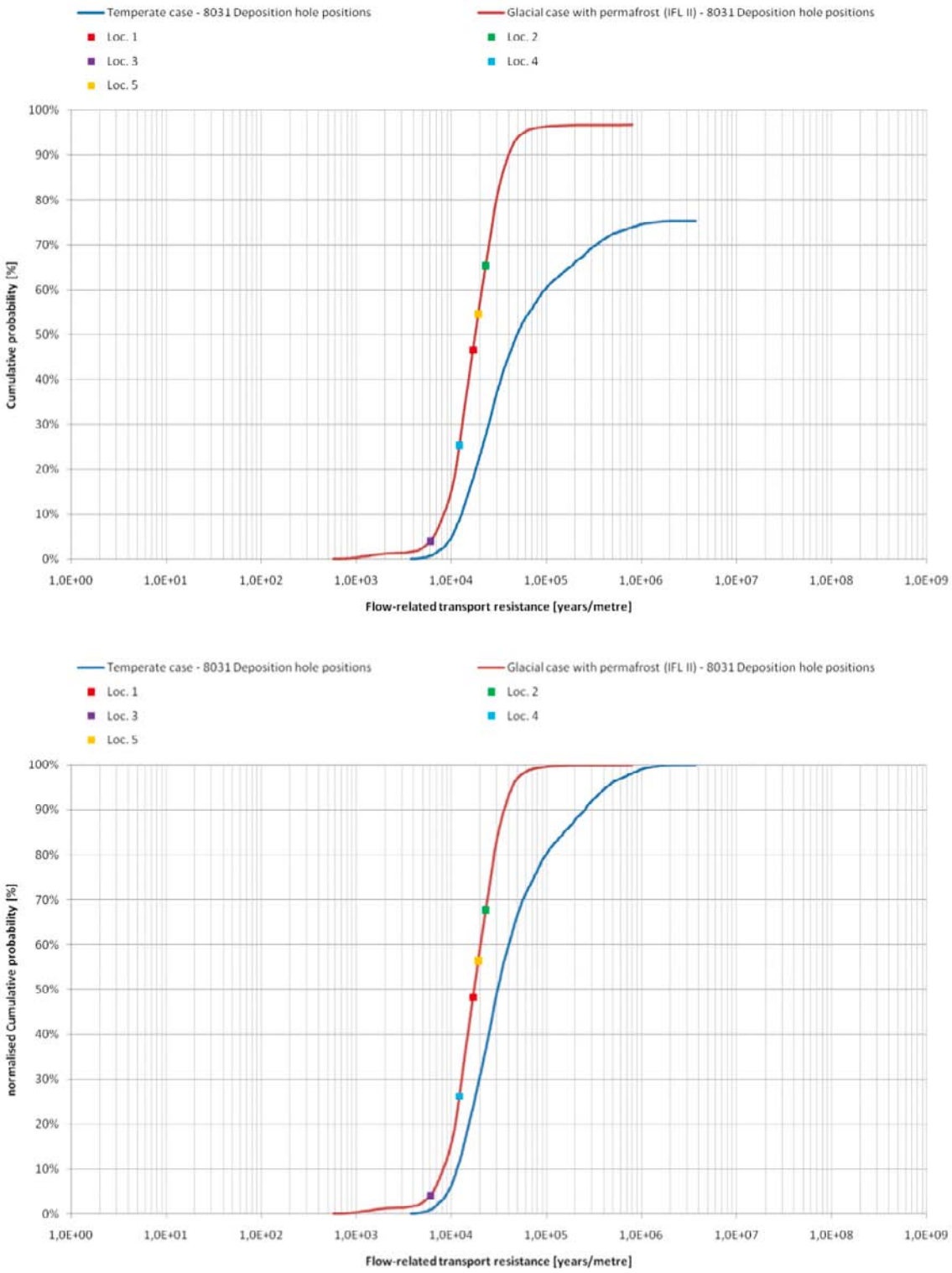

Figure F-16. *Cumulative distribution (probability) plots for the simulated discharge flow-related transport resistances, F_D, when the ice sheet margin is at IFL II. The distribution for the temperate case is also shown as well as the data for ML 1-5 at IFL II. The maximum value in the upper plot is set to 100% in the lower plot.*